Measuring the distribution of stars and dark matter in galaxy-scale strong gravitational lenses: lessons from an automated approach

ETHERINGTON, AMY

Measuring the distribution of stars and dark matter in galaxy-scale strong gravitational lenses: lessons from an automated approach

Amy Etherington

Abstract: In this thesis, I constrain the distributions of mass and light of the largest sample of galaxy-scale strong lens systems modelled using an automated approach to this date. New surveys will soon observe hundreds of thousands of galaxy lenses requiring reliable automated methods to be exploited. With this in mind, I present not only the successful model fit results, but also the reasons why some lenses failed initially and the strategies we adopted to ultimately fit all the galaxies with minimal intervention. I discuss what we can learn from this process that could benefit future large scale studies.

I propose and evaluate a likelihood cap method to avoid the underestimation of errors due to noisy likelihood evaluations that appear in pixel-based source reconstruction methods. I test the method on a large sample of mock galaxies which significantly improves the coverage probabilities on all of the model parameters. With this approach to error estimation I find that the Einstein radius is typically constrained to $\sim 1\%$ and the errors on the model parameters including density profile slope do not degrade with redshift. This will be beneficial for studies of galaxy evolution.

I measure an average mass density slope of $\langle\gamma\rangle = 2.075^{+0.023}_{-0.024}$ with little intrinsic scatter $\sigma_\gamma = 0.172^{+0.022}_{-0.032}$ for the (typically) early-type galaxies acting as lenses in our sample. This is consistent with those measured using an independent lensing and dynamics approach. More generally, this result supports the empirical coincidence that the total mass profiles of early-type galaxies can be well described by a single power law – known as the 'bulge-halo conspiracy'. However, I reveal a 3σ disagreement between our measurements of the coefficient describing the relationship between slope and surface mass density $\frac{\partial\langle\gamma\rangle}{\partial\Sigma_{\rm tot}} = -0.432^{+0.175}_{-0.191}$ and that inferred for the slopes measured using the independent method. This can potentially be explained by finer structure in the mass density profile. Finally, I demonstrate that the 'external shear' parameters commonly adopted in strong lens models can not be assumed to represent perturbations only external to the mass model. Instead, they highlight the inability of the power law to fit the distribution of mass in these types of galaxies. Future strong

lensing studies will require more complex mass models to appropriately describe the lens galaxy, and avoid biases on high precision measurements of galaxy masses, cosmological parameters H_0, and dark matter substructures.

Measuring the distribution of stars and dark matter in galaxy-scale strong gravitational lenses: lessons from an automated approach

Amy Etherington

A thesis presented for the degree of
Doctor of Philosophy

Centre for Extragalactic Astrophysics
Department of Physics
Durham University
United Kingdom

December 2022

Dedicated to

Grandad Harry and Grandad Tom

Contents

List of Figures

List of Tables

Declaration

The work in this thesis is based on research carried out in the Centre for Extragalactic Astrophysics, Department of Physics, Durham University, United Kingdom. No part of this thesis has been submitted elsewhere for any other degree or qualification and it is all my own work unless referenced to the contrary in the text.

The content presented in Chapter 2 has been published in the form of a paper:
Etherington, Amy; Nightingale, James W.; Massey, Richard; Cao, XiaoYue; Robertson, Andrew; Amorisco, Nicola C.; Amvrosiadis, Aristeidis; Cole, Shaun; Frenk, Carlos S.; He, Qiuhan; Li, Ran; Tam, Sut-Ieng. **Automated galaxy-galaxy strong lens modelling: no lens left behind** *Monthly Notices of the Royal Astronomical Society (2022)*, Volume 517, Pages 3275–3302

The content presented in Chapter 3 has been submitted in the form of a paper:
Etherington, Amy; Nightingale, James W.; Massey, Richard; Cao, XiaoYue; Robertson, Andrew; Amvrosiadis, Aristeidis; Cole, Shaun; Frenk, Carlos S.; He, Qiuhan; Lagattuta, David J.; Lange, Samuel; Li, Ran; **Beyond the bulge-halo conspiracy? Density profiles of Early-type galaxies from extended-source strong lensing** *ArXiv Astrophysics e-prints*, arXiv:2207.04070.

The author intends to submit the material comprising Chapter 4 in the form of a paper. The weak lensing shape measurements described in Section 4.4.1 were provided by a collaborator. The author of the thesis was primarily responsible for all other aspects of this publication.

Acknowledgements

Richard and James, thank you both for being so welcoming when I naively thought I was embarking on a single year Masters degree. You made it an easy decision to stay at Durham to instead complete my Doctorate. Richard, I have you to thank for making that possible, I can only wish I could have the enthusiasm for science that you do. James, you've been available at almost any moment to chat and answer my questions, even when I feared my questions didn't make any sense, for that I am grateful.
To the lensing group - Carlos, Shaun, Andrew, Qiuhan, Aris, Ran, and XiaoYue - thank you all for welcoming me into the group meetings, for your comments and suggestions on my papers I am very grateful. Thanks in particular to Andrew for having the clearest explanations and answers to my questions outside of these meetings also.
My thanks go out to everyone in the department at Durham for creating such a warm environment to work in. Although I've spent a lot of the past year working from home there never failed to be a friendly face to speak to when I showed my face in the office. A few special mentions must first go out to Jake, I'm so grateful you too lived in Newcastle throughout the pandemic, our weekly walks and rants about PhD life kept me going. You never failed to make me laugh, even when I was struggling at times, thank you. Ellen, Vicky, and Alice, seeing three amazing women doing great science has been a source of inspiration for me, thank you for that and for all the good times too. Miguel, thanks for all the climbing psyche, it's been a joy to climb with you. Thanks also for all the long chats on the way to the crag. Jack, thanks for keeping me distracted from my work (when I wanted to be!) with a good conversation, I can only hope you wanted to be distracted too. Thanks to Aidan for providing these same welcome distractions in my first year.
Mam and Dad, I'm not sure I'd be here without you. Especially Dad, when deciding between an art or physics degree your disapproval of me doing art (although I'm not sure you told me this it certainly felt that way) surely tipped me into choosing physics instead. Mam, thanks for being there when I need a chat especially during covid, and for the reminders not to get too stressed when I needed that too. Ben, I'm so grateful we get to share climbing together, thanks for all the sessions that have kept me going through the past few years. My thanks go out to all the rest of my family, not excluding

Alex's family whom I must thank for checking in with me when you knew I was stressed. Shout out to Dan for the thesis writing hype, and to Jules also for the kind words.

Alex, no combination of words could truly express my gratitude for you throughout this process. You're the reason I've maintained what little sanity I feel I have left. Although, choosing to convert a van together in the final year of my PhD has certainly tested my sanity. Thanks for embarking on this crazy journey with me. Thanks for all the silliness. I can only apologise for keeping us stuck in the North East for the past few years while I study some galaxies nobody cares about, I'm thoroughly looking forward to whatever comes next.

Chapter 1

Introduction

1.1 General Relativity: A foundation for understanding the Universe

Gravity is the fundamental force that dominates at large scales of the Universe. Our current description of gravity is a geometric one; introduced by Albert Einstein in 1915 (Einstein, 1915), the General Theory of Relativity has stood the test of time remaining the simplest theory consistent with experimental data (Abbott et al., 2016, 2021; Castelvecchi, 2022). Before General Relativity (GR) questions about the geometry of space and the role of gravity on cosmological scales were studied separately. We give a brief overview of Einstein's realisation that they are fundamentally linked, providing the framework that the majority of astrophysicists use to study the Universe today.

1.1.1 The equivalence principle

Historically deemed the starting point of a series of discoveries that culminated in Einstein's formulation of GR is his realisation of the importance of the equivalence of the gravitational and inertial mass (Einstein, 1907). Although, knowledge of the equivalence already existed, for example Galileo experimentally expressed that the acceleration of some mass due to gravity does not depend on the amount of mass being accelerated, it was Einstein who formally introduced the concept as a physical principle. The equivalence principle (EP) arose from one of Einstein's famous thought experiments (Einstein, 1920).

He considered an observer in a spacious chest freely falling in a large portion of empty space. Since objects fall with the same acceleration, the observer would consider themself and any released objects weightless, since they would not appear to fall. The observer would thus be justified in interpreting their state as at rest, with gravity ceasing to exist. Continuing the experiment, Einstein considered how

the observer would perceive themself if the chest was then pulled upwards in space with a uniform acceleration. The observer would now find themselves standing on the floor, which transmits the acceleration to them through its reaction, and other objects would now fall to the floor with that same acceleration. Thus, Einstein concludes the observer's perceptions are consistent with being in a uniform gravitational field. The EP states that accelerating frames of reference are just frames with gravity, and can be treated in exactly the same way as inertial frames - those without gravity.

The EP in its strong form[1] extends the equivalence to all laws of nature in freely falling systems of local inertia, to which Einstein applied the physics of his special theory of relativity. Armed with the equivalence principle Einstein set out to formulate gravity such that all observers could agree on the definition, regardless of their motion relative to each other. The consequence of which was his proposal that the gravitational field *is* curved space-time.

1.1.2 Mathematical framework

In his theory of special relativity (SR) Einstein unified space and time by treating time and space coordinates equally in a single vector (Einstein, 1907). This four-dimensional manifold, known as Minkowski space, has coordinates $x^\mu = (x^0, x^1, x^2, x^3) = (ct, x, y, z)$, where ct is the time coordinate with c equal to the speed of light, and x, y, and z are spatial coordinates. The interval between two events (world points) in Minkowski space, which require all four coordinates to be defined, is given by the spacetime interval

$$ds^2 = -c^2dt^2 + dx^2 + dy^2 + dz^2 \tag{1.1.1}$$

$$= \eta_{\mu\nu}dx^\mu dx^\nu, \tag{1.1.2}$$

which is analogous to a distance in three-dimensional space. The Einstein summation convention[2] has been used to arrive at the final form for ds^2, and we have defined the Minkowski metric

$$\eta_{\mu\nu} = \begin{pmatrix} -1 & 0 & 0 & 0 \\ 0 & 1 & 0 & 0 \\ 0 & 0 & 1 & 0 \\ 0 & 0 & 0 & 1 \end{pmatrix}. \tag{1.1.3}$$

The metric describes the geometry of the manifold which, given it is a constant in Minkowski space, is described as being flat. The negative value of the metric component $\eta_{00} = -1$ is the only differentiating

[1] The weak equivalence principle, also known as the Galilean equivalence principle, is restricted to the physics of mechanics and is essentially a restatement of the fact that the inertial mass equals the gravitational mass.

[2] In the summation convention identical upper and lower indices are implicitly summed over all their possible values.

factor from the familiar Euclidean geometry that permeates our every day experience. Transitioning from this pseudo-Euclidean flat spacetime to one that could be curved required Einstein to formulate the concepts of GR in a non-Euclidean space, for which Reimann provided the appropriate geometrical framework (Riemann, 1854).

Reimannian geometry is essentially an extension of Gauss's theory of curved surfaces to higher dimensional curved spaces. With this geometrical prescription points in space can be labelled without reference to objects outside of that space using generalised Gaussian coordinates. In GR a given set of coordinates of the spacetime manifold are related to the invariant interval ds^2 through

$$ds^2 = g_{\mu\nu} dx^\mu dx^\nu, \tag{1.1.4}$$

where the metric $g_{\mu\nu} \neq \eta_{\mu\nu}$ is no longer constant as in SR. Although locally the metric does describe a Minkowskian spacetime, globally it is curved. The metric encodes the information necessary to determine this *curvature* of spacetime, the nonlinear second derivative of the metric which measures the deviations from Euclidean geometry.

To describe how a particle travels in this curved spacetime, we replace the concept of a straight line with the geodesic which describes the shortest and straightest possible path a particle can take. From equation 1.1.4 we can define the length of a curve between two points

$$s = \int ds = \int \sqrt{g_{\mu\nu} dx^\mu dx^\nu} = \int \sqrt{g_{\mu\nu} \frac{dx^\mu}{d\lambda} \frac{dx^\nu}{d\lambda}} d\lambda = \int L d\lambda, \tag{1.1.5}$$

where we have both introduced the affine parameter λ, and defined the 'Lagrangian'

$$L = L(x, \dot{x}) = \sqrt{g_{\mu\nu} \frac{dx^\mu}{d\lambda} \frac{dx^\nu}{d\lambda}}, \tag{1.1.6}$$

where $\dot{x} = dx/d\lambda$. To determine the shortest possible path this curve can take in curved space, we impose the extremization condition for variation of the path with end points fixed

$$\delta s = \delta \int L(x, \dot{x}) d\lambda = 0. \tag{1.1.7}$$

By calculus of variation this can be translated into the Euler-Lagrange partial differential equation

$$\frac{d}{d\lambda} \frac{\partial L}{\partial \dot{x}^\rho} - \frac{\partial L}{\partial x^\rho} = 0. \tag{1.1.8}$$

We will now pass the Lagrangian (equation 1.1.6) through this equation to determine the shortest path in the general spacetime metric $g_{\mu\nu}$. We begin by calculating the partial differential in the first term

using the chain rule

$$\frac{\partial L}{\partial \dot{x}^\rho} = \frac{1}{2\sqrt{g_{\mu\nu}\dot{x}^\mu \dot{x}^\nu}} \frac{\partial}{\partial \dot{x}^\rho}\left(g_{\mu\nu}\dot{x}^\mu \dot{x}^\nu\right) \tag{1.1.9}$$

$$= \frac{1}{2L}(g_{\mu\nu}\delta^\mu_\rho \dot{x^\nu} + g_{\mu\nu}\delta^\nu_\rho \dot{x^\mu}) = \frac{1}{2L}(g_{\rho\nu}\dot{x^\nu} + g_{\rho\mu}\dot{x^\mu}) \tag{1.1.10}$$

$$= \frac{1}{L} g_{\rho\mu}\dot{x}^\mu, \tag{1.1.11}$$

where in the last step we used the symmetry of the metric. If we now use the definition of s in equation 1.1.5 to note that $\frac{ds}{d\lambda} = L$ then we can obtain

$$\frac{\partial L}{\partial \dot{x}^\rho} = \frac{1}{L} g_{\rho\mu}\frac{dx^\mu}{ds}\frac{ds}{d\lambda} = \frac{1}{L} g_{\rho\mu}\frac{dx^\mu}{ds} L \tag{1.1.12}$$

$$= g_{\rho\mu}\frac{dx^\mu}{ds}. \tag{1.1.13}$$

Evaluating the second term in equation 1.1.8 we have

$$\frac{\partial L}{\partial x^\rho} = \frac{1}{2L}\frac{\partial g_{\mu\nu}}{\partial x^\rho}\dot{x}^\mu \dot{x}^\nu = \frac{1}{2L}\frac{\partial g_{\mu\nu}}{\partial x^\rho}\frac{dx^\mu}{ds}\frac{ds}{d\lambda}\frac{dx^\nu}{d\lambda} \tag{1.1.14}$$

$$= \frac{1}{2}\frac{\partial g_{\mu\nu}}{\partial x^\rho}\frac{dx^\mu}{ds}\frac{dx^\nu}{d\lambda}. \tag{1.1.15}$$

Substituting the terms derived in equations 1.1.11 and 1.1.15 into the Euler-Lagrange equation (equation 1.1.8) and multiplying both sides by $d\lambda/ds$ then

$$\frac{d}{d\lambda}\left(g_{\rho\mu}\frac{dx^\mu}{ds}\right) - \frac{1}{2}\frac{\partial g_{\mu\nu}}{\partial x^\rho}\frac{dx^\mu}{ds}\frac{dx^\nu}{d\lambda} = 0 \tag{1.1.16}$$

$$\frac{d}{ds}\left(g_{\rho\mu}\frac{dx^\mu}{ds}\right) - \frac{1}{2}\partial_\rho g_{\mu\nu}\frac{dx^\mu}{ds}\frac{dx^\nu}{ds} = 0. \tag{1.1.17}$$

We have arrived at the geodesic equation. This can equivalently be written in the following form

$$\frac{d^2x^\lambda}{ds^2} + \Gamma^\lambda_{\mu\nu}\frac{dx^\mu}{ds}\frac{dx^\nu}{ds} = 0, \qquad \text{with} \qquad \Gamma^\lambda_{\mu\nu} = \frac{1}{2}g^{\lambda\rho}(g_{\mu\rho,\nu} + g_{\nu\rho,\mu} - g_{\mu\nu,\rho}), \tag{1.1.18}$$

where $g_{\mu\nu,\rho}$ is the first derivative of the metric with respect to ρ. To determine the form of the metric function, hence the geometry of spacetime itself, one must solve the equations underpinning the general theory of relativity; Einstein's field equations

$$R_{\mu\nu} - \frac{1}{2}g_{\mu\nu}R = \frac{8\pi G}{c^4}T_{\mu\nu} + \Lambda g_{\mu\nu}, \tag{1.1.19}$$

where the Ricci tensor $R_{\mu\nu}$ and Ricci scalar R are functions of the metric $g_{\mu\nu}$, $T_{\mu\nu}$ is the energy momentum tensor, and Λ is a constant of integration. Thus, the equations describe how the energy momentum of a field of matter (encompassed in $T_{\mu\nu}$) relates to the curvature of spacetime. Although

often difficult to solve[3], through determining $g_{\mu\nu}$, Einstein's field equations predict a number of interesting and useful physical consequences.

1.1.3 The deflection of light and other consequences

From consideration of the EP alone, Einstein had deduced that light rays will be deflected by massive objects. With completion of the mathematical formulation of GR, he was now able to describe the trajectory of a photon in the presence of matter that distorts spacetime. We will now derive the angular deflection of light by a point mass, demonstrating how Einstein was able to predict how much the light of a star grazing past the sun would be deflected. The geometry of spacetime induced by a static, spherically symmetric mass M is described by the Schwarzschild metric

$$ds^2 = -\left(1 - \frac{2GM}{rc^2}\right)c^2dt^2 + \left(1 - \frac{2GM}{rc^2}\right)^{-1} dr^2 + r^2d\theta^2 + r^2\sin^2\theta d\phi^2, \tag{1.1.20}$$

which is the vacuum solution ($T_{\mu\nu} = 0$) to Einstein's field equations (equation 1.1.19) under these assumptions. Light travels along null geodesics in spacetime whose tangent vector must be equal to zero,

$$g_{\mu\nu}\frac{dx^\mu}{d\lambda}\frac{dx^\nu}{d\lambda} = 0, \tag{1.1.21}$$

where λ is an affine parameter. Considering the trajectory of a photon in the equatorial plane ($\theta = \pi/2$) of the Schwarzschild metric, then we have

$$-\left(1 - \frac{2M}{r}\right)\left(\frac{dt}{d\lambda}\right)^2\left(1 - \frac{2M}{r}\right)^{-1}\left(\frac{dr}{d\lambda}\right)^2 + r^2\left(\frac{d\phi}{d\lambda}\right)^2 = 0, \tag{1.1.22}$$

where we have now adopted gemoetrised units $c = G = 1$ units. Due to the independence of the metric (equation 1.1.20) in both t and ϕ, there exists two killing vectors $k^t = (1, 0, 0, 0)$ and $k^\phi = (0, 0, 0, 1)$ that leave the metric unchanged under infinitesimal coordinate changes. Hence, we can define the two constants

$$e = k_t\frac{dt}{d\lambda} = -\left(1 - \frac{2M}{r}\right)\frac{dt}{d\lambda} \tag{1.1.23}$$

$$l = k_\phi\frac{d\phi}{d\lambda} = r^2\frac{d\phi}{d\lambda}, \tag{1.1.24}$$

which satisfy the geodesic equation (equation 1.1.18). Substituting these into equation 1.1.22 and rearranging we find

$$\frac{e^2}{l^2} = \frac{1}{l^2}\left(\frac{dr}{d\lambda}\right)^2 + \frac{1}{r^2}\left(1 - \frac{2M}{r}\right), \tag{1.1.25}$$

[3]Somewhat unsurprisingly for a set of no less than ten non-linear equations which must be solved for simultaneously

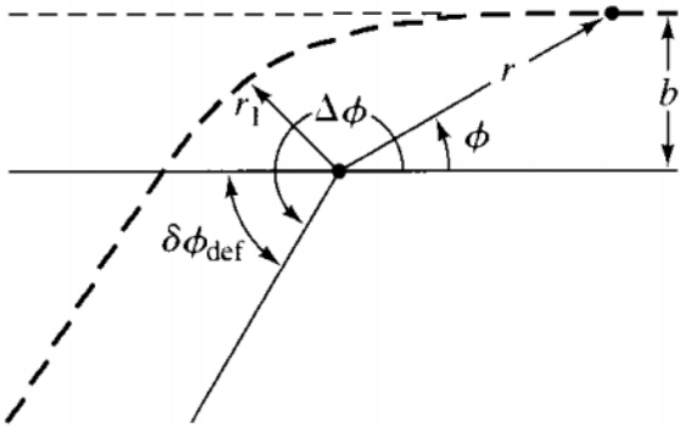

Figure 1.1: The trajectory of a photon in the curved spacetime induced by a point mass. The photon enters right with an impact parameter b, approaching the mass until the turning point r_1 where it exits to infinity. The deflection angle $\delta\phi_{\rm def}$ from the photon's original parallel trajectory is therefore $\delta\phi_{\rm def} - \pi$, where $\Delta\phi$ is total angle swept out by the photon's orbit. Figure reproduced from Hartle (2003).

which takes the form of an energy integral for radial motion.

We now define the constant

$$b = \left|\frac{l}{e}\right| = \frac{r^2}{-\left(1 - \frac{2M}{r}\right)}\frac{d\phi}{dt}, \tag{1.1.26}$$

which represents the *impact parameter* since far away from the source of curvature ($r >> 2M$) the light ray will travel in a straight line with a perpendicular distance b from the source (see Figure 1.1). Solving equation 1.1.24 for $\frac{d\phi}{d\lambda}$ and equation 1.1.25 for $\frac{dr}{d\lambda}$ and dividing the two we arrive at

$$\frac{d\phi}{dr} = \pm\frac{1}{r^2}\left[\frac{1}{b^2} - \frac{1}{r^2}\left(1 - \frac{2M}{r}\right)\right]^{-1/2}, \tag{1.1.27}$$

where we have simplified using $b^2 = l^2/e^2$. We note that the point of closest approach r_1 is the radius where

$$b^2 = \frac{r_1^2}{\left(1 - \frac{2M}{r_1}\right)}. \tag{1.1.28}$$

Noting that the magnitude of the total angle $\Delta\phi$ swept out by the light ray that enters from and emerges to infinity is just twice the angle swept out from the turning point $r = r_1$ to infinity then we can write

$$\Delta\phi = 2\int_{r_1}^{\infty}\left[\frac{1}{b^2} - \frac{1}{r^2}\left(1 - \frac{2M}{r}\right)\right]^{-1/2} dr. \tag{1.1.29}$$

We can now use the first order approach

$$\Delta\phi \approx \Delta\phi\Big|_{M=0} + M\frac{\partial\Delta\phi}{\partial M}\Big|_{M=0} \tag{1.1.30}$$

to calculate the angle swept out by the light ray to first order in M. We first make the convenient change of variables $u = 1/r$, for which equation 1.1.29 becomes

$$\Delta\phi = 2\int_0^{1/r_1} \frac{du}{(b^{-2} - u^2 + 2Mu)^{1/2}}. \tag{1.1.31}$$

The first term in equation 1.1.30 can therefore be straightforwardly evaluated

$$\Delta\phi\big|_{M=0} = 2\int_0^{1/r_1} \frac{du}{(b^{-2} - u^2)^{1/2}} \tag{1.1.32}$$

$$= 2\sin^{-1}(b/r_1). \tag{1.1.33}$$

Recognising that this is just the case of a flat spacetime where $b = r_1$, then we have

$$\Delta\phi\big|_{M=0} = \pi, \tag{1.1.34}$$

where the light travels in a straight line. The second term in equation 1.1.30 therefore represents the light bending effect due to the Schwarzchild geometry i.e. the angular deflection $\delta\phi_{\rm def}$ in Figure 1.1 (valid to first order in M). Substituting equation 1.1.28 into equation 1.1.31 we obtain

$$\Delta\phi = 2\int_0^{1/r_1} \frac{du}{(r_1^{-2} - 2Mr_1^{-3} - u^2 + 2Mu^3)^{1/2}}, \tag{1.1.35}$$

which can be differentiated with respect to M at fixed r_1 to find

$$\frac{\partial(\Delta\phi)}{\partial M} = 2\int_0^{1/r_1} \frac{(r_1^{-3} - u^3)du}{(r_1^{-2} - 2Mr_1^{-3} - u^2 + 2Mu^3)^{3/2}}. \tag{1.1.36}$$

Hence, we can evaluate the deflection angle

$$\delta\phi_{\rm def} = M\frac{\partial(\Delta\phi)}{\partial M}\bigg|_{M=0} = 2M\int_0^{1/r_1} \frac{(r_1^{-3} - u^3)du}{(r_1^{-2} - 2Mr_1^{-3} - u^2 + 2Mu^3)^{3/2}}\bigg|_{M=0} \tag{1.1.37}$$

$$= 2M\int_0^{1/b} \frac{(b^{-3} - u^3)}{(b^{-2} - u^2)^{3/2}}du \tag{1.1.38}$$

$$= \frac{4M}{b}. \tag{1.1.39}$$

Reinserting the speed of light and the gravitational constant we have the final result

$$\delta\phi_{\rm def} = \frac{4GM}{c^2 b}, \tag{1.1.40}$$

which predicts a deflection angle of $\approx 1.74''$ for light passing near the Sun. A short time after this value was first predicted by Einstein, Sir Arthur Eddington observed the Solar eclipse of May 29 1919, providing verification that the light of stars were deflected by the Sun by exactly the predicted amount (Dyson & Davidson, 1920). This was not only the first consequence of GR that was confirmed, but also the first observational use of gravitational lensing, the astrophysical tool that forms the basis of

this thesis.

Subsequent observational confirmations of GR include the perihelion precession of Mercury(Le Verrier, 1859; Einstein, 1920), the gravitational redshift of light (Adams, 1925), and more recently the direct observation of black holes (Castelvecchi, 2022) and detection of gravitational waves (Abbott et al., 2016, 2021). Further testament to the theory's success is its role in cosmology, the study of the Universe as a whole, physical system. Since gravity determines the behaviour of all matter on cosmic scales, GR provides a framework for studying the structure and origin of the Universe, and has accommodated observational results such as Hubble's detection of an expanding Universe (Hubble, 1929). The expanding Universe models of GR lead to the prediction of the existence of a singularity at the very beginning, with infinite temperature and density.

It is here, at some point early in the Universe, where we must note that Einstein's equations break down due to the extreme physical conditions present. Einstein himself expressed that one can not "assume the validity of the equations for very high densities and it is just possible that in a unified theory there would be no such singularity" (Einstein, 1956). This remains to be seen, gravity is yet to be reconciled with the three fundamental non-gravitational forces: strong, weak, and electromagnetic, that are described by the standard model of particle physics. Fortunately, soon after the singularity GR, in combination with the standard model, can be regarded as an accurate description of the Universe, providing us with the foundation for the standard model of cosmology that we describe in the subsequent chapter.

1.2 ΛCDM: our current cosmological model

Under the assumption that GR is the correct description of gravity, to study cosmology we require a single further assumption known as the cosmological principle. This principle states that on large scales the Universe is homogeneous and isotropic around any point. Evidently, this is not true on the small scales we observe in our daily lives and even in our own galaxy. It may seem surprising then that the cosmological principle has been assumed to be true for decades now. Although in practise it allows for the simplification of Einstein's field equations (equation 1.1.19) when applied to the large scale behaviour of the Universe. Only fairly recently, have we obtained observational evidence that it does in fact appear to hold true (Fixsen et al., 1996; Wu, 1999)

1.2.1 Hot Big Bang: our expanding Universe

The most general space-time metric that satisfies the cosmological principle is the Robertson-Walker (RW) metric

$$ds^2 = -c^2dt^2 + a^2(t)\left[\frac{dr^2}{(1-kr^2)} + r^2(d\theta^2 + \sin^2\theta d\phi^2))\right] \tag{1.2.1}$$

(Robertson, 1935; Walker, 1936), where k is a constant that describes the curvature of the Universe, and $a(t)$ is a time dependent scale-factor that describes how the spatial distance between two events evolves with time. From a metric like this one, Hubble's law naturally emerges

$$\boldsymbol{v} = H\boldsymbol{r}, \tag{1.2.2}$$

which describes how the velocity $\boldsymbol{v}$ of a galaxy in the Universe receding from an observer is proportional to its distance $\boldsymbol{r}$ (Hubble, 1929). The constant of proportionality $H = \frac{\dot{a}(t)}{a(t)}$ is known as Hubble's constant. To understand the expansion history of the Universe one must solve Einstein's equations (equation 1.1.19) assuming the RW metric. A full derivation is given by Peebles (1993), the result of which is the Friedmann equations

$$\left(\frac{\dot{a}}{a}\right)^2 = \frac{8\pi G}{3}\rho - \frac{kc^2}{a^2} + \frac{\Lambda}{3} \tag{1.2.3}$$

$$\left(\frac{\ddot{a}}{a}\right)^2 = -\frac{4\pi G}{3}\left(\rho + \frac{3p}{c^2}\right), \tag{1.2.4}$$

that describe the evolution of $a(t)$ and its relation to the pressure p, density ρ, and geometry of the Universe k. Ultimately, the picture that emerges from this mathematical framework is that of the Hot Big Bang, which took place approximately 13.8 billion years ago. This model for the early Universe predicts that shortly after its origin the infinitely hot and dense Universe began to expand and cool, continuing to do so until this day. The cooling allowed for the formation of the first baryons, which after a few minutes into the expansion, underwent a process called big bang nucleosynthesis (BBN). Here, neutrons and protons combined to produce the Universe's first deuterium and helium nuclei. This process provides strong evidence for the Big Bang since the observed abundances of these light elements in the Universe are consistent with those predicted from baryon densities assuming BBN (Boesgaard & Steigman, 1985).

Much later, approximately 400,000 years after the Big Bang, the temperature dropped sufficiently to undergo recombination. This is when the Universe became transparent to radiation after protons and electrons first became bound to form atomic hydrogen. The radiation emitted during recombination can still be observed today as the cosmic microwave background (CMB). The first detection of the CMB was made by Penzias & Wilson (1965) who measured a homogeneous microwave radiation

with a temperature close to 3 Kelvins. Today, the CMB has been measured with great precision, Planck Collaboration et al. (2018) measure a temperature of T=2.725K, and is considered one of the strongest observational pieces of evidence in favour of the Big Bang. The CMB also provides us with an independent measurement of the aforementioned baryon density which is consistent with BBN. Moreover, it allows us to constrain the constituent parts of the energy density of the universe.

1.2.2 Contents of the Universe

The density in equation 1.2.4 refers not just to the mass-density but all forms of energy-density. This will be illuminated if we first define the density parameter

$$\Omega_m = \frac{\rho}{\rho_c}, \qquad \text{with} \qquad \rho_c \equiv \frac{3H^2}{8\pi G}, \tag{1.2.5}$$

which dictates the density of the Universe relative to the critical density ρ_c it would need to be flat ($k = 0$) with $\Lambda = 0$. Critical energy density parameters for radiation Ω_r, the curvature parameter Ω_k, and the cosmological constant Ω_Λ can be defined in a similar manner that when substituted into equation 1.2.4, arrives at

$$H^2 = H_0^2(\Omega_{m,0}/a^3 + \Omega_{r,0}/a^4 + \Omega_{k,0}/a^2 + \Omega_{\Lambda,0}), \tag{1.2.6}$$

where the subscript 0 denotes the value at the present day. These are the components that make up the ΛCDM Universe.

The Planck satellite's measurements of the CMB are consistent with a flat Universe $\Omega_k = 0.001 \pm 0.002$, and measures $\Omega_\Lambda = 0.6847 \pm 0.0073$, $\Omega_m = 0.315 \pm 0.007$, and $\Omega_r = 9.1 \times 10^{-5}$ (Planck Collaboration et al., 2018) . Thus, today there is a negligible contribution of radiation to the energy density budget. However, this was not the case early in the Universe, prior to recombination the Universe was in a radiation dominated era, after which it began to transition into a matter dominated era. At present times matter makes up only $\sim 32\%$ of the energy density of the Universe, and only $\sim 5\%$ is baryonic matter - the visible matter we observe here on Earth and the luminous matter we observe directly in our observations of galaxies. The other $\sim 27\%$ is Cold Dark Matter (CDM), a form of matter that interacts only through gravity and not the electromagnetic field. Hence, it does not emit, absorb, or reflect electromagnetic radiation rendering it invisible.

Although yet to be detected directly, the overwhelming evidence in favour of dark matter (DM) places it firmly in the standard ΛCDM cosmology. Zwicky (1937) provided the first evidence for DM in 1933 after measuring the total mass of the Coma cluster using the virial theorem and noting that it was orders of magnitude larger than that of the luminous matter. Since then, many more dynamical

measurements like these have confirmed that there is a dominant mass component that is unaccounted for in the luminous matter, although the factor difference in mass has reduced to ~ 5 Gould (1995). Many other lines of evidence corroborate this, for example since dark matter is a component of mass it has a gravitational lensing effect. As we will describe in detail in Section 1.4.1, by measuring the observed geometries of images that are distorted by an intervening object, for example a cluster, the mass and the mean density of that cluster can be inferred. These measurements relative to those of baryonic matter suggest the majority of the lensing effect is due to DM (Massey et al., 2010).

Further evidence comes from the CMB that is in fact *not* precisely homogeneous. It contains tiny temperature perturbations of order $10^{-3}\%$ that are thought to trace the density perturbations of matter in the early Universe that lead to the formation of the structure that we observe today Spergel et al. (2003); Planck Collaboration et al. (2018). Through evolution of density perturbations it can be shown that the fluctuations in the CMB are too small to explain the present day overdensities. For this, DM provides a solution which, in the case of cold dark matter[4], decoupled from radiation earlier in the evolution of the Universe than baryons did allowing its fluctuations to grow independently until recombination where the baryons fall into the already present DM overdensities. Thus, leading to larger overdensities as measured today.

The final component of the ΛCDM Universe is the cosmological constant Λ itself, which currently dominates the energy-density budget of the Universe at $\sim 68\%$. This so called *dark energy* can be thought of as the energy-density of the vacuum itself. It drives an accelerated expansion of the late time Universe, since unlike matter densities it does not get diluted by cosmic expansion. This accelerated expansion has been confirmed through observations of the distance-redshift relation of Type1a supernovae and also the Baryonic Acoustic Oscillations (Astier, 2012; Dawson et al., 2013). Further evidence for dark energy is in its success at producing the present large scale structure of the Universe in models of its evolution. Notably, although we have gained an understanding of the effects of dark energy through empirical evidence, we are yet to understand the fundamental form this energy takes. This pursuit is an active field of research today.

1.2.3 Inflation and Large Scale Structure

The aforementioned primordial density perturbations are thought to have arisen from a rapid phase of exponential expansion early in the Universe called inflation (Guth, 1968). This inflationary period provides a dynamical mechanism that produces an observable Universe that both satisfies the cosmological principle and is flat. These properties would otherwise permit a very specific set of initial

[4]Where cold refers to its slow speed compared to the speed of light.

conditions to be present at the beginning of the Universe. Moreover, inflation theory predicts the exact one part in 100,000 inhomogeneities that are observed in the CMB.

In a ΛCDM Universe these density perturbations lead to a hierarchical formation of structure where small overdensities gravitationally collapse first forming small masses that then merge with other collapsed structures, ultimately producing the large scale structure (LSS) of filaments, clusters, and galaxies we observe today. Large scale N-body simulations, like the Millenium simulation (Springel et al., 2005), have been crucial in furthering our understanding of this process, which becomes nonlinear once the perturbations have grown sufficiently. These simulations, which typically model of order millions of CDM particles, have been incredibly successful at reproducing the LSS.

They demonstrate the hierarchical growth of the so-called DM *haloes* through the accretion of smaller subhaloes in a self similar way. Thus, a key prediction of these N-body simulations is the subtructure hierarchy – that every dark matter halo has orbiting within it the subhaloes it has accreted (Springel et al., 2008). This systematic growth leads to a universal DM mass profile (Navarro et al., 1997), known as the NFW profle, which is another key prediction of these models. On smaller scales, like that of a single halo, tension arises between these models and our observations of the real Universe. This may be due to their ignorance to baryonic physics, a mechanism which significantly complicates the modelling process. Nevertheless, to understand processes such as galaxy evolution baryonic physics can not be ignored.

1.3 Galaxy formation and evolution

1.3.1 Classifying Galaxies

The observable photometric properties of galaxies provide us with valuable information to study their evolution histories. Firstly, we use these properties to divide galaxies into different classes, as was first done by Edwin Hubble in 1926 based on their visual appearance (Hubble, 1926). Hubble's classification scheme broadly divides galaxies into two populations based on their morphology; early-type galaxies (ETGs) and late-type galaxies (LTGs). ETGs are made up of relatively smooth elliptical and lenticular galaxies, whereas LTGs have a more complex disc-like structure with extended spiral arms, roughly half of which contain a bar-like structure in the centre.

Today, these morphological classifications are usually quantified through structural parameters defined in their light distribution. ETGs are often described by a Sérsic profile while LTGs are typically described by an exponential profile, that is a particular case of the Sérsic profile with an index fixed to 1 (Sersic, 1968). From these profiles the galaxy's size can be constrained, often by defining

the effective radius[5](Graham & Driver, 2005) which is the radius which contains half of the total luminosity of the galaxy. We note that, while useful for broadly classifying types of galaxies and quantifying structural properties, these simple profiles are not able to truly capture the complexity of the structure that we observe in these systems. For example, we know that both ETGs and LTGs may consist of a compact 'bulge' component as well as a more extended 'disc' component (Oh et al., 2017; Vika et al., 2014). As well as this ETGs are not strictly elliptical, with isophotal shapes that can be classified as boxy or discy, as determined by the type of perturbation relative to a true elliptical isophote (Naab et al., 1999).

ETGs and LTGs can also be classified by their colour, which is indicative of the types of stars that are found in the galaxy - its stellar population (Strateva et al., 2001; Blanton et al., 2003). ETGs lie on the *red sequence* of a galaxy colour-magnitude diagram, a very narrow region of red passive galaxies. These contain older populations of lower mass stars and have therefore mostly ceased star formation. LTGs, however, are actively star forming, appearing much bluer in colour as a result of the ultra-violet/optical emitted from young high-mass stars. They occupy a much broader region of the colour-magnitude diagram known as the *blue cloud* (Tojeiro et al., 2013). In between the red sequence and blue cloud lies an under populated region of galaxies known as the green valley (Salim, 2014; Eales et al., 2018). Blue galaxies, which are more common at high redshifts, are believed to transition into red galaxies that become more common at low redshifts. The almost dichotomous behaviour in the colour evolution suggests the mechanism behind star formation quenching acts relatively quickly. The question of how galaxies quench their star formation remains one of the fundamental questions of extragalactic astronomy, for which the green valley may be a useful tool for studying such mechanisms.

We can gain further insight into the evolution of galaxies by combining photometric observables with spectroscopic parameters. For example, ETGs exhibit a scaling relation known as the fundamental plane (FP) relation that describes the correlation between the size, surface brightness, and stellar velocity dispersion of the galaxies, which put tight constraints on models for their formation and evolution Djorgovski & Davis (1987). Since this thesis is concerned only with ETGs, which are more likely to act as strong lenses due to their large masses, in the following section we specifically describe the status of our understanding of these types of galaxies which form the end products of the hierarchical merging paradigm.

[5]Also known as the half-light radius

1.3.2 Structure and evolution of Early-type Galaxies

In ΛCDM the first luminous galaxies formed in the potential wells of the largest DM haloes through the infall of baryonic material in to these high density regions. For a galaxy to form the gas must rapidly collapse under gravity to overcome the internal pressure of the gaseous matter. Furthermore, gas cooling, through the emission of photons, must prevail over the heating that occurs from the contraction of the gas. However, if this gas cooling is particularly efficient, as it is predicted to be in the high redshift DM haloes where these galaxies form, then the majority of baryonic material will cool and form stars, which is not what we observe in the Universe (Schaye et al., 2015; Vogelsberger et al., 2014). Thus, some kind of feedback mechanism is required to limit the formation of new stars. To this end, active galactic nuclei (AGN), which are powered by the accretion of material onto supermassive black holes (SMBH) that reside at the centres of all massive galaxies, are thought to play a valuable role (Richardson et al., 2021; Torrey et al., 2020; Irodotou et al., 2022).

After the early phases of galaxy formation, hierarchical merging ensues. From this point onwards, galaxies may follow a wide variety of evolutionary paths depending on the properties of the gas, the mergers it undergoes and the conditions these occur in. Hence, to successfully understand galaxy formation and evolution one requires a self-consistent treatment of baryonic physics (such as multi-phase gas physics and dynamics, radiative transfer, star formation, and feedback), its interaction with DM through gravity, and its kinematics and evolution within an expanding Universe. A number of numerical codes with this goal in mind have emerged over the past couple of decades which incorporate hydro-dynamical gas simulations into the N-body methods that are successful at reproducing the LSS. Comparing the results from these different codes, which often differ in the types of baryonic physics they implement and the scales on which they're simulated, with observations is proving to be invaluable in furthering our understanding of this complex evolutionary process (Wang et al., 2019, 2020).

As mentioned in the previous section the FP relation of ETGs puts tight constraints on the evolution of these types of galaxies. This is because, although the FP exhibits no evolution with redshift, strong evolution is evident in its projection in the size-stellar mass space out to redshifts ~ 2 (Daddi et al., 2005; Trujillo et al., 2007). This, along with other observations that indicate these are passive galaxies, implies they have experienced dramatic growth in size whilst remaining at a constant stellar mass through a growth mechanism that does not involve the formation or accretion of young stars. Further to this, observations have shown that the mean distribution of dark plus baryonic matter in the central few effective radii of ETGs is such that their combined density profile is roughly isothermal, $\rho(r) \propto r^{-\gamma}$, with $\gamma \sim 2$. This has been consistently observed by many observational techniques: dynamically modelled local ETGs (Tortora et al., 2014; Serra et al., 2016; Li et al., 2019; Cappellari

et al., 2013), X-ray studies (Humphrey et al., 2006; Humphrey & Buote, 2010), weak lensing (Gavazzi et al., 2007), and combined strong lensing and dynamical modelling (Koopmans et al., 2009; Auger et al., 2010a; Li et al., 2018).

Numerical simulations are beginning to understand the origin of these empirical relations. The current consensus for the formation of ETGs, often referred to as a 'two phase' assembly (Oser et al., 2010), begins with an initial stage of active star formation and adiabatic contraction at redshift $z \gtrsim 2$, followed by growth through major and minor merging events to the present (Naab & Ostriker, 2009; Van Dokkum et al., 2010; Remus et al., 2017). However, details of the physical processes that modify the mass distributions throughout this formation process are yet to be well understood. Fine-tuning between the baryonic and dark matter distributions would be necessary to produce the distribution of near-isothermal total mass profiles that are observed, a result hydrodynamic simulations have been unable to accomplish whilst simultaneously reproducing the observed distribution of dark matter fractions (Duffy et al., 2010; Dubois et al., 2013; Xu et al., 2017). It is unclear whether this discrepancy is a result of an inadequacy in the cosmological simulations or a systematic bias in the determination of the observed mass-density slopes.

1.4 Strong gravitational lensing

As introduced in Section 1.1.3, gravitational lensing is the phenomenon whereby light is distorted by massive objects. Since light propagates along geodesics in the spacetime metric which is curved in the presence of matter, although the trajectory of the photon remains straight in its own reference frame, the light rays appear curved to the outside observer. Although GR provides the correct description of the curvature of these light rays, most astrophysically relevant scenarios, namely those in this thesis, can be adequately described by a simple approximation formalised in gravitational lensing theory (Kochanek, 2004) which we cover in section 1.4.1.

This thesis is mostly concerned with gravitational lensing in the strong regime, where the distortions are large enough to produce multiple images or arcs. Although Einstein had predicted the multiple image phenomenon he expected that it was improbable that it would ever be resolvable in observations, calculating the separation due only to a star (which is of the order milli-arcseconds). It was Fritz Zwicky who considered the possiblity of larger distortions by *galaxies* acting as lenses that he estimated would in fact be observable (Zwicky, 1937). Indeed, in 1979 the first gravitationally lensed object was observed, the Twin Quasar Q0957+561A (Walsh et al., 1979). Since then many more strong lensing events have been observed, particularly with the advent of surveys specifically designed to search for strong lenses which we describe in more detail in section 1.4.4.

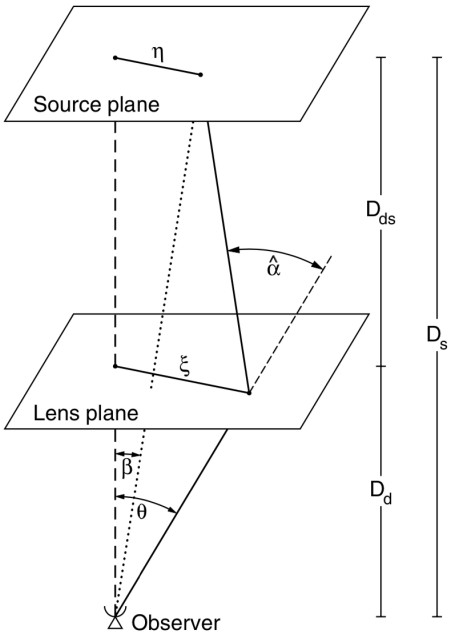

Figure 1.2: The geometry of the single plane lens. A source galaxy in the source plane at a distance D_s from an observer is deflected by a lens in the lens plane at a distance D_d from the observer. The distance D_{ds} represents the distance between the lens plane and source plane. All distances correspond to angular diameter distances. Figure reproduced from Peter Schneider (2006).

With these observations of strong lens systems comes a wealth of astrophysical applications. Since the effects of gravity are felt by all matter, including dark matter, one can constrain the properties of dark matter. The Hubble constant, too, can be constrained with lensed quasars, a method known as time-delay lensing, providing an independent probe (Suyu et al., 2017). Further tests of cosmology can be made by detecting small substructures, that also perturb the multiple images, that are expected to exist in different abundances depending on the choice of cosmological model (Gilman et al., 2020; Miranda & MacCiò, 2007; Hezaveh et al., 2016). The assumption underpinning all of these science goals is that one can accurately model the strong lens system, constraining the mass distribution of the object that is doing the lensing, and recovering the distribution of light from the multiple images as they would appear had they not been lensed. We describe a common mass profile that is assumed for the lens galaxy, and is used throughout this thesis, in Section 1.4.2 and give an overview of the methods that could be used to constrain such a profile in Section 1.4.3.

1.4.1 Lensing Theory

The lens equation

Although the actual light rays are curved by the mass of the deflector, if the deflection is small then one can invoke the geometrically thin lens approximation that the rays are straight lines with a single

angular deflection in the plane of the mass distribution[6]. A typical single plane lens system is plotted in Figure 1.2, where a mass at a distance D_d from the observer deflects the light from a source at a distance D_s (where the distances quoted are angular diameter distance). To satisfy the condition of a thin lens the extent of the mass distribution must be much smaller than both D_d and D_ds.

For a surface mass density $\Sigma(\boldsymbol{\xi})$ projected on to the plane of the incoming light ray (known as the lens plane), the deflection angle of the light ray amounts to

$$\boldsymbol{\alpha}(\boldsymbol{\xi}) = \frac{4G}{c^2}\int d^2\xi' \Sigma(\xi')\frac{\boldsymbol{\xi}-\boldsymbol{\xi}'}{|\boldsymbol{\xi}-\boldsymbol{\xi}'|^2}, \tag{1.4.1}$$

where $\boldsymbol{\xi} = (\xi_1, \xi_2)$ is a 2D vector of impact parameters in the lens plane, G is the gravitational constant and c is the speed of light. From simple geometric considerations of the system in Figure 1.2, including the small angle approximation $\sin\theta \approx \theta \approx \tan\theta$, we can write that

$$\boldsymbol{\eta} = \frac{D_\mathrm{s}}{D_\mathrm{d}}\boldsymbol{\xi} - D_\mathrm{ds}\boldsymbol{\alpha}(\boldsymbol{\xi}). \tag{1.4.2}$$

This can be re-written in terms of angular coordinates, by introducing $\boldsymbol{\eta} = D_\mathrm{s}\boldsymbol{\beta}$ and $\boldsymbol{\xi} = D_\mathrm{d}\boldsymbol{\theta}$, to produce the well known lens equation

$$\boldsymbol{\beta} = \boldsymbol{\theta} - \boldsymbol{\alpha}(\boldsymbol{\theta}), \tag{1.4.3}$$

which describes how the observed image positions $\boldsymbol{\theta} = (\theta_1, \theta_2)$ of light rays in the image plane are deflected from a source at position $\boldsymbol{\beta} = (\beta_1, \beta_2)$ in the source plane. Here we have also introduced the reduced deflection angle $\boldsymbol{\alpha}(\boldsymbol{\theta}) = \frac{D_\mathrm{ds}}{D_\mathrm{s}}\boldsymbol{\alpha}(\boldsymbol{\xi})$ which can be expressed in terms of a dimensionless surface mass density $\kappa(\boldsymbol{\theta})$ as

$$\boldsymbol{\alpha}(\boldsymbol{\xi}) = \frac{1}{\pi}\int d^2\theta' \kappa(\theta')\frac{\boldsymbol{\theta}-\boldsymbol{\theta}'}{|\boldsymbol{\theta}-\boldsymbol{\theta}'|^2}. \tag{1.4.4}$$

The dimensionless surface mass density, also known as the convergence, is defined by

$$\kappa(\boldsymbol{\theta}) = \frac{\Sigma(D_\mathrm{d}\boldsymbol{\theta})}{\Sigma_\mathrm{crit}}, \qquad \text{with} \qquad \Sigma_\mathrm{crit} = \frac{\mathrm{c}^2}{4\pi\mathrm{G}}\frac{D_\mathrm{s}}{D_\mathrm{d}D_\mathrm{ds}}, \tag{1.4.5}$$

where we have introduced the critical surface mass density for lensing Σ_crit. The lensing properties of a galaxy with κ are characterised by the projected gravitational potential ϕ that satisfies the Poisson equation: $\nabla^2\psi = 2\kappa$. Consequently, the deflection angle field is related to the potential of the lensing galaxy through $\boldsymbol{\alpha} = \nabla\psi$.

The critical surface mass density crudely distinguishes between the strong and weak regimes of lensing. Strong lensing typically occurs in regions where the surface mass density of the lens exceeds

[6]This corresponds to the Born approximation in atomic and nuclear physics

that of the critical surface mass density ($\kappa > 1$). In this regime, the lens equation (equation 1.4.3) has multiple solutions corresponding to the number of multiple images that are observed.

Magnification and distortion

Assuming local linearity – that the size of the source is negligible compared to the scales on which the gravitational field and deflection angle field vary – then the Jacobian of the lens equation can be defined

$$A_{ij} \equiv \frac{\partial \beta_i}{\partial \theta_j} = \delta_{ij} - \frac{\partial \alpha_i}{\partial \theta_j}, \tag{1.4.6}$$

which describes the distortions to a source galaxy that produce its lensed appearance. In the case of the single lens plane, the Jacobian can then be expressed in terms of the convergence

$$A_{ij} = \delta_{ij} - \frac{\partial^2 \psi}{\partial \theta_i \theta_j} \equiv \begin{pmatrix} 1-\kappa-\gamma_1 & -\gamma_2 \\ -\gamma_2 & 1-\kappa-\gamma_1 \end{pmatrix}, \tag{1.4.7}$$

where we have introduced the two components of shear

$$\gamma_1 = \frac{1}{2}(\psi_{,11} - \psi_{,22}), \qquad \gamma_2 = \psi_{,12}. \tag{1.4.8}$$

If we re-write the Jacobian (equation 1.4.7) in the following form

$$A_{ij} = (1-\kappa)\begin{pmatrix} 1 & 0 \\ 0 & 1 \end{pmatrix} - \gamma \begin{pmatrix} \cos 2\phi & \sin 2\phi \\ \sin 2\phi & \cos 2\phi \end{pmatrix}, \tag{1.4.9}$$

where ϕ is the angle of the shear pseudo-vector $\gamma = (\gamma_1, \gamma_2)$, the affect of the shear and convergence become evident. The convergence is responsible for magnifying the source, the factor $(1-\kappa)$ does not affect the shape of the image but performs an isotropic stretching of it. Further, the shear $\gamma \equiv \gamma_1 + i\gamma_2$ can be recognised as the component that distorts the image through a tangential stretching.

Since lensing conserves surface brightness the ratio of the fluxes observed from the image and from the unlensed source, known as the magnification μ, is the inverse of the determinant of the Jacobian

$$\mu \equiv \det M = \frac{1}{\det A} = \frac{1}{(1-\kappa)^2 - |\gamma|^2}, \tag{1.4.10}$$

where the matrix M is known as the magnification tensor. The eigenvalues of M

$$\mu_t = \frac{1}{\lambda_t} = \frac{1}{1-\kappa-\gamma} \qquad \text{and} \qquad \mu_r = \frac{1}{\lambda_r} = \frac{1}{1-\kappa+\gamma}, \tag{1.4.11}$$

measure the amplification in the tangential and radial directions respectively, where λ_t and λ_r are the eigenvalues of the Jacobian matrix.

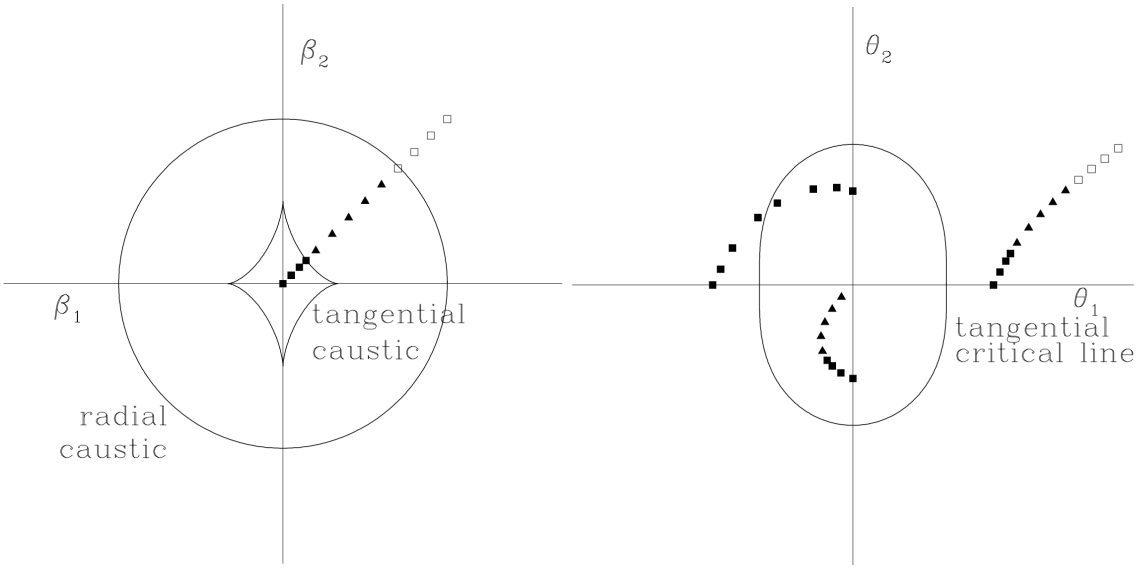

Figure 1.3: Example critical curves and caustics. The multiplicity of a source at different positions relative to these curves is demonstrated. The figure is reproduced from Peter Schneider (2006).

The region where the magnification is ideally infinite, i.e. det$\mathbf{A} = 0$, defines two curves in the lens plane known as the tangential and radial critical curves. The tangential and radial critical curves occur when $1 - \kappa - \gamma = 0$ and $1 - \kappa + \gamma = 0$, respectively. Images near the tangential critical curve are tangentially magnified, and those near the radial critical curve are radially magnified. Mapping the critical curves from the lens plane to the source plane through the lens equation (equation 1.4.3) defines the caustics. The image multiplicity of a lens system is separated into regions relative to the caustics. This is demonstrated in Figure 1.3, where a source within the tangential caustic is observed as four multiple images (filled square points) , a source between the tangential and radial caustic is doubly imaged (triangular points), and outside of the radial caustic only a single distorted image appears in the lens plane (open square points)[7] The example given in Figure 1.3 is known as the *fold* configuration. It demonstrates how a fold merger can occur for an extended source located at the caustic where, for example, at the radial caustic only the part of the source located within the caustic is multiply imaged. Here, the images are highly distorted in the direction of the eigenvector and strongly elongated multiple images merge to produce the giant arcs that are ubiquitous with strong lensing. If the source is located along the β_1 or β_2 axis, the configuration is known as a *cusp*.

[7]Due to the odd number theorem, the number of multiple images that are produced by a bounded transparent lens are in fact odd. The central, *type III*, image is typically demagnified and and not detected in observations.

Observable properties

For axisymmetric lenses the tangential critical curve is circular, corresponding to the *Einstein ring*. The radius of this curve defines the Einstein radius $R_{\rm Ein}$. The mean surface mass density inside $R_{\rm Ein}$ is equal to the critical surface mass density $\Sigma_{\rm crit}$ of the lens equation (equation (1.4.5)). The Einstein radius and enclosed Einstein mass

$$M_{\rm Ein} = \pi R_{\rm Ein}^2 \Sigma_{\rm crit}, \tag{1.4.12}$$

are thus uniquely defined in the axisymmetric case, quantifying the size and efficiency of the lens.

For asymmetric, irregular and realistic lenses, the definition of Einstein radius must be generalised. Several conventions are possible (see Meneghetti et al. 2013 for a good overview) but we choose to use the *effective* Einstein radius

$$R_{\rm Ein,eff} = \sqrt{\frac{A}{\pi}}\,, \tag{1.4.13}$$

where A is the area enclosed by the tangential critical curve. This definition is self-consistent across different mass density profiles, and clearly recovers the definition of $R_{\rm Ein}$ in the case of a circular critical curve. Unless stated otherwise the Einstein radii calculated in this thesis are effective Einstein radii, we refer to them as $R_{\rm Ein}$ at times for brevity.

1.4.2 Mass Profiles

For strong lens systems, gravitational lens theory aims to determine which combination of lens and source properties can reproduce the observed multiple image configuration. To this end, analytic mass profiles are crucial in predicting the lensed properties of an assumed source. For some simple lens models their lensing properties can be derived analytically. The Power-Law Ellipsoidal Mass Distribution (PLEMD)[8] is often assumed to be able to capture the combined mass distribution of both baryonic and dark matter in ETGs. A number of different acronyms exist in the literature that often refer to the same profile, for brevity we hereafter refer to the PLEMD as simply PL.

The convergence of the PL distribution is given by

$$\kappa(x, y) = \frac{\Sigma(x, y)}{\Sigma_{\rm crit}} = \frac{3 - \gamma'}{1 + q}\left(\frac{b}{\sqrt{x^2 + y^2/q^2}}\right)^{\gamma' - 1} \tag{1.4.14}$$

(Suyu, 2012), where γ' is the logarithmic slope of the mass distribution in 3D, $1 \geq q > 0$ is the projected minor to major axis ratio of the elliptical isodensity contours, and $b \geq 0$ is the angular

[8] We note that this differs from the Power-Law Ellipsoid Potential (PLEP), which defines the elliptical coordinates in the radial potential distribution of the lens galaxy as opposed to the convergence. This leads to slightly different properties, such as peanut shaped isodensity contours for highly elliptical distributions. Kassiolia & Kovner (1993) give a good overview of the differences between elliptical potential and elliptical mass distributions.

scale length of the profile. We note that b is referred to in some papers as the Einstein radius, but is distinct from the more robust *effective* Einstein radius in equation 1.4.13). The special case $\gamma = 2$ recovers the Singular Isothermal Ellipse (SIE) mass distribution, in which the steady-state motions of particles have constant 1D velocity dispersion $\sigma_{\rm SIE}$, when projected along any line of sight. For this distribution of mass, the critical curve is the ellipse at $\kappa = 1/2$. Our definition of effective Einstein radius (equation 1.4.13) means that the ellipse is $R_{\rm Ein,eff} = qx^2 + y^2/q$, and the velocity dispersion is

$$\sigma_{\rm SIE} = \mathrm{c}\sqrt{\frac{R_{\rm Ein} D_{\rm s}}{4\pi D_{\rm l} D_{\rm ls}}} \,. \tag{1.4.15}$$

Given that the convergence profile is elliptical, a number of normalisation conventions may be adopted to define the surface density contours. Bolton et al. (2008a) adopt an intermediate-axis normalisation for the SIE profile that is different to the normalisation defined in equation 1.4.14, which in turn leads to a slightly different form of the analytically tractable deflection angles for the two SIE profiles. In Appendix A we show that they are in fact equivalent up to a normalisation factor, albeit with different definitions of coordinates. This motivates the definition of Einstein radius in this work which is equivalent for both normalisations of the SIE profile.

As described in the previous section, the PL distribution will have an associated shear that is responsible for the non-isotropic distortion of the light rays. However, the primary lens galaxy is not the only source of shear in a gravitational lens. Perturbations occur as a result of galaxies or clusters nearby the lens galaxy, and structures along the ray path. Hence, it is generally considered necessary to account for these *external* perturbations in the immediate environment of the lens system. Assuming the mass distributions do not overlap, a nearby object does not contribute convergence κ to the deflection of light. All external perturbations can therefore be characterised by an additional constant *external shear* contribution

$$\gamma_{\rm ext} \equiv \gamma_{1_{\rm ext}} + i\gamma_{2_{\rm ext}} = |\gamma_{\rm ext}| e^{2i\phi} \tag{1.4.16}$$

where $\gamma_{1_{\rm ext}}$ and $\gamma_{2_{\rm ext}}$ are constants represented by a potential, as in equation 1.4.8, with constant components.

1.4.3 Methods

There are a variety of approaches to strong lens modelling. These methods constrain the mass distribution of the deflector lens with the lensing constraints available in the observations. To achieve this, the goal is always to solve lens equation (equation 1.4.3). For any realistic mass distribution this

will be a non-linear equation that can only be solved numerically[9]. Through defining a goodness of fit statistic, statistical methods must therefore be employed to find the model parameters that best-fit the data and their associated uncertainties. Lens modelling can be considered either a "forward" or "inverse" problem, where the image positions are predicted from an assumed source and mass in the forward problem, or the observed images are used to reconstruct a model of the source and mass in the inverse problem. Both approaches are often required in the analysis of real lenses.

We first distinguish between point-like and extended sources which differ largely in the complexity of the method that must be employed to solve the lens equation. Point-like sources, for example lensed quasars like the Twin Quasar that was first discovered, provide constraints on the potential of the lens galaxy and its derivatives at discrete positions. The required goodness of fit statistic is relatively straightforward. If the image is extended, like the galaxy-galaxy strong lenses that we model in this thesis, the lens equation must be solved for every pixel within the extended image, thereby reconstructing the distribution of light in the source plane. The relative information between pixel data provides extra constraints on the potential of the lens galaxy, namely its second derivative (γ' in the PL distribution - equation 1.4.14). However, the fitting procedure also requires more free parameters to describe the unknown shape of the source galaxy that, depending on the particular method used, can significantly increase the complexity of the goodness of fit statistic and the parameter space that is to be sampled by the numerical solver.

This thesis is concerned with the strong lens modelling of extended images. As such we describe the methods that exist to do so, which can broadly be split into two categories; parametric methods, that assume an analytic profile (or sum of profiles) for the source galaxy (Tessore et al., 2016) and, pixel-based methods, that reconstruct the source galaxy's surface brightness distribution on a pixel grid or mesh (Warren & Dye, 2003; Suyu et al., 2006; Dye & Warren, 2005; Vegetti & Koopmans, 2009; Nightingale & Dye, 2015; Nightingale et al., 2018; Joseph et al., 2019; Galan et al., 2021). Parametric methods are the simplest approach, where the lens and source parameters create the fully non-linear parameter space for the non-linear method to solve. Owing to their simplicity, they are also typically the fastest of the methods to converge on a solution. However, increasing the complexity of the lens models can significantly complicate the parameter space, increasing the chances of incorrect local best-fit solutions being produced. For applications wishing to constrain only the Einstein radius or mass of a lens system these methods are sufficient and they have seen extensive use to do this in the literature (e.g. Bolton et al., 2008b; Gavazzi et al., 2012). However, more complex lens modelling techniques are required to constrain more complex mass profiles and account for irregularities in the

[9]although a few simple cases can be solved analytically

source's morphology.

Pixel-based methods were developed with this in mind. The source reconstruction is performed by discretizing the source plane into a grid of pixels. This requires a penalty function, known as regularisation, to ensure the source appears physical. Here, the forward problem is solved, ray-tracing source-plane pixels to the image plane to be compared with the data image. Before Warren & Dye (2003, hereafter WD03) introduced the semi-linear inversion (SLI) method, which writes the lens equation as a matrix equation, pixel based methods independently varied each of the source pixels until a threshold goodness of fit was achieved. The SLI method simplifies the problem, allowing the the best-fit source reconstruction to be obtained in a single linear step.

Since it was introduced, many strong lens modelling software have adopted the SLI method, particularly since Suyu et al. (2006, hereafter S06) placed the method into a Bayesian framework that objectively determines the degree of regularisation that is required to reconstruct the source galaxy's light distribution. The methods differ mostly in the choice of pixelation that is used in the source plane. The earliest methods employed a Cartesian square grid (WD03), with extensions to this being introduced in the form of square grids that split source pixels above a magnification threshold (Dye & Warren, 2005; Tagore & Keeton, 2014), and rectangular grids that change depending on the size of the source (S06)(Collett & Auger, 2014). More recent implementations have employed irregular grids/ tessellations that can adapt to the emission of the source galaxy (Vegetti & Koopmans, 2009; Nightingale & Dye, 2015; Nightingale et al., 2019), and others have employed a basis of shapelets to describe the source as opposed to source pixels (Birrer et al., 2015; Shajib et al., 2018). The strong lens analysis in this thesis is carried out using the strong lens modelling software `PyAutoLens`, described by Nightingale et al. (2018). `PyAutoLens` ultimately reconstructs the source on an adaptive Voronoi mesh, but uses both parametric and pixel-based methods to do so with an approach termed 'non-linear search chaining' that composes pipelines capable of fitting lens models that gradually increase in complexity. We describe the specific method we adopt in detail in Section 2.4.

1.4.4 Samples of lenses

In the early years of gravitational lens detection most systems were discovered accidentally. The majority of these discoveries were lensed quasars, owing to their extreme luminosities increasing the chances of them being observable at the high redshifts required for lensing. Although the first lens detected with extended emission was also serendipitous (Hewitt et al., 1988). Around a similar time the first giant luminous arcs were detected, and later confirmed to be resulting from a cluster-scale lens (Giraud, 1988; Paczynski, 1987). The launch of the Hubble Space Telescope (HST) was undoubtedly

a blessing to the field of lensing, allowing for the confirmation and detailed investigation of lenses with high-resolution imaging. More importantly, the arrival of expansive data-archive surveys like the Sloan Digital Sky Survey (SDSS) (York et al., 2000; Abazajian et al., 2003) saw a boom in lens discovery with dedicated teams dedicated to searching for strong lenses in surveys such as these.

Galaxy-galaxy strong lens systems, those with a regular non-active source galaxy, now outnumber the quasar lens detections. Spectroscopic searches have been hugely successful at detecting these systems. The approach is typically to examine residual spectra of high mass ETGs for higher redshift emission lines that are indicative of a source galaxy being present along the line of sight. The largest sample of lenses detected in this way in the SDSS survey is the Sloan Lens ACS (SLACS) survey Bolton et al. (2006, 2008b); Auger et al. (2009) which has detected over one hundred strong lenses, remaining the largest sample to date. A similar search within the BOSS survey lead to 25 lenses detected in the BOSS Emission Line Lens (BELLS) survey (Brownstein et al., 2012) which was extended to the BELLS GALaxy-Lyα EmitteR sYstems (BELLS GALLERY) (Shu et al., 2016b,a) survey to specifically search for source galaxies that are Lyman-alpha emitters. A similar search for Lyman-alpha emitter sources was made in the LEnSed laeS in the EBOSS suRvey (LESSER) (Cao et al., 2020) survey.

Another approach to lens detection is to search for giant arcs and rings in photometric datasets. For this, the Strong Lensing Legacy (SL2S) survey (Gavazzi et al., 2012) used the algorithm `RingFinder` (Gavazzi et al., 2014) to search for lenses in the Canada-France-Hawaii Telescope (CFHT) Legacy Survey (Cabanac et al., 2007). The code removes the lens galaxy's light from multi-wavelength imaging and searches for remaining flux indicative of a higher redshift source galaxy. This technique usually finds higher redshift lens galaxies with larger Einstein radii than the spectroscopic approach does, although with the use of deeper spectroscopic data and selection for higher redshift spectra samples like BELLS GALLERY have similar properties to SL2S. We note that the selection procedure of the different surveys leads to differences in the biases on the sample of galaxies from the general population given the probability of multiple imaging being detected in each survey.

These selection effects are further combined with the fact that particular parameters of the lens galaxy are more likely to produce a strong lens than others, for example the surface mass density must be larger than the critical surface mass density (equation 1.4.5). Consequently, it is very difficult to understand how the samples differ from the parent population. Recent work by Sonnenfeld (2021b,a, 2022) has begun to quantify the biases these selection effects have on studies that wish to infer galaxy properties or cosmological parameters from a population of strong lenses. These investigations are crucial since population level studies are set to become a particularly powerful tool with the advent

of next generation wide-field surveys. During the next decade, a couple of hundred *thousand* strong lenses are expected to be discovered by surveys like these including Euclid, LSST, and SKA (Collett, 2015), a thousand-fold increase in the data that is available to us now.

Chapter 2

Automated galaxy-galaxy strong lens modelling: no lens left behind

2.1 Introduction

Galaxy-scale strong lensing is the distortion of light rays from a background source into multiple images, by the gravitational field of a foreground galaxy along the same line of sight. From the apparent position, shape and flux of those multiple images, it is possible to infer both the intrinsic morphology of the background galaxy at magnified resolution, and the distribution of (all gravitating) mass in the foreground lens.

In combination with kinematic measurements, lensing methods have inferred the mean total density profile of massive elliptical galaxies and how that evolves with redshift (Gavazzi et al., 2007; Koopmans et al., 2009; Auger et al., 2010a; Sonnenfeld et al., 2013b; Bolton et al., 2012), and put constraints on their dark matter content, stellar mass-to-light ratio, and inner structure (Sonnenfeld et al., 2012; Oldham & Auger, 2018; Nightingale et al., 2019; Shu et al., 2015, 2016c). If the background source is variable and the mass model known, measurements of time delays between multiple images can constrain the value of the Hubble constant (Suyu et al., 2017; Wong et al., 2019). If the lens galaxy contains small substructures, they also perturb the multiple images, and provide a clean test of the nature of dark matter (Vegetti et al., 2010; Li et al., 2016, 2017; Hezaveh et al., 2016; Ritondale et al., 2019; Despali et al., 2019; Amorisco et al., 2022; He et al., 2021).

Currently, a couple of hundred strong lensing systems have been observed, by dedicated surveys such as the Sloan Lens ACS (SLACS) (Bolton et al., 2006; Auger et al., 2010a), BOSS Emission Line Lens (BELLS) (Brownstein et al., 2012), Strong Lensing Legacy (SL2S) (Gavazzi et al., 2012) surveys,

BELLS GALaxy-Lyα EmitteR sYstems (BELLS GALLERY) (Shu et al., 2016b,a), the SLACS Survey for the Masses (S4TM) Survey (Shu et al., 2017), LEnSed laeS in the EBOSS suRvey (LESSER) (Cao et al., 2020), and the Spectroscopic Identification of Lensing Objects (Talbot et al., 2018, 2021).

During the next decade, a couple of hundred *thousand* strong lenses will be discovered by wide-field surveys including Euclid, LSST, and SKA (Collett, 2015). Such large samples of strong lenses will contain rare 'golden' systems such as double or triple source plane systems (Collett & Auger, 2014; Collett & Bacon, 2016; Collett & Smith, 2020), and unlock considerable scientific potential through vastly improved statistics (e.g. Birrer et al., 2020; Sonnenfeld & Cautun, 2021; Sonnenfeld, 2021a; Cao et al., 2020; Orban De Xivry & Marshall, 2009). To tackle the forthcoming thousand-fold increase in data volume, model inference must be automated, and made robust without human intervention.

Convolutional Neural Networks (CNNs) are a fast approach that have recently been shown to be successful at lens modelling. Hezaveh et al. (2017) and Levasseur et al. (2017) modelled nine lens systems observed by the Hubble Space Telescope (HST). However, this approach requires a large, and significantly varied and unbiased training set of mock lenses to learn from. These are requirements that can be difficult to guarantee, which could be problematic for source galaxies with irregular morphologies. Using a different method, Shajib et al. (2021) used the `DOLPHIN` software to model 23 lenses from an initial sample of 50 SLACS lenses.

We use the `PyAutoLens` software (Nightingale & Dye 2015, hereafter N15; Nightingale et al. 2018, hereafter N18), an open-source Bayesian forward-modelling project designed specifically with automation in mind. We develop an automated data analysis pipeline that models the distribution of foreground light and mass as a sum of smooth analytic functions, and the background light as either another sum of analytic functions (e.g. Tessore et al., 2016), or as a pixellated image (Warren & Dye, 2003; Suyu et al., 2006; Dye & Warren, 2005; Vegetti & Koopmans, 2009; Joseph et al., 2019; Galan et al., 2021). By fitting a mock sample of $\sim$ 500 lenses we further show that previous versions of `PyAutoLens` (like many lens fitting algorithms) underestimated the width of posterior probability distributions of lens model parameters. We will refer to the corresponding errors estimated from the credible regions of the posteriors as the 'statistical uncertainty' throughout this thesis. A major component of this is a discretization effect inherent to pixel-based source reconstructions — for which we provide a solution.

We apply our automated lens modelling pipeline to a uniform sample of 59 SLACS and BELLS GALLERY lenses that were observed with the Hubble Space Telescope. Our goal is to model every single lens and therefore *leave no lens behind*: if we were analysing $\sim 100,000$ lenses, even a low rate of (unflagged) failures would require unfeasible human intervention, and would bias the increasingly

tight statistical precision of subsequent scientific analysis. Our first, 'blind' analysis achieves a promising success rate of 85%. We then emphasise trying to understand *why* some lenses are not well fit, and improve our pipeline until they are. This mirrors the kind of methodology that will be possible with future large samples: a fairly fixed initial framework, that is adapted after early results. In this paper we are trying to establish that first fixed framework.

With the full sample modelled, we investigate the accuracy to which the Einstein radius is recovered. Cao et al. (2020) recently demonstrated the robustness of the measurement by comparing the Einstein radii of power-law fits to mock lenses with complex mass distributions, inferred from SDSS-MaNGA stellar dynamics data, to their true values. They showed that the Einstein radius was recovered to 0.1% accuracy, taking into account both systematic and statistical sources of uncertainty. We examine how this compares to the statistical uncertainties we infer for the Einstein radii of the SLACS and GALLERY sample. Further, we compare to previous literature measurements (Bolton et al., 2008a; Shu et al., 2016a) to verify our results and quantify how the uncertainty varies due to different methods and assumptions. Our work therefore provides an outlook on the accuracy to which we can anticipate measuring the Einstein radius in upcoming large samples of tens of thousands of lenses.

This paper is structured as follows. In Section 2.2 we give a brief overview of lensing theory and provide the mass and light profile parameterisations we adopt. Section 2.3 describes the sample selection and data reduction procedure for the data images of the SLACS and GALLERY samples. The method is then explained in detail in Section 2.4 and applied to a sample of mock data in Section 2.5 to investigate problems associated with pixelised source reconstructions. The results of applying the automated procedure to the SLACS and GALLERY samples are then presented in Section 2.6. Finally we discuss the implications for the future of automated analyses in Section 2.7 and summarise in Section 2.8. Throughout this work we assume a Planck 2015 cosmological model Ade et al. (2016). The results of every fit to the SLACS and GALLERY datasets can be found at the following link `https://zenodo.org/record/6104823`.

2.2 Lens Modelling Theory

The aim of this study is to investigate the practicalities of automated extended source modelling to infer the mass distributions of a large sample of lenses. The theory relevant for this analysis was given in Section 1.4.1. We will now describe our choice of mass and light profile parameterisations in Sections 2.2.1 and 2.2.2, respectively.

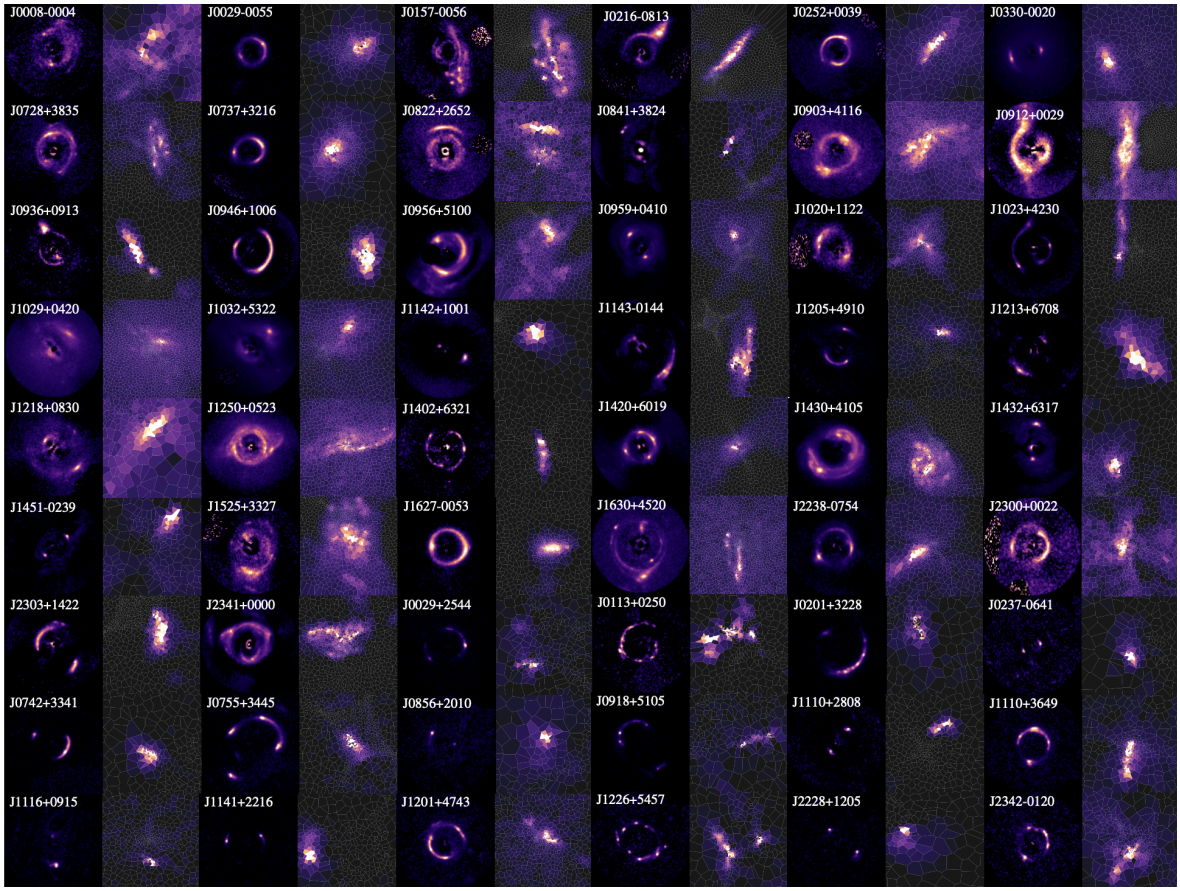

Figure 2.1: Lens subtracted data images (left) and their corresponding pixel-grid reconstructions (right) for the "Gold" sample of lens galaxies (see Section 2.6.1 for a description of our classification process). Lenses are in order of Right Ascension, with SLACS lenses appearing first, followed by GALLERY lenses. The full model fits for these lenses, plotted with an indication of scale, are available in Appendix D.

2.2.1 Mass profile parameterisation

We model the distribution of mass in the lens galaxy as a Power-Law Ellipsoidal Mass Distribution (PLEMD), with convergence given by equation 1.4.14. We assume this is able to capture the combined mass distribution of both baryonic and dark matter. The profile has additional free parameters for the central coordinates (x_c, y_c) and position angle ϕ, measured counterclockwise from the positive x-axis, and external shear. When varying the ellipticity, we actually sample from and adjust free parameters

$$\varepsilon_1 = \frac{1-q}{1+q}\sin 2\phi\,, \qquad \varepsilon_2 = \frac{1-q}{1+q}\cos 2\phi\,. \tag{2.2.1}$$

because these are defined continuously in $-1 < \varepsilon_i < 1$, eliminating the periodic boundaries associated with angle ϕ and the discontinuity at $q = 0$. We further assume external perturbations are captured by the external lensing shear which are parameterised by components $\gamma_{1\text{ext}}$ and $\gamma_{2\text{ext}}$ (equation 1.4.16). The external shear magnitude γ_{ext} and angle ϕ_{ext} are recovered from these parameters by

$$\gamma_{\text{ext}} = \sqrt{\gamma_{1\text{ext}}^2 + \gamma_{2\text{ext}}^2}\,, \qquad \tan 2\phi_{\text{ext}} = \frac{\gamma_{2\text{ext}}}{\gamma_{1\text{ext}}}\,. \tag{2.2.2}$$

2.2.2 Light profile parameterisation

We model the foreground galaxy's light distribution as the sum of two Sérsic profiles with different ellipticities but a common centre. This replicates the bulge and disc components that constitute an Early-type Galaxy (ETG) (Oh et al., 2017; Vika et al., 2014), and significantly increased the Bayesian evidence compared to a single Sérsic model, in a precursor study of three SLACS galaxies (Nightingale et al., 2019). The Sérsic profile is

$$I(x, y) = I_{\text{eff}}\,\exp\left\{-k_{\text{eff}}\left[\left(\frac{\sqrt{qx^2 + y^2/q}}{R_{\text{eff}}}\right)^{\frac{1}{n}} - 1\right]\right\}, \tag{2.2.3}$$

where I_{eff} is the surface brightness at the effective radius R_{eff}, defined here in the intermediate axis normalisation[1], n is the Sérsic index, and k_{eff} is a normalisation constant related to n such that R_{eff} encloses half of the total light from the model (Graham & Driver, 2005). The axis ratio and position angle of each component are parameterized during the fitting process, using elliptical components as in equation (2.2.1). Aside from the two components' common centre, all free parameters are fitted independently of each other to allow for more complex light distributions. For example, the flux ratio of the two Sérsics is unconstrained, and the profiles may be elongated by different amounts and rotationally offset from one another.

[1]This definition keeps the area enclosed within a given isophote constant as q is varied, and is distinct from 'major axis normalisation' where the term $(qx^2 + y^2/q)$ would instead be $(x^2 + y^2/q^2)$.

We model the distribution of light in the source galaxy as either a single Seŕsic profile or using a pixelated source reconstruction depending on the phase of the automated procedure, described in Section 2.4.3. The source galaxy is ultimately reconstructed on an adaptive Voronoi mesh, for which the procedure is described in detail in Section 2.4.2.

2.3 Data

2.3.1 Lens sample selection

We analyse strong gravitational lenses around massive elliptical galaxies drawn from the SLACS (Bolton et al., 2008b) and BELLS GALLERY samples (Shu et al., 2016a). The lenses in the SLACS sample were identified using SDSS spectroscopy to find higher redshift emission lines after subtracting a principle component model of the foreground galaxy spectrum (Bolton et al., 2006). This technique was modified for the GALLERY survey, to specifically select even higher redshift Lyα-emitting (LAE) source galaxies (Shu et al., 2016a). Spectroscopic redshifts of the lens and source are known, and follow-up high resolution imaging has been carried out for all systems.

To keep the data quality reasonably uniform (as it would be for a large future survey), we restrict the SLACS sample to the 43 lenses imaged to at least 1-orbit depth in the HST Advanced Camera for Surveys (ACS) F814W band. We add the 17 grade-A confirmed LAE lenses from GALLERY, all of which have been observed to 1-orbit depth in the HST Wide Field Camera 3 (WFC3) F606W band. Several systems have second or third foreground lenses of low mass. However, for this first attempt at automation we shall try to fit only a single main lens. Therefore, we have not considered GALLERY lens J0918+4518, which has two equally bright lens galaxies. We end up with a set of 59 lenses.

2.3.2 Data reduction

HST imaging of both the SLACS and GALLERY samples was reduced using custom pipelines. The procedure for the SLACS sample is described in Bolton et al. (2008a) and produces images with 0.05”pixels; the procedure for GALLERY is described in Brownstein et al. (2012) and Shu et al. (2016b), and produces images with 0.04”pixels. The point spread function (PSF) was determined for both samples using the `Tiny Tim` software Krist (1993). The aforementioned papers also describe an optional method to subtract the lens galaxy’s light by fitting it with a b-spline. Our pipeline benefits from fitting the lens light simultaneously with its mass, so we shall generally not use the b-spline data. However, our pipeline struggles to automatically deblend the lens and source light of three systems, so we shall try the b-spline data there.

2.4 Method

2.4.1 Overview

Our strong lens analysis is carried out using the software `PyAutoLens`[2], which is described in N18, building on the works of Warren & Dye (2003, hereafter WD03), Suyu et al. (2006, hereafter S06) and N15.

To fit a lens model to an image, `PyAutoLens` first assumes a parameterisation for the distribution of light and mass in the lens, and the distribution of light in the source, using the parametric profiles described in Sections 2.2.1 and 2.2.2. The parameterised intensity I of the lens light is evaluated at the centre of every image pixel, convolved with the instrumental PSF, and subtracted from the observed image. The mass model is then used to ray-trace image-pixels from their image-plane positions θ to source-plane positions β (via the lens equation 1.4.3). The source analysis finally follows, which `PyAutoLens` performs using one of two approaches: (i) parametric profiles in the source-plane (e.g. the Sérsic profile) are used to simply evaluate I at every value of β; (ii) a pixelized source reconstruction is performed on an adaptive Voronoi mesh, where the values of β are used to pair image-pixels to the Voronoi source pixels which reconstruct the source (see WD03, S06, N15 and N18 for a full description of lensing analyses with pixelized source reconstructions).

The following link (`https://github.com/Jammy2211/autolens_likelihood_function`) contains Jupyter notebooks that provide a visual step-by-step guide of the `PyAutoLens` likelihood function used in this work. The notebooks aims to clarify this and provides links to all previous literature describing the `PyAutoLens` likelihood function, alongside an explanation of the technical aspects of the linear algebra and Bayesian inference. We provide a brief description of the `PyAutoLens` likelihood function below, but we recommend these notebooks to the interested reader if anything is unclear.

2.4.2 Source Reconstruction

After subtracting the foreground lens emission and ray-tracing coordinates to the source-plane via the mass model, the source is reconstructed in the source-plane using an adaptive Voronoi mesh which accounts for irregular or asymmetric source morphologies (see Figure 2.1). Our results use the `PyAutoLens` pixelisation `VoronoiBrightnessImage`, which adapts the centres of the Voronoi pixels to the reconstructed source morphology, such that more resolution is dedicated to its brighter central regions (N18).

[2]The `PyAutoLens` software is open source and available from `https://github.com/Jammy2211/PyAutoLens`

Pipeline	Phase	Galaxy Component	Model	Varied	Prior Info	Phase Description
Source Parametric	**SP**^{1}	Lens light	Sérsic + Exp	✓	-	Fit only the lens light model and subtract it from the data image.
	SP^2	Lens mass	SIE + shear	✓	-	Fit the lens mass model and source light profile, comparing the lensed source model to the lens light subtracted image from **SP**^{1}.
		Source light	Sérsic	✓	-	
	SP^3	Lens light	Sérsic + Exp	✓	-	Refit the lens light model with default priors and fit the mass and source models with priors informed from **SP**^{2}.
		Lens mass	SIE + shear	✓	**SP**^{2}	
		Source light	Sérsic	✓	**SP**^{2}	
Source Inversion	**SI**^{1}	Lens light	Sérsic + Exp		**SP**^{3}	Fix lens light and mass parameters to those from the source parametric pipeline and fit pixelization and regularisation parameters on magnification adaptive pixel-grid.
		Lens mass	SIE + shear		**SP**^{3}	
		Source light	MPR	✓	-	
	SI^2	Lens light	Sérsic + Exp		**SP**^{3}	Refine the lens mass model parameters, keeping lens light and source-grid parameters fixed to those from previous phases.
		Lens mass	SIE + shear	✓	**SP**^{3}	
		Source light	MPR		**SI**^{1}	
	SI^3	Lens light	Sérsic + Exp		**SP**^{3}	Fit BPR pixelization and regularisation parameters, using the lensed source image from **SI**^{2} to determine the source galaxy pixel centres. Lens light and mass parameters are fixed to those from previous phases.
		Lens mass	SIE + shear		**SP**^{3}	
		Source light	BPR	✓	-	
	SI^4	Lens light	Sérsic + Exp		**SP**^{3}	Refine lens mass model parameters on the BPR grid, keeping lens light and source-grid parameters fixed to those from previous phases.
		Lens mass	SIE + shear	✓	**SI**^{2}	
		Source light	BPR		**SI**^{3}	
Light Parametric	**LP**^{1}	Lens light	Sérsic + Sérsic	✓	-	Fit lens light parameters, with lens mass and source parameters fixed to the result of the source inversion pipeline.
		Lens mass	SIE + shear		**SI**^{4}	
		Source light	BPR		**SI**^{3}	
Mass Total	**MT**^{1}	Lens light	Sérsic + Sérsic		**LP**^{1}	Fit the lens mass parameters, now with the slope of the density profile free to vary within the uniform prior [1.5-3.0], all other mass priors are informed from **SI**^{4}. The lens and source light are fixed to those from the **LP**^{1} pipeline.
		Lens mass	PLEMD + shear	✓	**SI**^{4}	
		Source light	BPR		**SI**^{3}	
	MT$^1_{\rm ext}$	Lens light	Sérsic + Sérsic		**LP**^{1}	An extension of the **MT**^{1} phase to ensure robust error inference on parameters. The lens mass parameters are re-fitted, capping likelihood evaluations to a fixed value (See Section 2.5 for details.)
		Lens mass	PLEMD + shear	✓	**MT**^{1}	
		Source light	BPR	✓	**MT**^{1}	

Table 2.1: Composition of the pipelines that make up our uniform analysis. Where prior info is not passed from previous pipelines see Table B.2 for the specific priors used on each model parameter.

The reconstruction computes the linear superposition of PSF-smeared source pixel images which best fits the observed image. This uses the matrix f_{ij}, which maps the jth pixel of each lensed image to each source pixel i. Following the formalism of (Warren & Dye, 2003, WD03 hereafter), we define the vector $\vec{D}_i = \sum_{\mathrm{j}=1}^{J} f_{ij}(d_j - b_j)/\sigma_j^2$ and curvature matrix $F_{ik} = \sum_{\mathrm{j}=1}^{J} f_{ij} f_{kj}/\sigma_j^2$, where d_j are the observed image flux values with statistical uncertainties σ_{j} and b_j are the model lens light values. The source pixel surface brightness values are given by $s = F^{-1}D$ which are solved via a linear inversion that minimizes

$$\chi^2 = \sum_{\mathrm{j}=1}^{J} \left[\frac{(\sum_{\mathrm{i}=1}^{I} s_i f_{ij}) + b_j - d_j}{\sigma_j} \right]. \tag{2.4.1}$$

The term $\sum_{\mathrm{i}=1}^{I} s_i f_{ij}$ maps the reconstructed source back to the image-plane for comparison with the observed data.

This matrix inversion is ill-posed, therefore to avoid over-fitting noise the solution is regularized using a linear regularization matrix H (see WD03). Regularization acts as a prior on the source reconstruction, penalizing solutions where the difference in reconstructed flux of these two neighboring Voronoi source pixels is large. Our results uses the `PyAutoLens` regularization scheme `AdaptiveBrightness`, which adapts the degree of smoothing to the reconstructed source's luminous emission . This has three hyper parameters, the inner regularization coefficient, outer regularization coefficient and a parameter that controls how the outer and inner regions of the source plane are defined for regularization. The degree of smoothing is chosen objectively using the Bayesian formalism introduced by Suyu et al. (2006). The likelihood function used in this work is taken from (Dye et al., 2008) and is given by

$$\begin{aligned} -2\ln\epsilon &= \chi^2 + s^T H s + \ln\left[\det(F+H)\right] - \ln\left[\det(H)\right] \\ &\quad + \sum_{\mathrm{j}=1}^{J} \ln\left[2\pi(\sigma_j)^2\right] . \end{aligned} \tag{2.4.2}$$

2.4.3 Automated Procedure

`PyAutoLens`

`PyAutoLens` is designed to approach lens modelling in a fully automated way (N18, Nightingale et al., 2021a). This uses a technique we term 'non-linear search chaining', which sequentially fits lens models of gradually increasing complexity. By initially fitting simpler lens models one can ensure that their corresponding non-linear parameter spaces are sampled in an efficient and robust manner that prevents local maxima being inferred. The resulting lens models then act as initialisation in subsequent model-fits which add more complexity to the lens model, guiding the non-linear search on where to look in parameter space for the highest likelihood lens models, ensuring the global maximum

model has the highest chance of being inferred. Non-linear search chaining is performed using the probabilistic programming language `PyAutoFit` (`https://github.com/rhayes777/PyAutoFit`), a spin off project of `PyAutoLens` which generalises the statistical methods used to model strong lenses into a general purpose statistics library.

To perform model-fitting `PyAutoLens` uses the nested sampling algorithm `dynesty` (Speagle, 2020), which obtains the posterior probability distributions for a given lens model's parameters. Nested sampling's ability to robustly sample from low dimensional (e.g. fewer than $\sim$ 30 parameters), complex parameter space distributions makes it well suited to lens modelling. We use `dynesty`'s random walk sampling for every model-fit performed in this work, which we found gave a significant improvement over other sampling techniques owing to its better accounting of the covariance between lens model parameters. Since nested sampling starts by randomly sampling from the prior, the size and choice of priors directly impact the expected number of nested sampling iterations alongside how likely it is that a local maximum is incorrectly inferred. As such, using more informative priors will reduce the amount of time needed to integrate over the posterior and guide towards sampling the highest likelihood global maxima solutions.

Non-linear search chaining allows us to construct informative priors from the results of one `dynesty` search and pass them to subsequent model-fits, thereby guiding them on where to sample parameter space. This uses a technique called prior passing (see N18), which sets the prior of each parameter as a Gaussian whose mean is that parameter's previously inferred median PDF (probability density function) value and its width is a customisable value specific to every lens model and parameter. The specific order of prior passing used in this study is given in Table 2.1. The prior widths have been carefully chosen to ensure they are broad enough not to omit valid lens model solutions, but sufficiently narrow to ensure the lens model does not inadvertently infer local maxima. More quantitatively, the prior widths are typically greater than $\sim$ 10 times the errors we ultimately infer on each parameter, meaning it has negligible impact on the posterior (see Section 2.5).

User Setup

In this work, we use the standardised Source Light and Mass (SLaM) pipelines that are available, and fully customisable, in `PyAutoLens`. From these, we construct a pipeline that chains together a total of 11 `dynesty` searches which we apply to every lens in our sample, which we describe in detail in Section 2.4.3. Before we run the SLaM pipelines a few brief pre-processing steps must be carried out; we describe those here, as well as our chosen pipeline settings.

We define a circular mask centred on the lens galaxy that defines the image pixels we fit to. For the

SLACS and GALLERY lenses we use a standard size of 3.5″ and 3.0″ radius, respectively. This is increased to 4.0″ for the SLACS lenses J0912+0029 and J0216-0813, and for the GALLERY lens J0755+3445. All image pixels outside this mask are completely omitted from the analysis, meaning they are not traced to the source plane and included in the source reconstruction procedure.

We create scalable noise maps, unique to each lens, that define any regions inside the mask that we do not wish to fit (e.g. unrelated astronomical sources projected by chance along adjacent lines of sight). In these regions the image values are scaled to near zero and the noise-map values to large values such that the likelihood calculation effectively ignores them. Such areas of high flux would otherwise be indistinguishable from the source flux to the fitting procedure. We adopt this noise map approach, over the complete removal of such regions, since image-pixels are still traced to the source-plane and included in the source reconstruction procedure. This avoids creating discontinuities or 'holes' in the source pixelisation which can degrade the quality of the overall reconstruction. The maps are produced in a graphical user interface (GUI) available in `PyAutoLens`, designed to reduce the human time necessary for creating each unique map (~1 minute per lens). We acknowledge this task is overly time-intensive when considering the incoming samples of tens of thousands of lenses and provide a discussion of possible routes to automation of this pre-processing step in Section 2.7.1.

Finally, we store an array containing the coordinates of the pixels containing the peak surface brightness of each multiple image of the source galaxy, again selected by the user via a GUI. These coordinates are used to remove local maxima from the parameter spaces explored throughout the pipeline. In practise, this is done by discarding any models where the ray-traced points in the source plane are not within a positions threshold value of each other. This value is initially set to 0.7″[2]. Both the threshold and the positions themselves are then iteratively updated throughout the SLaM pipeline, by solving the lens equation using the maximum likelihood mass model estimated in a previous fit. For each iteration, the value is set to three times the separation of the positions found after solving the lens equation or a value of 0.2″, whichever is largest. This ensures that, as we progress from parametric to pixelised source reconstructions, we avoid the under and over-magnified solutions that can be problematic for these methods Maresca et al. (2020).

[2]This choice of arcsecond value reflects a low threshold for what we consider a plausible lens model, removing only extremely unphysical mass models. For example, without it the mass model could choose to be close to zero by fitting a source to only one multiple image with its centre aligned directly behind that image. We note this means we do not require the locations of the multiple images to be extremely accurate.

Uniform Analysis

The uniform analysis ultimately aims to constrain the parameters describing the mass and light distributions. The lens galaxy's mass is parameterized as a PLEMD (equation 1.4.14), while the lens light is modelled as a double Seŕsic profile, which is a sum of two Sérsic profiles (equation 2.2.3) with a common centre. This is achieved by reconstructing the source galaxy's light distribution on an adaptive Brightness-based Pixelisation and Regularisation (BPR) grid. The uniform analysis is constructed from multiple pipelines that each focus on fitting a specific aspect of the lens model which we describe below. For an overview of the composition of the overall method see Table 2.1. A scaled down version of this pipeline was used by Cao et al. (2020) to model fifty simulated strong lenses.

We begin with the Source Parametric (SP) pipeline that fits the foreground lens galaxy's light profile, alongside a robust initialisation of less complex models for the mass distribution of the lens and light distribution of the source galaxy. The lens mass is modelled as an SIE (equation 1.4.14 with $\gamma = 2$) plus external shear. The lens light is modelled by the sum of a Sérsic and Exponential (equation 2.2.3 with n=1) profile. The source galaxy's light is described by a single Sérsic profile; this is key to the initialisation of the model using the SP pipeline, as it allows us to compute an initial estimate of the mass profile without `dynesty` getting stuck in a local maximum (as methods with a pixelised source frequently do; N18, Maresca et al. 2020).

The Source Inversion (SI) pipeline then refines the lens galaxy's mass distribution by modelling the source galaxy using an adaptive pixelisation. This allows more realistic morphologies of the source galaxy to be recognised, which in turn improves the model for the lens galaxy's mass. The pixelisation and its pixel-to-pixel regularisation are described by a set of hyper-parameters (see Section 2.4.2 for more details), that are fitted for as free parameters in the fit. These are first initialised using a Magnification based Pixelisation and Regularisation (MPR) grid. The source model from this fit is then used to inform the the BPR pixelisation that adapts to the surface brightness of the source galaxy, thereby reconstructing areas of high flux with higher resolution and lower regularisation relative to areas of low flux.

The Light Parametric (LP) pipeline re-fits the lens galaxy's light profile. This produces a more accurate estimate of the lens galaxy's light than previously, because the lensed source galaxy's light is now reconstructed using the Voronoi pixelisation, thereby reducing residuals which otherwise impact the lens light model fit. The lens light model is now composed of two Sérsic profiles (the second component now has a free Sérsic index). This fit is performed using broad uninformative priors and thus does not use any information about the lens galaxy's light profile estimated by the previous pipelines.

Finally, the Mass Total (MT) pipeline extends the complexity of the model of the lens galaxy's mass to that of the PLEMD (equation 1.4.14), whereby the slope of the density profile (γ) is now a free parameter in the model. A uniform prior between 1.5 and 3 is assumed on the slope. To ensure robust error inference on the parameters of our final model, the MT phase is extended by re-running the same model with a 'likelihood cap' applied (see Section 2.5 for details). The term 'Mass Total' is used to distinguish this pipeline from the 'Mass Light Dark' SLaM pipeline which is not used in this work. Instead of fitting a mass model that represents the total mass distribution this pipeline fits one that separately models the light and dark mater (Nightingale et al., 2019).

Results Database

Upon completion of a uniform pipeline there are `dynesty` samples of 11 different model-fits, alongside additional metadata describing quantities such as each parameter's estimate, their errors and the `PyAutoLens` settings. Across our sample of 59 strong lenses this creates over 500 lens modelling results, necessitating tools to automate their processing and inspection. `PyAutoFit` outputs all modelling results to a queryable SQLite database (Hipp, 2020) such that they can be easily loaded into a Jupyter notebook or Python script post-analysis. By adopting `PyAutoFit`, all `PyAutoLens` results support this SQLite database which is the primary tool we use for analysing lens modelling results.

2.5 Dealing with noise in likelihood evaluations

N15 demonstrated that pixelised source reconstructions can be subject to a discretization bias that ultimately leads to the underestimation of errors calculated by a typical non-linear search (N15). This is a result of discrete jumps in the likelihood as the lens model parameters are smoothly varied, which hinders convergence and parameter marginalisation. N15 suggests this may be a common problem for methods that employ pixelised sources. Here, we investigate the effects of the bias further using a large sample of mock observations.

2.5.1 Mock data sample

We create 59 synthetic lenses similar to our SLACS and GALLERY lenses, to approximately resemble the real data but with known truths. The mass distribution of each synthetic lens is a PLEMD; we set the radius b and ellipticity parameters ε_1 and ε_2 to those of the SIE lens model measured in previous lensing analyses (see Table 5 of Bolton et al. (2008b) and Table 2 of Shu et al. (2016b) for SLACS and GALLERY parameters, respectively). We set the slope γ of the density profiles to the lensing and

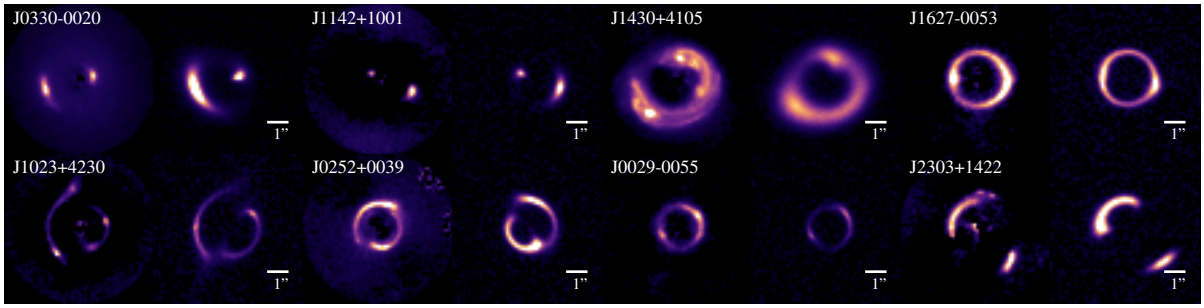

Figure 2.2: We create a sample of mock lenses that closely resemble each of the 59 SLACS and GALLERY lenses in our observed data sample, which we use for testing for data discretization bias. We show eight of these mock images (right panel) alongside the real data image they were simulated to represent (left panel with lens name). The mock images are simulated without light from the lens galaxy, as such we compare to the data images where the lens galaxy's (double Seŕsic) light profile has been subtracted.

dynamics measurements of Auger et al. (2010a) (SLACS) and Shu et al. (2016b) (GALLERY). Where the slope of the density profile is not available, we instead use the values inferred by preliminary runs of our own strong lensing-only analysis. The surface brightness of each source galaxy is simulated as an elliptical Sérsic, the parameters of which are set to those inferred during preliminary runs of our Source Parametric Pipeline[1]. The redshifts of the lens and source are set to those known for the corresponding real strong lens.

For every synthetic lens configuration, we create six mock observations, each with different realisations of observational noise. To mimic the HST observations the lensed image of the source is generated with a pixel scale of $0.05''$ (SLACS) and $0.04''$ (GALLERY) and convolved with the instrumental point spread function (PSF) modelled from the actual image of the strong lens we are simulating. The synthetic images include a flat sky background of 37.5 (SLACS) and 31.5 electrons per second (GALLERY) and six different realisations of Poisson noise. We choose not to simulate light from the lens galaxy since this has the potential to introduce systematic effects that we are not interested in investigating with this sample (see Section 2.5). Across the resulting suite of 354 synthetic observations, the S/N of the brightest pixel in each image ranges from 4 to 68. Figure 2.2 compares a subset of simulated mock lenses with their real data counterparts.

[1]The Sérsic source parameters were optimised for an SIE mass profile but simulated with a PLEMD, leading to a difference in magnification of the source galaxy in the mock data. As a result, some lensed sources were simulated with lower signal-to-noise ratio (S/N) values than observed. In these cases we manually adjust their intensity value to give a peak S/N$\gtrsim$3.

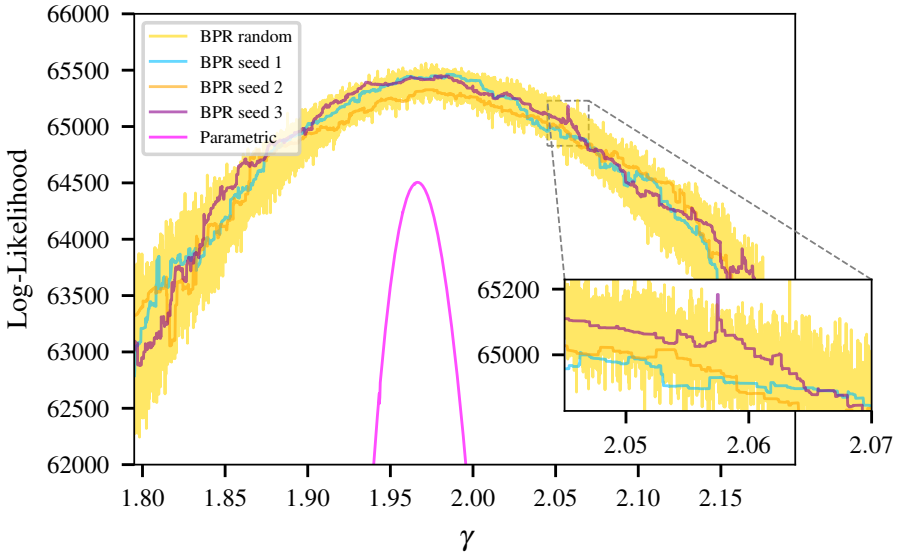

Figure 2.3: Comparison of the log likelihood as a function of density profile slope when using a parametric source (pink curve) or Brightness-based pixelisation and Regularisation (BPR) pixelisations to fit to mock data. All model parameters other than the slope are fixed to their true values. The yellow line reveals the full level of noise in the likelihood due to the particulars of the source plane pixelisation, by using a new random seed for the k-means algorithm that pixelates the source plane for every likelihood evaluation. The other three colours use fixed k-means seeds, as is done throughout the rest of this paper.

2.5.2 The origin of discretization bias and error underestimation

First, we investigate how discretization bias manifests in `PyAutoLens`, whose source pixelisation differs in its implementation from N15 and N18. This is illustrated in Figure 2.3, which plots the variation of the log likelihood of a lens model when changing only the slope parameter γ of the mass distribution (fixing all other parameters to their true values). The parametric source model produces a smooth likelihood curve. The BPR pixelisation methods produce a higher likelihood, but one that is subject to seemingly random noise. These 'spikes' in log likelihood occur over small ranges in the slope parameter; at least an order of magnitude smaller than the errors one infers for γ when fitting this lens with a parametric source. This confuses the nested sampler, which converges to positive spikes in likelihood that are tiny volumes of the multi-dimensional parameter space, and thus significantly underestimate the total statistical uncertainty.

To perform a source reconstruction using a pixelised source, one must first define a procedure that determines the shape and locations of the source-plane pixels, its discretization. For example, in the case of `PyAutoLens`, one can alter the random seed that determines the centres of the Voronoi source pixels. This element of choice makes the likelihood ill-determined, as is demonstrated in Figure 2.3 by the three different realisations of noise that are uncovered for the differently seeded grids (the only

difference between the fits that produces the blue, orange, and purple likelihood surface is the choice of k-means seed that determines the source-pixel centres). If we choose to pass a random k-means seed to each individual fit (the yellow curve in Figure 2.3) the full scale of the noise due to different source discretizations is revealed, likelihood evaluations of almost identical lens models can yield very different likelihood values when the source pixelisation changes. Sampling the parameter space when using a random k-means seed is therefore prohibitively slow, ultimately leading to the non-linear search becoming stuck and being unable to converge.

In fact, repeat likelihood evaluations of an identical lens model also yield different likelihood values if the source pixelisation's discretization changes. Figure 2.4 shows the result of doing exactly this, where log likelihood values are computed using an identical lens model 500 times (we use the best fit lens model parameters from our fitting procedure to do this), with each computation using only a different Voronoi mesh to reconstruct the source. The three different coloured histograms show the results of this procedure for three of the six noise realisation images of a lens, that arrive at three different best fit lens models. In all cases, the histograms of log likelihood values show that changes in log likelihood of order ~ 50 are possible by just changing the source pixelisation. To perform parameter estimation, changes in log likelihood of order ~ 10 define how precisely a parameter is estimated at $\sim 3\sigma$ confidence. Thus, if our log likelihoods can fluctuate by of order ~ 50 in a seemingly arbitrary way, this will be detrimental to parameter and error estimation.

Why does the log likelihood vary when we change the source pixelisation? For a given lens model, there are certain source pixelisations where the centres of their Voronoi source pixels line up with the locations of the traced image-pixels mapped from the image data in a 'preferable' way. Their alignment allows the source pixels to reconstruct the image data more accurately, in a way that is penalised less by regularisation (see S06). This produces what we consider an artificial 'boost' in likelihood. Conversely, other pixelisations have a less fortuitous alignment, such that their reconstruction of the image data is worse and they are more heavily penalised by regularisation, producing an artificial 'drop' in log likelihood. Figure 2.4 shows that the distribution of log-likelihoods appears to be Gaussian, a property we will use when we put forward a solution to this problem.

We are now in a position to explain the spiky likelihood surface shown for the fixed seed BPR pixelisations in Figure 2.3. Let us first consider in more detail the BPR pixelisation implemented in `PyAutoLens`. To construct the source-pixel centres, the BPR pixelisation applies a weighted k-means algorithm in the image plane to determine a set of coordinates that are adapted to the lensed source's surface brightness. This k-means algorithm is seeded such that the same image-plane coordinates are inferred if the procedure (using the same inputs) is run multiple times (thus the completely random

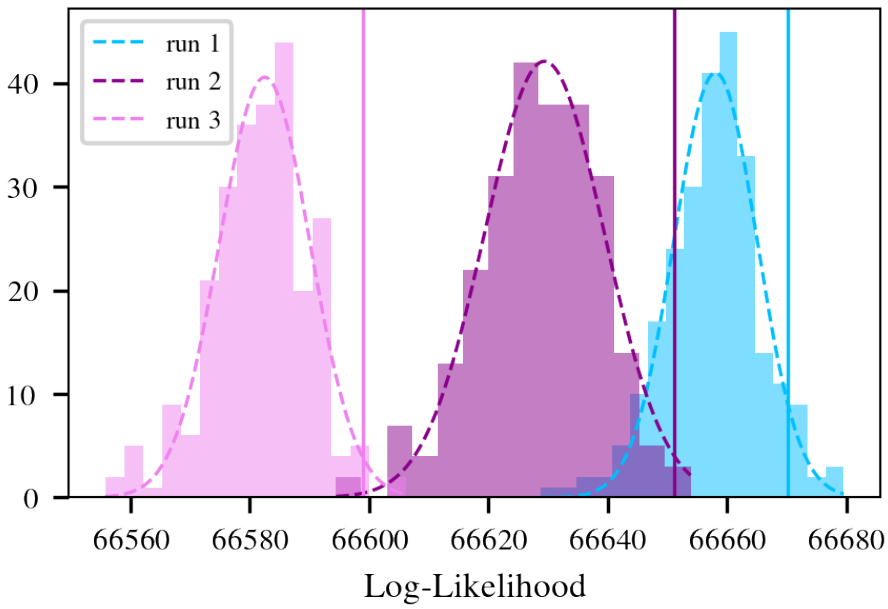

Figure 2.4: Histogram of log-likelihood values from re-fitting the best-fit model with a new k-means seed 500 times, while keeping the model parameters fixed. The dashed line is the fitted Gaussian curve to these values. The vertical line shows the maximum likelihood value of the best-fit parameters found without a likelihood cap, which is always boosted by noise to extremely high likelihood. For clarity we show three of the six distributions from different noise realisation images of the mock lens, the same behaviour is evident in the three distributions not shown here.

changes to the source pixelisation used to construct the histograms shown in Figure 2.4 cannot explain these likelihood spikes). These image-plane coordinates are then ray-traced via the mass model to the source-plane and are used as the centres of the source pixels of the Voronoi mesh. To produce the blue, orange, and purple curves shown in Figure 2.3, the coordinates that construct the source pixelisation are therefore fixed in the image-plane, but vary smoothly with the mass model in the source plane. The spiky likelihood surface can therefore be explained by how the continuous change in the positions of the source pixels generating the Voronoi pixelisation produces discrete changes in the Voronoi mesh (either creating new cells or changing the value of flux across cell boundaries - these changes may occur less frequently with interpolation of the source pixel grid). The reconstruction then receives boosts and drops in log likelihood as for certain mass models (values of γ) since the positions of the source pixels align more or less favourably with the data.

2.5.3 Testing for error underestimation in lens modelling

In the context of a full non-linear search which varies every lens model parameter, we expect that likelihood spikes due to this preferable alignment of the source pixelisation with the data will be present, negatively impacting our inference on each parameter's PDF. To investigate this, we fit the

full sample of 354 mock images (see section 2.5.1) with a uniform pipeline constructed from the SLaM pipelines in `PyAutoLens`. The pipeline is the equivalent of that described in Section 2.4.3 but created for fitting images without the lens galaxy's light distribution (see Appendix B.1 for an overview of the pipeline). The pipeline, then, infers the mass parameters of the lens galaxy described by a PLEMD, while reconstructing the source galaxy on a BPR pixelisation. We choose not to fit for an external shear (which is not present in the lens models of the simulated data) in order to simplify our investigation of likelihood boosts. Our main goal, here, is to determine if the error estimates inferred by the non-linear search are being underestimated as a result of the data discretization bias.

Figure 2.5 shows the posterior PDFs obtained for individual runs of two lenses in our mock sample. For each lens, six realisations of the image data with different noise maps were simulated and fitted, which correspond to the six individual PDFs shown on each panel of Figure 2.5. Not only do the PDF contours rarely contain the true parameter (represented by the grey dashed lines) they also rarely overlap with each other. To verify this is due to data discretization bias, for each of the 354 synthetic images we now produce 500 new likelihood evaluations — fixing all lens and source model parameters to the best-fit values, but randomising the k-means seed used to pixelate the source plane. For 94.6% of these 177,000 calculations, the new likelihood is lower than the best-fit model likelihood, indicating that the likelihood values inferred by `dynesty` were systematically boosted relative to the majority of possible source pixelisations. Figure 2.4 shows this for three example cases, where the solid lines show the maximum log likelihood model inferred via `dynesty` compared to a histogram of these 500 models drawn using random k-means seeds.

The likelihood boosted solutions inferred by `dynesty` occupy a tiny volume of parameter space, such that parameter marginalisation significantly underestimates the width of the posterior PDF. For each of the lens model parameters we calculate the percentage of the 354 model fits that recover the true parameter within their 1D marginalised 68.7%, 95%, and 99% credible regions (blue bars in Figure 2.6). On average for all lens model parameters the truth is recovered only 30% or 50% of the time at the 68.7% and 95% credible regions. These coverage probabilities are significantly smaller than the percentage credible regions they were calculated for — the reported uncertainties are too small.

2.5.4 Likelihood Cap for improving sample statistics

We now investigate the efficacy of placing a 'log likelihood cap' on the non-linear search, where this cap is estimated in a way that seeks to smooth out likelihood spikes in parameter space. The cap is computed by taking the maximum likelihood lens model of the non-linear search inferred by the

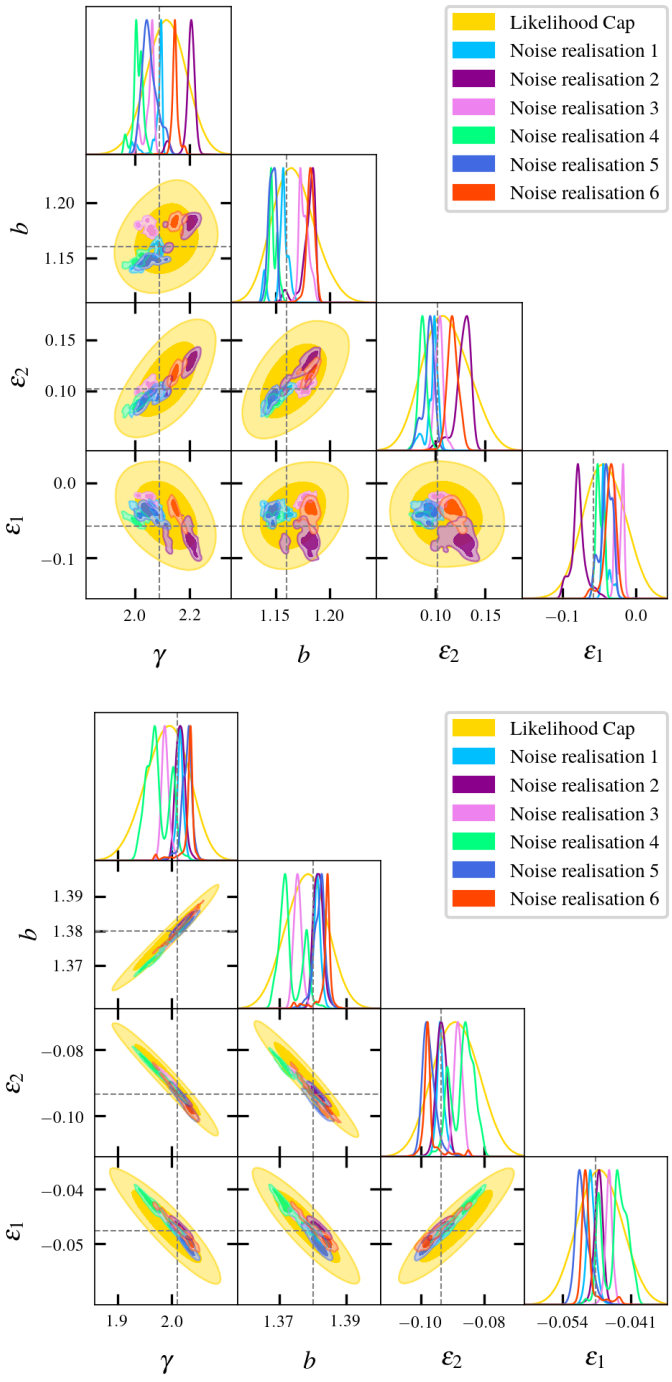

Figure 2.5: For two typical synthetic lenses, the posterior PDF of model parameters inferred from mock observations. With a likelihood cap (yellow), these PDFs have sufficient width to include the true value (crossed lines). Without a likelihood cap, the PDFs from mock data with different realisations of observational noise (six other colours) are too narrow because of noise in the likelihood evaluations. Fitted parameters shown are the mass-density slope (γ), mass normalisation ($R_{\rm al}$), and two components of ellipticity (ε_1, ε_2); all other free parameters are marginalised over.

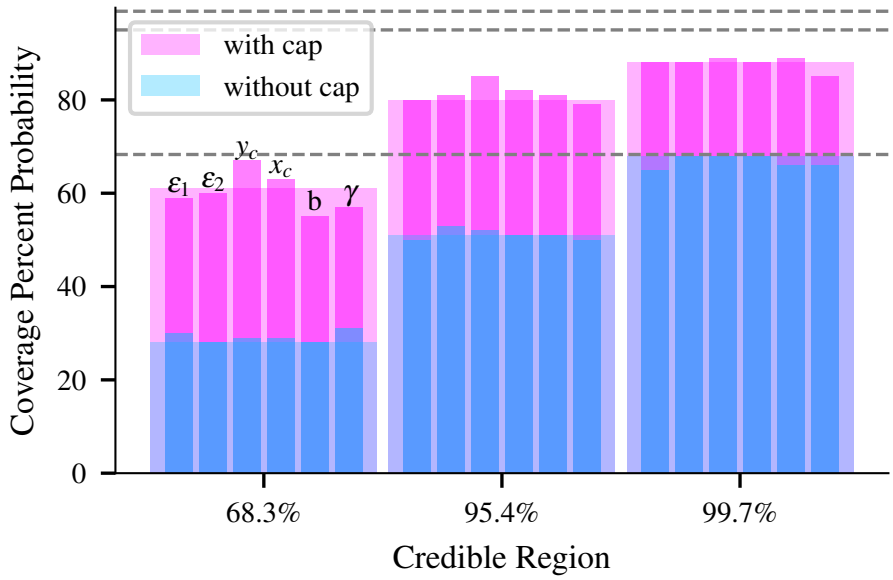

Figure 2.6: Coverage probabilities of the lens model parameters with (pink) and without (blue) a likelihood cap applied to the non-linear search. The thin bars give the coverage probabilities of individual lens model parameters as labelled, and the wider bars represent the average of these values.

$\mathbf{MT}^1_{\text{ext}}$ search in the SLaM pipeline and computing 500 likelihood evaluations using this model but each with a different k-means seed. This process produces the histograms shown in figure 2.4, which are fitted with a Gaussian whose mean then acts as the log likelihood cap. We then repeat the final $\mathbf{MT}^1$ search of the pipeline (with identical parameters, hyper-parameters, k-means seed, etc.), but any log likelihood evaluation now returns no more than this value. If a log likelihood is computed above this cap, it is rounded down to the cap's value before it is returned to `dynesty`. We note that this assumes that `dynesty` has not converged on a local maximum in $\mathbf{MT}^1$. The yellow shaded contours in Figure 2.5 show the PDFs inferred by $\mathbf{MT}^1_{\text{ext}}$ using this log likelihood cap, which now appear larger, smoother, and do not have undesirable properties such as islands and discontinuities that are seen for the PDFs inferred without this cap.

When performed on our 354 synthetic images, the final parameter estimation now converges more consistently for different realisations of noise (for the sake of visual clarity, Figure 2.5 only shows one PDF, but all six PDFs do now overlap for each dataset). The coverage probabilities for the 1D marginalised 68.7% or 95% and 99% credible regions have increased significantly for all lens model parameters with the use of the likelihood cap (see Figure 2.6 for the comparison with and without the likelihood cap). On average the true lens model parameters are recovered 61% and 80% of the time at the 68.7% or 95% credible regions, respectively. Although we do not obtain full coverage, this is a significant improvement in error estimation compared to not including the likelihood capped phase. Furthermore, for each lens model parameter we compare the mean of the best fit values of the six

noise realisations, and find that these are recovered 74% of the time at the 68.7% credible region on average for all parameters. This suggests that the likelihood cap is producing errors that are consistent with the uncertainty due to random noise in the image, and that our posteriors recover the true values slightly less frequently than hoped due to systematic biases in particular lens configurations that offset the inferred parameters from the truth.

Further testing is necessary to understand the systematics that result from the source discretization bias as well as any systematic offsets in inferred lens parameters in particular lens configurations. This would require a larger set of mocks than was simulated for this study (see Section 2.7.4 for more discussion) and is beyond the scope of this work. At present, it appears that the likelihood cap is effective at improving the coverage probability of the 68.7% credible region (only 7% shy of achieving coverage for lens models parameters on average). Since the mock data was simulated to be representative of the observed data, we assume this will be true of the errors on the data adopting the same approach. As such, all errors quoted in this work are those at the 68.7% credible region of the PDFs inferred by the likelihood capped $\mathbf{MT}^{1}_{\mathrm{ext}}$ phase.

2.6 Results

2.6.1 Automation

We now inspect the results of our automated modelling procedure on the SLACS and BELLS GALLERY samples and quantify what fraction of lenses were fitted with a reliable lens model without human intervention. To facilitate this, we visually inspect every lens model, first after the **SP** pipeline and then again on completion of the uniform procedure. We label the final model of every lens in one of four categories:

- **Gold (54/59):** The fit represents a physically plausible model of the lens and source.
- **Silver (4/59):** The fit represents a physically plausible model of the lens and source. However, achieving this required changes to data pre-processing that may not be easy to automate (e.g. masking, lens light subtraction), and may degrade the quality of the inferred lens model.
- **Bronze (1/59):** The fit represents a physically plausible model of the lens (with the correct number of multiple images), but other features in the data (e.g. residuals from lens light subtraction) visibly degrade the quality of the source model.
- **Failure (0/59):** The fit produces a physically implausible lens model (e.g. with an incorrect number of multiple images).

After a first blind run, we find 9 galaxies outside the "Gold" sample. In 8/9 cases, they went wrong during the first **SP** pipeline. We determine what went wrong, describe simple interventions, and rerun the pipeline. Our interventions successfully move all of these lenses into the "Bronze", "Silver" or "Gold" categories. Through this process, we suggest ways to reduce the failure rate in analyses of future large samples of lenses. For future analysis of large lens samples, one can anticipate undergoing this process on a subset of lenses before modelling the full sample.

If a lens ends up in the "Gold", "Silver", or "Bronze" categories, we consider its effective Einstein Radius $R_{\rm Ein,eff}$ to be measured accurately. If a lens is in the "Gold" or "Silver" categories, we also consider more detailed quantities of the mass model (e.g. the slope γ) to be reliable. Indeed, we shall find our best-fit models broadly consistent with those from previous literature, in Sections 2.7.2 and 2.7.3.

Fully automated success

We immediately place 50/59 lenses (85%) in the "Gold" sample after the first, blind run of our uniform pipeline. These models show low levels of residuals and physically plausible source galaxy morphologies. Best-fit model parameters are listed in Tables 2.2 (SLACS) and 2.3 (GALLERY), and reconstructions are shown in Appendix D.

Semi-automated success

Fits to 4/59 lens systems converge to models with the wrong number of lensed images. In all four cases, the fits incorrectly converge to a highly elliptical mass distribution early in the **SP** pipeline, and could not recover the better solution in the **SI** or subsequent pipelines. The model of J1451−0239 fits 4 images to what is (by eye) a 2 image system (Figure 2.7). Fits to J0237−0239 and J0856+2010 converge to single-image models, each missing a central counter-image that is close to the centre of the lens galaxy and therefore difficult to disentangle from the lens galaxy's light (Figure 2.8). The model of J0841+3824 is multiply imaged, but its very faint counter image is in the wrong location (Figure 2.9).

We fixed this by rerunning the pipeline for these lenses, but restricting the $\mathbf{SP}^2$ phase to more circular mass models, via a uniform prior $\varepsilon_i \in [-0.2, 0.2]$, instead of a Gaussian with $\sigma = 0.3$. To better find the global maximum likelihood solution for lenses J0237−0239, J0841+3824, and J0856+2010, we also increased the number of `dynesty` live points to 600 from 200 in $\mathbf{SP}^2$ (this was not necessary for J1451-0239, where a change has no consequences other than increased runtime). With these settings,

Class	Lens Name	$R_{\rm Ein,eff}$	γ	q	ϕ	$\gamma^{\rm ext}$	$\phi^{\rm ext}$
Gold	J0008-0004	$1.15^{+0.007}_{-0.009}$	$2.08^{+0.08}_{-0.07}$	$0.72^{+0.03}_{-0.03}$	$42^{+5.1}_{-6.1}$	$0.023^{+0.018}_{-0.014}$	96^{+15}_{-23}
	J0029-0055	$0.934^{+0.007}_{-0.008}$	$2.32^{+0.13}_{-0.13}$	$0.78^{+0.06}_{-0.07}$	$22^{+9.3}_{-12}$	$0.013^{+0.019}_{-0.012}$	11^{+32}_{-44}
	J0157-0056	$0.912^{+0.013}_{-0.012}$	$2.23^{+0.08}_{-0.09}$	$0.56^{+0.07}_{-0.05}$	$112^{+4.8}_{-7.6}$	$0.182^{+0.021}_{-0.027}$	$102^{+3.0}_{-3.2}$
	J0216-0813	$1.183^{+0.014}_{-0.011}$	$1.99^{+0.05}_{-0.06}$	$0.8^{+0.04}_{-0.03}$	$75^{+9.2}_{-6.3}$	$0.009^{+0.012}_{-0.011}$	2^{+37}_{-55}
	J0252+0039	$1.024^{+0.004}_{-0.002}$	$1.92^{+0.08}_{-0.11}$	$0.89^{+0.02}_{-0.02}$	$111^{+3.5}_{-4.0}$	$0.024^{+0.005}_{-0.003}$	$117^{+6.1}_{-6.4}$
	J0330-0020	$1.088^{+0.009}_{-0.012}$	$2.15^{+0.02}_{-0.02}$	$0.79^{+0.07}_{-0.08}$	94^{+11}_{-14}	$0.041^{+0.021}_{-0.018}$	54^{+12}_{-15}
	J0728+3835	$1.244^{+0.012}_{-0.008}$	$1.99^{+0.12}_{-0.1}$	$0.68^{+0.05}_{-0.04}$	$65^{+3.4}_{-3.4}$	$0.068^{+0.015}_{-0.021}$	$61^{+5.5}_{-6.3}$
	J0737+3216	$0.976^{+0.003}_{-0.002}$	$2.28^{+0.07}_{-0.07}$	$0.86^{+0.04}_{-0.03}$	$96^{+5.4}_{-5.6}$	$0.109^{+0.007}_{-0.011}$	$10^{+1.7}_{-1.4}$
	J0822+2652	$1.129^{+0.011}_{-0.018}$	$2.1^{+0.08}_{-0.07}$	$0.54^{+0.04}_{-0.05}$	$75^{+4.9}_{-4.3}$	$0.1^{+0.021}_{-0.018}$	$72^{+6.6}_{-6.3}$
	J0841+3824	$0.956^{+0.096}_{-0.063}$	$2.27^{+0.2}_{-0.16}$	$0.69^{+0.15}_{-0.14}$	117^{+24}_{-28}	$0.144^{+0.047}_{-0.031}$	$117^{+6.8}_{-7.2}$
	J0903+4116	$1.261^{+0.005}_{-0.005}$	$2.23^{+0.05}_{-0.05}$	$0.88^{+0.04}_{-0.03}$	$52^{+12}_{-7.6}$	$0.062^{+0.01}_{-0.012}$	$63^{+5.6}_{-4.9}$
	J0912+0029	$1.393^{+0.011}_{-0.007}$	$2.14^{+0.05}_{-0.05}$	$0.79^{+0.04}_{-0.04}$	$27^{+8.1}_{-6.9}$	$0.033^{+0.011}_{-0.012}$	$126^{+12}_{-9.3}$
	J0936+0913	$1.081^{+0.004}_{-0.005}$	$2.13^{+0.08}_{-0.08}$	$0.79^{+0.05}_{-0.05}$	$134^{+4.9}_{-5.8}$	$0.061^{+0.013}_{-0.011}$	$105^{+6.6}_{-7.4}$
	J0946+1006	$1.409^{+0.001}_{-0.001}$	$2.06^{+0.03}_{-0.03}$	$0.9^{+0.0}_{-0.01}$	$68^{+1.8}_{-2.2}$	$0.09^{+0.004}_{-0.003}$	$68^{+0.79}_{-0.65}$
	J0956+5100	$1.314^{+0.002}_{-0.001}$	$2.05^{+0.02}_{-0.02}$	$0.79^{+0.01}_{-0.01}$	$143^{+1.0}_{-1.3}$	$0.066^{+0.003}_{-0.005}$	$53^{+1.4}_{-0.97}$
	J0959+0410	$0.985^{+0.014}_{-0.017}$	$2.08^{+0.07}_{-0.07}$	$0.52^{+0.07}_{-0.1}$	$59^{+5.3}_{-6.2}$	$0.038^{+0.024}_{-0.025}$	60^{+18}_{-33}
	J1020+1122	$1.065^{+0.011}_{-0.009}$	$2.15^{+0.11}_{-0.12}$	$0.54^{+0.04}_{-0.04}$	$131^{+3.3}_{-2.8}$	$0.159^{+0.023}_{-0.024}$	$131^{+3.2}_{-4.3}$
	J1023+4230	$1.411^{+0.009}_{-0.009}$	$1.95^{+0.16}_{-0.12}$	$0.92^{+0.05}_{-0.04}$	177^{+14}_{-17}	$0.023^{+0.01}_{-0.009}$	68^{+18}_{-25}
	J1029+0420	$0.947^{+0.01}_{-0.01}$	$1.43^{+0.05}_{-0.06}$	$0.62^{+0.02}_{-0.03}$	$111^{+3.4}_{-3.4}$	$0.152^{+0.02}_{-0.02}$	$100^{+2.3}_{-4.5}$
	J1032+5322	$1.03^{+0.011}_{-0.007}$	$2.11^{+0.02}_{-0.03}$	$0.69^{+0.07}_{-0.05}$	$143^{+5.5}_{-6.3}$	$0.039^{+0.019}_{-0.019}$	167^{+13}_{-19}
	J1142+1001	$0.908^{+0.024}_{-0.027}$	$2.03^{+0.1}_{-0.1}$	$0.49^{+0.11}_{-0.06}$	$144^{+4.7}_{-4.7}$	$0.21^{+0.04}_{-0.05}$	$148^{+5.0}_{-6.3}$
	J1143-0144	$1.611^{+0.013}_{-0.014}$	$2.15^{+0.03}_{-0.03}$	$0.73^{+0.04}_{-0.04}$	$116^{+5.6}_{-4.5}$	$0.038^{+0.01}_{-0.01}$	$166^{+13}_{-9.1}$
	J1205+4910	$1.218^{+0.008}_{-0.008}$	$1.92^{+0.07}_{-0.09}$	$0.74^{+0.08}_{-0.06}$	$149^{+6.8}_{-5.6}$	$0.019^{+0.011}_{-0.019}$	99^{+33}_{-28}
	J1213+6708	$1.322^{+0.018}_{-0.023}$	$2.8^{+0.07}_{-0.07}$	$0.92^{+0.07}_{-0.11}$	3^{+74}_{-49}	$0.045^{+0.018}_{-0.019}$	9^{+15}_{-15}
	J1218+0830	$1.217^{+0.01}_{-0.008}$	$2.35^{+0.07}_{-0.06}$	$0.35^{+0.03}_{-0.02}$	$144^{+1.4}_{-2.0}$	$0.353^{+0.011}_{-0.021}$	$140^{+1.3}_{-0.96}$
	J1250+0523	$1.144^{+0.006}_{-0.005}$	$1.84^{+0.04}_{-0.04}$	$0.91^{+0.03}_{-0.04}$	$129^{+7.2}_{-7.6}$	$0.024^{+0.014}_{-0.01}$	$132^{+15}_{-9.9}$
	J1402+6321	$1.349^{+0.005}_{-0.007}$	$2.00^{+0.18}_{-0.13}$	$0.72^{+0.04}_{-0.04}$	$63^{+3.1}_{-2.6}$	$0.030^{+0.019}_{-0.014}$	$1^{+14}_{-9.9}$
	J1420+6019	$1.075^{+0.002}_{-0.002}$	$1.94^{+0.04}_{-0.04}$	$0.43^{+0.02}_{-0.02}$	$111^{+0.45}_{-0.60}$	$0.118^{+0.009}_{-0.009}$	$110^{+1.1}_{-1.0}$
	J1430+4105	$1.481^{+0.002}_{-0.002}$	$2.02^{+0.01}_{-0.01}$	$0.91^{+0.01}_{-0.01}$	$120^{+2.1}_{-1.9}$	$0.088^{+0.002}_{-0.002}$	$22^{+0.64}_{-0.53}$
	J1432+6317	$1.284^{+0.01}_{-0.009}$	$1.79^{+0.06}_{-0.04}$	$0.88^{+0.05}_{-0.05}$	102^{+12}_{-11}	$0.099^{+0.016}_{-0.016}$	$115^{+3.8}_{-5.0}$
	J1451-0239	$0.96^{+0.017}_{-0.015}$	$2.29^{+0.1}_{-0.11}$	$0.54^{+0.06}_{-0.07}$	$30^{+3.7}_{-4.5}$	$0.193^{+0.042}_{-0.025}$	$27^{+3.6}_{-3.1}$
	J1525+3327	$1.29^{+0.012}_{-0.007}$	$1.92^{+0.06}_{-0.05}$	$0.59^{+0.04}_{-0.04}$	$117^{+2.8}_{-3.1}$	$0.14^{+0.01}_{-0.011}$	$87^{+3.1}_{-3.2}$
	J1627-0053	$1.217^{+0.002}_{-0.002}$	$2.08^{+0.08}_{-0.09}$	$0.84^{+0.03}_{-0.01}$	$8^{+2.6}_{-3.2}$	$0.019^{+0.005}_{-0.004}$	$6^{+6.8}_{-7.9}$
	J1630+4520	$1.791^{+0.006}_{-0.004}$	$1.96^{+0.09}_{-0.08}$	$0.83^{+0.01}_{-0.01}$	$70^{+2.7}_{-2.5}$	$0.023^{+0.006}_{-0.004}$	$59^{+7.6}_{-9.8}$
	J2238-0754	$1.268^{+0.004}_{-0.003}$	$2.07^{+0.09}_{-0.07}$	$0.83^{+0.03}_{-0.04}$	$137^{+5.8}_{-6.0}$	$0.004^{+0.007}_{-0.006}$	3^{+52}_{-35}
	J2300+0022	$1.219^{+0.008}_{-0.005}$	$2.55^{+0.07}_{-0.16}$	$0.62^{+0.05}_{-0.04}$	$74^{+3.8}_{-3.7}$	$0.094^{+0.012}_{-0.018}$	$9^{+4.0}_{-3.3}$
	J2303+1422	$1.628^{+0.007}_{-0.005}$	$2.09^{+0.04}_{-0.04}$	$0.53^{+0.05}_{-0.05}$	$34^{+1.6}_{-1.4}$	$0.002^{+0.007}_{-0.005}$	171^{+44}_{-49}
	J2341+0000	$1.338^{+0.009}_{-0.005}$	$2.12^{+0.06}_{-0.05}$	$0.8^{+0.03}_{-0.03}$	$81^{+3.7}_{-3.5}$	$0.027^{+0.009}_{-0.014}$	$167^{+8.9}_{-10.}$
Silver	J0959+4416	$0.972^{+0.023}_{-0.02}$	$2.5^{+0.19}_{-0.23}$	$0.67^{+0.14}_{-0.1}$	$83^{+16}_{-9.8}$	$0.027^{+0.037}_{-0.026}$	88^{+57}_{-29}
	J1016+3859	$1.004^{+0.026}_{-0.02}$	$2.23^{+0.15}_{-0.2}$	$0.56^{+0.13}_{-0.13}$	$92^{+11}_{-10.}$	$0.217^{+0.05}_{-0.042}$	$113^{+6.1}_{-4.9}$
	J1153+4612	$1.029^{+0.007}_{-0.005}$	$1.72^{+0.08}_{-0.1}$	$0.61^{+0.03}_{-0.03}$	$104^{+1.9}_{-1.6}$	$0.181^{+0.013}_{-0.013}$	$101^{+1.9}_{-2.1}$
	J1416+5136	$1.246^{+0.014}_{-0.018}$	$2.0^{+0.01}_{-0.01}$	$0.73^{+0.11}_{-0.09}$	$103^{+7.9}_{-3.9}$	$0.152^{+0.025}_{-0.032}$	$108^{+4.7}_{-2.8}$
Bronze	J1103+5322	$1.065^{+0.007}_{-0.007}$	$1.79^{+0.01}_{-0.01}$	$0.53^{+0.04}_{-0.04}$	$49^{+1.8}_{-1.5}$	$0.103^{+0.013}_{-0.009}$	$0^{+3.2}_{-2.2}$

Table 2.2: Best-fit physical parameters for SLACS lenses. These are derived quantities, obtained from the varied parameters of the lens mass model (Table C.1). Lens light model parameters are presented in (Table C.4).

Class	Lens Name	$R_{\rm Ein,efff}$	γ	q	ϕ	$\gamma^{\rm ext}$	$\phi^{\rm ext}$
Gold	J0029+2544	$1.347^{+0.014}_{-0.012}$	$2.05^{+0.12}_{-0.15}$	$0.65^{+0.07}_{-0.08}$	$128^{+6.7}_{-7.6}$	$0.029^{+0.033}_{-0.018}$	$149^{+40.}_{-31}$
	J0113+0250	$1.329^{+0.006}_{-0.005}$	$1.77^{+0.15}_{-0.11}$	$0.75^{+0.02}_{-0.02}$	$178^{+2.8}_{-4.4}$	$0.079^{+0.014}_{-0.012}$	$15^{+3.9}_{-5.9}$
	J0201+3228	$1.713^{+0.011}_{-0.005}$	$2.09^{+0.09}_{-0.1}$	$0.78^{+0.03}_{-0.02}$	$125^{+5.4}_{-3.6}$	$0.063^{+0.016}_{-0.014}$	$53^{+4.7}_{-5.7}$
	J0237-0641	$0.619^{+0.02}_{-0.025}$	$1.91^{+0.18}_{-0.1}$	$0.79^{+0.12}_{-0.09}$	$131^{+30.}_{-17}$	$0.027^{+0.044}_{-0.033}$	6^{+36}_{-55}
	J0742+3341	$1.241^{+0.01}_{-0.013}$	$2.21^{+0.06}_{-0.08}$	$0.29^{+0.04}_{-0.04}$	$56^{+3.4}_{-3.0}$	$0.107^{+0.016}_{-0.023}$	$44^{+6.4}_{-8.7}$
	J0755+3445	$2.073^{+0.005}_{-0.004}$	$1.77^{+0.08}_{-0.05}$	$0.53^{+0.01}_{-0.01}$	$15^{+1.9}_{-1.5}$	$0.24^{+0.006}_{-0.006}$	$28^{+1.6}_{-1.1}$
	J0856+2010	$0.951^{+0.035}_{-0.04}$	$2.23^{+0.08}_{-0.09}$	$0.36^{+0.09}_{-0.06}$	$45^{+5.9}_{-4.3}$	$0.153^{+0.023}_{-0.03}$	$93^{+6.5}_{-7.2}$
	J0918+5105	$1.645^{+0.005}_{-0.009}$	$2.38^{+0.16}_{-0.18}$	$0.78^{+0.04}_{-0.06}$	$95^{+18}_{-9.4}$	$0.259^{+0.034}_{-0.02}$	$125^{+0.60}_{-1.3}$
	J1110+2808	$0.904^{+0.027}_{-0.026}$	$2.03^{+0.09}_{-0.07}$	$0.82^{+0.08}_{-0.07}$	77^{+22}_{-16}	$0.123^{+0.043}_{-0.028}$	$55^{+7.1}_{-6.3}$
	J1110+3649	$1.151^{+0.001}_{-0.001}$	$2.23^{+0.07}_{-0.08}$	$0.77^{+0.02}_{-0.02}$	$174^{+1.4}_{-1.5}$	$0.025^{+0.005}_{-0.005}$	$64^{+5.6}_{-5.8}$
	J1116+0915	$0.811^{+0.053}_{-0.054}$	$2.22^{+0.16}_{-0.17}$	$0.21^{+0.05}_{-0.05}$	$86^{+4.3}_{-3.5}$	$0.393^{+0.053}_{-0.046}$	$88^{+3.6}_{-2.8}$
	J1141+2216	$1.283^{+0.027}_{-0.019}$	$2.13^{+0.09}_{-0.11}$	$0.58^{+0.09}_{-0.09}$	$57^{+5.5}_{-7.6}$	$0.043^{+0.026}_{-0.022}$	$38^{+23}_{-30.}$
	J1201+4743	$1.171^{+0.004}_{-0.002}$	$2.74^{+0.05}_{-0.21}$	$0.82^{+0.06}_{-0.06}$	$130^{+14}_{-7.8}$	$0.069^{+0.004}_{-0.01}$	$42^{+3.7}_{-3.4}$
	J1226+5457	$1.398^{+0.004}_{-0.003}$	$2.24^{+0.07}_{-0.1}$	$0.86^{+0.02}_{-0.02}$	$130^{+6.6}_{-7.9}$	$0.189^{+0.012}_{-0.012}$	$156^{+0.76}_{-0.75}$
	J2228+1205	$1.21^{+0.024}_{-0.024}$	$2.2^{+0.14}_{-0.1}$	$0.51^{+0.1}_{-0.05}$	$116^{+5.7}_{-8.0}$	$0.202^{+0.026}_{-0.023}$	$141^{+5.7}_{-3.3}$
	J2342-0120	$1.091^{+0.006}_{-0.004}$	$2.34^{+0.07}_{-0.09}$	$0.44^{+0.05}_{-0.03}$	$114^{+3.6}_{-2.5}$	$0.13^{+0.009}_{-0.016}$	$94^{+4.4}_{-2.6}$

Table 2.3: Best-fit physical parameters for BELLS GALLERY lenses. These are derived quantities, obtained from the varied parameters of the lens mass model (Table C.2). Lens light model parameters are presented in (Table C.3).

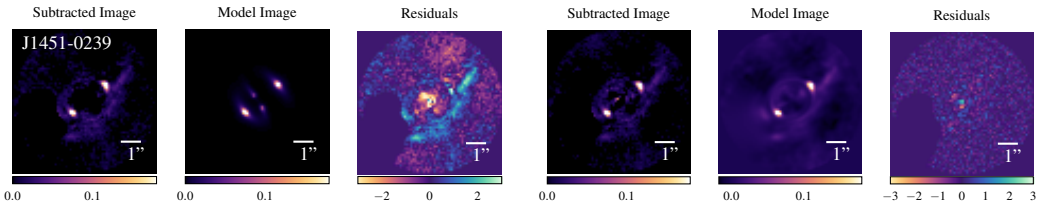

(a) Unsuccessful model fit in the Source Parametric pipeline.

(b) Successful model fit on completion of the pipeline.

Figure 2.7: (a) Model fits for the system that misses the counter image. (b) After tightening the prior on the elliptical components of the mass distribution to $\varepsilon_I \in [-0.2, 0.2]$, the system is fitted successfully, and is classified as a "Gold" model.

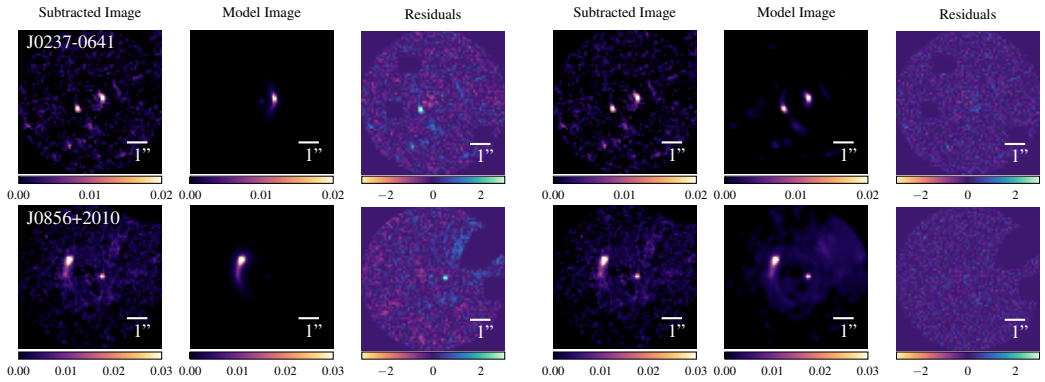

(a) Unsuccessful model fit in the Source Parametric pipeline.

(b) Successful model fit on completion of the pipeline.

Figure 2.8: (a) Model fits for the systems that fail to fit the counter image in the Source Parametric phase. (b) After tightening the prior on the elliptical components of the mass distribution to $\varepsilon_I \in [-0.2, 0.2]$, the systems are fitted successfully, and are classified as "Gold" models.

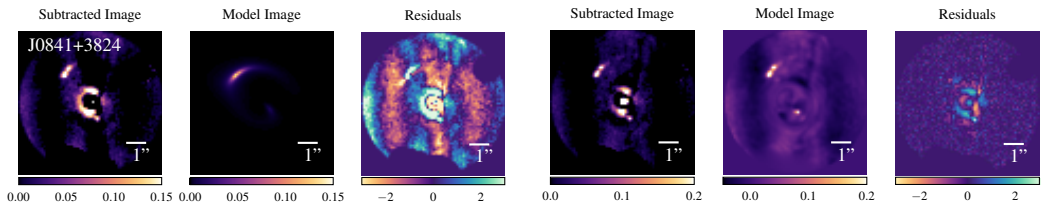

(a) Unsuccessful model fit in the Source Parametric pipeline.

(b) Successful model fit on completion of the pipeline.

Figure 2.9: (a) Model fits for the system that misses the counter image. (b) After tightening the prior on the elliptical components of the mass distribution to $\varepsilon_I \in [-0.2, 0.2]$, the system is fitted successfully, and is classified as a "Gold" model.

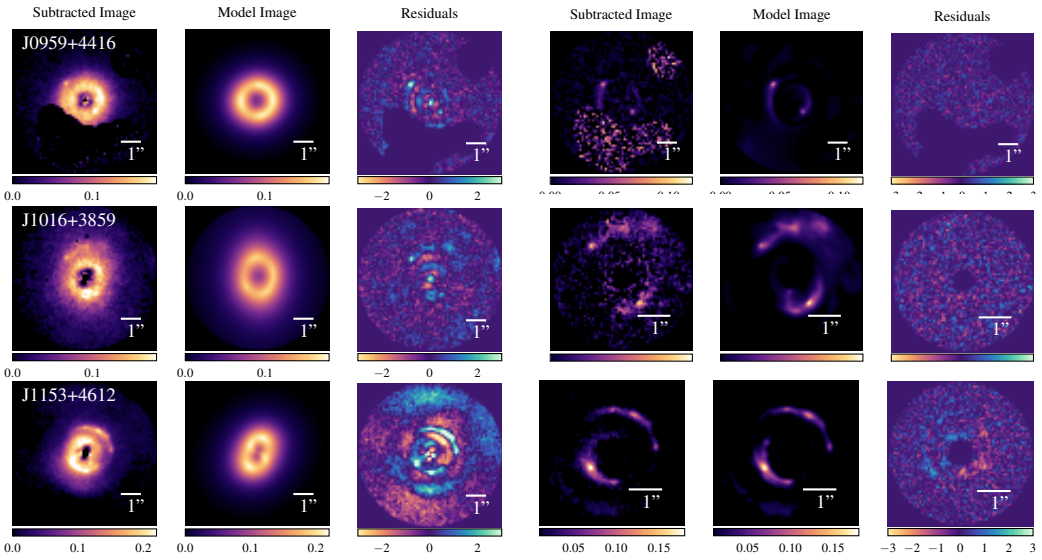

(a) Unsuccessful model fit in the Source Parametric pipeline.

(b) Successful model fit on completion of the pipeline.

Figure 2.10: (a) Model fits for the lens systems that fail to fit successful models in the Source Parametric pipeline as a result of bad lens light subtractions. The model reproduces lens light emission that remains in the subtracted image and significant residuals can be seen where the source emission is being ignored by the model. (b) For these systems we replace the data with b-spline subtracted data and use custom masks to arrive at successful model fits classified as “Silver” models.

the automated modelling procedure is a success and the models (also shown in Figure 2.1) are moved into the “Gold” sample.

These fits can be easily fixed by a more restrictive (or an all-round better) early initialisation. Our solution of forcing fairly circular models works well for early-type galaxy lenses, but would need to be rethought if the sample could include late-type galaxies with (edge-on) discs. Since spectroscopic lens detection techniques also identify the lens galaxy type, a different prior could be used for each.

For now, we conclude that the biggest challenge of scaling up lens modelling to large samples is fitting an initial, physically plausible lens model. Once a simple lens model is correctly initialised, nothing prevents subsequent convergence of increasingly complex distributions of source light and lens mass. We shall discuss this further in Section 2.7.1.

Success with human intervention

Fits to 3/59 lens systems converge to a model in which imperfect lens light subtraction has left a spurious, residual ring of lens light that becomes considered part of the source. This again happens during the early **SP** pipeline, after which the Sérsic model of the source is too large (Figure 2.10a). Subsequent pixelised source models also include the residual lens light. Unlike the previous failure

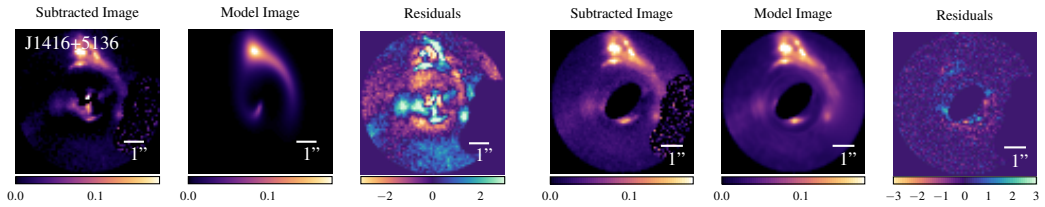

(a) Unsuccessful model fit in the Source Parametric pipeline.

(b) Successful model fit on completion of the pipeline.

Figure 2.11: (a) Model fits for the lens system that misses the counter image, instead fitting a counter image to lens light residuals. (b) The lens requires rerunning with our own double Sérsic subtracted data using the without lens light pipeline, as well as a custom mask, to arrive at the successful "Silver" model fit.

modes, we could not find small changes to the automated pipeline that fix these model fits.

For lenses J1153+4612, J1016+3859, and J0959+4416, we instead use the b-spline subtracted data (Section 2.3.2). These versions pre-subtract the lens galaxy's light more cleanly than our double Sérsic fit. Even then, we mask small remaining residuals near the centre of J1153+4612 and J1016+3859. We finally refit all three lenses using the version of the pipeline (which was also for the mock data) that does not fit the lens light. This results in successful models, as assessed by our visual inspection criteria (Figure 2.10b). Although we arrive at successful model fits, we categorise these lenses in the "Silver" sample, because the lens light was not fitted in a Bayesian manner.

The fit to 1/59 lens systems includes a counter-image that reproduces a residual knot of lens light emission instead of the adjacent but fainter true counter-image (Figure 2.11). It can be fixed by masking the knot of lens light and rerunning the pipeline. However, this process would be difficult to automate with monochromatic imaging, so we place J1416+5136 in the "Silver" sample.

Remaining problematic lens

The lens J1103+5322 is the only system that is unable to pass our visual inspection criteria on completion of the uniform pipeline. In the SP pipeline the model fits an appropriate model that fits the global lensed structure of the source, however significant residuals are present in the fit. The lens light subtraction leaves a quadrupole-like feature in the centre of the subtracted image as well as flux extending past the Einstein-ring feature. The SP pipeline is able to fit a model that fits solely to the source light, however continuation of the pipeline leads to a final model that reconstructs the lens light residual structure, which in Figure 2.12 can be seen to extend far beyond the emission from the source. This feature could impact the measurement of parameters which depend on the gradient of the flux in the lensed source, like the slope of the mass model. Replacing the data with

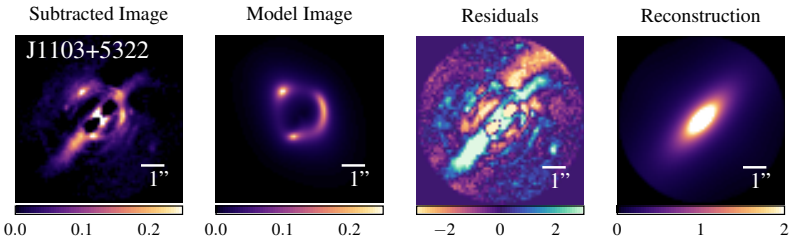

(a) Successful model fit in the Source Parametric pipeline.

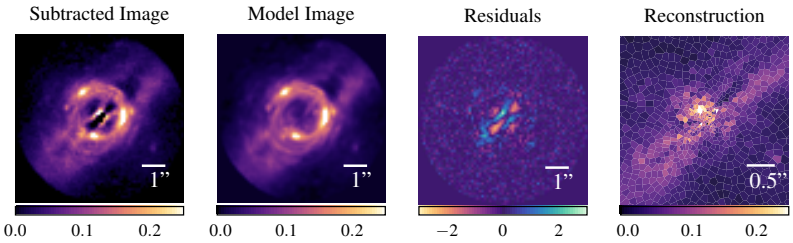

(b) Unsuccessful model fit on completion of the pipeline.

Figure 2.12: (a) The single lens J1103+5322 is successful on completion of the Source Parametric pipeline, the parametric source avoids fitting to lens light residuals that remain in the subtracted image. (b) However, on completion of the pipeline the pixelised source reconstruction is unable to avoid fitting to these residuals, leading to this lens's classification of "Bronze".

the b-spline subtracted data resulted in similar residual lens light emission being reconstructed by the source galaxy. Nevertheless, we believe that this model estimates $R_{\mathrm{Ein,eff}}$ accurately, our measurement is within 5% of previous literature measurements (see Section 2.7.2 for a discussion on the expected uncertainty between these methods). As a result, we place this lens in our "Bronze" sample.

Model Parameter	**Mean Error**		**Median Error**	
	cap	without cap	cap	without cap
b	0.036	0.010	0.027	0.005
γ	0.087	0.014	0.079	0.002
ε_1	0.039	0.010	0.028	0.005
ε_2	0.038	0.025	0.031	0.015
$\gamma_{1_{\mathrm{ext}}}$	0.018	0.005	0.016	0.003
$\gamma_{2_{\mathrm{ext}}}$	0.019	0.009	0.017	0.004
x_{c}	0.016	0.006	0.014	0.003
y_{c}	0.016	0.004	0.013	0.004

Table 2.4: Summary of the average 68% credible region errors inferred for all mass model parameters with and without a likelihood cap applied to the non-linear search.

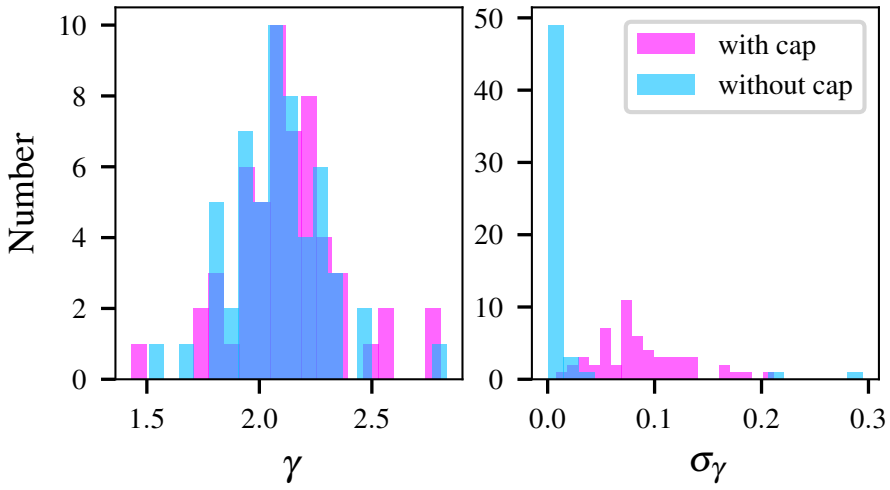

Figure 2.13: Comparison of the distribution of inferred slopes (left) and their associated 1σ credible region (right) with and without a likelihood cap applied to the non-linear search.

2.6.2 Statistical uncertainty on measurements

Effect of the Likelihood Cap

In Section 2.5 we demonstrated the necessity of a likelihood capped phase ($\mathbf{MT}^1_{\rm ext}$) to increase the formal statistical errors inferred by the non-linear search such that they better recovered the true parameters on mock data. We now quantify the affect this phase has on the uncertainties inferred on real data (see Figure 2.13 for its affect on the density profile slope errors). On average, we find that this approach has increased the inferred non-linear search errors by a factor of ~ 5, as assessed by the median of individual factor increases for all mass model parameters. We quote the median increase to avoid bias from 5 lenses whose errors increase by a factor of over 1000 upon introduction of the log likelihood cap. On investigation, we found these lenses correspond to those with the largest difference between the likelihood inferred in $\mathbf{MT}^1$ and the likelihood cap applied to $\mathbf{MT}^1_{\rm ext}$ (defined as the mean of 500 repeated likelihood evaluations with the same mass model, but different data discretizations). Hence, these lenses are the ones that were in the most "likelihood-boosted" regions of parameter space and as a result significantly underestimated the error. In the most extreme example, J0755+3445, the error inferred on the slope parameter with a likelihood cap is 64453 times larger than that inferred without a cap (see Ritondale et al., 2019, for a discussion of this lens). This highlights the scale at which the certainty of parameters can be incorrectly inferred without consideration of the source discretization bias. Further quantification of the average errors inferred at the 68% credible region for each mass model parameter with and without a likelihood cap is given in Table 2.4.

Of all the mass model parameters, the likelihood cap has the largest effect on the density profile slope.

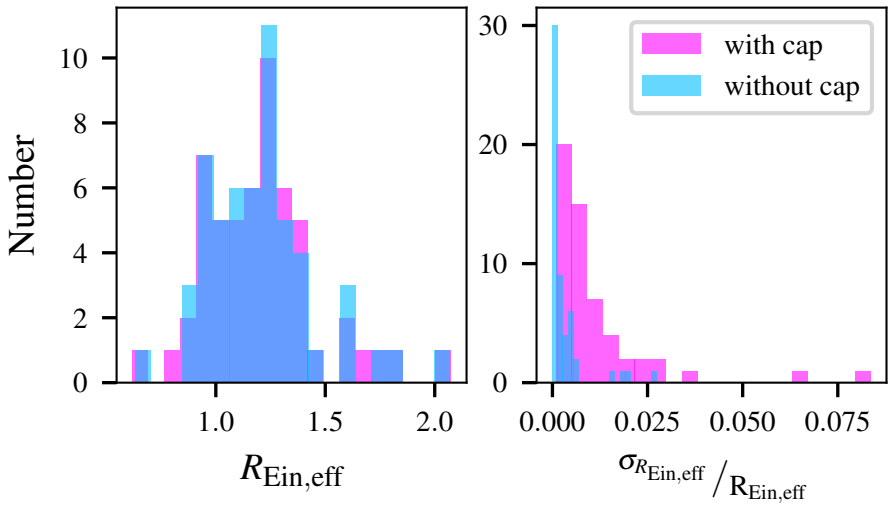

Figure 2.14: Comparison of the distribution of inferred Einstein radii (left) and their associated percentage error at the 1σ credible region (right), with and without a likelihood cap applied to the non-linear search.

The median factor increase in the error size before and after the cap is 24. The distribution of the 68% credible region errors with and without the cap are plotted in the right panel of Figure 2.13. Notably there are two extreme outliers in the distribution of errors inferred without a cap, that are the two largest errors inferred across both distributions. For the lenses J1016+3859 and J0959+4416, both of which were replaced with b-spline subtracted data as an intervention to achieve model fits, the error actually decreases when the likelihood cap is applied. Although the uncertainty on the slope measurement is in general, as expected, significantly increased in $\mathbf{MT}^{1}_{\mathrm{ext}}$ relative to $\mathbf{MT}^{1}$, the distribution of slopes inferred does not change significantly (left panel of Figure 2.13). The mean increases from 2.08 to 2.12, and the standard deviation increases from 0.21 to 0.24.

We derive errors on the effective Einstein radius by calculating a posterior PDF from all possible effective Einstein radii given the accepted non-linear search samples and their weights. We find the inclusion of the likelihood cap increases the mean 68% credible region error on the effective Einstein radius from 0.3% to 1.1%, and does not affect the distribution of $R_{\mathrm{Ein,eff}}$ we infer (see Figure 2.14). This suggests that, on average, the Einstein radius can be measured to $\sim$ 1% uncertainty, taking into account uncertainties in the noise and source discretization. We note that this does not account for any systematic error that would result from discrepancies between the assumed mass model and the underlying mass distribution. However, although the mean uncertainty on $R_{\mathrm{Ein,eff}}$ is low, two lenses (J0841+3824 and J1116+0915) have anomalously large uncertainties of 8.6% and 6.6% respectively. Hence, for some lens configurations it appears the Einstein radius can not be determined with such certainty. This may be an indication that the underlying mass distribution for these lenses is more

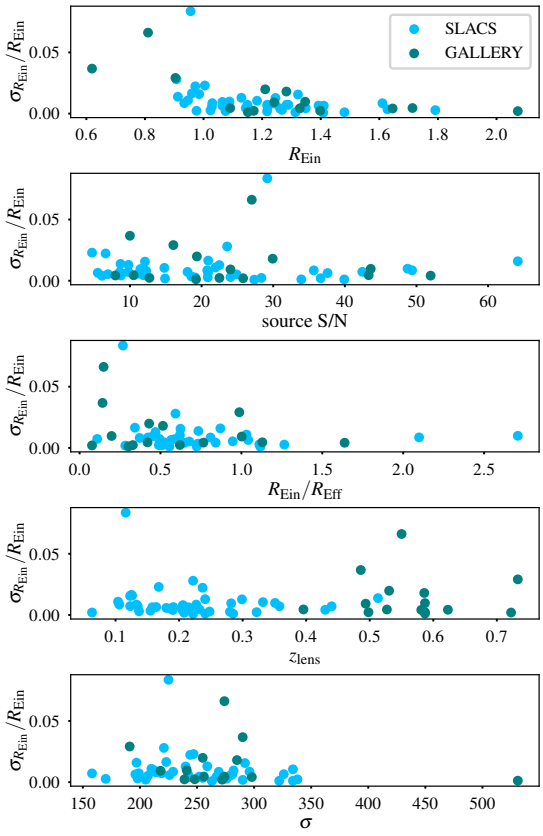

Figure 2.15: Inferred percentage errors on the Einstein radii at the 68% credible region as a function of observable properties of the lens galaxy, and the S/N of the source. Parameters for linear fits to these data are given in Table 3.2.

complex than the PLEMD that we assume in our model fits. This seems reasonable for these two lenses since J0841+3824 is one of the few disky galaxies in the sample, with obvious extended spiral features in the data, and J1116+0915 contains a visible mass clump to the North of the lens that we do not fit for with our uniform approach.

What drives the precision of a lens model?

To investigate what properties of the lens or data (if any) drive the precision of the lens model, we measure correlation coefficients between statistical uncertainty on the effective Einstein radius and observable properties of the lens galaxy: including the Einstein radius itself, the ratio of the Einstein radius to the effective radius, the lens redshift, the velocity dispersion of the lens, and the peak S/N of the source (Figure 2.15). Linear fits show no clear trend with most of these parameters. The only non-negligible correlation (defined as a non-zero gradient with $>3\sigma$ significance) is with the Einstein radius. The correlation remains when we repeat the linear fit removing the two uncertainties that are larger than 5% that could bias the relation, although the effect size does reduce by over a third

Parameter	Gradient	Intercept
$R_{\mathrm{Ein,eff}}$ ($''$)	-0.027 ± 0.007	0.044 ± 0.008
$R_{\mathrm{Ein,eff}}$ ($''$) [$> 5\%$ removed]	-0.017 ± 0.004	0.029 ± 0.004
peak source S/N	$(0.0 \pm 1.0) \times 10^{-4}$	0.011 ± 0.004
$R_{\mathrm{Ein,eff}}/R_{\mathrm{eff}}$	$(-6.4 \pm 4.0) \times 10^{-4}$	0.015 ± 0.004
z_{lens}	0.0 ± 0.01	0.010 ± 0.004
$\sigma\left(kms^{-1}\right)$	$(-3.4 \pm 3.7) \times 10^{-5}$	0.020 ± 0.010

Table 2.5: Linear fit results for the correlations with the uncertainty on the Einstein radius. Errors quoted on the gradient and intercept are the 1σ confidence intervals.

(Table 3.2).

2.7 Discussion

2.7.1 Can we truly leave no lens behind?

The success of our uniform pipeline makes us optimistic for the future of automated strong lens analysis. We initially fitted 50/59 (85%) lenses in a blind run. We increased this to 54/59 (92%) "Gold" lenses after tweaking model priors, 58/59 (98%) "Gold" or "Silver" lenses with some pre-fitting and masking of lens light, and 59/59 (100%) including one successful model of the lens whose model of the source includes poorly-subtracted residuals of lens light. With just one pipeline, we have inferred parameters for 59/59 lenses that measure the lens galaxy's Einstein radius and other mass distribution parameters (of the power-law profile with an external shear we assume) that depend on only the first derivative of the potential of the lens galaxy. For 58/59 systems, we measure parameters describing their mass (including the parameters that depend on the gradient of the source flux such as γ). As well as this, we reconstruct a de-lensed image of the source galaxy, enabling study of its morphology. For 54/59 systems, we measure parameters describing their mass distribution *and* light distribution (as a double Sérsic profile) as well as reconstructing a de-lensed image of the source galaxy.

The most challenging step in automating lens modelling is in the initial estimation of a simple lens model (in this work, we use an SIE plus shear). Notably, once our early **SP** phases arrived at a successful fit to this model, the rest of our pipeline always ran to completion, successfully increasing the model complexity. We therefore recommend that effort to further improve automation should focus on 'lens model initialisation' and find ways to avoid or flag the problematic solutions that occur at early stages of the analysis. Provided that our sample of lenses is representative of the larger population of lenses that will be discovered by future surveys, this strategy will lead to a high success rate for

even complex mass fits and reduce the need for visual inspection of the results. An obvious starting point to improve lens model initialisation by `PyAutoLens` would be to further simplify the non-linear parameter space of the **SP** pipeline, for example by assuming models for the lens and source light with fewer parameters (e.g. Massey & Refregier, 2005; Birrer et al., 2015; Tagore & Jackson, 2016; Bergé et al., 2019).

Convolutional Neural Networks (CNNs) have also been suggested as a fast method for automated lens fitting (Hezaveh et al., 2017; Levasseur et al., 2017; Morningstar et al., 2018). They provide a particularly compelling solution to the problem of lens model initialisation. For example, Pearson et al. (2021) combined a CNN with `PyAutoLens`, using models from the CNN to initialise the mass model priors of a `PyAutoLens` model-fit. In the majority of cases tested on mock data, the authors argued that a combination of the two methods outperformed either method individually. Indeed, the strengths of a CNN (fast run-times, avoidance of unphysical solutions) complement the weaknesses of Bayesian inference approaches like `PyAutoLens`. It is conceivable that a CNN could replace `PyAutoLens`'s initial lens model fits altogether and allow the method to focus entirely on fitting more complex lens models with well characterised errors: a task better suited to `PyAutoLens`'s fully Bayesian approach than a CNN. At least, a CNN might be able to identify and isolate which lenses will eventually make the gold sample, and reduce manual intervention Maresca et al. (2020). CNNs will also have an as-yet unquantified fraction of failures. If the lenses where a CNN fails are different to where traditional model-fitting approaches fail, combining the two may be key to maximising the success rate of lens model initialisation.

The second major challenge for automated lens modelling is deblending the foreground lens light. Within our sample, `PyAutoLens` could not deblend the lens and source light in 3/59 systems, and required visual inspection to recognise these bad fits. In these cases, we instead used b-spline fits that were created via a time-consuming manual process. This issue will be more prevalent in Euclid, owing to its lower spatial resolution than HST and lens samples with smaller Einstein radii (Collett, 2015) — both of which move the source's light closer to that of the lens. Furthermore, our analysis included pre-processing steps that manually removed the light of foreground stars and interloper galaxies via a GUI, a task which is overly time-intensive for an individual scientist to perform on larger samples of lenses.

We propose two directions for future work that could improve automatic deblending, CNNs being the first approach. There are CNN architectures dedicated to the task of image deblending and segmentation (these architectures do not attempt to estimate the lens model parameters). These have been applied successfully on galaxy catalogues (Burke et al., 2019; Hausen & Robertson, 2020)

and in studies of strong lenses (Rojas et al., 2021), with multi-wavelength imaging seen to improve debelending quality. Furthermore, Pearson et al. (2021) showed that lens modelling with a CNN is viable with the lens light still present. Alternatively, this task seems well suited to citizen science (Küng et al., 2015; Marshall et al., 2016; More et al., 2016), whereby members of the public could use a GUI to mark-out regions of the data they believe correspond to the lens, source and other objects. The desired outputs of either approach are pixel-level masks describing where the source, lens and other objects are in the image data, which could be used for the automated removal or masking of contaminating light before lens modelling begins.

2.7.2 Einstein radius measurements and uncertainty

The statistical precision with which the Einstein radius can be measured is promising for many possible scientific studies. For example, Sonnenfeld & Cautun (2021)'s proposed method to constrain the population-level parameters of lens galaxies relies on being able to accurately measure the Einstein radii of the sample of galaxies. Previous studies have attempted to account for the very small formal statistical uncertainties on model parameters (in particular those inferred with parametric source methods) and associated systematic uncertainties by comparing the fractional difference of parameter estimates using different approaches. Bolton et al. (2008b) and Sonnenfeld et al. (2013a) reported a typical expected systematic uncertainty on the Einstein radius of ~2–3%. This value of uncertainty is often adopted over (or combined with) those determined from the non-linear search. Furthermore, given the Einstein radius is expected to be a model-independent quantity (E. E. Falco, M. V. Gorenstein & I.I.Shapiro, 1985; Unruh et al., 2017; Cao et al., 2020), it is typically assumed that this amount of uncertainty accounts for differences in the assumed parameterisation of the mass model.

Einstein radii compared to previous measurements

In a similar fashion to Bolton et al. (2008b) and Sonnenfeld et al. (2013b) we now compare our measurements of Einstein radii with those that exist in the literature (see Figure 2.16) and estimate the uncertainty introduced as a result of the different methods. The full SLACS and GALLERY samples have previously been modelled with SIE profiles to measure the Einstein radii for supplementing a dynamical analysis of the lenses (SIE models of SLACS by Bolton et al. 2008a and SIE or SIE+shear models of GALLERY by Shu et al. 2016b). In this comparison, therefore, not only are the lensing methods very different, but we have also assumed the more complex PLEMD plus external shear (PL+ext) mass distribution for the lens galaxy. Compared to these previous measurements, we find

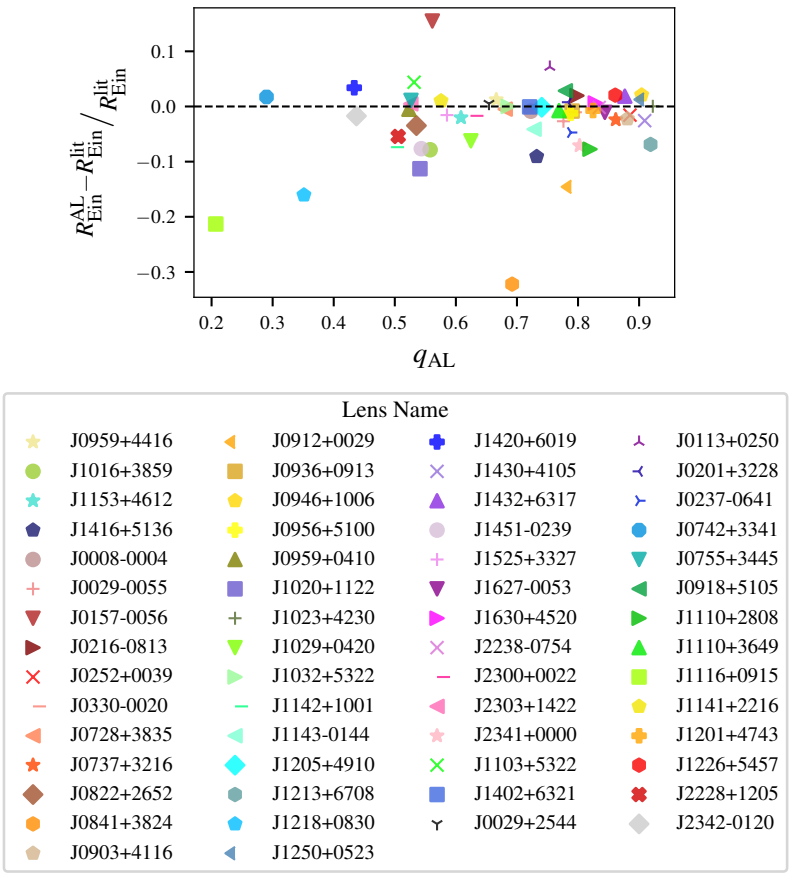

Figure 2.16: The Einstein radii measured by `PyAutoLens` ($R_{\rm Ein}^{\rm AL}$) are generally consistent with those measured by previous analyses of the SLACS (Bolton et al., 2008a) and GALLERY (Shu et al., 2016b) lenses ($R_{\rm Ein}^{\rm lit}$). This shows the fractional difference between new and old measurements, as a function of PyAutoLens axis ratio, $q_{\rm AL}$.

Einstein radii with root mean square (RMS) fractional difference of 7.4%. This is larger than the (empirically motivated) $\sim$ 2–3% uncertainty that is typically assumed.

Several differences between the methods could lead to variation between their inferred Einstein radii. Bolton et al. (2008a) and Shu et al. (2016b) model the background source using either a single or multiple Sérsic ellipsoid components, and both choose different approaches to the lens light subtraction procedure than the one we adopt. While Bolton et al. (2008b) and Sonnenfeld et al. (2013b) investigated differences like these, neither were concerned with differences in the assumed mass model. Indeed, for a subset of 14 lenses that were also analysed by Shajib et al. (2021) assuming a PL+ext model, the RMS fractional difference is only 1.6%, it may be that the reduced uncertainty is a result of fitting the same mass model. Although, this is not of concern if the Einstein radius is indeed model-independent. For this Cao et al. (2020) provide good evidence, showing that the assumption of the PL+ext exhibits only 0.05 ± 0.17% systematic error on the Einstein radius relative to complex "MaNGA" mock data.

Notably, though, we find that five of the six lenses whose $R_{\rm Ein}$ differ by over 10% in the SLACS and GALLERY samples, are accompanied by extremely large values of external shear magnitude (ranging from 0.16 to 0.39) when fitted with our PL+ext models. If these high shear lenses are removed from the comparison, the RMS fractional difference drops to 4.2%. Cao et al. (2020) also demonstrated that the asymmetry in complex mass distributions can lead to the inference of spurious external shears. On average, they inferred an external shear magnitude of 0.015, despite the mock data being generated without external shear. In this work, we infer an average of 0.096 shear magnitude for the SLACS and GALLERY lenses. These large shear values may be partly a result of the additional complexity in the asymmetry of real lenses. Cao et al. (2020) required the Multiple Gaussian Expansion components, that represented the stellar mass, to share a common axis ratio and position angle — this may not be a realistic representation of the angular structure of real lenses (Nightingale et al., 2019). Given that it is the lenses with high external shears that differ most from previous literature measurements of $R_{\rm Ein}$, we speculate that the assumption of a different mass model (in particular the assumption of external shear) may drive the larger fractional uncertainty. This would imply that the Einstein radius is more model-dependent than is often assumed. Further work to test this hypothesis would be valuable.

Statistical uncertainty on Einstein radii

We now consider the size of the errors we measure on the Einstein radius, based entirely on our own PL+ext models. Our likelihood cap method (Section 2.5) addressed the small formal statistical uncertainties on the mass model parameters and allows us to infer uncertainties that account for differences in possible noise realisations and the choice of data discretization. Moreover, since pixel-

grid methods have the flexibility to reconstruct the source with as much complexity as the data needs, they are not subject to the overfitting that occurs in parametric source methods due to overly simplistic source assumptions. With this approach, we measure a mean uncertainty on the inferred Einstein radius of ∼1%, albeit with a wide range of outliers, and 2/59 lens configurations exceeding 5%. Adopting a uniform uncertainty could therefore be problematic for some statistical inferences.

For example, determining the population level parameters of hundreds of thousands of lenses, as described by Sonnenfeld & Cautun (2021); Sonnenfeld (2021a); Sonnenfeld et al. (2013b) might suffer from such inaccurate individual posteriors as those with up to 5% uncertainty on the Einstein radius. The increase in the width of the posteriors inferred as a result of the likelihood cap approach demonstrated in this work should avoid biases in the population level parameters constrained in studies such as these. However, they will in turn increase the amount of lenses required to be able to make such a constraint. Moreover, the coverage probabilities of the lens model parameters with a likelihood cap (see Figure 2.6) did not quite reach the expected level, potentially indicating an under confidence in the posterior. Under confidence in the posterior could lead to biases in estimates of the population parameters such as an overestimate in the scatter of the population (Wagner-Carena et al., 2021). We discuss the importance of further testing of the confidence of the individual posteriors further in Section 2.7.4.

For comparison, Cao et al. (2020) inferred an average of 0.01% statistical uncertainty on the Einstein radius when fitting to mock data simulated using "MaNGA" galaxies without the use of a likelihood cap. This order of magnitude difference from the uncertainties inferred in this study is likely a combination of the use of the likelihood cap increasing the errors in this work, and differences in the quality of the data. Cao et al. (2020)'s mock lensed sources are simulated with S/N of 50 and have visible extended arcs (or complete Einstein rings) that the lenses with the largest errors on $R_{\rm Ein}$ inferred in this work do not, often appearing closer to point-like. Furthermore, they do not include the lens galaxy's light, a component which we have shown in this study can hinder the lens model fitting procedure.

Based on the empirical relations we derived in Section 2.6.2, the certainty to which one can measure the Einstein radius is remarkably independent of a number of data properties and galaxy observables. For example, it might be expected that a higher S/N source galaxy image would tighten the constraints, however this does not appear to be the case for the Einstein radius measurement. This is encouraging for future surveys that will not achieve as high S/N as the HST data used in this study.

The only parameter we investigate that exhibits a statistically significant correlation with measurement uncertainty on the Einstein radius is the Einstein radius itself. Measurements of the Einstein radius

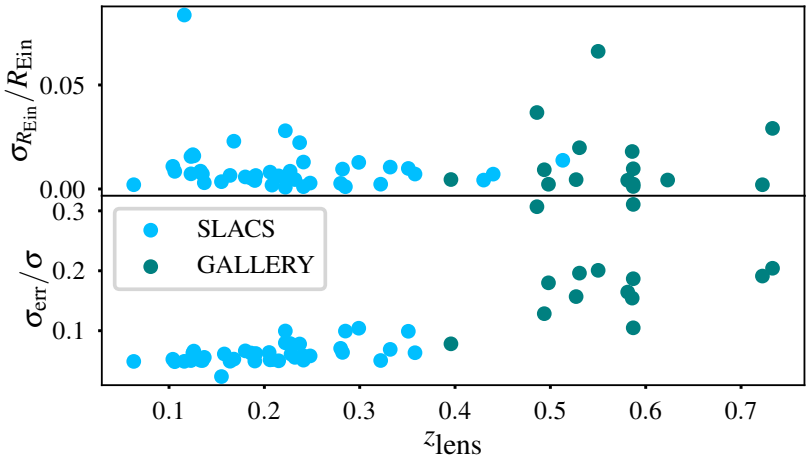

Figure 2.17: The statistical uncertainty on a galaxy's total mass, when measured from its effective Einstein radius, does not degrade with lens redshift $z \lesssim 0.7$ (top panel). This is in stark comparison to most astrophysical observables. For example, the uncertainty on a galaxy's total mass when measured from stellar dynamics (velocity dispersion) increases for more distant galaxies because of cosmological dimming and beam smearing (bottom panel).

become less certain for small Einstein radii, and therefore low mass galaxies. This could also be relevant for surveys such as Euclid that are forecast to detect samples of lenses with smaller Einstein radii (typically ~0.5"according to Collett 2015). Interpolating from our empirical relationship, fitted to the sample excluding the two with anomalously large uncertainty, a lens with this Einstein radius should be measurable to $\sim 2.1\%$ accuracy. However, since the pixel-scale and PSF of the Euclid VIS instrument are roughly twice that of HST, this should be considered a lower limit.

Implications for studies of galaxy evolution

Notably, there does not appear to be a correlation between the lens redshift and measurement uncertainty on the Einstein radius. This highlights the power of strong lensing as a tool for investigations into galaxy evolution. If the lensing measurements do not degrade with redshift, then inferences of how galaxy properties evolve will be well constrained even to high redshift. This is in contrast to e.g. stellar dynamics data, where cosmological dimming effects reduce the certainty of the stellar velocity dispersion (and therefore dynamical mass) of distant galaxies. The increase in fractional uncertainty of the velocity dispersion, σ_{err}/σ, within our SLACS and GALLERY samples is shown in Figure 2.17. Within both samples $\sigma_{\rm err}/\sigma$ increases with redshift (the difference in fibre apertures used for SLACS and GALLERY means direct comparison of their errors is not straightforward, albeit they still highlight that in general higher redshift galaxy measurements are lower S/N).

This creates an interesting dichotomy between using strong lensing to study galaxy evolution and

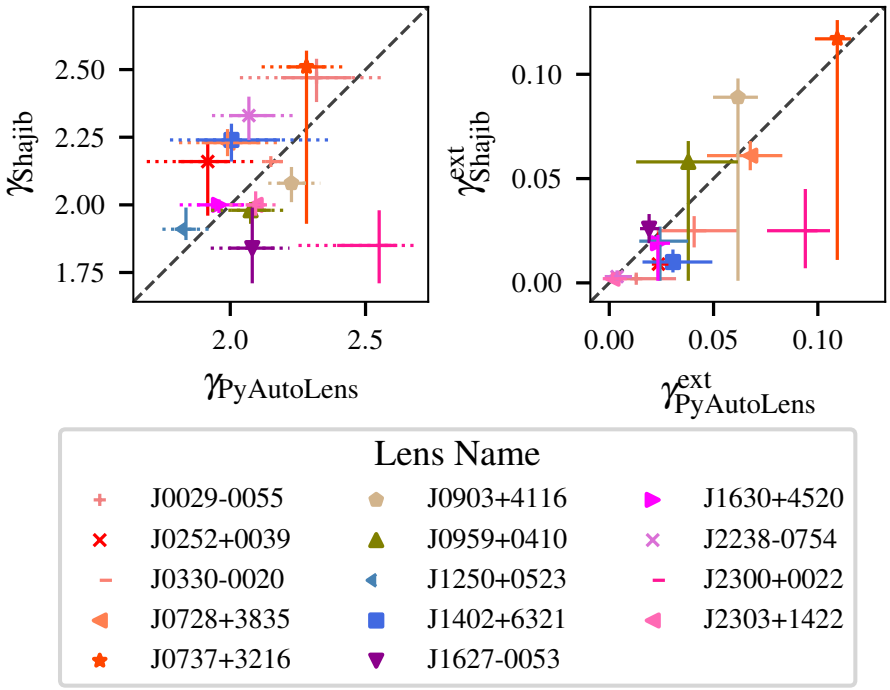

Figure 2.18: Our measurements of the density profile slope (left) and the magnitude of external shear (right) in SLACS lenses, compared with previous, independent measurements by Shajib et al. (2021).

other methods. In lensing, provided we are able to find the lenses at the highest redshifts (surveys such as Euclid and the Vera Rubin Observatory will observe lenses at redshift of up to ~ 2 (Collett, 2015)) we can anticipate that we will be able to measure their properties as well as those at lower redshifts. Issues that plague comparisons between the properties of low and high redshift galaxies via a technique like stellar dynamics, for example beam smearing Tiley et al. (2019), will therefore be less problematic. However, whilst comparing their properties may be more straightforward, strong lens samples will have complicated selection effects Sonnenfeld (2022) that a carefully constructed dynamics sample can more easily mitigate. The reduced lensing efficiency of lower mass galaxies may also restrict the high redshift samples to only the most massive galaxies, albeit this is a limitation for most observing techniques. A strength of lensing, therefore, is that it offers a different means by which to study galaxy evolution that complements the strengths and weaknesses of other techniques.

2.7.3 Measurements of other lens model parameters

In addition to the total mass enclosed within the Einstein radius, strong lensing information also constrains quantities like gradients of the distribution of mass, and the amount of external shear. This is captured in a model-dependent way via the parameters of our PL+ext mass model (see Sonnenfeld & Cautun 2021 for a model-independent expression of this information). We shall now compare our

measurements of radial density gradient γ and shear magnitude $\gamma^{\rm ext}$, to measurements made using previous, independent analyses of overlapping sets of lenses.

Shajib et al. (2021) modelled 23 SLACS lenses, including 14 in our sample. Like us, they used a uniform pipeline that simultaneously modelled the distribution of mass and light. They too described the lens galaxy's light as a double Sérsic profile whose centres are aligned. However, unlike us, they fixed the Sérsic index of each to values of $n = 1$ and $n = 4$ (the exponential and de Vaucouleurs profiles respectively) and join the axis ratios of the two profiles. A major difference in the two techniques lies in the source reconstruction; Shajib et al. (2021) reconstructed the source using a Sérsic profile and shapelet basis functions.

For all but one lens, Shajib et al. (2021) and our measurements of γ and $\gamma^{\rm ext}$ are consistent (Figure 2.18). For the discrepant lens J2300+0022, `PyAutoLens` infers $\gamma = 2.55$ and $\gamma^{\rm ext} = 0.08$, compared to Shajib et al. (2021)'s $\gamma = 1.85$ and $\gamma^{\rm ext} = 0.03$. We believe this discrepancy could be a result of the different order of operations in a model fit. Shajib et al. (2021) initialise their lens model assuming $\gamma^{\rm ext} = 0.0$ and relax this assumption once other components of the model are fit. In contrast, the first mass model we fit in our analysis assumes priors on the shear parameters that allow values up to $\gamma^{\rm ext} = 0.2$. Indeed, for J2300+0022 our search yields a best-fit shear of $\gamma^{\rm ext} = 0.07$. Discarding this lens, we find a mean difference of -0.07 ± 0.07 between the slopes inferred by the two methods, where the error is propagated from the standard error on the means of the two samples. On average, `PyAutoLens` measures slightly shallower slopes than Shajib et al. (2021), although this is not a significant difference – the mean discrepancy for the sample is consistent with zero at the current uncertainty level. A larger sample of measurements may be able to discern if there are systematic differences introduced on the density slope as a result of the lensing technique. We note that we measure a scatter of 0.17 between the slope measurements suggesting there may be systematic uncertainty between the two methods.

Ritondale et al. (2019) modelled 17 GALLERY lenses, including 15 in our sample. Although they do not adopt a uniform analysis pipeline, their lens modelling technique more closely resembles ours, because they reconstruct the source galaxy using a pixelisation. On average, `PyAutoLens` measures a 0.13 ± 0.21 steeper density slope (Figure 2.19). The scatter in this difference is comparable to the average uncertainty that we infer for the GALLERY lenses (0.11) but an order of magnitude larger than the average uncertainty inferred by Ritondale et al. (2019) (left panel of Figure 2.20). In fact, the uncertainties inferred by Ritondale et al. (2019) more closely resemble those from `PyAutoLens` before we used a likelihood cap to avoid source discretization bias (Section 2.5). This suggests that discretization bias may also affect the pixelised-source method of Ritondale et al. (2019). Conversely, the uncertainties derived by Shajib et al. (2021), whose analytic approach to source reconstruction

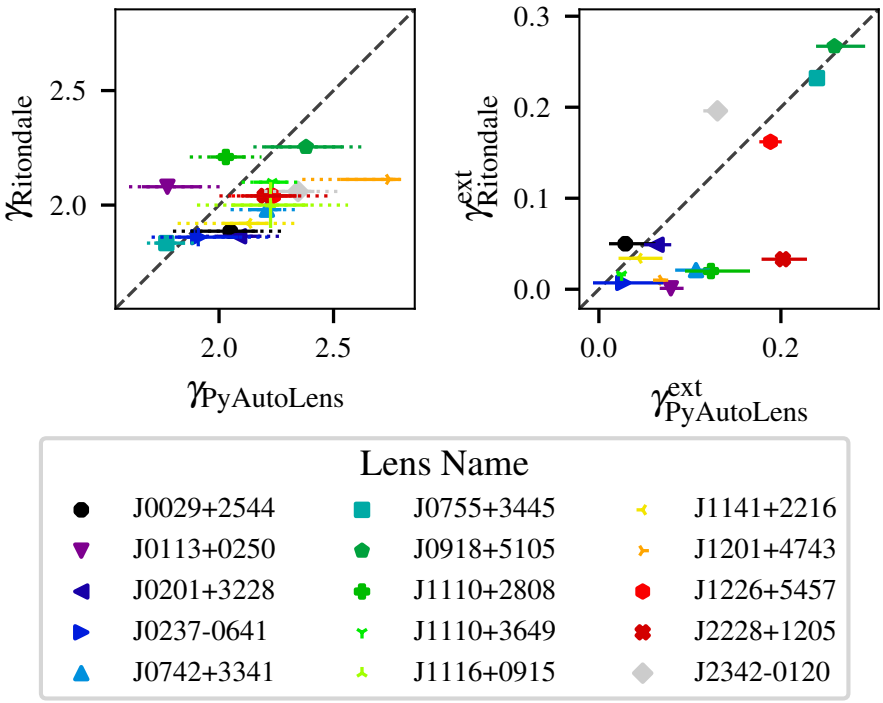

Figure 2.19: Our measurements of the density profile slope (left) and the magnitude of external shear (right) in BELLS GALLERY lenses, compared with previous, independent measurements by Ritondale et al. (2019).

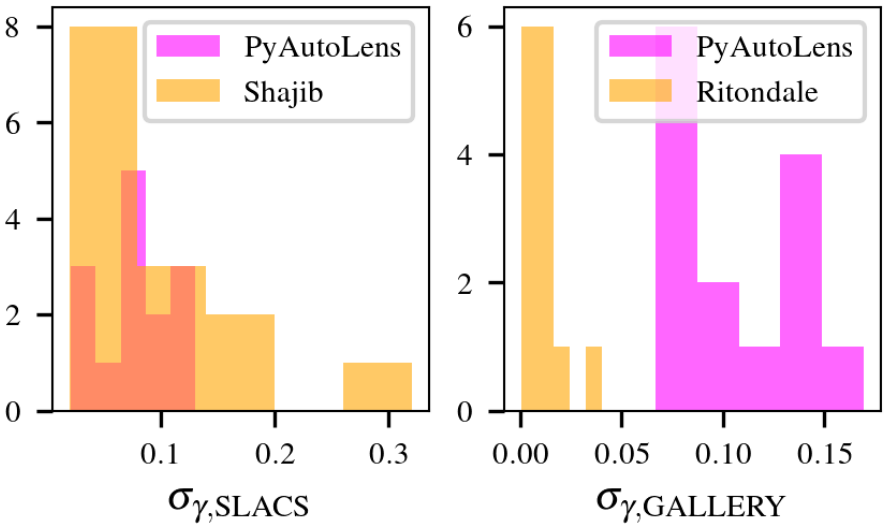

Figure 2.20: The statistical uncertainty on measurements of the radial gradient of the total lens mass, reported by `PyAutoLens` are similar to those found by Shajib et al. (2021) for SLACS lenses (left). However, the uncertainty reported by Ritondale et al. (2019) for GALLERY lenses (right) is an order of magnitude smaller. That method uses a pixelised source, and may be subject to the source discretization bias that we discuss in Section 2.5.

can not be affected by discretization bias, are similar to ours with the likelihood cap (right panel of Figure 2.20).

It is reassuring that independent analyses yield results that are consistent in many ways. However, the relatively small number of lens systems in common to multiple analyses prevents much more detailed comparison between codes or modelling assumptions. The inconsistencies in other aspects of results highlights an urgent need for larger-scale tests.

2.7.4 Large-scale tests of lens modelling

A vital but unintended consequence of this paper, is a solution to, and better understanding of the source discretization bias that previously caused parameter uncertainties to be underestimated. This occurred in both synthetic and real lenses, as a result of noise in the likelihood evaluations of methods using a pixelised source reconstruction (due to particular alignments of source pixels being arbitrarily more or less penalised by regularisation). Our likelihood cap solution successfully reduced noise and smoothed posterior PDFs. It increased the size of our uncertainties such that they had roughly the expected level of coverage, and improved the recovery of all parameters in our synthetic data. Although the likelihood cap was determined in an empirical way, the size of the inferred errors is inherently linked to this choice of likelihood cap. It may be that a different choice of likelihood cap could provide better coverage probabilities than the one we adopted. Further investigation would be warranted to understand at a deeper level what causes these spikes in likelihood in pixelised source reconstructions, as improvements may be possible by changing the approach to pixelising the source plane, or regularising the pixelised source.

Our work shows the importance of testing strong lens modelling methods on larger samples than previously attempted. Even our mock sample comprising 6 noise realisations of 59 lens configurations yields insufficient statistics to determine whether the inferred central values and statistical uncertainty on mass model parameters are consistent with the expectations of drawing each measurement from a normal distribution. Equally, whilst there is evidence for small systematic biases in the estimates of certain mass model parameters, we do not have enough unique lens configurations to determine the primary causes. Given that we are just a few years away from modelling samples of tens of thousands of lenses, tests of strong lens modelling methodology on synthetic data with complex mass distributions (e.g. Mukherjee et al., 2018; Enzi et al., 2019; Cao et al., 2022; He et al., 2022) must now scale up to ensure that error estimates are robust and systematic biases understood.

2.7.5 Computational Costs

Every SLACS and GALLERY lens modelled in this work was analysed using a single 2x Intel Xeon Gold 5120 x @ 2.20GHz CPU, on the Distributed Research Utilising Advanced Computing (DiRAC) Data-Centric System on the COSMA7 machine at Durham University. Run times depend primarily on the number of image pixels fitted after masking, which due to the standard 3.5" circular mask used to fit most lenses is fixed. The lower resolution of SLACS lenses ($0.05\,''\,\text{pixel}^{-1}$) means they contain fewer image pixels than GALLERY lenses ($0.04\,''\,\text{pixel}^{-1}$) and the fits were therefore faster. For SLACS lenses, the source parametric pipeline takes between $10 - 24$ hours, the source inversion pipeline $10 - 36$ hours, the light pipeline $10 - 72$ hours and mass pipeline $6 - 48$ hours. GALLERY lenses take longer on average, where the source parametric pipeline takes between $10 - 36$ hours, the source inversion pipeline $10 - 48$ hours, the light pipeline $12 - 144$ hours and mass pipeline $12 - 72$ hours. The scatter in run times is due to many factors: lens galaxy S/N, source galaxy S/N, lens configuration, lens morphology, source morphology, etc.

Based on the longest GALLERY run times, the upper limit for the overall run time is 300 CPU hours. For 100 000 strong lenses this would require 30 000 000 CPU hours over the $5 - 10$ year lifetime of a survey like *Euclid*, producing an upper limit of $\sim 6\,000\,000$ CPU hours per year. For the recent DiRAC resources allocation call, this amount of CPU time is a 'small' project. We therefore anticipate that the analysis performed in this work will not be limited by CPU resources in the near future. Based on profiling of `PyAutoLens`, we anticipate the run time of a single lens will reduce by a factor of four or above when fitting lower resolution wide-field imaging data (e.g. the resolution of *Euclid* data is $0.1\,''\,\text{pixel}^{-1}$). The 3.5" circular masks assumed throughout this work are also unnecessarily large for many lens systems, and reducing the mask size to 2.5" speeds up the analysis by factors of three and above.

2.8 Summary

Tens of thousands of strong gravitational lenses will be imaged in the next few years, but current analysis techniques are labour-intensive. We use open source software `PyAutoLens` to develop a fully automated, Bayesian analysis of all 59 strong galaxy-galaxy lenses that have been observed by the Hubble Space Telescope (HST) under certain conditions. Adopting the open source software `PyAutoLens` provides an optimistic outlook for the future of automated analysis: for 54/59 lenses (92%) we achieved successful model fits (determined via visual classification) with no human intervention. We illustrate why other fits initially went wrong, and present solutions that allowed us to

infer accurate models for all 59/59 lenses (100%) and recommend steps necessary for analysing the larger incoming samples. Notably, the difficulties primarily happen at the beginning of the analysis when attempting to determine an initial, approximate, lens model — and often reflect confusion between light from the foreground lens and background source. Once a simple model is initialised, our pipeline worked flawlessly to automatically fit a sequence of more complex models that measure more detailed properties of the lens galaxy. We therefore discuss how combining a Convolutional Neural Network with a Bayesian approach like `PyAutoLens` could increase the automation success rate whilst extracting maximum physical information from each strong lens.

We also use synthetic observations of $\sim$ 500 lenses to explain and solve a problem common to pixel-based strong lensing methods that causes the statistical uncertainty on model parameters to be underestimated. This is fundamentally due to noise in likelihood evaluations, caused by discretization effects in pixelised reconstructions of the source galaxy. We implemented an empirical correction that 'caps' the likelihood value to suppress noise. This significantly improves the measurement of the synthetic lens parameters, and leads to error estimates on different noise realisations of identical datasets that are more consistent with one another. On the real data we found this empirical correction (using the likelihood cap) gave a five fold average increase in the inferred uncertainties on model parameters. Comparing to previous literature results, we suggested this bias may be leading to uncertainty under estimation in other studies that use similar methods. Given the incoming samples of tens of thousands of strong gravitational lenses, we believe more detailed study of such systematics on larger mock samples is key.

Accurately knowing the systematic uncertainty on measurements of Einstein radius (total galaxy mass) will become vitally important for large samples of lenses, which beat down statistical uncertainty. Previous studies often assume a constant uncertainty of 2–3%. We find substantial variation between lenses, with a mean of 1% and 57/59 lenses with $< 3\%$, but 2/59 lenses with $> 5\%$. Future analysis of large samples, where careful control of systematics is paramount, must therefore adopt more rigorous errors. Our Einstein radii measurements assumed only a single type of parametric mass model and we do not investigate the degree of uncertainty that results from making different mass model assumptions.

Notably, the uncertainty on our measurements of Einstein radii (and those of the lens models in general) do not increase with redshift. That is, we learn as much about the strong lenses at redshift ~ 0.7 as those at redshift ~ 0.1. This is in stark contrast to other astrophysical probes of a galaxy's structure (e.g. dynamics, morphology), where cosmological dimming effects and beam smearing degrade measurements of distant galaxies. Nor does uncertainty on Einstein radii depend strongly upon the signal-to-noise ratio of our data. This makes strong lensing a compelling technique to study

galaxy evolution: once high redshift strong lenses are found, it should be straight forward to measure their properties. Of course, the technique has its own challenges, for example complicated selection effects, but it should nevertheless provide an invaluable tool for studies of galaxy evolution over the next decade.

Chapter 3

Beyond the bulge-halo conspiracy? Density profiles of Early-type galaxies from extended-source strong lensing

3.1 Introduction

Early-type galaxies (hereafter ETGs) are the end product of the hierarchical merging paradigm central to the Λ-Cold Dark Matter (CDM) cosmological model (White & Rees, 1978; Cole et al., 1994). They are built from the successive mergers between more and more massive objects, and hence provide tests of the entire process of galaxy formation and evolution. The distribution of mass in their baryon-dominated inner regions are especially sensitive, because baryonic physics significantly redistributes mass at various stages of evolution. The inner mass-density profile may become steeper as a result of higher baryon densities from dissipative gas cooling processes and the inflow of gas (Blumenthal & Faber, 1986; Silk, 1993; Velliscig et al., 2014). They may become softened by outflows of gas driven by feedback processes such as active galactic nuclei and supernovae (Velliscig et al., 2014; Dubois et al., 2013). Measurements of ETG inner mass-density profiles are therefore fundamental in understanding the relative strength and timing of these physical processes.

Observations have shown that the mean distribution of dark plus baryonic matter in the central few effective radii of ETGs is such that their combined density profile is roughly isothermal, $\rho(r) \propto r^{-\gamma}$, with $\gamma \sim 2$. This has been consistently observed by many observational techniques: dynamically modelled local ETGs (Tortora et al., 2014; Serra et al., 2016; Li et al., 2019; Cappellari et al., 2013), X-ray studies (Humphrey et al., 2006; Humphrey & Buote, 2010), weak lensing (Gavazzi et al.,

2007), and combined strong lensing and dynamical modelling (Koopmans et al., 2009; Auger et al., 2010a; Li et al., 2018). The latter is the most prevalent of these results, with the 'standard' procedure developed by Treu & Koopmans (2002) constraining the total mass inside two different radii: the galaxy light's effective radius from measurements of the velocity dispersion, and the galaxy mass's Einstein radius from lensing. In this way, Auger et al. (2010a) measured a mean logarithmic density slope $\langle\gamma\rangle = 2.078 \pm 0.027$, with intrinsic scatter between galaxies of $\sigma_\gamma = 0.16 \pm 0.02$, for the largest single sample of strong lenses that make up the Sloan Lens ACS (SLACS) survey (Bolton et al., 2008a).

The near-isothermality of mass in ETGs is often termed the 'bulge-halo conspiracy', referring to the apparent coincidence that despite diverse assembly histories, and although neither their baryonic nor dark matter components follow a single power law, their sum approximately does (Treu et al., 2006; Humphrey & Buote, 2010). The galaxies' homogeneity is further evident in the well-known ETG scaling laws such as the fundamental plane relations (Djorgovski & Davis, 1987) and the $M_{\rm BH} - \sigma_{\rm c}$ relation (Hyde & Bernardi, 2009). Furthermore, the total mass-density slopes correlate with a number of galaxy parameters including effective radius, stellar surface mass density, and central dark matter fraction, as well as being observed to mildly soften with increasing redshift up to $z \sim 1.0$ (Auger et al., 2010a; Ruff et al., 2011; Sonnenfeld et al., 2013a; Li et al., 2018).

Numerical simulations are invaluable in understanding the origin of these empirical relations, and are now beginning to account for the physical processes involved in their formation. The current consensus for the formation of ETGs, often referred to as a 'two phase' assembly (Oser et al., 2010), begins with an initial stage of active star formation and adiabatic contraction at redshift $z \gtrsim 2$, followed by growth through major and minor merging events to the present (Naab & Ostriker, 2009; Van Dokkum et al., 2010; Remus et al., 2017). However, details of the physical processes that modify the mass distributions throughout this formation process are yet to be well understood. Fine-tuning between the baryonic and dark matter distributions would be necessary to produce the distribution of near-isothermal total mass profiles that are observed, a result hydrodynamic simulations have been unable to accomplish whilst simultaneously reproducing the observed distribution of dark matter fractions (Duffy et al., 2010; Dubois et al., 2013; Xu et al., 2017). It is unclear whether this discrepancy is a result of an inadequacy in the cosmological simulations or a systematic bias in the determination of the observed mass-density slopes.

Comparing observed and simulated mass-density slopes is difficult. Wang et al. (2019) demonstrated that IllustrisTNG reproduces many of the observed mass-density slope correlations, assuming the best fit total power-law density slope within the radial interval $[0.4\mathrm{R}_{1/2}, 4\mathrm{R}_{1/2}]$ of their simulated sample

of ETGs. Although tensions do exist, the authors find a negative correlation with central velocity dispersion (σ) for the simulated galaxies whereas observational datasets tend towards a positive correlation. This is the case for both strong lensing and dynamical observations. Li et al. (2019) show that both IllustrisTNG and EAGLE simulations are unable to reproduce the $\gamma - \sigma$ trend observed from a dynamical analysis of over 2000 galaxies in the SDSS-IV (Sloan Digital Sky Survey IV) MaNGA survey; both simulations typically predict shallower slopes than those observed for the high velocity dispersion galaxies in their sample.

Furthermore, cosmological simulations typically exhibit a mild steepening of the density slope with redshift up to $z \sim 2.0$, in contrast with the mild softening observed (Johansson et al., 2012; Remus et al., 2017; Xu et al., 2017). Xu et al. (2017) and Remus et al. (2017) demonstrated the Illustris and Magneticum simulations show better agreement with the observations when using a different estimator for the power-law slope that better resembles the observational methods. However, the estimator differs between the two studies, and a direct comparison to observations must still be approached with caution. For example, Xu et al. (2017) note that their observational slope estimator results in a sampling bias whereby the simulated sample have relatively lower mean slopes due to a larger fraction of systems with lower mass and/or smaller normalised Einstein radii. An appropriate comparison would require strictly adopting observational criteria to estimate the slopes and select the simulated samples. Further to this, the necessary observational data for a large sample of galaxies out to high redshifts would allow for a more complete comparison to the simulations.

In this work, we build on the results presented in Chapter 2, where we used strong gravitational lensing *alone* to measure the total mass-density profiles of 59 lenses from the SLACS (Bolton et al., 2006) and BELLS GALLERY (Shu et al., 2016a) samples. Previous lensing and dynamical analyses exploited only one lensing observable, the Einstein radius, and inferred the logarithmic density slope by combining this with measurements of stellar kinematics. However, in Chapter 2 we used the fact that light rays emitted from opposite sides of an extended source are deflected by different amounts. Using the lens modelling software `PyAutoLens` (Nightingale et al., 2018, 2021a), we fitted the full surface brightness profile of observed arcs to constrain the total mass-density profile of these 59 lens galaxies. The measurement was automated, to ensure that it will also be able to exploit the tens of thousands of lenses expected to be observed by LSST and Euclid (Collett, 2015). Since this measurement uses only imaging data, and does not require expensive spectroscopy for stellar kinematics, it has the potential to measure the formation and accumulation of mass around galaxies out to redshift $z = 2.0$ and beyond (Sonnenfeld & Cautun, 2021; Sonnenfeld, 2021a, 2022).

We introduce the samples of lenses that we study in this work which have total mass density slopes

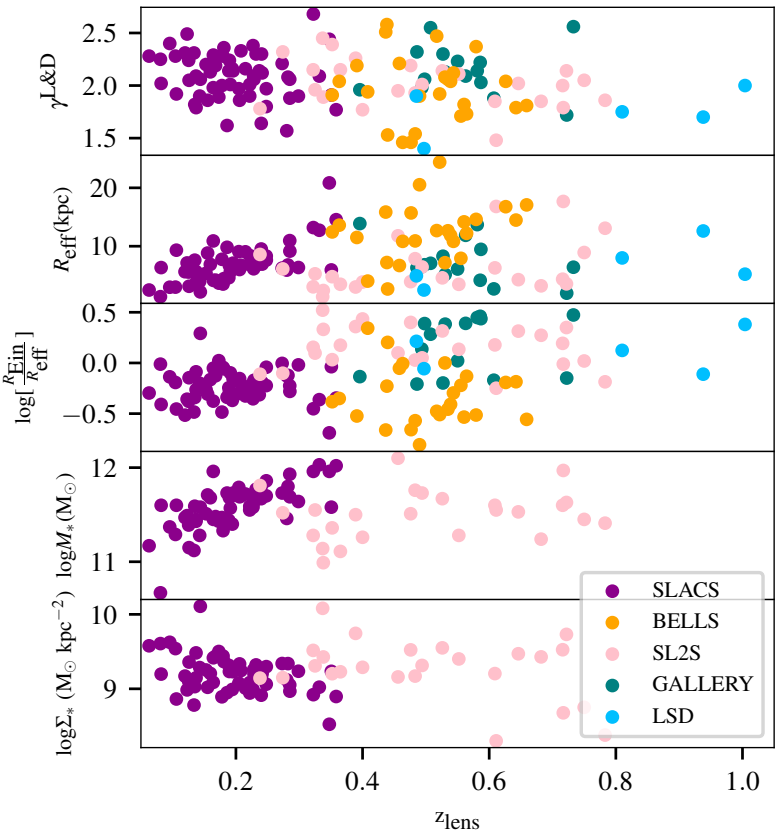

Figure 3.1: Various galaxy quantities plotted as a function of redshift for the complete lensing&dynamics sample. Stellar masses (hence stellar surface mass densities) have not been measured for BELLS, GALLERY, or LSD samples. Where necessary throughout this study we instead use total masses, derived from equation 3.2.2.

derived from either lensing-only, lensing and dynamics, or both, in Section 3.2. In Section 3.3 we investigate the assumption of the power law mass distribution by comparing to what extent the two methods infer the same slope. We then quantify the dependence of the slopes, measured with both methods, on redshift in Section 3.4, before discussing the results in Section 3.5, and concluding in Section 3.6. Throughout this work we assume a Planck 2015 cosmological model (Ade et al., 2016).

3.2 Observational Samples of Galaxies

3.2.1 Complete sample: Lensing & Dynamics (L&D) measurements from the literature

Hundreds of galaxy-scale strong lenses have been discovered by dedicated surveys during the past two decades, with measurements of their mass profiles by e.g. Treu et al. (2006); Koopmans et al. (2006); Auger et al. (2010a); Sonnenfeld et al. (2013a) and Li et al. (2018). The method, initially developed by

Treu & Koopmans (2002), models the stellar plus dark matter distribution of total mass in each galaxy as $\rho \propto r^{-\gamma}$. By further assuming a stellar density profile (treated as a massless tracer of the total density profile), with effective radii fixed to those observed (typically from de Vaucouleurs models), the spherical Jeans equations can be solved to calculate the velocity dispersion for a given model. The total mass-density slope γ can then be constrained using the mass within the Einstein radius and the stellar velocity dispersion by comparing the model values to those observed – the Einstein radius is typically measured from fits to imaging data assuming a singular isothermal ellipse mass model (SIE) (Kormann et al., 1994).

We have collated a "complete Lensing & Dynamics sample" of 123 lens galaxies from Sloan Lens ACS (SLACS), (Bolton et al., 2006; Auger et al., 2010a), BOSS Emission Line Lens (BELLS) (Brownstein et al., 2012), BELLS GALaxy-Lyα EmitteR sYstems (GALLERY) (Shu et al., 2016b,a), Strong Lensing Legacy (SL2S) (Gavazzi et al., 2012) surveys, and Lenses Structure and Dynamics (LSD) surveys Treu & Koopmans (2004) for which measurements of the total-mass density slope from the combined lensing and dynamics (L&D) analysis have previously been carried out. Lens galaxies were selected in the following different ways in the various surveys:

- **SLACS (50 lenses)**: spectroscopic search within the SDSS database, using a 3″ fibre, examining residual spectra for higher redshift emission lines[1].
- **BELLS (25 lenses)**: spectroscopic search within the BOSS database, using a 2″ fibre, examining residual spectra for higher redshift emission lines.
- **GALLERY (15 lenses)**: same technique as BELLS with an additional selection for higher redshift, compact Lyman-α-emitting (LAE) source galaxies.
- **SL2S (25 lenses)**: imaging data is analysed for an excesses of blue features that indicate the presence of lensed features (Gavazzi et al., 2014).
- **LSD (5 lenses)**: systems selected from the CfA-Arizona Space Telescope Lens Survey (CASTLeS)[2] sample of known galaxy-scale systems for their morphology (E/S0) and brightness ($I \lesssim 22$).

To our knowledge, this is the first time all these observations have been studied in one analysis. As well as L&D total mass density slopes, we gather literature measurements of a number of galaxy observables

[1] Auger et al. (2010a) find that six of the SLACS galaxies are significant outliers of the fundamental hyper-plane relation (the relationship between the effective radius, velocity dispersion, central stellar mass, and central total mass), which may be a a result of significantly underestimated velocity dispersion errors Jiang & Kochanek (2007). In keeping with previous studies we remove those from our sample.

[2] see the CASTLeS web-page at `http://cfa-www.harvard.edu/castles/`

including velocity dispersions, effective radii, Einstein radii (which we normalise by the effective radii throughout this study), stellar masses, and stellar surface mass densities ($\Sigma^* = M^*/(2\pi \mathrm{R}_{\mathrm{eff}}^2)$), which are plotted as a function of redshift of the lens galaxy in Figure 3.1.

Total-mass density slopes have been shown to correlate with both total and stellar surface mass-densities (Auger et al., 2010b; Sonnenfeld et al., 2013a). We must account for this relationship if we wish to study how the density profile depends on redshift, because stellar density also evolves with redshift. Notably, stellar masses (hence stellar surface mass densities) have not been measured for BELLS, GALLERY, or LSD samples. Following (Auger et al., 2010a), we therefore calculate *total* surface mass densities

$$\Sigma_{\mathrm{tot}} = \frac{M_{\mathrm{tot}}}{R_{\mathrm{eff}}^2}, \tag{3.2.1}$$

where R_{eff} is the effective radius of the galaxy and

$$M_{\mathrm{tot}} = \Sigma_{\mathrm{crit}} \pi R_{\mathrm{Ein}}^{\gamma-1} \left(\frac{R_{\mathrm{eff}}}{2} \right)^{3-\gamma} \tag{3.2.2}$$

is the total projected mass within half the effective radius inferred from power-law models with Einstein radii R_{Ein} and total mass-density slope γ. The total projected mass is calculated within half the effective radius, which typically closely resembles the Einstein radius, to reduce errors from extrapolating the power law model.

3.2.2 Complete sample: new measurements using Lensing-only

If a lensed galaxy is spatially resolved, the apparent shape of the arc can be used to infer the distribution of total mass-density around a foreground lens, without any spectroscopic information about stellar kinematics. The source flux in every image pixel can be ray-traced back to the source plane, and the shape of the source galaxy is modelled as a sum of analytic functions (Tessore et al., 2016), possibly combined with a basis of shapelets (Birrer et al., 2015; Shajib et al., 2018), or a pixelised source (Warren & Dye, 2003; Suyu et al., 2006; Dye & Warren, 2005; Vegetti & Koopmans, 2009; Nightingale & Dye, 2015; Nightingale et al., 2018; Joseph et al., 2019; Galan et al., 2021). The configuration of ray-tracing required to map multiple images in the lens plane onto consistent morphologies in the source plane constrains parameters of the mass model, including its logarithmic density slope γ.

In chapter 2 we used this approach to model a sub-sample of 43 SLACS and 15 GALLERY lenses. Here we consider only the 53 "Gold" and 4 "Silver" lenses for which an automated analysis reliably fitted the data without residuals (see section 2.6.1 for the details of the categories). We refer to this sample of 57 lenses as the "complete lensing-only sample". We note that, with the lensing-only technique, the density profile constraints from compact LAE sources in the GALLERY sample are not

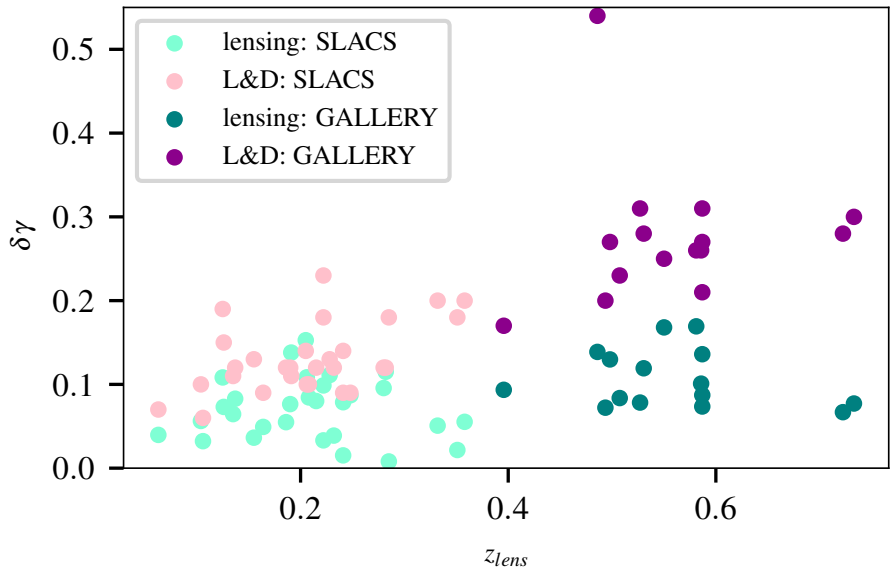

Figure 3.2: Measurement uncertainties on the slopes from lensing only and lensing & dynamics as a function of redshift of the lens galaxy.

as tight as constraints from the more extended sources in the SLACS sample. However, the slopes of GALLERY lenses are still better constrained than the slopes measured for the same lenses using the L&D analysis (Figure 3.2).

3.2.3 Overlapping sample: new measurements using Lensing-only, as well as Lensing & Dynamics

For a direct comparison between the two methods we select the lenses that have measurements of the density slope from both the lensing-only and L&D analyses. This requires excluding 1 GALLERY and 6 SLACS lenses from the complete lensing-only sample whose mass slopes have not previously been measured using the L&D method. As in the complete sample, we also exclude 3 SLACS lenses suspected to have anomalous measurements of velocity dispersion. We shall refer to the remaining 48 lenses as the "overlapping sample".

As for the complete L&D sample we gather literature measurements of a number of galaxy observables including velocity dispersions, effective radii, and normalised Einstein radii (plotted as a function of redshift in Figure 3.3). We also calculate total masses (equation 3.2.2) and surface mass densities (equation 3.2.1). Note that the effective radius of all galaxies in the overlapping sample has been measured at least twice: assuming de Vaucouleurs surface brightness profiles in L&D analyses (e.g. Auger et al., 2010a) and double Sérsic profiles in our lensing analysis (see Table 3.1). Since the L&D mass density slopes were calculated using de Vaucouleurs effective radii, we use these for consistency

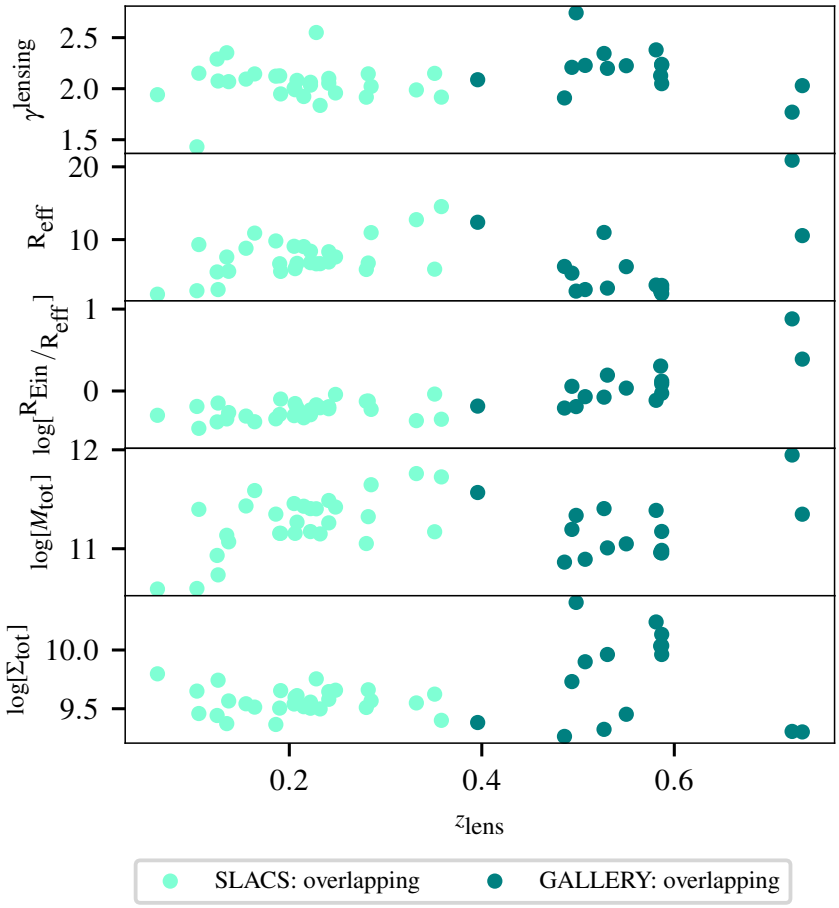

Figure 3.3: Galaxy observables as a function of lens redshift for the overlapping sample. From top to bottom panel the quantities are as follows: lensing only total mass density slope (γ^{lensing}), de Vaucouleurs effective radius R_{eff} in units of kpc, Einstein radius normalised by the effective radius ($\log[^{R_{\text{Ein}}}/_{R_{\text{eff}}}]$), total mass within half the effective radius ($\log[M_{\text{tot}}]$), and total surface mass density ($\log[\Sigma_{tot}]$). The total masses and total surface mass densities plotted here are those derived from the lensing quantities (γ^{lensing} and $R_{\text{Ein}}^{\text{PL}}$ in equations 3.2.2 and 3.2.1), we note that they do not change significantly when derived from L&D quantities (see Table 3.1 for both values).

with previous literature whenever we quote an effective radius. The lensing-only analyses do not use their measurements of effective radius.

3.3 Do the lensing-only and lensing & dynamics methods measure the same density slopes?

Although the lensing-only and L&D methods aim to measure the same quantity γ, the assumption of the power-law profile is critical in this endeavour. The L&D analysis is averaged between mass measurements at the Einstein and effective radii, whereas the lensing method is constrained by the pixel information of the source galaxy that, by definition, occurs near the Einstein radius. Any deviation of the galaxy's true mass-density profile from a power law could therefore lead to biases in γ that behave differently between the two methods (e.g. Schneider & Sluse 2013b; Kochanek 2020; Cao et al. 2020). We therefore investigate to what extent the methods infer the same slope, first by comparing the sample averages in Section 3.3.1, measurements of individual galaxies in Section 3.3.2, then correlations between galaxies' slopes and other observable quantities in Section 3.3.3.

3.3.1 Sample distribution of total-mass density slopes

We assume that each individual galaxy's mass-density slope γ_i belongs to an underlying Gaussian distribution of slopes with mean $\langle\gamma\rangle$ and intrinsic scatter σ_γ. The likelihood function of $\langle\gamma\rangle$ and σ_γ is

$$\mathscr{L}(\langle\gamma\rangle, \sigma_\gamma | \{\gamma_i\}) = \prod_i \frac{\exp\left[-\frac{(\gamma_i - \langle\gamma\rangle)^2}{2(\sigma_\gamma^2 + \sigma_{\gamma_i}^2)} \right]}{\sqrt{2\pi(\sigma_\gamma^2 + \sigma_{\gamma_i}^2)}}, \tag{3.3.1}$$

where σ_{γ_i} is the uncertainty on the individual slope measurements γ_i. One can then infer the posterior probability distribution function (PDF) of $\langle\gamma\rangle$ and σ_γ using Bayes' theorem

$$p(\langle\gamma\rangle, \sigma_\gamma | \{\gamma_i\}) \propto p(\langle\gamma\rangle, \sigma_\gamma) \mathscr{L}(\langle\gamma\rangle, \sigma_\gamma | \{\gamma_i\}), \tag{3.3.2}$$

where $p(\langle\gamma\rangle, \sigma_\gamma)$ is the prior. We assume uniform priors on $\langle\gamma\rangle$ and σ_γ and fit for them using the nested sampling algorithm `dynesty` (Speagle, 2020) via an implementation using the probabilistic programming language `PyAutoFit` (Nightingale et al., 2021b). Note that lensing-only analysis uses a non-linear fitting procedure that yields asymmetric and non-Gaussian uncertainties on lensing slopes σ_{γ_i}. We approximate these as a split normal distribution, i.e. Gaussian uncertainty with

$$\sigma_{\gamma_i} = \sigma_{\gamma_i}^{\text{ue}} \qquad \text{if} \qquad \gamma_i < \langle\gamma\rangle, \tag{3.3.3}$$

Sample	Lens Name	$z_{\rm lens}$	$z_{\rm source}$	σ	$R_{\rm Ein}^{\rm PL}$	$R_{\rm Ein}^{\rm SIE}$	$\gamma^{\rm lensing}$	$\gamma^{\rm L\&D}$	$R_{\rm eff}^{\rm Sérsic\ x2}$	$R_{\rm eff}^{\rm dev}$	$M_{\rm tot}^{\rm lensing}$	$M_{\rm tot}^{\rm L\&D}$	$\Sigma_{\rm tot}^{\rm lensing}$	$\Sigma_{\rm tot}^{\rm L\&D}$
	J0216-0813	0.332	0.523	319	$1.183^{+0.014}_{-0.011}$	1.16	$1.99^{+0.05}_{-0.06}$	2.09 ± 0.2	$9.1^{+4.59}_{-0.81}$	12.74	11.76	11.75	9.55	9.53
	J0252+0039	0.280	0.982	170.	$1.024^{+0.004}_{-0.002}$	1.04	$1.92^{+0.08}_{-0.11}$	1.57 ± 0.12	$3.43^{+0.09}_{-0.06}$	5.90	11.05	11.00	9.51	9.46
	J0330-0020	0.351	1.071	213	$1.088^{+0.009}_{-0.012}$	1.10	$2.15^{+0.02}_{-0.02}$	1.91 ± 0.18	$1.99^{+0.03}_{-0.03}$	5.94	11.17	11.11	9.62	9.57
	J0728+3835	0.206	0.688	210.	$1.244^{+0.012}_{-0.008}$	1.25	$1.99^{+0.12}_{-0.1}$	1.86 ± 0.1	$11.32^{+1.28}_{-1.01}$	6.01	11.16	11.14	9.60	9.58
	J0822+2652	0.241	0.594	254	$1.129^{+0.011}_{-0.018}$	1.17	$2.1^{+0.08}_{-0.07}$	2.12 ± 0.14	$9.16^{+0.59}_{-0.58}$	6.93	11.26	11.28	9.58	9.60
	J0912+0029	0.164	0.324	304	$1.393^{+0.011}_{-0.007}$	1.63	$2.14^{+0.05}_{-0.05}$	1.98 ± 0.09	$6.93^{+0.24}_{-0.23}$	10.89	11.59	11.68	9.51	9.60
	J0936+0913	0.190	0.588	236	$1.081^{+0.004}_{-0.005}$	1.09	$2.13^{+0.08}_{-0.08}$	2.24 ± 0.12	$5.29^{+0.17}_{-0.12}$	6.69	11.16	11.16	9.51	9.51
	J0946+1006	0.222	0.609	253	$1.409^{+0.001}_{-0.001}$	1.38	$2.06^{+0.03}_{-0.03}$	2.01 ± 0.18	$4.51^{+0.17}_{-0.19}$	8.41	11.41	11.39	9.56	9.54
	J0956+5100	0.241	0.470	323	$1.314^{+0.002}_{-0.001}$	1.33	$2.05^{+0.02}_{-0.02}$	2.3 ± 0.09	$6.9^{+0.27}_{-0.24}$	8.33	11.49	11.51	9.65	9.67
	J0959+0410	0.126	0.535	196	$0.985^{+0.014}_{-0.017}$	0.99	$2.08^{+0.07}_{-0.07}$	2.05 ± 0.15	$2.55^{+0.08}_{-0.07}$	3.14	10.74	10.73	9.74	9.74
	J1020+1122	0.282	0.553	279	$1.065^{+0.011}_{-0.009}$	1.20	$2.15^{+0.11}_{-0.12}$	2.08 ± 0.12	$10.02^{+2.1}_{-1.9}$	6.78	11.32	11.37	9.66	9.71
	J1023+4230	0.191	0.696	238	$1.411^{+0.009}_{-0.009}$	1.41	$1.95^{+0.16}_{-0.12}$	2.01 ± 0.11	$4.31^{+0.1}_{-0.11}$	5.63	11.16	11.17	9.65	9.67
	J1029+0420	0.104	0.615	208	$0.947^{+0.01}_{-0.01}$	1.01	$1.43^{+0.05}_{-0.06}$	2.28 ± 0.1	$1.75^{+0.06}_{-0.04}$	2.98	10.60	10.71	9.65	9.76
	J1142+1001	0.222	0.504	216	$0.908^{+0.024}_{-0.027}$	0.98	$2.03^{+0.1}_{-0.1}$	1.9 ± 0.23	$5.48^{+0.45}_{-0.36}$	6.83	11.17	11.21	9.50	9.54
SLACS	J1143-0144	0.106	0.402	247	$1.611^{+0.013}_{-0.014}$	1.68	$2.15^{+0.03}_{-0.03}$	1.92 ± 0.06	$3.87^{+0.15}_{-0.14}$	9.32	11.40	11.45	9.46	9.52
	J1205+4910	0.215	0.481	269	$1.218^{+0.008}_{-0.008}$	1.22	$1.92^{+0.07}_{-0.09}$	2.16 ± 0.12	$8.6^{+0.64}_{-0.51}$	9.04	11.43	11.42	9.52	9.51
	J1218+0830	0.135	0.717	207	$1.217^{+0.01}_{-0.008}$	1.45	$2.35^{+0.07}_{-0.06}$	1.82 ± 0.11	$5.9^{+0.27}_{-0.26}$	7.61	11.14	11.26	9.37	9.50
	J1250+0523	0.232	0.795	247	$1.144^{+0.006}_{-0.005}$	1.13	$1.84^{+0.04}_{-0.04}$	2.3 ± 0.12	$8.11^{+1.99}_{-1.78}$	6.69	11.15	11.19	9.50	9.54
	J1402+6321	0.205	0.481	255	$1.349^{+0.005}_{-0.007}$	1.35	$2.0^{+0.18}_{-0.13}$	1.97 ± 0.14	$11.82^{+0.0}_{-0.3}$	9.08	11.46	11.46	9.54	9.54
	J1420+6019	0.063	0.535	199	$1.075^{+0.002}_{-0.002}$	1.04	$1.94^{+0.04}_{-0.04}$	2.28 ± 0.07	$2.57^{+0.06}_{-0.05}$	2.50	10.59	10.58	9.80	9.78
	J1430+4105	0.285	0.575	309	$1.481^{+0.002}_{-0.002}$	1.52	$2.02^{+0.01}_{-0.01}$	2.06 ± 0.18	$11.46^{+0.82}_{-1.06}$	10.96	11.65	11.66	9.57	9.58
	J1451-0239	0.125	0.520	214	$0.96^{+0.017}_{-0.015}$	1.04	$2.29^{+0.1}_{-0.11}$	2.24 ± 0.19	$6.29^{+0.25}_{-0.39}$	5.56	10.93	10.98	9.44	9.49
	J1525+3327	0.358	0.717	150.	$1.29^{+0.012}_{-0.007}$	1.31	$1.92^{+0.06}_{-0.05}$	1.77 ± 0.2	$10.66^{+0.57}_{-0.62}$	14.54	11.73	11.74	9.40	9.41
	J1627-0053	0.208	0.524	283	$1.217^{+0.002}_{-0.002}$	1.23	$2.08^{+0.08}_{-0.09}$	2.33 ± 0.1	$14.67^{+2.45}_{-1.46}$	6.74	11.27	11.30	9.61	9.64
	J1630+4520	0.248	0.793	269	$1.791^{+0.006}_{-0.004}$	1.78	$1.96^{+0.09}_{-0.08}$	1.97 ± 0.09	$6.27^{+0.43}_{-0.28}$	7.62	11.42	11.42	9.66	9.66
	J2238-0754	0.137	0.713	191	$1.268^{+0.004}_{-0.003}$	1.27	$2.07^{+0.09}_{-0.07}$	1.79 ± 0.12	$5.8^{+4.97}_{-7.44}$	5.65	11.07	11.06	9.57	9.56
	J2300+0022	0.228	0.463	273	$1.219^{+0.008}_{-0.005}$	1.24	$2.55^{+0.07}_{-0.16}$	2.06 ± 0.13	$4.7^{+0.3}_{-0.2}$	6.68	11.40	11.35	9.75	9.70
	J2303+1422	0.155	0.517	240.	$1.628^{+0.007}_{-0.005}$	1.62	$2.09^{+0.04}_{-0.04}$	1.86 ± 0.13	$5.97^{+0.31}_{-0.27}$	8.81	11.43	11.43	9.54	9.54
	J2341+0000	0.186	0.807	196	$1.338^{+0.009}_{-0.005}$	1.44	$2.12^{+0.06}_{-0.05}$	1.62 ± 0.12	$6.15^{+0.2}_{-0.16}$	9.81	11.35	11.41	9.37	9.42
	J0029+2544	0.587	2.450	240.	$1.347^{+0.014}_{-0.012}$	1.34	$2.05^{+0.12}_{-0.15}$	2.03 ± 0.27	$45.05^{+23.89}_{-23.89}$	9.46	11.43	11.42	9.47	9.47
	J0201+3228	0.396	2.821	245	$1.713^{+0.011}_{-0.005}$	1.70	$2.09^{+0.09}_{-0.1}$	1.96 ± 0.17	$8.1^{+1.11}_{-1.11}$	13.88	11.61	11.59	9.33	9.31
	J0237-0641	0.486	2.249	295	$0.619^{+0.02}_{-0.025}$	0.65	$1.91^{+0.18}_{-0.1}$	2.32 ± 0.54	$26.27^{+23.57}_{-23.57}$	6.31	10.86	10.92	9.26	9.32
	J0742+3341	0.494	2.363	221	$1.241^{+0.01}_{-0.013}$	1.22	$2.21^{+0.06}_{-0.08}$	1.98 ± 0.2	$7.51^{+17.87}_{-17.87}$	6.49	11.26	11.17	9.63	9.54
	J0755+3445	0.722	2.635	302	$2.073^{+0.005}_{-0.004}$	2.05	$1.77^{+0.08}_{-0.05}$	1.72 ± 0.28	$195.47^{+20.94}_{-20.94}$	1.95	10.68	10.62	10.10	10.04
	J0856+2010	0.507	2.234	337	$0.951^{+0.035}_{-0.04}$	0.98	$2.23^{+0.08}_{-0.09}$	2.55 ± 0.23	$4.86^{+1.03}_{-1.03}$	7.07	11.17	11.26	9.47	9.56
	J0918+5105	0.581	2.403	289	$1.645^{+0.005}_{-0.009}$	1.60	$2.38^{+0.16}_{-0.18}$	2.14 ± 0.26	$6.62^{+0.97}_{-0.97}$	13.70	11.74	11.67	9.46	9.40
GALLERY	J1110+2808	0.733	2.400	207	$0.904^{+0.027}_{-0.026}$	0.98	$2.03^{+0.09}_{-0.07}$	1.88 ± 0.3	$6.66^{+0.52}_{-0.52}$	2.91	10.81	10.74	9.88	9.81
	J1110+3649	0.587	2.502	546	$1.151^{+0.001}_{-0.001}$	1.16	$2.23^{+0.07}_{-0.08}$	2.56 ± 0.32	$25.22^{+12.2}_{-12.2}$	5.82	11.23	11.37	9.70	9.84
	J1116+0915	0.550	2.454	280.	$0.811^{+0.053}_{-0.054}$	1.03	$2.22^{+0.16}_{-0.17}$	2.23 ± 0.25	$35.01^{+56.93}_{-56.93}$	6.09	11.04	11.17	9.47	9.60
	J1141+2216	0.586	2.762	299	$1.283^{+0.027}_{-0.019}$	1.27	$2.13^{+0.09}_{-0.11}$	2.22 ± 0.26	$16.46^{+3.17}_{-3.17}$	4.16	11.10	11.15	9.86	9.91
	J1201+4743	0.498	2.126	234	$1.171^{+0.004}_{-0.002}$	1.18	$2.74^{+0.05}_{-0.21}$	2.09 ± 0.27	$21.68^{+2.84}_{-2.84}$	11.15	11.49	11.42	9.39	9.33
	J1226+5457	0.587	2.732	251	$1.398^{+0.004}_{-0.003}$	1.37	$2.24^{+0.07}_{-0.1}$	2.06 ± 0.21	$14.93^{+4.58}_{-4.58}$	7.41	11.40	11.32	9.66	9.58
	J2228+1205	0.530	2.832	263	$1.21^{+0.024}_{-0.024}$	1.28	$2.2^{+0.14}_{-0.1}$	2.13 ± 0.28	$17.73^{+2.54}_{-2.54}$	5.16	11.16	11.16	9.73	9.73
	J2342-0120	0.527	2.265	274	$1.091^{+0.006}_{-0.004}$	1.11	$2.34^{+0.07}_{-0.09}$	2.3 ± 0.31	$16.3^{+7.64}_{-7.64}$	8.28	11.33	11.33	9.49	9.49

Table 3.1: Lens parameters for the overlapping sample.

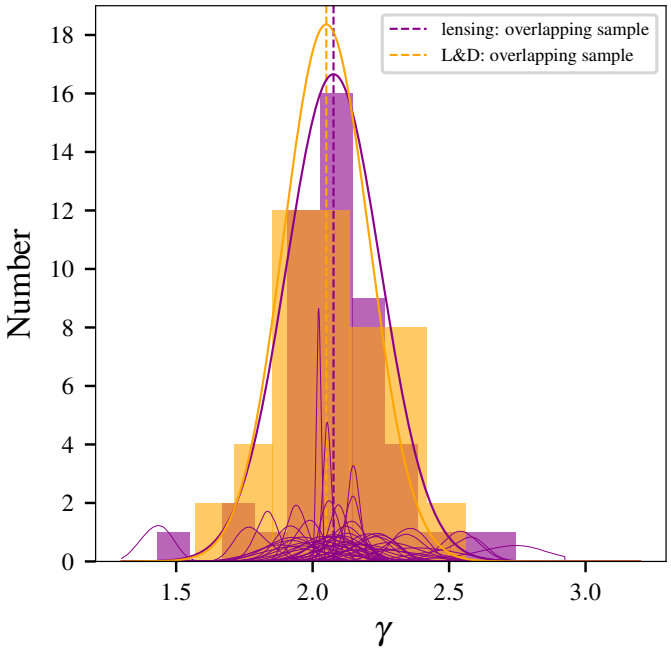

Figure 3.4: Logarithmic slopes γ of galaxies' total mass density $\rho(r) \propto r^{-\gamma}$, measured using Lensing-only and Lensing & Dynamics techniques, for a common "overlapping" sample of 48 galaxies. The two high Gaussian curves and dashed lines illustrate the best-fit mean and intrinsic scatter fitted via Equation 3.3.1. Lower curves show the posterior PDFs of individual lensing measurements, to illustrate their additional measurement uncertainty.

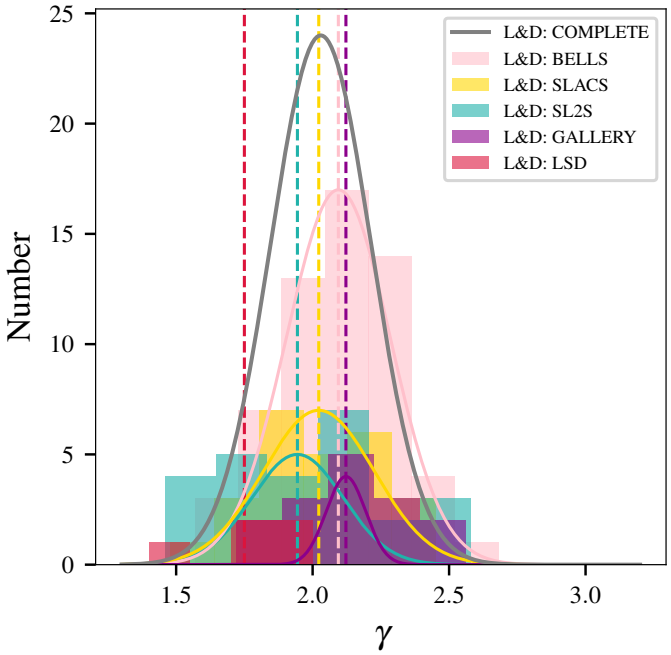

Figure 3.5: Logarithmic total mass-density slopes measured using the lensing & dynamics method for the "complete" sample of 123 galaxies, but split into the SLACS, BELLS, GALLERY, SL2S, and LSD samples. Coloured curves show the best-fit mean and intrinsic scatter of galaxies in each survey, calculated as in figure 3.4. The grey curve shows the best fit to all 123 galaxies.

$$\sigma_{\gamma_i} = \sigma^{\rm le}_{\gamma_i} \qquad \text{if} \qquad \gamma_i > \langle\gamma\rangle, \tag{3.3.4}$$

where $\sigma^{\rm ue}_{\gamma_i}$ and $\sigma^{\rm le}_{\gamma_i}$ correspond to the upper and lower uncertainties at the 68.7% credible region of the individual $\gamma^{\rm lensing}$ PDF.

For galaxies in the overlapping sample, we measure mean logarithmic density slope $\langle\gamma\rangle = 2.075^{+0.023}_{-0.024}$ and intrinsic scatter $\sigma_\gamma = 0.172^{+0.022}_{-0.032}$ (purple curve in figure 3.4). Errors quoted are at the 68% credible region. This is consistent with Lensing & Dynamics measurements from the literature for the same sample, $\langle\gamma^{\rm L\&D}\rangle = 2.050^{+0.0232}_{-0.031}$ and $\sigma^{\rm L\&D}_\gamma = 0.156^{+0.030}_{-0.026}$ (orange curve in figure 3.4).

Robustly for different methods, we thus confirm a slightly super-isothermal distribution of mass around galaxies in our overlapping sample. This is consistent with Auger et al. (2010a)'s original Lensing & Dynamics analysis of the entire SLACS sample, $\langle\gamma\rangle^{\rm L\&D} = 2.078 \pm 0.027$ and $\sigma^{\rm L\&D}_\gamma = 0.16 \pm 0.02$, which has been verified in repeat analyses (Ruff et al., 2011; Li et al., 2018). We confirm that this result is also reproduced in an analysis of L&D measurements for our complete sample $\langle\gamma^{\rm L\&D}\rangle = 2.030^{+0.019}_{-0.020}$ and $\sigma^{\rm L\&D}_\gamma = 0.184^{+0.020}_{-0.019}$ (grey curve in figure 3.5).

Splitting our complete sample into its parent surveys (figure 3.5), we note that the (high redshift) GALLERY lenses are the only sample with a mean logarithmic slope steeper than the (low redshift) SLACS sample. This remains true for the sub-samples of SLACS and GALLERY lenses that go into our overlapping sample. The posterior PDF contours in figure 3.6 show that lenses in the GALLERY sample have steeper slopes with smaller intrinsic scatter, for both lensing-only (dark green) and Lensing & Dynamics (dark purple) measurements, than for the SLACS sample (light green and purple). Something may be unusual in the selection technique used to find GALLERY lenses (see Sections 3.5.3 and 3.5.4 for further discussion).

3.3.2 Comparison of total mass-density slopes inferred by lensing and dynamics and lensing only

To further test whether the lensing-only and Lensing & Dynamics methods are measuring the same total mass-density slopes, Figure 3.7 compares their measurements for the 48 galaxies in the overlapping sample. Assuming the measurement errors are correct, we investigate to what extent the true underlying slope measurements for this sample of galaxies are correlated. To do this we assume that the combination of $\gamma^{\rm lensing}$ and $\gamma^{\rm L\&D}$ can be described by a bi-variate Gaussian distribution with likelihood

$$\mathscr{L}(\mu, \mathbf{\Sigma}_{\rm int}|\gamma_i) = \prod_i \frac{\exp\Big(-\frac{1}{2}(\gamma_i - \mu)^T \mathbf{\Sigma}_i^{-1}(\gamma_i - \mu)\Big)}{\sqrt{(2\pi)^2|\mathbf{\Sigma}_i|}}, \tag{3.3.5}$$

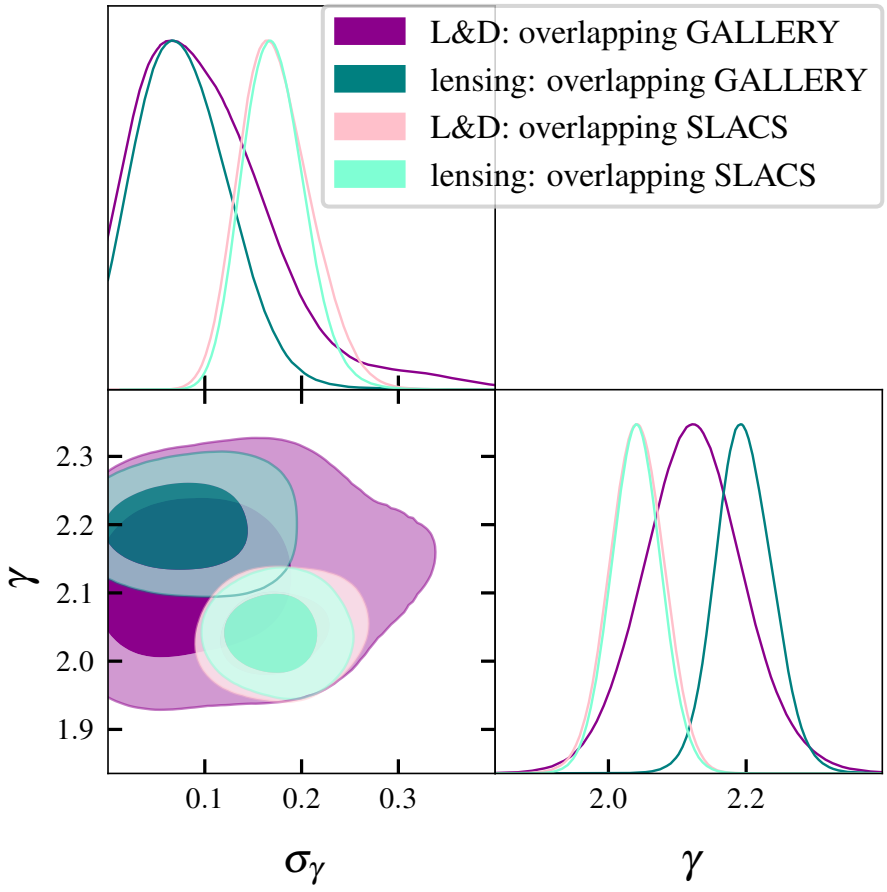

Figure 3.6: Posterior PDFs from fitting the mean γ and intrinsic scatter σ_γ of the SLACS and GALLERY overlapping sample of lenses assuming a Gaussian parent distribution. The GALLERY lenses have on average steeper density slopes than SLACS with both the lensing and dynamics (L&D) and lensing only approach.

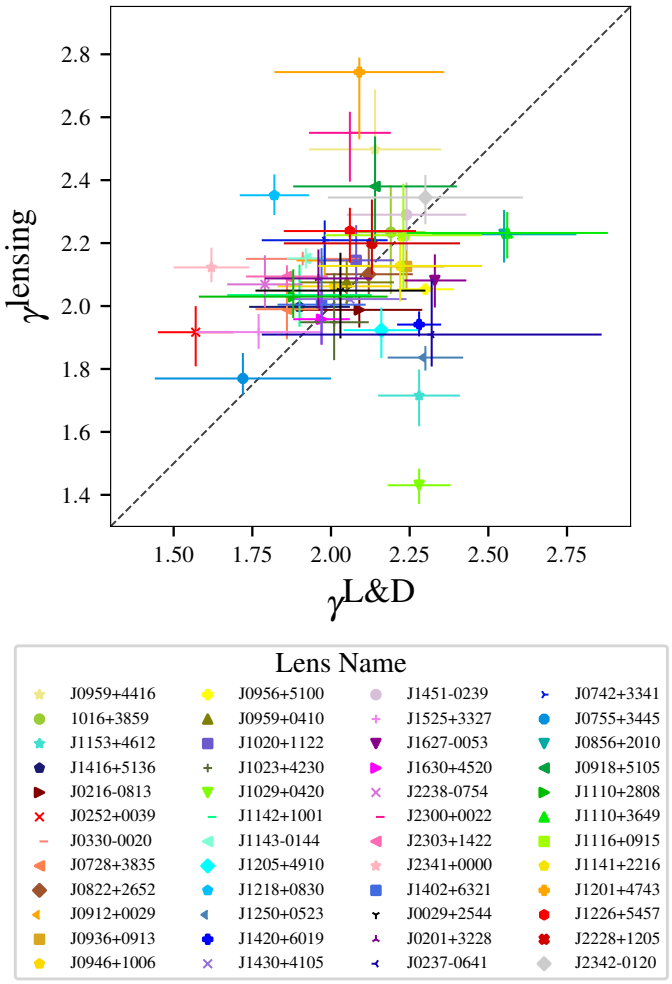

Figure 3.7: Logarithmic mass-density slopes of 48 individual galaxies in our "overlapping" sample, measured using lensing and stellar kinematics $\gamma^{\mathrm{L\&D}}$ or lensing-only $\gamma^{\mathrm{lensing}}$ methods. The identity line is plotted solely to guide visualisation. In the legend 33 SLACS lenses are listed first, followed by 15 GALLERY lenses.

where $\mu = [\langle\gamma^{\rm lensing}\rangle, \langle\gamma^{\rm L\&D}\rangle]$ is the vector mean, $\mathbf{\Sigma}_i = \mathbf{\Sigma}_{\rm int} + \mathbf{\Sigma}_{\rm err,\,i}$ is the covariance matrix, and $\gamma_i = [\gamma_i^{\rm lensing}, \gamma_i^{\rm L\&D}]$ are the individual slope measurements. The vector mean μ and the covariance matrix

$$\mathbf{\Sigma}_{\rm int} = \begin{bmatrix} (\sigma_\gamma^{\rm lensing})^2 & \rho\sigma_\gamma^{\rm lensing}\sigma_\gamma^{\rm L\&D} \\ \rho\sigma_\gamma^{\rm lensing}\sigma_\gamma^{\rm L\&D} & (\sigma_\gamma^{\rm L\&D})^2 \end{bmatrix}, \tag{3.3.6}$$

together describe the intrinsic distribution of the lensing-only and L&D slopes, where ρ is the intrinsic correlation between $\gamma^{\rm lensing}$ and $\gamma^{\rm L\&D}$. We assume the two measurement errors are uncorrelated such that the covariance matrix $\mathbf{\Sigma}_{\rm err,\,i}$ is given by

$$\mathbf{\Sigma}_{\rm err,\,i} = \begin{bmatrix} \left(\sigma_{\gamma,i}^{\rm lensing}\right)^2 & 0 \\ 0 & \left(\sigma_{\gamma,i}^{\rm L\&D}\right)^2 \end{bmatrix}, \tag{3.3.7}$$

where $\sigma_{\gamma,i}^{\rm lensing}$ and $\sigma_{\gamma,i}^{\rm L\&D}$ are the individual measurement errors on $\gamma^{\rm lensing}$ and $\gamma^{\rm L\&D}$, respectively. Note that in this case we approximate the asymmetric lensing-only measurement errors as Gaussian with $\sigma_{\gamma,i} = (\sigma_{\gamma,i}^{\rm ue} + \sigma_{\gamma,i}^{\rm le})/2$.

Using Bayes' theorem (equation 3.3.2) we infer the PDFs of the independent parameters $\langle\gamma^{\rm lensing}\rangle$, $\langle\gamma^{\rm L\&D}\rangle$, $\sigma_\gamma^{\rm lensing}$, $\sigma_\gamma^{\rm L\&D}$, and ρ in equation 3.3.5. We fit for these parameters with an MCMC sampling process using the Python implementation `emcee` (Foreman-Mackey et al., 2013).The means $\langle\gamma^{\rm lensing}\rangle = 2.085^{+0.031}_{-0.030}$ and $\langle\gamma^{\rm L\&D}\rangle = 2.050^{+0.034}_{-0.033}$, and intrinsic scatters $\sigma_\gamma^{\rm lensing} = 0.191^{+0.027}_{-0.023}$ and $\sigma_\gamma^{\rm L\&D} = 0.159^{+0.031}_{-0.027}$ inferred with this bi-variate model agree with those fitted separately in Section 3.3.1. We infer a correlation co-efficient $\rho = -0.150^{+0.223}_{-0.217}$, consistent with no correlation at the 68% credible region. At 2σ confidence the model implies a wide range of correlation coefficients, both negative and positive (-0.554 - 0.276), are consistent with the data. With this level of measurement uncertainty, we cannot definitively detect a correlation between the slopes measured with lensing and those measured with L&D. There is, however, no obvious systematic offset between the two methods: the mean difference is $\langle\gamma^{\rm lensing} - \gamma^{\rm L\&D}\rangle = 0.031 \pm 0.042$ and the data points appear scattered randomly either side of the identity line.

3.3.3 Correlations with the total-mass density slope

Since it is difficult to quantify for individual galaxies whether the (lensing-only and Lensing & Dynamics) methods are measuring the same slope, we instead investigate whether they infer the same global dependence with other observable properties of galaxies. We continue to assume that the slopes are drawn from a parent Gaussian distribution, but we now assume the mean of the distribution (in

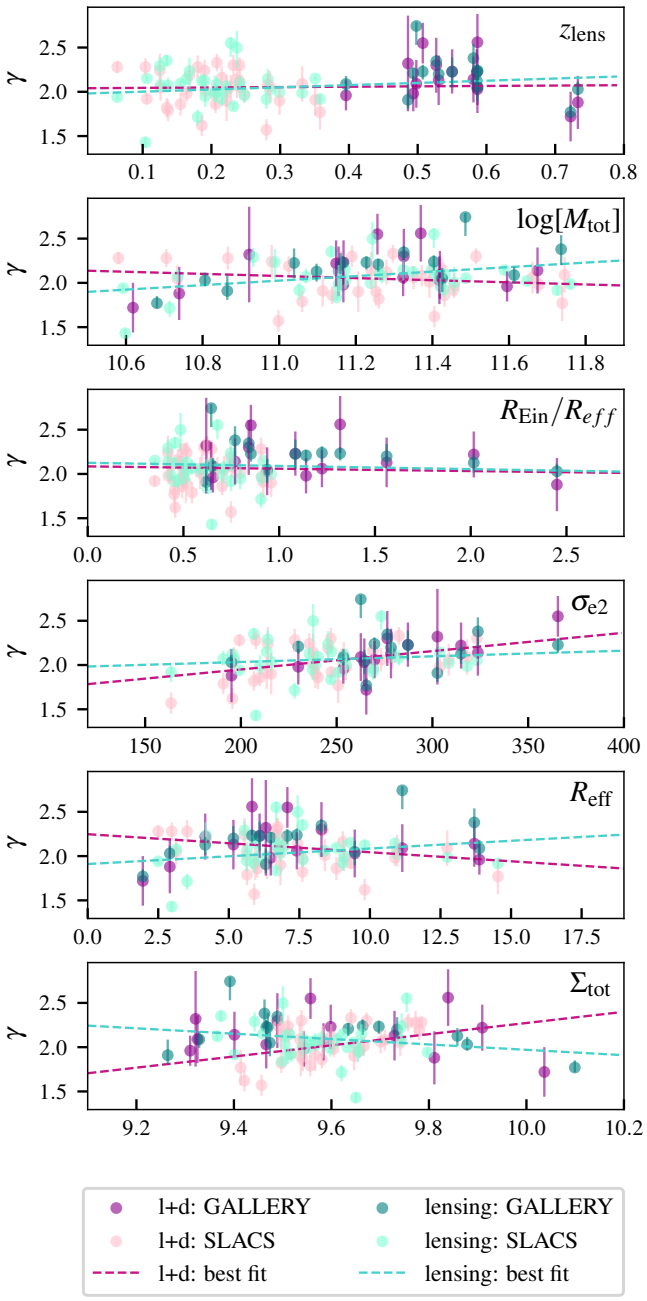

Figure 3.8: Correlation between total mass-density slopes γ and other properties of a lens galaxy. Measurements with lensing-only or Lensing & Dynamics techniques are consistent, except for the correlation with total mass density $\Sigma_{\rm tot}$. Numerical parameters of the best-fit lines are listed in Table 3.2.

Covariate (x)	$\langle x \rangle$	Gradient ($\frac{\partial \langle \gamma \rangle}{\partial x}$)		Intercept ($\langle \gamma_0 \rangle$)		Scatter (σ_γ)	
		γ^{lensing}	$\gamma^{\text{L\&D}}$	γ^{lensing}	$\gamma^{\text{L\&D}}$	γ^{lensing}	$\gamma^{\text{L\&D}}$
z_{lens}	0.319	$0.248^{+0.174}_{-0.178}$	$0.043^{+0.215}_{-0.224}$	$2.077^{+0.029}_{-0.028}$	$2.058^{+0.031}_{-0.039}$	$0.173^{+0.026}_{-0.022}$	$0.165^{+0.034}_{-0.028}$
R_{eff}	7.27	$0.017^{+0.009}_{-0.009}$	$-0.02^{+0.01}_{-0.013}$	$2.076^{+0.024}_{-0.027}$	$2.054^{+0.024}_{-0.029}$	$0.169^{+0.027}_{-0.02}$	$0.155^{+0.029}_{-0.033}$
$\log[M_{\text{tot}}]$	11.2	$0.254^{+0.082}_{-0.088}$	$-0.12^{+0.118}_{-0.108}$	$2.076^{+0.032}_{-0.029}$	$2.054^{+0.038}_{-0.037}$	$0.165^{+0.026}_{-0.022}$	$0.158^{+0.033}_{-0.028}$
$R_{\text{Ein}}/R_{\text{eff}}$	0.91	$-0.036^{+0.025}_{-0.023}$	$-0.026^{+0.046}_{-0.041}$	$2.076^{+0.027}_{-0.026}$	$2.049^{+0.036}_{-0.033}$	$0.173^{+0.031}_{-0.024}$	$0.162^{+0.024}_{-0.026}$
σ_{e2}	260	$0.001^{+0.0}_{-0.0}$	$0.002^{+0.001}_{-0.001}$	$2.072^{+0.03}_{-0.024}$	$2.073^{+0.032}_{-0.025}$	$0.172^{+0.024}_{-0.023}$	$0.138^{+0.033}_{-0.021}$
$\log[\Sigma_{\text{tot}}]$	9.6	$-0.304^{+0.167}_{-0.152}$	$0.631^{+0.221}_{-0.285}$	$2.078^{+0.024}_{-0.028}$	$2.049^{+0.03}_{-0.025}$	$0.167^{+0.024}_{-0.019}$	$0.131^{+0.033}_{-0.027}$

Table 3.2: Correlations between galaxies' total mass-density slopes γ and other galaxy observables, as visualised in Figure 3.8. Uncertainties are the 1σ credible regions on the gradient, intercept, and scatter on the covariate x, as in Equation (3.3.8).

Equation 3.3.1) is described by

$$\langle \gamma \rangle(x) = \langle \gamma \rangle_0 + \frac{\partial \langle \gamma \rangle}{\partial x}(x - \langle x \rangle), \tag{3.3.8}$$

where x is the galaxy observable. The free parameters in the model are now the mean slope $\langle \gamma \rangle_0$ at the average of the chosen galaxy observable $\langle x \rangle$, the intrinsic scatter of the distribution of slopes σ_γ, and the linear correlation coefficient $\frac{\partial \langle \gamma \rangle}{\partial x}$. We again use `dynesty` to fit these free parameters, in successive analyses where x represents the redshift of the lens galaxy, its effective radius, its total mass (equation 3.2.2), its normalised Einstein radius, its velocity dispersion, or its total surface mass density. The best fit parameters from this procedure are listed in Table 3.2 and visualised in Figure 3.8.

For most galaxy observables, we find correlations with the logarithmic density slope that are consistent (at 2σ confidence) for the lensing-only and L&D analyses. The only exception is the dependence upon total surface mass density. The L&D slopes imply a positive correlation of $\frac{\partial \langle \gamma \rangle}{\partial \Sigma_{\text{tot}}} = 0.631^{+0.434}_{-0.492}$ (2σ uncertainty), which is in agreement with previous L&D slope measurements for larger samples (Auger et al., 2010a; Sonnenfeld et al., 2013a), whereas the lensing slopes imply zero or slightly negative correlation $\frac{\partial \langle \gamma \rangle}{\partial \Sigma_{\text{tot}}} = -0.304^{+0.358}_{-0.357}$. This may indicate that the methods are measuring different slopes, and we shall investigate this further in Section 3.4.1.

We find that $\langle \gamma^{\text{L\&D}} \rangle$ has non-zero correlation (at $> 2\sigma$ statistical significance) with only two lens observables: total mass density, and velocity dispersion. Whereas, $\langle \gamma^{\text{lensing}} \rangle$ has non-zero correlation with only total mass. Given that our analysis does not account for uncertainty on the x variable, we caution that these coefficients may be overestimated – particularly for the dependence with velocity dispersion, for which typical measurements have $\sim 10\%$ uncertainty.

3.4 Dependence of the total-mass density slope on redshift

The logarithmic density slope of mass in a galaxy is governed by the relative amounts of stellar and dark matter, and the physical processes that modify their distribution as the galaxy evolves. Studying how $\langle\gamma\rangle$ depends upon redshift can therefore constrain universal models of galaxy formation.[3]

To quantify the dependence of the mean density profile slope on redshift, it is necessary to account for any other confounding variables by including them as covariates in the model. We investigate variables that are well motivated from previous L&D analyses (Sonnenfeld et al., 2012; Auger et al., 2010a; Li et al., 2018), the total surface mass density and normalised Einstein radius. These two variables are strongly correlated (with a Pearson correlation coefficient of 0.66), to the degree that including both of them as covariates would yield degenerate and unphysical coefficients. Therefore we fit only one of these covariates at a time, modelling the mean logarithmic density slope

$$\langle\gamma\rangle(z_{\rm lens}, x) = \langle\gamma\rangle_0 + \frac{\partial\langle\gamma\rangle}{\partial z}(z_{\rm lens} - 0.3) + \frac{\partial\langle\gamma\rangle}{\partial x}(x - \langle x\rangle), \tag{3.4.1}$$

where the free parameters to be fitted are $\langle\gamma\rangle_0$, the mean slope at $z_{\rm lens} = 0.3$ and $x = \langle x\rangle$, as well as $\frac{\partial\langle\gamma\rangle}{\partial z}$ and $\frac{\partial\langle\gamma\rangle}{\partial x}$, the linear coefficients of covariates $z_{\rm lens}$ and x. We again perform fits using the nested sampling algorithm `dynesty` via the probabilistic programming language `PyAutoFit`.

3.4.1 Allowing for dependence on surface mass density

Previous studies have shown that a galaxy's logarithmic density slope measured using L&D (Auger et al., 2010b; Sonnenfeld et al., 2013a) correlates with both its total and stellar surface mass density. In Section 3.3.3 we confirmed this for the L&D slopes but found that lensing-only slopes were consistent with zero correlation at 2σ. We investigate whether this discrepancy persists when we fit the density slopes of galaxies in the overlapping sample, but allowing for simultaneous variation with both redshift and total mass density (equation (3.4.1)). When fitting to lensing-only results, we use covariate $x = \Sigma_{\rm tot}^{\rm lensing}$, which uses $R_{\rm Ein}^{\rm PL}$ in equation (3.2.1). When fitting to L&D results, we use covariate $x = \Sigma_{\rm tot}^{\rm L\&D}$, the power law density profiles inferred by L&D analyses in the literature, but using $R_{\rm Ein}^{\rm SIE}$ in equation (3.2.1).

Best-fit parameters for lensing-only and L&D analyses of the overlapping sample are listed in Table 3.3,

[3] As emphasised by Sonnenfeld et al. (2013b), these measurements represent how the population mean density slope depends on the population parameters of the galaxies included in the model, and not how the mass-density slope evolves for an individual galaxy. By combining their measurements with literature values for the evolution of the mass and size of early-type galaxies, Sonnenfeld et al. (2013b) measured the average redshift evolution of an individual galaxy to be consistent with zero $\frac{d\gamma^{\rm L\&D}}{dz} = 0.10 \pm 0.12$.

Sample	$\langle\gamma\rangle_0$	σ_γ	$\frac{\partial\langle\gamma\rangle}{\partial z}$	$\frac{\partial\langle\gamma\rangle}{\partial\Sigma_{\rm tot}}$
complete: LD	$2.024^{+0.019}_{-0.021}$	$0.126^{+0.023}_{-0.015}$	$-0.259^{+0.084}_{-0.082}$	$0.423^{+0.068}_{-0.075}$
overlapping: LD	$2.051^{+0.031}_{-0.037}$	$0.127^{+0.028}_{-0.024}$	$0.045^{+0.217}_{-0.177}$	$0.659^{+0.250}_{-0.264}$
overlapping: lensing	$2.071^{+0.027}_{-0.026}$	$0.159^{+0.028}_{-0.018}$	$0.345^{+0.144}_{-0.167}$	$-0.432^{+0.175}_{-0.191}$
complete: lensing	$2.097^{+0.032}_{-0.029}$	$0.202^{+0.023}_{-0.023}$	$0.147^{+0.174}_{-0.154}$	$-0.225^{+0.181}_{-0.151}$

Table 3.3: Best-fit values of free parameters in a two-covariate model (equation 3.4.1) describing the correlation between the sample mean of galaxies' logarithmic density slopes, $\langle\gamma\rangle$, with redshift z and total surface mass density $\Sigma_{\rm tot}$. The total surface mass density is calculated inside the effective radius of a de Vaucouleurs fit to the stellar emission (equation 3.2.1). The intrinisic dispersion of the sample of galaxies σ is also a free parameter in the fit.

and the full posterior probability distributions are shown in Figure 3.9. The coefficient for variation with redshift is consistent between the two methods at 2σ. Surprisingly, however, our lensing-only analysis suggests that $\frac{\partial\langle\gamma\rangle}{\partial z} = 0.345^{+0.144}_{-0.167}$ is greater than zero at 2σ confidence. L&D analysis of the same galaxies implies that $\frac{\partial\langle\gamma^{\rm L\&D}\rangle}{\partial z} = 0.045^{+0.217}_{-0.177}$ is consistent with zero. Fitting the complete sample of L&D slopes (blue contours in Figure 3.9) yields a value less than zero at 4σ confidence $\frac{\partial\langle\gamma^{\rm L\&D}\rangle}{\partial z} = -0.259^{+0.084}_{-0.082}$, (in better agreement with measurements in the literature Auger et al., 2010a; Bolton et al., 2012; Sonnenfeld et al., 2013a; Li et al., 2018, see Table 3.5).

Coefficients describing the dependence of density slope on surface mass density are inconsistent between lensing-only and L&D analyses. For the overlapping sample of galaxies, the lensing-only coefficient is $\frac{\partial\langle\gamma\rangle}{\partial\Sigma_{\rm tot}} = -0.432^{+0.175}_{-0.191}$, while L&D suggests $\frac{\partial\langle\gamma^{\rm L\&D}\rangle}{\partial\Sigma_{\rm tot}} = 0.659^{+0.250}_{-0.264}$. Note that these results come from reasonably small populations of galaxies, and may be subject to outliers. For the complete lensing only sample, the increase in sample size leads to correlation coefficients with both redshift and surface mass density that are consistent with zero at 2σ confidence (see Table 3.3). Nonetheless, the coefficient with $\Sigma_{\rm tot}$ remains inconsistent with those inferred for both the complete and overlapping L&D samples.

3.4.2 Allowing for dependence on the radius where measurements are made

If measurements of the density slope are sensitive to the radius at which the measurement is constrained, this could bias our inference about redshift dependence of the mean slope. Because the normalised Einstein radius $^{\rm R_{Ein}}/_{\rm R_{eff}}$ typically increases with redshift for geometric reasons, one should simultaneously fit variation with $^{\rm R_{Ein}}/_{\rm R_{eff}}$ and $z_{\rm lens}$ so as to not bias either result. Indeed, Li et al. (2018) demonstrated that L&D slopes display an increasing trend with radius, whilst still inferring a negative trend with redshift, for the BELLS, GALLERY, and SL2S samples. We now fit the two-covariate

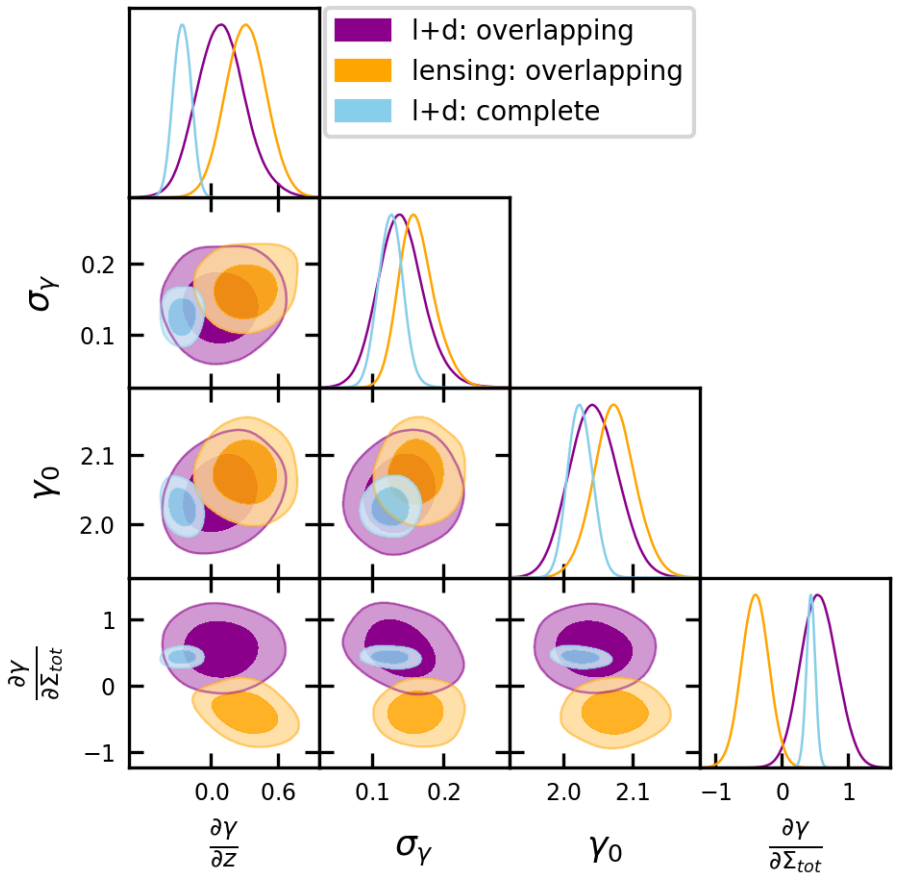

Figure 3.9: The 68% (dark) and 95% (light) marginalised confidence limits on posterior probabilities of the mean, intrinsic scatter, and linear coefficients for the dependence of slope on redshift and total surface mass density for both lensing-only (orange contours) and lensing&dynamics slopes (purple contours).

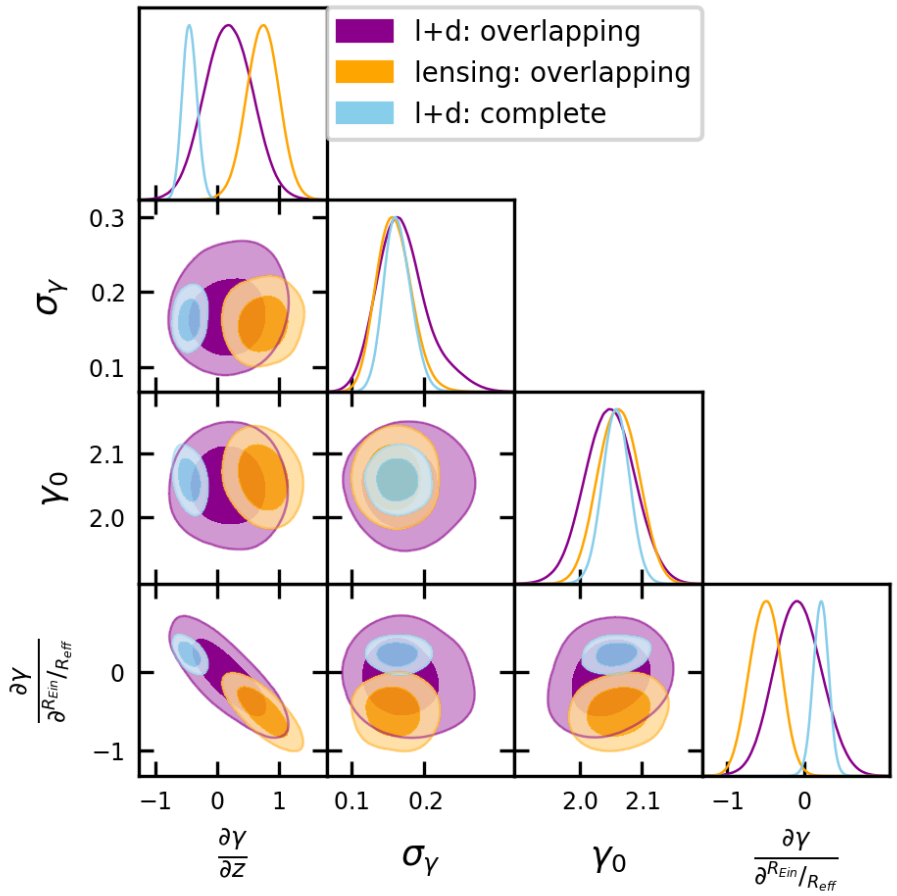

Figure 3.10: The 68% (dark) and 95% (light) marginalised confidence limits on posterior probabilities of the mean, intrinsic scatter, and linear coefficients for the dependence of slope on redshift and normalised Einstein radius for both lensing-only (orange contours) and lensing&dynamics slopes (purple contours).

model (Equation 3.4.1), with $x = \mathrm{R_{Ein}}/\mathrm{R_{eff}}$. Best-fit parameters for lensing-only and L&D analyses of the overlapping sample are listed in Table 3.4, and the full posterior probability distributions are shown in Figure 3.10.

Best-fit parameters of the lensing-only and L&D models are consistent at 2σ confidence for the overlapping sample. Albeit, for logarithmic density slopes measured with a lensing-only analysis, we infer relationships with redshift $\frac{\partial\langle\gamma\rangle}{\partial z} = 0.812^{+0.252}_{-0.263}$ and normalised Einstein radius $\frac{\partial\langle\gamma\rangle}{\partial \mathrm{R_{Ein}}/\mathrm{R_{eff}}} = -0.539^{+0.160}_{-0.191}$ at over 2σ confidence, whereas the L&D inference $\frac{\partial\langle\gamma\rangle}{\partial z} = -0.002^{+0.303}_{-0.265}$ and $\frac{\partial\langle\gamma\rangle}{\partial \mathrm{R_{Ein}}/\mathrm{R_{eff}}} = 0.074^{+0.194}_{-0.294}$ is consistent with no correlation at 2σ. Note that, as for the Σ_{tot} model, the coefficients for the complete lensing-only sample are both consistent with zero (see Table 3.4). The complete L&D sample infers coefficients $\frac{\partial\langle\gamma\rangle}{\partial z} = -0.428^{+0.119}_{-0.127}$ and $\frac{\partial\langle\gamma\rangle}{\partial \mathrm{R_{Ein}}/\mathrm{R_{eff}}} = 0.21^{+0.114}_{-0.100}$ that are consistent with measurements in the literature.

Sample	$\langle\gamma\rangle_0$	σ_γ	$\frac{\partial\langle\gamma\rangle}{\partial z}$	$\frac{\partial\langle\gamma\rangle}{\partial R_{\rm Ein}/R_{\rm eff}}$
complete: LD	$2.056^{+0.023}_{-0.022}$	$0.163^{+0.016}_{-0.019}$	$-0.428^{+0.119}_{-0.127}$	$0.210^{+0.114}_{-0.100}$
overlapping: LD	$2.053^{+0.033}_{-0.028}$	$0.165^{+0.027}_{-0.025}$	$-0.002^{+0.303}_{-0.265}$	$0.074^{+0.194}_{-0.294}$
overlapping: lensing	$2.063^{+0.028}_{-0.023}$	$0.156^{+0.027}_{-0.021}$	$0.812^{+0.252}_{-0.263}$	$-0.539^{+0.160}_{-0.191}$
complete: lensing	$2.095^{+0.03}_{-0.029}$	$0.199^{+0.027}_{-0.025}$	$0.331^{+0.216}_{-0.228}$	$-0.276^{+0.176}_{-0.156}$

Table 3.4: Best-fit values of free parameters in a two-covariate model (equation 3.4.1) describing the correlation between galaxies' logarithmic density slope, γ, with redshift z and normalised Einstein radius $R_{\rm Ein}/R_{\rm eff}$. The effective radius $R_{\rm Eff}$ is are literature values of de Vaucouleurs fits to the stellar emission.

3.5 Discussion and Comparison With Previous Studies

3.5.1 Bulge-halo conspiracy?

That the total mass-density profiles of massive elliptical galaxies is nearly isothermal has been observed in X-ray emission (Humphrey et al., 2006), dynamical modelling (Serra et al., 2016; Poci et al., 2017), and lensing and dynamical analyses (Koopmans et al., 2006; Barnabè et al., 2009; Auger et al., 2010a; Sonnenfeld et al., 2013a). Given that neither the stellar nor dark matter components are individually described by a single power law, this remarkable observation about their sum is known as the "bulge-halo consipracy". On average, taking into account current measurement uncertainties, our analysis is consistent with this result. By fitting to only the imaging data of a sample of 48 strong lenses from the SLACS and GALLERY surveys, we measure slightly super-isothermal total-mass density slopes, with mean $\langle\gamma\rangle = 2.075^{+0.023}_{-0.024}$ and intrinsic scatter $\sigma_\gamma = 0.172^{+0.022}_{-0.032}$. Previous L&D analyses of exactly the same galaxies yield consistent measurements $\langle\gamma^{\rm L\&D}\rangle = 2.050^{+0.023}_{-0.031}$ and $\sigma_\gamma^{\rm L\&D} = 0.156^{+0.030}_{-0.026}$.

If the true density profiles of massive elliptical lens galaxies are indeed power-law distributions, then one would expect a perfect correlation between the slopes constrained with the different methods. For a sample of 21 SLACS systems analysed using a similar lensing-only method, Shajib et al. (2021) were unable to detect a correlation between slopes measured using lensing only and L&D. They measured a bi-weight mid-correlation of 0.01 ± 0.16, where the errors on the correlation coefficient were calculated from the 68% confidence interval of the coefficients calculated from 1000 random draws of their lensing-only and L&D slopes from the posterior PDFs. With more than double the number of systems, if we adopt the same approach as Shajib et al. (2021), we continue to find no correlation between the lensing and L&D slopes (bi-weight mid-correlation $0.08^{+0.11}_{-0.12}$). Moreover, using our own approach that takes into account the covariance between the intrinsic distributions of slopes (described in Section 3.3.2), we measure a correlation coefficient of $-0.150^{+0.223}_{+0.217}$, suggesting

an even wider range of correlation coefficients are consistent with the data. Therefore, although we can not rule out the existence of a global power law given the measurement uncertainties, the lack of an obvious correlation between the slopes measured using the different methods may be indicating that some of the systems deviate from a strict power law.

3.5.2 Are the lensing and dynamics and lensing-only methods constraining the same quantity?

Although lensing-only and L&D analyses yield consistent *mean* values of logarithmic density slopes for a population of galaxies, this does not necessarily imply that the two analyses constrain the same quantity for each *individual* galaxy. Lensing-only analyses are sensitive to the profile at the Einstein radius (e.g. Koopmans et al., 2006; Treu, 2010; Suyu et al., 2017), whereas L&D analyses (combining measurements of velocity dispersion and Einstein radius) probe the integrated profile between the effective and Einstein radii. If galaxies' total density profiles deviate from a power law, measurements of the logarithmic slope at different radii will yield different results. Shankar et al. (2017) report a connection between the observed dependence of $\gamma^{\rm L\&D}$ on stellar mass and effective radius (hence stellar surface mass density) and the relative amounts of stellar and dark matter in the region of the mass density profile that is being probed. They find that steeper $\gamma^{\rm L\&D}$ are inferred from the inner profile where the stellar component steepens. Similarly, with models of early-type galaxies built from analytic stellar and dark matter profiles, Dutton & Treu (2014) showed that the strength of the correlation between $\gamma^{\rm L\&D}$ and dark matter fraction largely determines the strength of the correlation between $\gamma^{\rm L\&D}$ and stellar density (among other galaxy variables).

We found in Section 3.4 that measurements of a galaxy's logarithmic density slope can be made independently of most of its observable properties. The main complications are caused by variations in a galaxy's total surface mass density, $\Sigma_{\rm tot}$. For a lensing-only analysis, we obtain negative values of $\frac{\partial\langle\gamma\rangle}{\partial\Sigma_{\rm tot}}$, while L&D analyses are consistently positive (Table 3.3). A negative coefficient seemingly runs counter to the expectation (also demonstrated with stellar kinematics methods Poci et al. 2017) that galaxies with higher stellar densities have higher central densities, and hence steeper total mass-density slopes. This disagreement may therefore indicate that the L&D and lensing-only methods are constraining different quantities. Indeed, it is notable that the multivariate model we fit to the lensing-only analyses (overlapping and complete) with normalised Einstein radius as a second covariate, infer similar coefficients $\frac{\partial\langle\gamma\rangle}{\partial {\rm R_{Ein}/R_{eff}}}$ to the coefficients $\frac{\partial\langle\gamma\rangle}{\partial\Sigma_{\rm tot}}$ in the models fitted with surface mass density as a covariate (see Tables 3.4 and 3.3). Since these quantities are strongly correlated, and can therefore not be fitted for simultaneously, it is difficult to interpret the coefficients individually. It may be that the

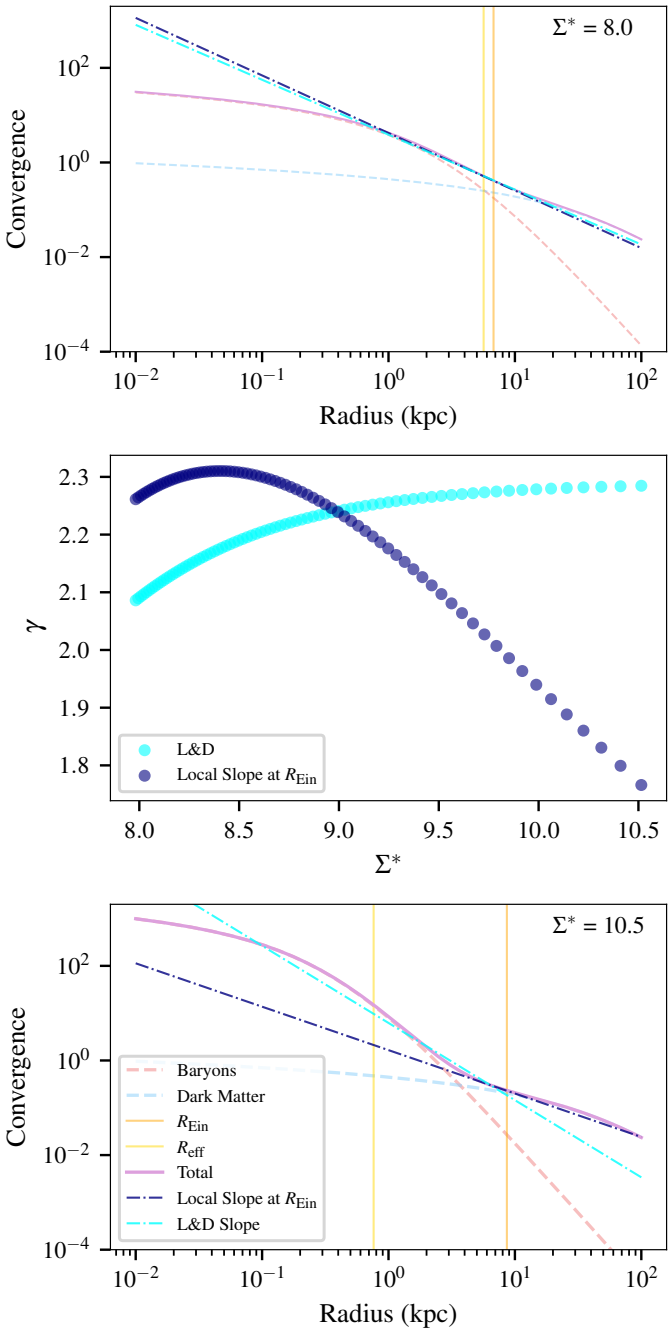

Figure 3.11: Analytic model of an azimuthally-symmetric lens, which reproduces and explains behaviour observed in the data. The distribution of mass is described as the sum of Hernquist (stellar) and NFW (dark matter) profiles. As the stellar surface mass density increases from the top to bottom panel, the slope of the total mass-density profile constrained between the Einstein radius and effective radius (cyan dash-dotted line) steepens, mimicking the lensing and dynamics positive relationship with surface mass density. Conversely, the slope constrained locally at the Einstein radius (dark blue dash-dotted line) flattens, reproducing the negative relationship with surface mass density observed for the slopes measured using lensing only. The top and bottom panel represent the mass density-profiles, and their fitted L&D and local slopes, for the first and last points plotted in the middle panel which shows how these quantities behave as the stellar surface mass density increases.

negative relationship we infer with total surface mass density is a consequence of a more fundamental dependence on the radius at which the lensing slope is measured.

We now put forward a toy model that can explain the observed behaviour. We first construct a model of the distribution of mass in an early type galaxy, comprising baryons in a spherically-symmetric Hernquist profile, and dark matter in a spherically-symmetric NFW profile (Figure 3.11). In line with previous studies (Dutton & Treu, 2014; Shankar et al., 2017), we found Salpeter-like values were necessary to produce values of total-mass density slope that were representative of the L&D observations. We fix the total stellar mass (at 11.64 $\log[M^*/M_\odot]$), then adjust the NFW parameters to obtain a dark matter fraction within half the effective radius representative of observations of early-type galaxies (these are small such that at this radius the stellar and total masses, hence surface densities, are similar). Following Dutton & Treu (2014) we then approximate the L&D mass-density slope measurement as the mass-weighted density slope within the effective radius

$$\gamma^{\rm L\&D}_{\rm proxy}(r) = \frac{1}{M(<{\rm R_{eff}})}\int_0^{\rm R_{eff}} -\gamma(r)4\pi r^2\rho(r)dr, \tag{3.5.1}$$

where $M(<{\rm R_{eff}})$ is the total mass within the effective radius, and $-\gamma(r) \equiv d\log\rho/d\log r$ is the local logarithmic slope of the given density profile $\rho(r)$. We then assume that the lensing-only method measures the local logarithmic slope at the Einstein radius. In this model, increasing the stellar surface mass-density from $\Sigma^* = 8$ $\log[M_\odot{\rm kpc}^{-2}]$, (left panel) to $\Sigma^* = 10.5$ $\log[M_\odot{\rm kpc}^{-2}]$, (right panel) by decreasing the effective stellar radius, raises the inferred L&D slope (cyan dot-dashed line) from 2.08 to 2.28 but reduces the inferred local logarithmic slope at the Einstein radius (navy dot dashed line) slope from 2.26 to 1.76 – similar to our observations of real galaxies.

The negative relationship of the local slope at $\rm R_{Ein}$ in this model (middle panel Figure 3.11) appears to occur at larger values of normalised Einstein radius. The effective radius is typically in a heavily baryon-dominated regime; the Einstein radius near an inflection point in the total density profile, created by the transition from baryon- to dark matter-domination. As we increase the stellar density, the steepening stellar profile strengthens the inflection point (deviating further from a power-law), and the Einstein radius moves out farther towards the inflection point and a shallower slope. However, all this is averaged over by a L&D measurement. That we observe the same behaviour in real galaxies suggests their total density profile might also contain a detectable inflection point. If further work supports this hypothesis, that the inflection is detected by a lensing-only measurement, but averaged over by a L&D measurement, future analyses that combine measurements may be able to constrain deviations from the bulge-halo conspiracy.

We acknowledge that it is a strong assumption that the lensing only measurement constrains the local

Study	Samples	$\langle\gamma\rangle_0$	σ_γ	$\frac{\partial\langle\gamma\rangle}{\partial z}$	$\frac{\partial\langle\gamma\rangle}{\partial\Sigma}$	$\frac{\partial\langle\gamma\rangle}{\partial R_{\rm Ein}/R_{\rm eff}}$
Bolton et al. (2012)	SLACS & BELLS	2.11 ± 0.02	0.14 ± 0.06	-0.60 ± 0.15	-	-
Sonnenfeld et al. (2013a)	SLACS, SL2S, & LSD	$2.08^{+0.02}_{-0.02}$	$0.12^{+0.02}_{-0.02}$	$-0.31^{+0.09}_{-0.10}$	$0.38^{+0.07}_{-0.07}$	-
Li et al. (2018)	SL2S, BELLS, & GALLERY	$1.981^{+0.024}_{-0.024}$	$0.168^{+0.021}_{-0.017}$	$-0.309^{+0.092}_{-0.083}$	-	$0.194^{+0.092}_{-0.083}$

Table 3.5: Comparison of the coefficients inferred for models in previous studies that have constrained the redshift dependence of lensing and dynamics total mass-density slopes.

slope at the Einstein radius. This neglects the constraining power of the positions of the arcs in the image (i.e. the Einstein radius) that are fit for simultaneously with the gradients of the deflection angle field that constrain the slope in a real lensing analysis. Kochanek (2020) emphasise that the only two quantities determined by lens data are the Einstein radius and the dimensionless and mass-sheet invariant quantity $\xi_2 = \mathrm{R_{Ein}}\alpha''(\mathrm{R_{Ein}})/(1-\kappa_{\rm Ein})$ where $\alpha''(\mathrm{R_{Ein}})$ is the second derivative of the deflection profile at $\mathrm{R_{Ein}}$. They argue that power law models have a one to one mapping between this quantity and the mass-density slope $\gamma = \xi_2/2+2$. With γ calculated in this way for the Hernquist+NFW profiles plotted in Figure 3.11, we do not find a negative relationship between total mass-density slope and stellar surface mass density. This may be implying that the mass-density profiles that make up our toy-model are too simplistic, that the way we induce an increase in stellar surface mass density is different to how this increase occurs in real galaxies, or that $\gamma = \xi_2/2+2$ does not well represent what we measure with lensing only in real galaxies.

Understanding what slope lensing constrains when the underlying profile deviates from a power law will be invaluable in interpreting the results presented in this work. Cao et al. (2020) showed that the true profile's mass weighted slope within the Einstein radius better matched the total mass-density slope of lensing only fits to mock images, simulated with complex multiple Gaussian expansion + NFW profiles, than the mass weighted slope between 0.8 - 1.2 $\mathrm{R_{Ein}}$. For these mock systems the mismatch between the power-law and the true density profiles can be compensated by a mass-sheet transformation (see Figure 8 of Cao et al. (2020)), which results in a fitted lensing only slope that resembles more closely the true density profiles' average slope over a local measurement as suggested in this work. Nonetheless, the 2σ disagreement between the lensing only and L&D surface mass density coefficients implies a deviation of the underlying profile from a power law distribution, and the negative relationship of the lensing only slopes with normalised Einstein radius may well be the result of an inflection zone like that described in the toy-model put forward in this work.

3.5.3 Evolution of massive elliptical galaxies

Although measurements of $\frac{\partial\langle\gamma\rangle}{\partial z}$ reflect the evolution of galaxy populations rather than individual galaxies, they can still inform models of the overall processes. For example, Shankar et al. (2018) found their observations could be reproduced only if the Sérsic index of stellar components vary with redshift. Our L&D analysis confirms previous measurements in the literature, that galaxies' logarithmic density slopes decrease with increasing redshift, i.e. they steepen with cosmic time (see Table 3.5). Interestingly, most cosmological simulations instead show a mild increase in density slopes with increasing redshift (Wang et al., 2020, 2019; Remus et al., 2017), which is inconsistent with L&D measurements but matches our lensing-only results. Typically, the density slope of a simulated galaxy is calculated to be the average mass density slope within some radial range. At present, it is not clear whether this discrepancy with L&D density slope measurements indicates a limitation of the simulations, systematics in the observations, or additional complexity in the physics, such as deviations from a power law profile. Notably, adjusting the method used to calculate density slopes in the Illustris simulation so it better represents the L&D observational technique suggests a mild shallowing of slopes with redshift, $\frac{\partial\langle\gamma\rangle}{\partial z} = -0.03 \pm 0.01$ (Xu et al., 2017). Nonetheless, those authors caution that the method still suffers from systematic biases and does not account for sampling bias that will be present in the observational data.

Galaxy selection effects are important. Both lensing-only and L&D analyses of our overlapping sample yield positive values of $\frac{\partial\langle\gamma\rangle}{\partial z}$ that do not match the results of larger samples (see Tables 3.3 and 3.4). The positive coefficients are driven by the GALLERY lenses, which constitute most high redshift lenses in the overlapping sample, and have the steepest mean slopes. The unusual properties of GALLERY systems may even explain the differences between the lensing-only and L&D coefficients. Because the constraining power of L&D analyses degrade at high redshift (see Section 3.5.4), the GALLERY sample does not contribute as much to the overall fit, and $\frac{\partial\langle\gamma\rangle}{\partial z}$ is not as significantly positive.

If lensing-only and L&D techniques measure different aspects of galaxies' mass distributions, as we suggested they might in Section 3.5.2, it is unclear whether we should expect the dependence of these measurements on redshift to agree. Nevertheless, with the current level of statistical precision, the lensing-only and L&D measurements are consistent when we model the same samples of lenses.

3.5.4 Benefits of lensing-only analyses

Measurements using our lensing-only method do not degrade at high redshift. This is illustrated in Figure 3.2, which compares the statistical uncertainty of lensing-only or L&D measurements of each

slope, $\delta\gamma$, as a function of redshift. For the L&D analysis of galaxies in the overlapping sample, we find a strong linear relationship between uncertainties and lens redshift, with slope 0.37±0.05 (1σ errors, i.e. significant at $>3\sigma$). However, for lensing-only measurements, we measure much less degradation, with slope 0.06±0.04 (1σ errors, i.e. consistent with zero at 2σ). Note that lensing-only measurements of (high redshift) GALLERY lenses have greater uncertainty than lensing-only measurements of (low redshift) SLACS lenses. This appears to be unrelated to the lens redshift, as we detect no correlation between measurement uncertainties and redshift for the SLACS and GALLERY samples separately. It is instead expected because the GALLERY lenses were selected due to Lyman-alpha emission from their source galaxies, which makes them inherently compact and less well resolved.

Despite this selection effect, which disfavours only the lensing method, the lensing-only measurements of the GALLERY sample are better constrained than L&D measurements, which degrade due to increasing uncertainty on velocity dispersion measurements at high redshift. This highlights the potential of the lensing-only method to extend this analysis to higher redshifts without losing constraining power. Deviations from a global power law, as discussed in Section 3.5.2, may complicate the interpretation of analyses like that presented in this study. In future, constraining how the parameters of more complex stellar plus dark matter distributions depend on redshift may be more appropriate to further our understanding of the evolution of ETGs, a problem well suited to strong lensing (Nightingale et al., 2021a). Sonnenfeld & Cautun (2021) demonstrated the ability of strong lensing alone to calibrate stellar masses and constrain the inner dark matter density profile of galaxies with a hierarchical approach.

In the next couple of decades, lensing-only analyses could be possible at redshifts up to $z \sim 2$, through surveys such as Euclid and the Vera Rubin Observatory that will discover large populations of high redshift lenses (Collett, 2015). Furthermore, the lensing-only measurements were constrained from the imaging data alone and can therefore scale to the hundreds of thousands of lenses that these surveys will observe, without requiring deep spectroscopic observations. Photometric redshifts (Sonnenfeld, 2022) and fully-automated analyses (Shajib et al., 2021) will be key in this endeavour.

3.6 Summary

We measure the distribution of mass around 48 early type galaxies in the SLACS and GALLERY strong lens surveys, to test the 'bulge-halo conspiracy' that stellar and dark matter together produce a power-law radial density profile with index γ. We compare two methods: a traditional Lensing & Dynamics (L&D) technique that combines the Einstein radius from lensing with stellar kinematic

data; and a new, lensing-only technique that fits every pixel in imaging data. The two methods yield consistent measurements of the parent distribution. Our lensing-only technique measures a population average $\langle\gamma\rangle = 2.075^{+0.023}_{-0.024}$ with intrinsic scatter between galaxies $\sigma_\gamma = 0.172^{+0.022}_{-0.032}$

Two results hint that the conspiracy breaks down. First, although the two methods yield consistent population-averaged measurements, they appear to differ for individual galaxies. If every galaxy has a single, well-defined power-law slope, although we can not rule out a global power law with the current level of measurement uncertainty, it is surprising that we infer a statistically insignificant correlation coefficient of $-0.150^{+0.223}_{+0.217}$. Second, although both methods can infer γ independently of most galaxy properties, measurements are correlated with total surface mass density (even when we fit multivariate models including redshift as a covariate). The lensing-only method yields negative correlation $\partial\langle\gamma\rangle/\partial\Sigma_{\rm tot} = -0.432^{+0.404}_{-0.348}$, whereas the L&D method yields positive correlation $\partial\langle\gamma^{\rm L\&D}\rangle/\partial\Sigma_{\rm tot} = 0.659^{+0.481}_{-0.474}$.

We discuss a hypothesis that explains these results. The L&D method measures a galaxy's mean density profile between the Einstein radius and its effective radius. This averages out deviations from a power law, indicating the 'bulge-halo conspiracy'. However, the lensing-only method is sensitive to the local slope at the Einstein radius. For galaxies in which the Einstein radius is larger than the effective radius, the Einstein radius typically occurs near the transition between stellar-dominated core and dark matter-dominated outskirts – an inflection point where the total mass profile deviates from a power law. The inflection gets stronger as the stellar mass density increases. Further studies (e.g. Cao et al., 2020; Kochanek, 2020) will be useful to test this hypothesis and to understand how deviations from a power-law could affect previously-obtained inferences about galaxy evolution.

Any study of galaxy evolution must deal with selection effects. Our results suggest that galaxy redshift and stellar surface density affect the mass profile inferred by lensing methods (partly because they usefully change the Einstein radius, so probe deviations from a power law mass distribution). If selection effects can be understood, the lensing-only method will be able to analyse the large samples of lenses expected from surveys such as Euclid. This is because it requires only imaging data, and can be automated. Its analysis will also be possible to higher redshifts than L&D techniques, whose statistical precision degrades with redshift due to difficulties obtaining spectroscopy.

In this study we measured a redshift dependence of $\partial\langle\gamma\rangle/\partial z = 0.345^{+0.322}_{-0.296}$ at fixed surface mass density for the lensing-only slopes, consistent with the same sample of L&D slopes but in tension with the complete L&D sample. A large sample of lenses from a single lens survey like Euclid will provide a tighter constraint on this result and remove any biases from the different selection effects of the combined surveys. This will offer new insights into the formation and evolution galaxies, out to

redshift 2.0 and beyond.

Chapter 4

Investigating strong lensing "external" shears

4.1 Introduction

So far in this thesis we have taken advantage of gravitational lensing in the strong regime to constrain the mass distribution of the lens galaxy from the multiple images that are produced. Gravitational lensing occurs along most lines of sight in the Universe in the weak regime, where the distortions occur primarily as small perturbations to galaxy shapes. These perturbations are known as cosmic shear when they are due to the large scale structure of the universe, but also occur in the outskirts of massive clusters or galaxies. Since the weak lensing shear causes coherent distortions in the images of background galaxies, wide-field galaxy surveys can be used to measure the lensing signal by correlating observed galaxy shapes of large number of objects.

Constraining the cosmic shear has become a powerful probe of cosmology, allowing us to infer the properties of dark energy, putting tight constraints on cosmological parameters (Kilbinger, 2015). This is possible since the growth of structure and the evolution of the LSS that is probed by weak lensing is inherently linked to the cosmological model. Recently, methods to combine the constraints from both strong and weak lensing to accurately infer the line of sight shear have been proposed (Birrer et al., 2017; Kuhn et al., 2020; Fleury et al., 2021).

Since strong and weak lensing probe different regions of the same matter density field, together the two methods provide independent constraints on the same distribution of matter. Although most regularly used as stand alone probes, this complementarity provides useful insight into the systematic uncertainties inherent to the individual methods. In our strong lensing models of the SLACS and

GALLERY samples in Chapter 2 we included two additional 'external shear' parameters in the model for the mass distribution, thus constraining the weak shear distortions in the environment of each lens galaxy.

Including external shear parameters in the model is commonplace in strong lensing methods, indeed it is a necessity if one wishes to account for all possible perturbations to the deflection angle field. However, the assumption that they account for perturbations from matter *only* external to the lens galaxy should possibly be approached with caution. Studies of quad lenses have shown that the models prefer values of external shear that are too large to be a result of cosmic shear or galaxy-scale perturbations alone (Keeton et al., 1997; Witt & Mao, 1997). More recently, Cao et al. (2022, hereafter C22) demonstrated using a mock sample of lenses that false inferences of external shear can be made if the model for the mass distribution is missing complexity that is in the true mass distribution.

To test the hypothesis that fitted values of external shear do not reflect the true shear along that line of sight, we study the subset of SLACS lenses for which we have sufficiently high S/N data to measure the weak lensing shear distortions. We shall compare these environmental shears measured using the weak lensing method to the external shears measured in our strong lensing analysis. We note that these would not be expected to arrive at identical results due to the different scales that they probe, however we would expect them to be strongly correlated. Kuhn et al. (2020) recently developed a self-consistent formalism for combining strong and weak lensing line of sight shears, taking into account covariances. The strong and weak lensing covariance they measured from three lenses in the COSMOS field was smaller than the difference observed for the individual systems, indicating more data was required for a detection. In this work, with a much larger sample of galaxies, we simply aim to detect a correlation between the two probes.

To gain further understanding of the external shears inferred using the strong lensing method we compare the results of the observed SLACS and GALLERY lenses to those from a mock sample of galaxies simulated by C22 to be similar to the SLACS population. These lenses were simulated with complex multiple elliptical gaussian (MGE) and NFW mass distributions that represent the stellar and dark matter respectively. No external shear was simulated in the mock data and yet C22 demonstrated that an external shear is recovered when they are fitted with a PL+ext profile. We will compare the behaviour of these shears to those inferred in real galaxies. Further, we carry out and investigate the results that are inferred in both the real and mock samples when the mass distribution is assumed to be just a PL, removing the external shear parameters from the fit.

We begin by recapping the gravitational lens theory in Section 4.2, specifically describing the weak lensing regime and the method to constrain the weak lensing shear. We then give an overview of

the observed and mock data in Section 4.3 and the strong and weak lensing analysis procedures in Section 4.4. The results are presented in Section 4.5 and discussed in Section 4.6, before we finally conclude in Section 4.7

4.2 Regimes of gravitational lensing

In Section 1.4.1 we covered strong gravitational lensing theory. In this strong regime, where ($\kappa > 1$), the lens equation (equation 1.4.3) has multiple solutions corresponding to the number of multiple images that are observed. Thus, assuming a model for the distribution of mass in the lens plane and the distribution of light in the source plane, the multiple images provide constraints on these distributions by solving the lens equation. In strong lensing studies it is common to assume that the mass distribution (and its associated shear) of the primary lens galaxy, which are typically Early-type galaxies, can be well approximated by an elliptical power law distribution (equation 1.4.14). The primary lens galaxy is not the only source of shear in a gravitational lens. It is generally considered necessary to allow for *external* perturbations caused by galaxies or clusters near the lens galaxy, or along the ray path. It is these external shear parameters (equation 1.4.16), that were constrained in Chapter 2, we will investigate in this chapter. We will compare these shear distortions from the strong lensing regime to those from the weak lensing regime, where the distortions and magnifications are small such that they can not be identified in individual sources, only statistically.

In the weak lensing regime, where $\kappa \ll 1$, the Jacobian (equation 1.4.6) is very close to the unit matrix, and only small magnifications and distortions occur. Under this definition of weak lensing the lens mapping can be linearised and the Jacobian can be expressed in terms of the convergence and the two components of shear (equation 1.4.7). The most readily observable effect in this regime are the shear distortions. Although, due to the invariance of the Jacobian matrix under the transformation $\mathbf{A} \rightarrow \lambda\mathbf{A}$ (known as the mass sheet degeneracy Schneider & Sluse (2013b)), only the reduced shear

$$g = \frac{\gamma}{1-\kappa}, \tag{4.2.1}$$

is measurable through observation and not the convergence κ or shear γ individually. Like γ, the reduced shear is a complex number $g = g_1 + ig_2$ and it's components describe the deformations that occur between the source and the image plane. Moreover, since the unlensed shape of a background source galaxy is unknown (and not circular), the measured ellipticity observed on the sky is

$$\epsilon = \epsilon_{\rm int} + Gg \tag{4.2.2}$$

where $\epsilon_{\rm int}$ is the intrinisic ellipticity of the source galaxy, g is the reduced shear, and G is the shear

'susceptibility' or 'responsivity' factor(Rhodes et al., 2000). The measured ellipticities do not usually change linearly with an applied shear. The shear responsivity factor encodes how these ellipticities respond to a small shear, allowing for an unbiased estimator of the reduced shear.

It is possible to measure the mean reduced shear in a patch of sky, by averaging galaxies' apparent shapes ϵ, under the assumption that their intrinisic shapes are randomly oriented, i.e. $\langle \epsilon_{\rm int} \rangle \approx 0$ (and after applying a correction for their shear susceptibility).

$$\langle g \rangle = \left\langle \frac{\epsilon}{G} - \epsilon_{\rm int} \right\rangle \approx \frac{\langle \epsilon \rangle}{\langle G \rangle} \tag{4.2.3}$$

In the weak lensing limit $\kappa \ll 1$, the reduced shear approximates the shear itself $g \approx \gamma$. Although the galaxy-scale lenses we are interested in are *not* in the weak lensing regime, we assume this approximation still holds since the vast majority of line of sights within the surrounding patch of sky will not be strongly lensed. Thus, the weak lensing shear measurements are statistical in nature, limited by the randomness in the distribution of the unknown intrinsic ellipticites termed 'shape noise'.

4.3 Data

4.3.1 Mock sample of galaxies

We shall compare the results from observations to a strong lensing analysis of a mock sample of 50 lens galaxies, generated to be well representative of SLACS lenses. The mock sample of lenses were generated by C22 for an investigation into the systematic errors induced by the elliptical powerlaw model in strong lens modelling. The authors give a detailed description of the simulation procedure in Section 2.4. We give a brief overview of the procedure below.

The surface mass density of the lens galaxy is described by two components: a dark matter halo, parameterised by the spherical generalised Navarro, Frenk & White (gNFW) profile (Cappellari et al., 2013), and; visible stellar matter, parameterised by a Multiple Gaussian Expansion (MGE) (Cappellari, 2002). The model parameters of the gNFW and MGE profiles of each lens galaxy are set to the best-fit parameters from fits of these distributions to SDSS-MaNGA stellar dynamics data, derived by Li et al. (2019) using the Jeans Anisotrpoic model (JAM) method. The position angle of each Gaussian component in the MGE is fixed, however their axis ratios are free to vary allowing for elliptical gradients in the mass distribution.

The light distribution of the source galaxy is modelled by a single Seŕsic profile (Graham & Driver, 2005) with effective radius $R_{\rm eff} = 0.15''$, Seŕsic index $n = 1$, axis ratio $q = 0.7$. The position in the

source plane (x_s, y_s) is drawn from a Gaussian distribution with mean $0''$ and standard deviation $0.1''$, and the position angle is uniformly selected between $0° - 180°$. The light from the source galaxy is ray-traced from the source plane to the image plane through the lens equation (equation 1.4.3), to simulate it's lensed appearance. Further, to mimic observational effects, the image is convolved with a Gaussian PSF with $0.05''$ standard deviation, and sampled by $0.05''$ square pixels. A flat background sky of 84 electrons per second is added, as well as Poisson noise. The signal to noise ratio of brightest pixel in the synthetic images is set to ~50, by adjusting the intensity of the Sérsic source accordingly. No external shear was simulated in the mock data sample.

4.3.2 Observed sample of galaxies

In this chapter, we choose to analyse the 42 SLACS and 15 GALLERY lenses that our automated analysis reliably fits without residuals (see chapter 2). These correspond to the combined 'Gold' and 'Silver' samples. On these galaxies, we will be running another strong lensing pipeline and analysing the wide-field images with a weak lensing analysis. The imaging data on which we perform the weak lensing analysis was reduced as described by (Tam et al., 2020) and the final spatial resolution is 0.03".

The weak lensing procedure will be applied to the SLACS lenses for which, unlike the GALLERY sample, higher wavelength imaging is available. We necessarily remove the lenses J1143-0144 and J1420+6019 from the sample, which due to telescope scheduling issues only have one exposure available. As a result, the final reduced images are not deep enough to detect sufficient background sources for the weak lensing analysis. The remaining 39 SLACS lenses make up our weak lensing sample.

4.4 Method

4.4.1 Weak Lensing analysis

The shapes of galaxies in the HST/ACS imaging mosaic, identified with the SExtractor photometry package (Bertin & Arnouts, 1996), were measured using the shape measurement method of Rhodes et al. (2000), implemented in practice as `PyRRG` code by (Harvey et al., 2019). This measures the apparent ellipticity and shear susceptibility of every galaxy from its weighted multipole moments, correcting them for blurring by the point spread function (PSF) using the `TinyTim` model Krist (1993). More details of the source detection and weak lensing shape measurement procedures are given by Tam et al. (2020).

We calculate the weak lensing shears averaged inside radii of 45, 60, and 90 arcseconds from the centre of the strong lens galaxy (no weights are applied to the galaxies that are averaged). For brevity we present only the results within an aperture of 60″, which on average include contributions from ∼140 galaxies. The uncertainties on the weak lensing shears are similar to those on the strong lensing measurements when averaged within this aperture. We have confirmed that the results do not change significantly if a different aperture is used.

When averaging over N galaxies that are all subject to the same shear, the uncertainty on the measured distortion from the true shear is $\sigma_{\rm int}/\sqrt{N}$, where $\sigma_{\rm int}$ is the standard deviation of the intrinsic ellipticity. For the weak lensing measurements made within 60" we individually measure $\sigma_{\rm int}$ and the corresponding RMS uncertainty on each component of shear for the 39 lenses. As expected from the literature we measure $\sigma_{\rm int} \sim 0.3$ (Leauthaud et al., 2007), which for each lens leads to an RMS uncertainty of ~ 0.02 on each component of shear.

Although we will measure the shear due to the PL mass profile of the strong lens galaxy, we choose not to subtract this shear measurement from the weak lensing shear measurements. Our investigations into the external shears of the strong lens models will also have implications on the mass model parameters and their associated shear. It is therefore unclear if we would be removing the correct amount of shear upon subtraction from the weak lensing measurements. To avoid this, we will simply compare the weak lensing shear parameters that include the shear from the strong lens to the external shears from strong lensing. We will keep this in mind when making inferences from these results.

4.4.2 Strong Lensing analysis

The strong lens analysis, performed on both the observed and mock data images, was carried out using the strong lens modelling software `PyAutoLens` described in detail by Nightingale et al. (2018). As described in Chapter 2, `PyAutoLens` uses a technique termed 'non-linear search chaining' to compose pipelines capable of fitting complex lens models by initially fitting simpler models, that gradually increase in complexity. Each individual model fit is performed using the nested sampling algorithm `dynesty`, which determines the posterior probability distributions of the model fit parameters. The results of a single `dynesty` search are used to construct informative priors that are passed to subsequent model fits, guiding the non-linear search towards the highest likelihood lens models. Details of the pipelines constructed to fit the observed and mock data samples are given in section 2.4 and C22, respectively.

Ultimately, we model the distribution of mass in both real and mock data using an elliptical power law (equation 1.4.14) plus external shear (equation 1.4.16). We model the distribution of light in the lens

galaxy (for the real data only) using a double Sérsic profile, and for the source galaxy using an adaptive Voronoi mesh. C22 performed two model fits on the mock data sample; one which reconstructs the source galaxy on an adaptive voronoi mesh, and one that models it as an elliptical Sérsic profile. In this chapter we will analyse the results from the elliptical Sérsic model fits. Since the mock data were simulated with a Sérsic source for the light galaxy these models can perfectly describe the source. Thus, any systematics we observe will be solely due to the mismatch in the assumed model of the mass distribution from that of the underlying truth, which is the point of interest in this chapter.

We further perform a strong lensing analysis that assumes the deflection of light is a result of only the power-law distribution of the lens galaxy. The procedure for this analysis applied to the observed and image data is identical to the pipelines described in the previous paragraph but without the parameters for external shear.

4.4.3 Multipole fitting

In Section 4.5.2 we will investigate if the strong lensing external shears depend on elliptical deviations of the mass profile. Specifically, we will quantify the *multipole* deviations of two types of contour; the iso-convergence contour at $\kappa = 1$ of the gNFW+MGE mock mass distributions, and the critical curves of both the mock galaxies and the observed galaxies. These contours are stored as a 2D array of points in polar coordinates $[\phi_{\rm contour}, R_{\rm contour}]$. We calculate the deviations of the contour from the true ellipse

$$R_{\rm el}(\phi) = \frac{b}{\sqrt{1 - \epsilon \cos^2(\phi - \phi_{\rm el})}}, \tag{4.4.1}$$

where b is the minor axis, $\phi_{\rm el}$ is the major axis orientation, and ϵ is the eccentricity. The deviations are then parameterised using multipoles

$$\delta R_m(\phi) = \sum a_m \cos(m(\phi - \phi_{\rm el})) + b_m \sin(m(\phi - \phi_{\rm el}))\,, \tag{4.4.2}$$

where m is the order of the multipole, and a_m and b_m are the magnitude of the deviations with symmetry along or at 45° to the major and minor axes, respectively. We then perform a non-linear search to fit the model

$$R(\phi) = R_{\rm el}(\phi) + \delta R_m(\phi), \tag{4.4.3}$$

to the radial values of the contour. We assume uniform priors on the free parameters in the fit over a reasonable range and fit for them using the nested sampling algorithm `dynesty`. We assume the

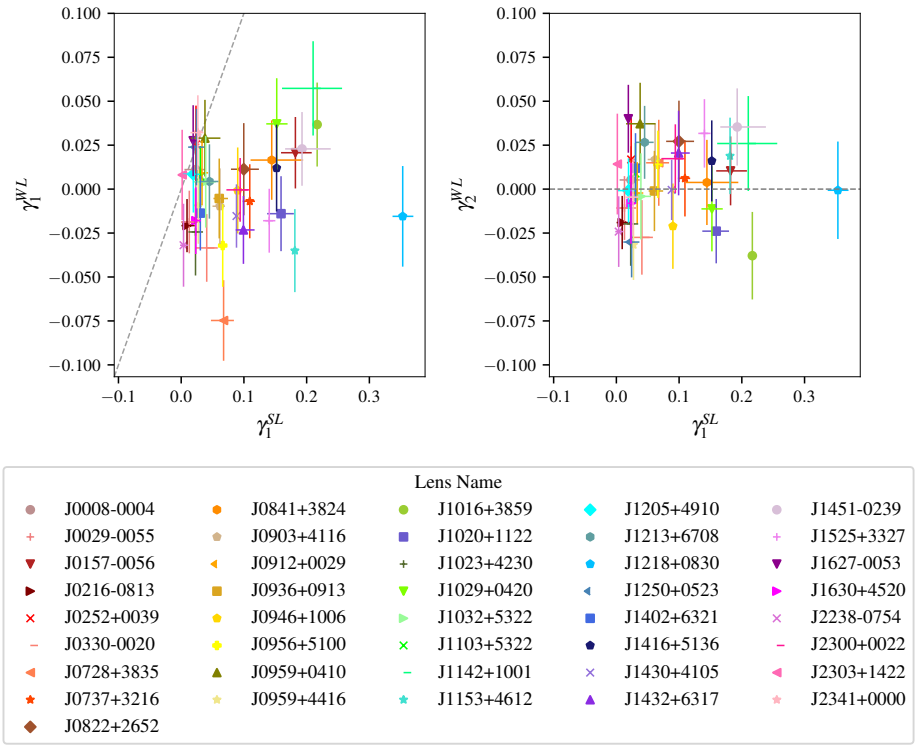

Figure 4.1: Measurements of weak lensing shear components $(\gamma_1^{\rm WL}, \gamma_2^{\rm WL})$ as a function of the inferred strong lensing shear component $\gamma_1^{\rm SL}$. To aid comparison, all shear components have been translated by the inferred strong lensing shear position angle $\phi_{\rm ext}^{\rm SL}$ of each system, such that $\gamma_1^{\rm SL} = \gamma_{\rm ext}^{\rm SL} > 0$, and $\gamma_2^{\rm SL} = 0$. The external shears inferred by strong lensing are consistently larger than those inferred by weak lensing.

residual errors can be described by a Gaussian distribution and maximise the likelihood

$$\mathscr{L}(R, \sigma | R_i) = \prod_i \frac{\exp\left[-\frac{(\mathrm{R}(\phi_\mathrm{i}) - \mathrm{R_i})^2}{2\sigma^2} \right]}{\sqrt{2\pi\sigma^2}}, \tag{4.4.4}$$

where R_i are the radial values of the contour and $R(\phi_i)$ are the model predicted values from equation 4.4.3 at each angular coordinate in the contour ϕ_i. The uncertainty σ on the contour's radial values is ill-defined since, at least in the case of the mock sample, the values are just known quantities. We therefore set this arbitrarily to 0.02 which is approximately equal to the pixel scale of the sub-grid that the contours are calculated on.

4.5 Results

4.5.1 Do the external shears from different regimes agree?

We wish to compare the external shear components inferred by the strong lensing analysis $(\gamma_1^{\rm SL}, \gamma_2^{\rm SL})$ with the shear components inferred from weak lensing $(\gamma_1^{\rm WL}, \gamma_2^{\rm WL})$. We will first use symmetries to

reduce these four numbers to just three in order to aid the comparison. This will require fewer plots to portray the necessary information. We rotate the shear components by an amount corresponding to the inferred strong lensing shear position angle for each lens system $\phi_{\rm ext}$. This transformation orients the strong lensing shears such that all $\gamma_1^{\rm SL}$ components are positive and equal to the inferred external shear magnitude $\gamma_1^{\rm SL} = \gamma_{\rm ext}^{\rm SL}$, and all $\gamma_2^{\rm SL} = 0$. If the methods are detecting shears with a similar strength and orientation, then we expect a correlation between the $\gamma_1^{\rm SL}$ and $\gamma_1^{\rm WL}$ components, and $\gamma_2^{\rm WL}$ to be scattered around zero. As can be seen from Figure 4.1, which plots the inferred weak lensing shear components as a function of $\gamma_1^{\rm SL}$, this is not the case.

The second components of the inferred weak lensing shears have a mean consistent with zero $\langle\gamma_2^{\rm WL}\rangle = 0.003 \pm 0.003$, where the error is the standard error on the mean. However the large scatter (0.02) indicates that the weak lensing shears are not consistently aligned with those inferred by the strong lensing analysis. Further, we do not infer a significant correlation between the first components of strong and weak lensing shear. We perform a linear fit ($\gamma_1^{\rm SL} = m\gamma_1^{\rm WL}$+c) to shears inferred from strong lensing and weak lensing, taking into account only the larger weak lensing errors, which infers a gradient of $m = 0.05 \pm 0.07$. Similarly, the Pearson correlation coefficient inferred is 0.17 ± 0.30.

Notably, the external shears inferred by strong lensing are significantly larger than those inferred by weak lensing. This is despite the fact that the shears measured from weak lensing have not had the shear component from the strong lens subtracted, implying the discrepancy may be even larger than we measure here. The mean difference between the inferred $\gamma_1^{\rm SL}$ and $\gamma_1^{\rm WL}$ components is $\langle\gamma_1^{\rm SL} - \gamma_1^{\rm WL}\rangle = 0.08 \pm 0.01$, and the mean difference between the inferred shear magnitudes is $\langle\gamma_{\rm ext}^{\rm SL} - \gamma_{\rm ext}^{\rm WL}\rangle = 0.06 \pm 0.01$. In fact, the average magnitude of the strong lensing shears for the full SLACS and GALLERY sample $\langle\gamma_{\rm ext}^{\rm SL}\rangle = 0.09$ (9%) is much larger than the typical $\sim 1-3\%$ external shear perturbations expected in the universe (Keeton et al., 1997). In the following sections we investigate the origin of these anomalously large external shears inferred by strong lensing.

4.5.2 Behaviour of strong lensing "external" shears

Mock tests

Despite the mock sample of galaxies being simulated without any external shear perturbations, in their study investigating systematic errors pertinent to the power-law profile, C22 demonstrated that the PL+ext model consistently inferred an external shear with an average of $\langle\gamma_{\rm ext}^{\rm SL}\rangle = 0.015$ shear magnitude. The authors revealed that the inferred external shears could be attributed to the lens galaxy, an "internal" shear, that results from the shears ability to mimic the deviations from elliptical

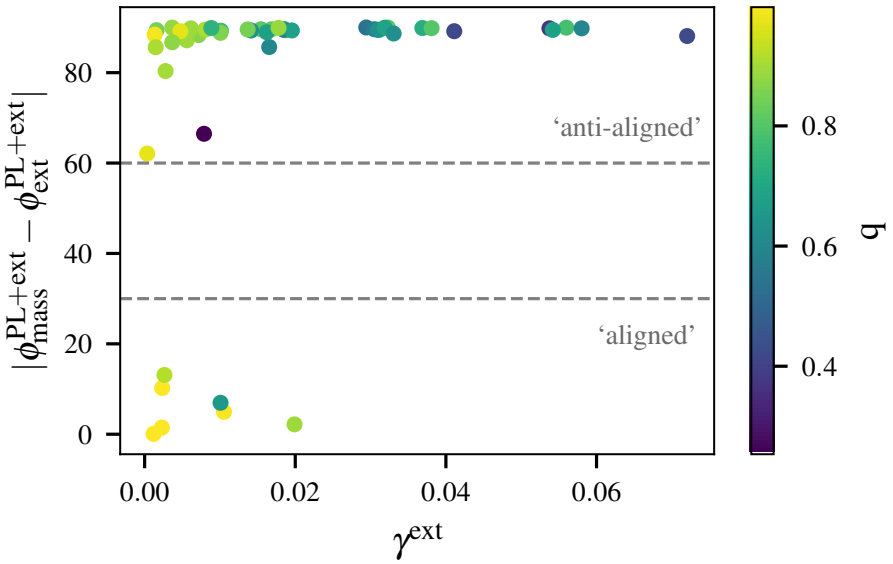

(a) Mock sample of lenses

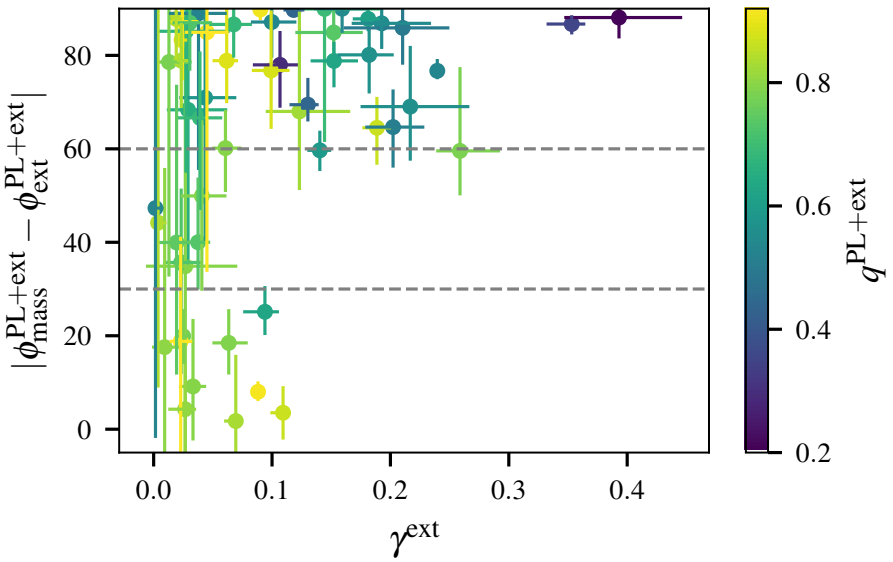

(b) SLACS and GALLERY lenses

Figure 4.2: Difference between the orientation angle of the mass distribution and the shear ($\phi_{\rm mass}^{\rm PL+ext} - \phi_{\rm ext}^{\rm PL+ext}$) as a function of inferred external shear magnitude ($\gamma_{\rm ext}$) for the mock (a) and real (b) lenses. The grey dashed lines delineate the regions where we classify the shears as 'aligned' (0° – 30° offset) and 'anti-aligned' (60° – 90° offset) with the mass distribution The points are coloured by the inferred axis ratio of the fitted power-law mass distribution. For both samples the mass distribution is typicallly more elliptical when higher external shear is inferred.

symmetry that are present in the true underlying (gNFW+MGE) mass distributions of the mock galaxies. In this work, we extend these results by investigating how these internal shears behave, and compare them to the unusually large strong lensing shears inferred in observations of real galaxies.

We find that the internal shears inferred in the mock data can be separated into two groups with very little scatter (top Figure 4.2 a): some aligned with the major axis of the mass distribution, and those perpendicular ('anti'-aligned) to it. We will classify the external shears as 'aligned' with the mass distribution when the angular offset lies between $0^\circ \leqslant \phi_{\rm mass}^{\rm PL+ext} - \phi_{\rm ext}^{\rm PL+ext} \leqslant 30^\circ$ (bottom third of Figure 4.2) and 'anti-aligned' with mass distribution when the angular offset lies between $60^\circ \leqslant \phi_{\rm mass}^{\rm PL+ext} - \phi_{\rm ext}^{\rm PL+ext} \leqslant 90^\circ$ (top third of Figure 4.2). Although these classifications are somewhat arbitrary they will be useful in describing the behaviours of the inferred external shears.

Most (85% of) external shears are anti-aligned with the mass distribution with very little scatter; we measure a mean of $\sim 3^\circ$ with a scatter of only $\sim 5^\circ$. The 14% of external shears that are aligned with the mass distribution, have a mean of $\sim 85^\circ$ and a similar scatter of $\sim 6^\circ$. Only one system (2% of the sample) has a best-fit external shear that is neither aligned nor anti-aligned according to our classifications. This system infers the lowest shear magnitude (0.0003) of the whole sample of mock galaxies. We note that for all the measurements of external shear, $\phi_{\rm ext}$ becomes ill-defined and noisy when $\gamma_{\rm ext}$ is low. Thus, we expect the distribution of shear alignments to be noisy in this region; the distinct groupings here are more arbitrary and uncertain. We notice that the inferred axis ratios of the power-law mass distribution tend to decrease (becoming more purple in colour in Figure 4.2) as the inferred external shear increases. We measure a Pearson correlation coefficient of -0.63 between the inferred axis ratios and external shears.

C22 demonstrated that the inclusion of 'external' shear parameters allows a mass model to better represent the deflection of light rays of the true underlying mass profile, and dubbed them 'internal' shears. For an example system, they showed that the critical curve inferred for the PL+ext profile more closely resembled the critical curve of the true underlying profile than any PL alone could (see Figure 6 therein). Therefore, we will now investigate if the true mass profiles deviations from elliptical symmetry can explain the dichotomous behaviour of aligned and anti-aligned 'internal' shears.

One type of deviation from elliptical symmetry is boxiness and diskyness (see Figure 4.4), which is quantified by the fourth order cosine perturbations (a_4 in equation 4.4.2) from a true ellipse. To quantify the boxiness and diskyness of the true mass distributions of the mock galaxies we measure the fourth order multipole deviations of the iso-convergence contour at $\kappa = 1$. This will be close to the Einstein radius, in the region where the lensing fitting procedure is expected to be most sensitive. On average the magnitude of the cosine perturbations are measured to be $\langle |a_4/a| \rangle = 0.01$, two orders

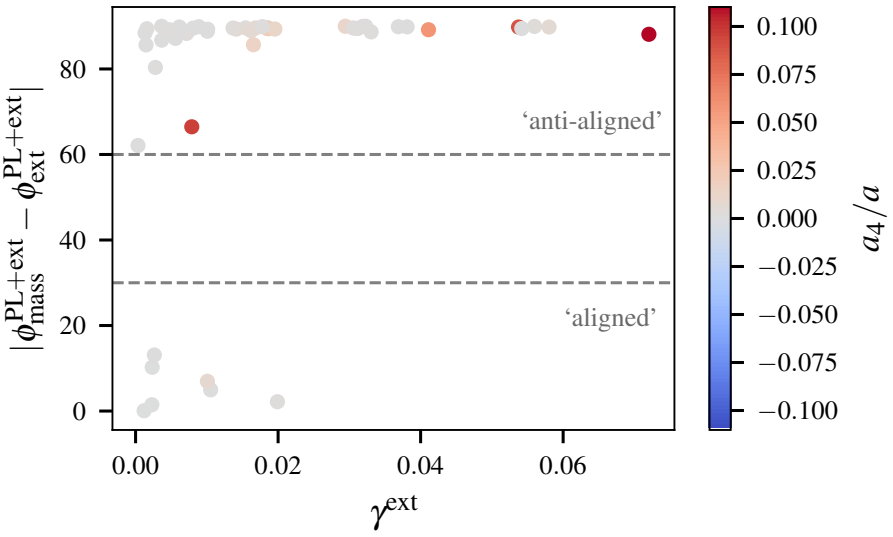

Figure 4.3: Difference between the orientation angle of the mass distribution and the shear ($\phi^{\mathrm{PL+ext}}_{\mathrm{mass}} - \phi^{\mathrm{PL+ext}}_{\mathrm{ext}}$) as a function of inferred external shear magnitude (γ_{ext}) for the mock sample of galaxies that were simulated without an external shear. Points are coloured by the magnitude of the inferred critical curves deviation from elliptical symmetry a_4/a, values of $a_4/a < 0$ correspond to boxy critical curves and $a_4/a > 0$ to disky ones.

of magnitude larger than the average sine perturbations $\langle|b_4/a|\rangle = 0.0005$. Since the b_4 perturbations are almost zero, we consider the measured a_4 perturbations to correspond to pure boxy and disky profiles. We find that the a_4 perturbations typically increase in magnitude with the external shear magnitude, we measure a Pearson correlation coefficient of 0.45. The a_4 perturbations also exhibit a strong correlation with the inferred axis ratio of the galaxy. We measure a Pearson correlation coefficient of −0.73.

The simulation procedure has only produced galaxies with mass distributions that are significantly disky and none that are significantly boxy. Only three galaxies are measured to be boxy ($a_4/a < 0$) and the magnitude of these boxy perturbations $\langle a_4/a\rangle = -0.0003$ are two orders of magnitude smaller than the disky perturbations $\langle a_4/a\rangle = 0.012$. Notably, all mass profiles that are anti-aligned with the inferred external shear measure disky a_4 components (red points in Figure 4.3) in the convergence, and the three mock lenses that are measured to be boxy infer shears aligned with their mass distribution. This may be tentative evidence that the dichotomy of aligned and anti-aligned shears is due to disky and boxy profiles. However, due to the noise and lack of a sample of galaxies with significant boxy perturbations we can not determine from these tests whether such a dichotomy exists.

We will now test if the fourth order perturbations of the mass distribution are well traced by the fourth order perturbations of the critical curve of the lens system. This will become useful in the following section. Consistent with the $\kappa = 1$ results, we do not measure any significant b_4 perturbations in

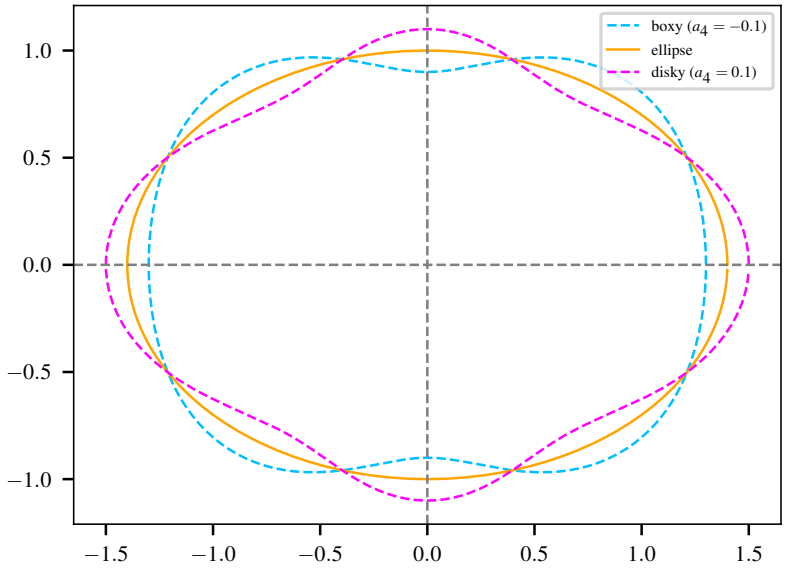

Figure 4.4: Examples of the appearance of boxy (blue dashed curve) and disky (pink dashed curve) deviations from a true elliptical contour (orange curve). Both the boxy and disky curves are 'pure' meaning that $b_4 = 0$ in equation 4.4.2 and they have the same magnitude $|a_4| = 0.1$ deviations. When a_4 is negative the deviations are classified as boxy and when a_4 is positive they are disky.

the critical curve - the average magnitude is $\langle |b_4/a| \rangle = 0.0001$. The majority of a_4 perturbations measured in the critical curves are captured well by the perturbations in the mass distribution (see Figure 4.5). In particular, for the mass distributions that are significantly disky, the a_4 perturbations measured from the critical curves are strongly correlated with those measured from the convergence. However, we did not measure any significantly boxy distributions in the iso-convergence contour, and yet we measure two systems with boxy perturbations $a_4/a < -0.01$ that are much greater than their perturbations measured in the mass distribution. With such few galaxies measured to be boxy in the $\kappa = 1$ convergence contour, we cannot be certain if this is just noise or a systematic bias whereby the critical curve measures boxiness that does not exist in the mass distribution.

Observations from real galaxies

We see a similar distribution of shear alignments for the SLACS and GALLERY lenses as for the mock data, albeit with more scatter (Figure 4.2). The inferred external shears anti-align with the mass distribution 68% of the time, are aligned 20% of the time, and 12% fall into neither category. If the external shears were truly measuring external perturbations, then one would expect a random distribution of shear orientations. The preference for anti-aligning with the mass distribution indicates that inferred external shears may be internal in nature (making up for deficiencies in the ability of the mass model to represent the distribution of mass in real galaxies), like those inferred in the mock data.

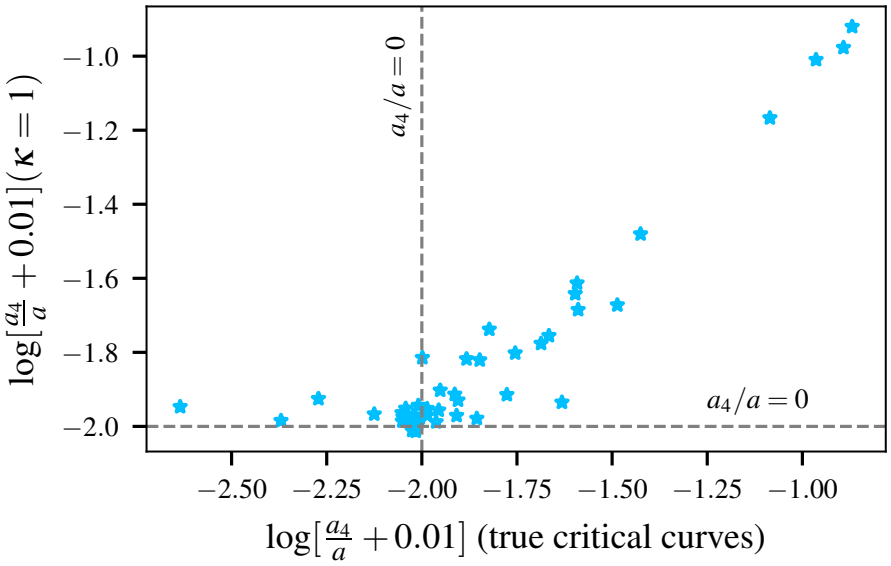

Figure 4.5: Comparison between the a_4/a perturbations as measured from the iso-convergence contour $\kappa = 1$ with those measured from the crticical curves. The values have been transformed by $\log[a_4/a+0.01]$ to better visualise the correlation between the points. The grey dashed lines represent where $a_4/a = 0$ which separates the measurements into boxy and disky perturbations. The disky ($a_4/a > 0$) perturbations in the $\kappa = 1$ contour are well recovered by those measured in the critical curves. This is not the case for the boxy $a_4/a < 0$ perturbations, where the critical curve measures some significantly boxy perturbations whereas $\kappa = 1$ measures none greater than 0.001.

We note that the coherent aligning of galaxies under tidal forces exerted by the same matter structure, such as the matter over-density of a filament in the large scale structure, could cause some preferential aligning of the shear and mass profile. However, these so-called 'intrinsic alignments' are expected to have only a small effect (Blazek et al., 2012).

Notably, at lower shear magnitudes ($\gamma_{\rm ext} \lesssim 0.05$) the shears appear more randomly distributed than at high values, and the 12% of shears that we classify as being neither aligned nor anti-aligned do not exceed 0.04 in magnitude. It may be that these shears are detecting (at least partially) genuine external perturbations to the system. Interestingly, for the subset of galaxies with shear magnitudes less than 0.05 we measure a linear correlation coefficient of 0.5 ± 0.41 between the γ_1 components from strong and weak lensing. Although this correlation is only detected at 1σ significance, this may be tentative evidence that the shears are at least in part measuring external perturbations to the lens. Low values of strong lensing external shears may better represent the true external shear. However, we do not detect a significant correlation between the subset of strong lensing external shears that have $30 < \phi^{\rm PL+ext}_{\rm mass} - \phi^{\rm PL+ext}_{\rm ext} < 60°$ and those inferred by the weak lensing.

In comparison to the mock data sample, the scale of the inferred strong lensing external shears is much larger, measuring an average shear magnitude of 0.09 for SLACS and GALLERY lenses compared to

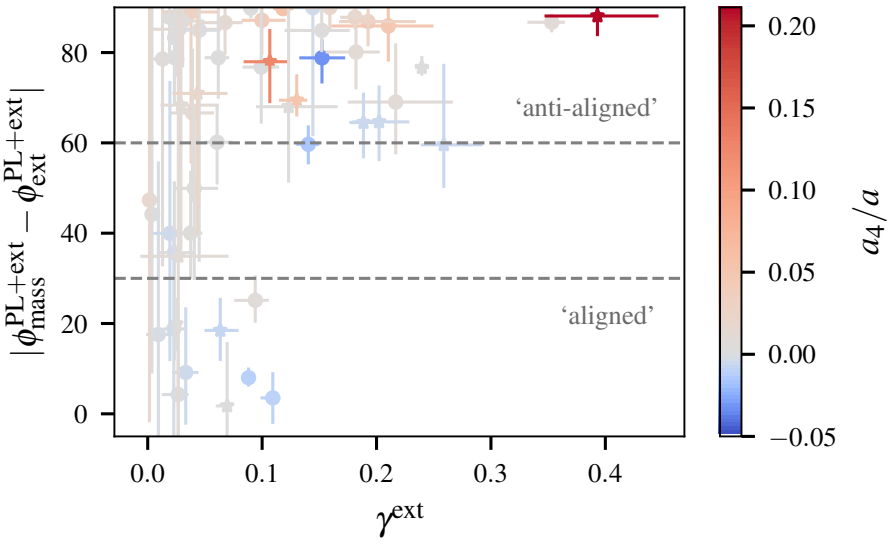

Figure 4.6: Same as for Figure 4.3 but for the observed sample of SLACS and GALLERY lenses. The inferred external shears have a similar distribution of aligned and anti-aligned shears as the mock data sample, indicating they too may be acting internally. Note the increase in the scale of shear magnitude $\gamma_{\rm ext}$ and elliptical deviations a_4/a compared to the mock data sample.

0.015 for the mock sample. This may, in part, be due to genuine external perturbations to the lens system; however, as we demonstrated in Section 4.5.1, there is no correlation between these shears and those detected by weak lensing, as one would expect if this were the case. We instead suspect that these larger shears are in fact larger measurements of internal shear, a result of more complex underlying mass distributions than were simulated in the mock data sample. A similar correlation between the inferred external shear magnitude and axis ratio of the PL mass distribution is present in the observations as in the mock data, we measure a Pearson correlation coefficient of -0.60. Despite the inferred external shears being an order of magnitude larger in the observations than in the mock data, the axis ratios are not significantly smaller. The SLACS and GALLERY lenses infer an average axis ratio 0.69 ± 0.17, compared to 0.77 ± 0.17 in the mock sample.

We now wish to quantify the boxiness and diskyness of the mass distributions of the SLACS and GALLERY lenses. The PL+ext profiles we fitted have profiles that are truly elliptical in the iso-convergence contours, since the external shear is assumed to have zero convergence. However, the external shear *does* perturb the critical curve of the lens system. In the previous section we showed that measurements of the fourth order multipole perturbations of the critical curves do a reasonable job of tracing the perturbations to the mass distribution of our mock sample. We therefore assume measurements of the fourth order multipole perturbations of the PL+ext critical curves tell us something about the elliptical deviations of the true underlying mass profile, although we note this may break down for boxy mass distributions.

Unlike the mock data sample the multipole perturbations are not typically *purely* boxy and disky ($b_4 = 0$); the sine perturbations in real galaxies are similar in magnitude $\langle|b_4/a|\rangle = 0.012$ to the cosine perturbations $\langle|a_4/a|\rangle = 0.016$. The b_4 perturbations are two orders of magnitude larger in the observations than they are in the mock data sample.

In the previous section we proposed that the alignments of the shears with the mass distribution could be being driven by boxy and disky underlying mass distributions. From our measurements of a_4/a in the critical curves the orientations of the inferred external shears with the mass distributions do not appear to be due solely to boxy and disky profiles (see Figure 4.6). However, for the majority (79%) of the galaxies with shears that anti-align with the mass distribution we do measure disky critical curves, and for the majority (70%) of the shears that are aligned with the mass distribution we measure boxy critical curves. Moreover, the largest perturbations occur for the shears that anti-align with the mass distribution, and these tend towards the largest external shears that are inferred. We measure Pearson correlation coefficient of 0.48 (0.65) between the a_4 (b_4) perturbations and the shear magnitude.

We note that for the PL+ext profile to produce critical curves that are not true ellipses, three parameters control the deviations from a true ellipse; the density profile slope, and the two parameters of shear. We demonstrate how these deviations from an SIE critical curve (which is a true ellipse at the Einstein radius) appear when changing the slope and shear parameters in Figure 4.7. Therefore one would possibly expect the shear to correlate with the measurements of a_4/a that also represent a deviation from a true elliptical contour. However, the shear is a second order perturbation, and clearly does not perturb the critical curve in the same manner as which the a_4 parameter does in Figure 4.4. Thus, it is somewhat surprising that the shear, in combination with the slope, is producing measurable fourth order perturbations to the critical curves. Further, the difference of the inferred slope from being isothermal is not as strongly correlated with the perturbations as the shear magnitude is. We measure a Pearson correlation coefficient of 0.02 and 0.21 for the a_4 and b_4 perturbations respectively, suggesting the shear plays a stronger role in causing the fourth order perturbations than does the slope.

Similar to the mock data sample, we find that the fourth order perturbations increase the more elliptical the mass distribution is inferred to be. We measure a correlation coefficient of -0.70 and -0.66 between the axis ratio and the a_4 and b_4 perturbations respectively. Although, given the degeneracy between the shear and the axis ratio, and the aforementioned correlation of the shear with the fourth order perturbations, it is difficult to determine if more elliptical galaxies are inherently more boxy/disky.

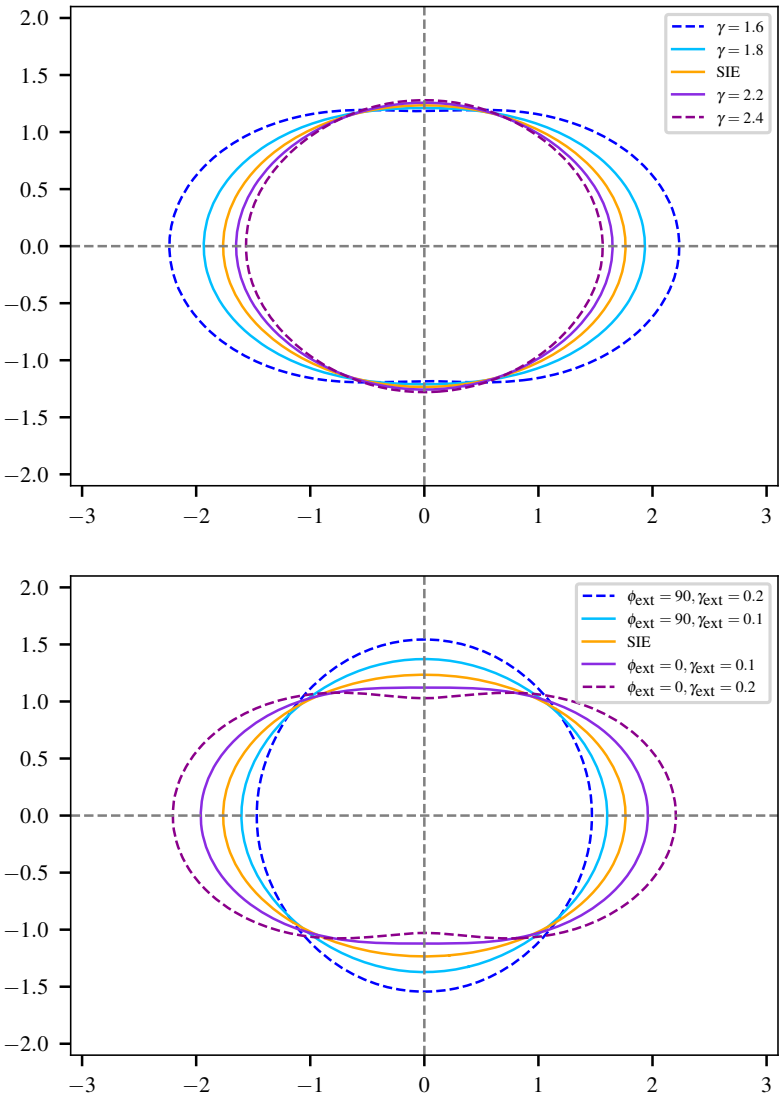

Figure 4.7: Appearance of deviations from the truly elliptical SIE critical curve by changing the slope of the density profile (top panel) or the shear parameters (bottom panel.)

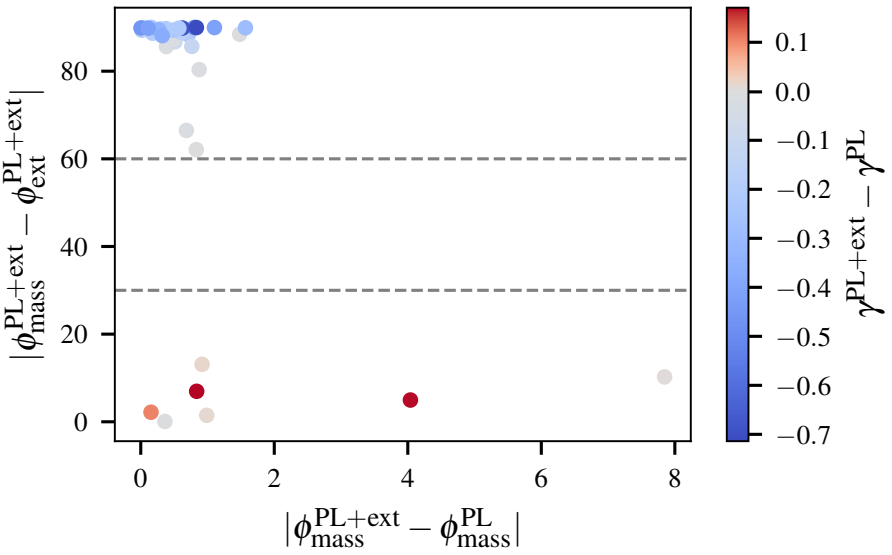

Figure 4.8: Orientation angle offset of the external shear from the PL+ext mass distribution ($\phi_{\rm mass}^{\rm PL+ext} - \phi_{\rm ext}^{\rm PL+ext}$) as a function of the difference in orientation angle when the mass distribution is fitted with and without an external shear ($\phi_{\rm mass}^{\rm PL+ext} - \phi_{\rm mass}^{\rm PL}$) for the mock data sample. Scatter points are coloured by the difference in power-law slope inferred between the models fitted with and without an external shear ($\gamma^{\rm PL+ext} - \gamma^{\rm PL}$). Systems that have shears that are anti-aligned with the mass distribution when the model includes an external shear systematically increase in power-law slope when the external shear is removed from the model (blue points). Aligned shears exhibit the opposite behaviour (red points).

4.5.3 Inference without shear parameters

Mock tests

To gain further insight into the significance of the external shear parameters, we compare the values of other parameters we infer for the power-law mass distribution, with and without the assumption of external shear. We do this first for the mock sample of galaxies. The orientation angle of the power-law is measured consistently, the average difference between inferred orientation angles with and without shear is $\langle \phi_{\rm mass}^{\rm PL+ext} - \phi_{\rm mass}^{\rm PL} \rangle \sim 1^\circ$ with only $\sim 1^\circ$ of scatter. However, the slope of the power-law distribution changes systematically depending on the alignment of the shear with the mass distribution. For shears that are anti-aligned, removing the external shear parameters from the model increases the best-fit power-law slope (red points in Figure 4.8). Whereas, for shears that prefer to align with the mass distribution their inferred power-law slope decreases when the shear parameters are removed from the fit (blue points in Figure 4.8).

Notably, due to the degeneracy between slope and Einstein radius, a similar systematic behaviour occurs for the inferred Einstein radii, although at a much lower level. For the aligned shears the Einstein radii decrease by $-0.08 \pm 0.1\%$ on average when the shear parameters are removed from

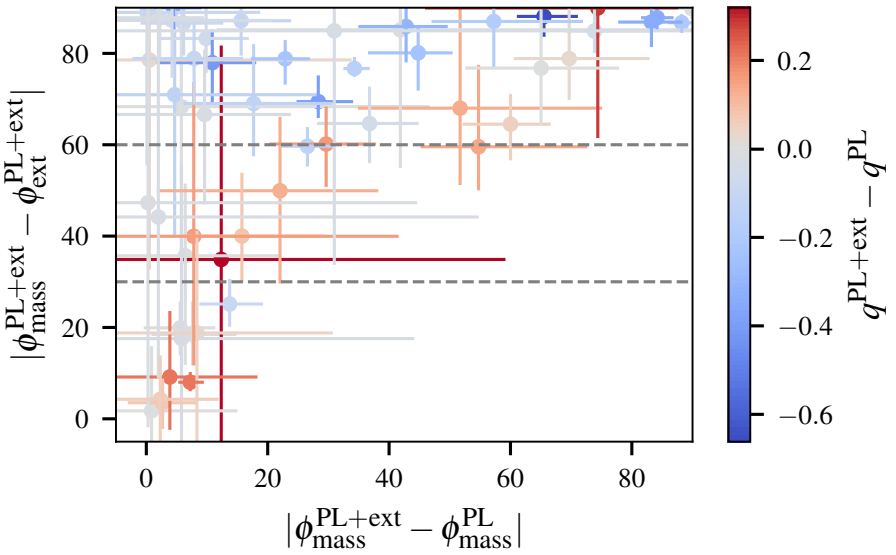

Figure 4.9: Orientation angle offset of the external shear from the PL+ext mass distribution ($\phi_{\rm mass}^{\rm PL+ext} - \phi_{\rm ext}^{\rm PL+ext}$) as a function of the difference in orientation angle when the mass distribution is fitted with and without an external shear ($\phi_{\rm mass}^{\rm PL+ext} - \phi_{\rm mass}^{\rm PL}$) for the observed SLACS and GALLERY samples. Scatter points are coloured by the difference in axis ratio of the models fitted with a PL+ext and a PL ($q^{\rm PL+ext} - q^{\rm PL}$).

the model, and the anti-aligned shears increase by $0.2 \pm 0.3\%$. C22 demonstrated that the Einstein radius of the true underlying mass distributions could be well recovered by the PL+ext models, with a relative systematic error of only $0.05 \pm 0.17\%$. For the models fitted without any external shear parameters in this work, we find that the relative systematic error is $-0.2\% \pm 0.4\%$. Although the true Einstein radii are still well recovered when we do not include an external shear in the model, the systematic error is four times greater than when one is included. The assumption of external shear appears to allow the model to better recover the true Einstein radius. We note that, despite there too being a degeneracy between shear and ellipticity, the axis ratio of the models with and without shear do not exhibit the systematic behaviour that we observe for the slope and Einstein radius parameters. The mean difference in the inferred axis ratio for the PL+ext and the PL models is 0.01 ± 0.05.

Observations from real galaxies

The PL+ext and PL models are less consistent for real SLACS or GALLERY data, than they were for mock data. First, the orientation angle of the mass distribution is no longer recovered consistently by the two models, with a mean difference $\langle \phi_{\rm mass}^{\rm PL+ext} - \phi_{\rm mass}^{\rm PL} \rangle \sim 27°$ and scatter $\sim 27°$ (note the difference in scale in the x-axis between Figures 4.8 and 4.9). We suspect this result is an indication that the underlying mass distributions are more complex than those that were simulated for the mock sample of galaxies. The mock systems were simulated with a spherical gNFW plus an MGE with gaussian

components that are fixed to the same position angle. Hence, there is a well defined position angle for these systems that the model accurately recovers (to within $\sim 1^\circ$ on average) regardless of the assumption of external shear. This is likely not the case for the SLACS and GALLERY systems: if real galaxies consist of multiple elliptical components that are rotationally offset from one another then this could explain the large increase in the mean difference (and scatter) of the orientation angle for the PL+ext and the PL models in the observed data compared to the mock data.

In the mock galaxies we saw that when the external shear parameters were removed from the fit there was a systematic steepening of the power-law slope for galaxies that had shears that were anti-aligned with the mass distribution, and a systematic shallowing of the slope for those that had shears that were aligned with the mass distribution. This systematic behaviour of the power-law slope does not appear to be present in the SLACS and GALLERY samples. There is, however, a reasonable amount of scatter in the best-fit slopes of models with and without external shear (the mean difference is $\langle \gamma^{\rm PL+ext} - \gamma^{\rm PL} \rangle = -0.09 \pm 0.28$). Although the slopes do not appear to change systematically, at least not in the same way as we observe in the mock data, they are not consistently recovered for the two models we fit with and without external shear parameters.

Instead, the dominant behaviour we observe in the real lenses is a change in *axis ratio* of the power-law mass distribution when the external shear is removed from the model (see Figure 4.9). On average, the systems that infer shears that align with the mass distribution become more elliptical, decreasing the axis ratio by -0.18 ± 0.016, without the assumption of external shear (bottom third of Figure 4.9). Whereas, the systems that infer shears that anti-align with the mass distribution tend to become more spherical, increasing in axis ratio by 0.08 ± 0.10, when the assumption of external shear is removed (top third of Figure 4.9). The systems that are neither aligned nor anti-aligned do not show consistent systematic behaviour, with exactly half of them increasing in axis ratio and the other half decreasing when the external shear is removed from the fit – the average change in axis ratio is -0.02 ± 0.04 for these systems.

The Einstein radii of the PL+ext and PL models do not appear to change systematically for the SLACS and GALLERY samples. In the mock tests the Einstein radii systematically increased (decreased) for the sample of lenses that inferred shears that were aligned (anti-aligned) when the shear parameters were removed from the fit. This behaviour is not observed in real galaxies. However, the scale of the fractional differences inferred in SLACS and GALLERY samples is an order of magnitude larger than in the mock sample, with a root mean square (RMS) fractional difference of 4.5% compared to 0.03%. Notably, although there does not appear to be a strong linear correlation between the fractional difference of PL+ext and PL Einstein radii and the shear magnitude, the scatter does appear to increase

with increasing external shear magnitude (see Figure 4.10).

4.6 Discussion

4.6.1 What are strong lensing external shears measuring?

External shear, as measured by strong lensing, does not correlate with the true shear along the line of sight, as measured independently from weak lensing (Figure 4.1). Rather, the external shear is compensating for the lack of azimuthal degrees of freedom in the mass distribution of the lens galaxy (assumed to be a power-law in this work). It appears that in some lenses the missing azimuthal asymmetry is, at least partly, boxiness and diskyness in the mass distribution (Section 4.5.2). However we suspect that isophotal twists, elliptical gradients, and offsets in the centres and alignments of dark and stellar matter components will all contribute to the scatter inferred in the external shear parameters. Although a fraction of the shear will be due to the true shear, the high values that are routinely inferred in the strong lensing analysis demonstrate this can indeed only be a fraction. Moreover, we can not determine what fraction this is.

This result is important for many scientific uses of strong lensing. The external shear parameters are rendered physically meaningless, since they do not solely account for external perturbations to the lens or azimuthal asymmetries of the mass distribution. Furthermore, these parameters are degenerate with other model parameters such as the density profile slope and the Einstein radius. We have shown that the Einstein radius is biased by $\sim 4.5\%$ on average when the shear parameters are removed from the fits to observations (Section 4.5.3). This could have repercussions on studies of galaxy stellar-to-halo mass, the Hubble constant, and other methods that use the Einstein radius as a principle constraint in the models.

The implications of these meaningless external shears are crucial to strong lensing studies, it is critical we understand these results. An important next step in this analysis, which will not be carried out in this thesis, is to perform a control test whereby the mock MGE+NFW data are simulated with an external shear. A set of mock data generated in this way will provide two test cases. First, when they are fitted with the true MGE+NFW+ext profile, i.e. when the model has the correct level of azimuthal complexity, are the external shears recovered correctly? Second, when fitted with a PL+ext profile, what is the behaviour of the inferred external shears? Do they now recover the input external shear, or are they still biased due to the insufficiency of the PL to fit the MGE+NFW profile? This latter test will provide a better comparison to the observed lens galaxy results that by nature have a real external shear component.

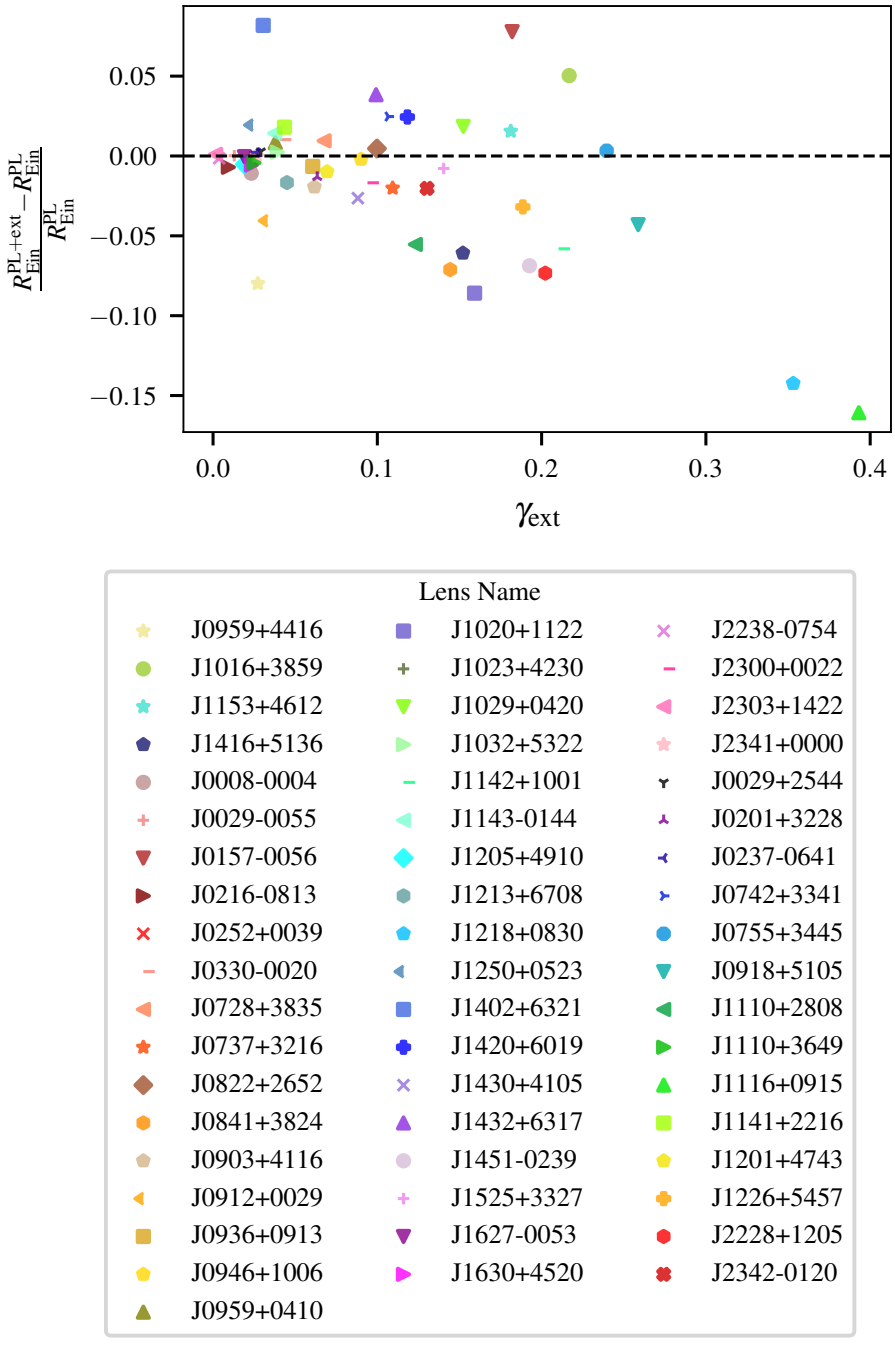

Figure 4.10: Fractional difference between Einstein radii inferred for models with and without the assumption of external shear plotted as a function of the magnitude of the inferred external shear.

4.6.2 Comparison with literature results

The external shears of SLACS and GALLERY lenses inferred from strong lensing are systematically larger than the weak lensing measurements, almost an order of magnitude larger on average (Section 4.5.1). Reaching up to 0.35 at their maximum, these estimates are larger than any external shears one would expect to measure in the universe. This is similar to the result of Keeton et al. (1997), who showed that a sample of four quads prefer models, in a chi-squared sense, with two independent shear axes (the ellipticity of the lens galaxy and an external shear) that require external shear perturbations of $10 - 15\%$ that are larger than shear along typical lines of sight through the Universe of $1 - 3\%$. Our results confirm that these unusually large external shears are inferred for a much larger sample of lenses, persisting when modelling extended light sources. Keeton et al. (1997) suggest this implies the second source of shear must be dominated by the primary lens galaxy and not external perturbations, with misalignments between the light and dark matter components being a possible cause of the extra asymmetry required by the models. Witt & Mao (1997) come to a similar conclusion, stating that the modelling of the lens potential is too simplistic, after deriving an analytical formalism to predict the required amount of shear by an elliptical potential to fit quadruple images. They apply the formalism to 7 quadruple lenses, finding results that are consistent with Keeton et al. (1997).

The PL mass density profile is indeed too simplistic. The inferred external shears show a very similar distribution of shear alignments in the observed data as they do in the mock data (Figure 4.2). Since the external shears in the mock data sample can only be due to the primary lens, being simulated without any external shear, the similarity of these results suggests the external shears inferred for the SLACS and GALLERY lenses are also internal in nature.

The 'internal' shears in the mock data sample result from the inability of the PL to represent the azimuthal asymmetries present in the gNFW+MGE mass distribution, as demonstrated by C22. Since the elliptical components of the MGE profile are allowed to vary in axis ratio when fitting to the MaNGA data, elliptical gradients are present in the convergence profiles of the mock data sample that can not be modelled by the PL alone. The consequences of elliptical gradients in lens modelling has since been further quantified by Van De Vyvere et al. (2022b). In their study, they created mock data with slices of decreasingly elliptical convergence at different radii and an external shear. When fitting these data with a a PL+ext model, they find the inferred external shears increase in magnitude by 0.01 and change in orientation by $11°$, relative to the fiducial case, when the elliptical gradients are outside the Einstein radius. Elliptical gradients inside or at the Einstein radius were found to mainly affect the recovery of the density slope, a result anticipated by Kochanek (2020).

We provide further evidence for the bias described by Kochanek (2020). When we remove the

external shear parameters from the model fit, reducing the azimuthal degrees of freedom, we observe a systematic change in the density profile slope (Figure 4.8). More generally, this means that the radial information in a lens can be incorrectly constrained by the angular structure of the gravity, if too few degrees of freedom are assumed for the model of the angular structure itself. Kochanek (2020) provides the example of fitting a PL model to a lens that increases in ellipticity with radius forces the density slope to shallower values to balance out the shear inside the Einstein radius relative to the shear outside of it. With this in mind, the results of the mock sample fits with and without an external shear suggest that the shears that align with the mass density profile correspond to underlying mass distributions that radially increase in ellipticity, and those that are anti-aligned radially decrease (see Figure 4.8). Although we did investigate a number of quantities derived from the axis ratios of the MGE components, we were unable to confirm that this is the underlying cause of the shear alignments.

Another possible deviation from elliptical symmetry that could falsely infer external shear is boxiness and diskyness in the mass distribution. We measured a_4 components in the convergence contours of our mock data and the critical curves of real galaxies that correlate with the external shear magnitude, implying these types of perturbations - like elliptical gradients - can too be absorbed by the shear parameters. Van De Vyvere et al. (2022a) found that this was only the case when the lens mass is aligned with the multipole, as it is in our mock data, and not for other test cases when they fitted an SIE+multipole+ext with an SIE+ext profile. Therefore, we suspect boxiness/diskyness is not the *only* type of elliptical deviation that causes the inference of external shear, although it evidently plays a role.

4.6.3 Evidence for extra complexity in real galaxies

The mass profiles of the SLACS and GALLERY sample appear to be more complex than was simulated in the mock data. The observations from real galaxies point towards twists in the mass distribution – multiple mass components that are rotationally offset from one another. The mock data inferred only cosine (boxy/disky) perturbations a_4 in the mass distribution, whereas the observations inferred both cosine a_4 and sine b_4 perturbations (as measured from the inferred PL+ext critical curve). Further, the lack of a consistently measured position angle when the observations are fitted with and without an external shear (see Figure 4.9) suggests some sort of twisting that is not present in the consistently measured position angles of the mock data. Van De Vyvere et al. (2022b) found that twists in the underlying mass distribution are typically absorbed by changes in orientation of the mass distribution and shear in a PL+ext profile, which supports our hypothesis that the changes in orientation are due to these type of features present in the data.

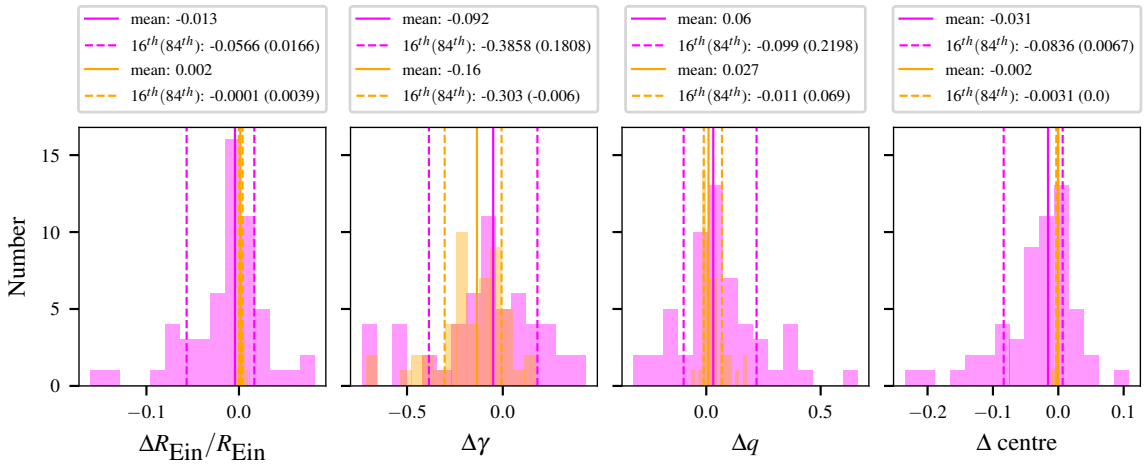

Figure 4.11: Histograms of the difference between inferred PL mass distriction model parameters with and without shear included in the model fit for the observed (pink) and mock data samples (orange). From left to right panaels the parameteers are: fractional Einstein radius, density profile slope, axis ratio, radial distance of the centre of the mass distribution.

The mean difference and scatter of PL parameters inferred with and without an external shear is larger in the observations for all but the slope parameter (see Figure 4.11) – another indication of extra complexity in the observations. Notably, the slopes inferred for the mock data fitted with an external shear better recover the global slope of the true underlying mass distribution, defined as the mass weighted density slope within the Einstein radius (equation 3.5.1), than the slopes inferred from fitting a PL alone. The mean difference is -0.017 ± 0.102 compared to -0.142 ± 0.196 when the shear is removed from the fit. As discussed in Section 4.5.3 the Einstein radii, although well recovered, are slightly better recovered when the external shear parameters are present in the fit. These results suggest the external shear parameters may have added sufficient angular degrees of freedom to account for the azimuthal asymmmetries present in the gNFW+MGE profiles that were simulated. However, the false inference of external shear remains problematic for methods that aim to use strong lensing to measure cosmic shear (e.g. Birrer et al., 2017; Fleury et al., 2021). Hogg et al. (2022) recently showed that the minimal line-of-sight model, which parametrizes the shear in a way that is less degenerate with lens model parameters than the conventional method, is also subject to biases in the shear parameters when simplifying assumptions are made for the lens model. We therefore recommend that lens models attribute extra angular degrees of freedom to the lens potential itself.

Although it appears the shear parameters allow for a more accurate recovery of the mass distribution parameters in the mock data, we can not be certain that the PL+ext has sufficient angular degrees of freedom to account for the extra complexity evident in the observed data sample. Two of our results suggest this is likely not the case. First, the centre of the mass distribution moves on average

by $-0.031 \pm 0.061''$ when the shear parameters are introduced in the model, and the centres remain an unphysical $0.05 \pm 0.06''$ from the centre of the light distribution on average. This is an order of magnitude more than is measured in the mock data sample on both accounts. Second, the 4.5% RMS fractional difference on the Einstein radii, a supposed model independent quantity, measured with and without external shear implies something more obscure about the data, one would typically expect to recover the Einstein radius to within $\sim 2\%$ (Bolton et al., 2008b; Sonnenfeld et al., 2013b). Further, since the external shears, which are reaching extreme values in the observations, contribute zero convergence, it is impossible to determine which of these Einstein radii (hence Einstein masses) better represent that of the underlying mass distribution without further testing. Further work (e.g. Cao et al., 2022; Van De Vyvere et al., 2020, 2022b) to understand the types of asymmetries that must be accounted for in the lens modelling, and the possibility of constraining such models, will be invaluable.

4.6.4 Impact on science cases

Accurate models of the mass density profile of galaxies are required for a number of science goals that are attainable through strong gravitational lensing. If, as we suspect, the large external shears inferred in this work are an indication that the PL+ext mass profile is not an accurate description of real galaxies, this could be detrimental to methods that assume this profile as part of the measurement process. We discuss the implications of this for two astrophysical problems that are essential to our understanding of cosmology; the determination of the Hubble constant, and the detection of dark matter substructures.

The power-law mass density profile is often employed in studies that use the time-delay strong lensing technique to infer the Hubble constant H_0 (Wong et al., 2019; Birrer et al., 2019; Suyu et al., 2017). The assumption of a mass-density profile artificially breaks the mass-sheet transformation which, given the invariance of the product of the Hubble constant and the time delay, can lead to systematic biases on the determination of H_0. Studies investigating the bias on H_0 associated with assuming the PL profile vary in their estimates, reaching up to 20-50% (Xu et al., 2016; Gomer & Williams, 2019; Kochanek, 2019; Schneider & Sluse, 2013a). Our mock tests (Section 4.5.3) highlight the coupling between angular and radial structure, described by Kochanek (2020), can significantly effect the slope, and hence the Hubble constant, that is inferred when angular degrees of freedom are removed from the model. Moreover, for a sub-sample of 37 lenses in this mock sample, C22 estimated a bias of $\sim 9\%$ on the Hubble constant using time delays inferred from the PL+ext lens models, demonstrating that the angular degrees of freedom allowed by the external shear are not sufficient to avoid these biases

for gNFW+MGE profiles.

Given that the SLACS and GALLERY observations appear to require more angular degrees of freedom than was simulated in the mock data, such as twists in the mass distribution, we suspect these biases will be stronger for real lensing systems. Indeed, Van De Vyvere et al. (2022b) find that the effect of twists and elliptical gradients in a single lens are just the sum of the effects of the two individually, increasing the biases on the shear orientation and strength, ultimately biasing H_0 up to $10\text{kms}^{-1}\text{MPc}^{-1}$ on an individual lens basis. Interestingly, they found that the azimuthal variations average out at a population level, for two mock samples based on observations and hydrodynamical simulations, allowing for an unbiased estimate of H_0. Van De Vyvere et al. (2022a) found the same result at a population level for biases induced by boxy and disky perturbations to the mass profile. These results require that an overpopulation of a particular subsample of azimuthal asymmetries is not present in the lensing sample to accurately infer H_0. It is not clear this is true of our SLACS and GALLERY lenses, the fourth order multipoles we infer for the PL+ext critical curves suggest an overpopulation of (71%) disky galaxies, although it is unclear how well these represent the perturbations to the underlying mass profiles. Further, we suspect the alignment (and anti-alignment) of the shear with the mass profile is a result of a particular feature in the underlying mass distribution, and we find a preference for anti-aligned shears (70% of the sample). It is plausible these sub-samples would be biased in opposite directions, that would not average out at a population level. Finally, Van De Vyvere et al. (2022a) did not investigate the effect of fourth order sine perturbations b_4, which our results suggest are present in the observed galaxies. Further testing is required to understand if the complexities in the mass distribution of real lenses can safely be ignored in the inference of the Hubble constant, by averaging over the biases on individual lenses.

Biases on an individual lens basis will undoubtedly be problematic for substructure detection, where an accurate macro model for the lens galaxy is key to avoiding false detections and correctly inferring the mass of real detections (He et al., 2022; Nightingale et al., 2022). Given the results of the observed data sample in this work, we suspect more complex mass profiles than the PL+ext will be necessary to accurately describe the macro model of real lens galaxies for these types of analyses. In particular, the large external shears, that we demonstrate to be internal in nature, may be able to account for missing angular structure in the lens galaxy, but the fact they contribute zero convergence (therefore mass) will almost certainly be problematic for a method that is attempting to detect missing mass in the lens model. Indeed, Nightingale et al. (2022) find that increasing the model complexity renders 11 detections with the PL+ext as being false detections, when applying their substructure procedure to 54 SLACS and GALLERY lenses. Further, He et al. (2022) demonstrated that correctly accounting for azimuthal asymmetries in the lens model can avoid false detections and correctly recover the subhalo

mass of a simulated system that appears disky in its convergence projection.

4.7 Summary

By independently constraining the environmental shears of a sample of SLACS lenses with both strong lensing and weak lensing methods we demonstrated that the strong lensing external shears are systematically larger than those inferred by the weak lensing. By comparing these results to those from a sample of mock data generated with complex gNFW+MGE profiles but fitted with a much simpler PL+ext profile, we have shown that this is driven by the strong lensing shears acting internally as opposed to externally. The inferred orientations of the strong lensing external shears show a strong preference (70% of the sample) for being anti-aligned with the orientation of the lens galaxy itself, replicating the behaviour of the spurious external shears inferred in the mock data that were in fact simulated without external shear.

Three results suggest that the underlying mass distributions of the observed SLACS and GALLERY lenses require complex mass models to avoid biases in the inference of model parameters. In particular, we suspect the mass model will require the freedom to produce twists in the mass distribution. First, the magnitude of the inferred external shears are much larger. On average they are six times greater, in the observations than in the mocks. Given the indication that these external shears are internal in nature, this implies the observed sample's mass distributions deviate more from a PL distribution than the mocks do. Although we acknowledge that some of the inference may be due to genuine external perturbations. Second, we measure both a_4 and b_4 perturbations in the observed lenses whereas we only measure significant a_4 perturbations in the mock sample. Finally, the behaviour of the PL orientation angle when the shear parameters are removed from the fit suggests there is not a well defined orientation angle in the observed sample of lenses, perhaps indicative of multiple mass components that are orientationally offset from one another.

We discuss the implication of these results being that we require more complex mass profiles than the PL distribution in order to adequately describe the mass distribution of observed ETGs. Further work is necessary to determine the appropriate form these complex mass profiles would take. One suggestion would be to decompose the stellar and dark matter distributions with constraints from the stellar distribution coming from the light profile of the galaxy itself. It may be that simply including fourth order multipoles to allow for boxiness and diskyness in the mass distribution will be sufficient. Notably, the azimuthal degrees of freedom must be defined appropriately to avoid the bias described by Kochanek (2020) on the radial constraint. This was highlighted in our mock data sample which

showed systematic behaviour on the inferred slope parameter when the shear parameters were removed from the fit. This could be a concern for studies that use the inferred macro model of the lens galaxy to study cosmology by inferring H_0 or searching for substructure. In light of the complexity that the observed data seem to require in this study, we suggest more studies (e.g. Cao et al., 2022; Van De Vyvere et al., 2020, 2022b) to quantify the impact these simplifying assumptions may have on these types of inference are necessary.

These results also allude to the possibility of constraining the boxy and disky populations of ETGs through their mass distribution. The inferred a_4 and b_4 perturbations in the critical curves of the observed data sample and their correlation with the inferred external shear magnitude is an indication that the shear parameters may be in part absorbing azimuthal asymmetries in the mass distribution of this form. Although with the use of mock data Van De Vyvere et al. (2022a) suggest that the detectability of multipole perturbations actually decreases if the shear parameters are able to absorb the multipole structure. However, their work indicates that it should be possible to detect multipole structure in the mass distribution of ETGs. Indeed, if our work is indicative of measurable multipole perturbations in the mass distribution, that trace those in the light distribution, then one could study these populations of galaxies at high redshift with relative ease.

Chapter 5

Conclusion

Despite huge efforts to collect high quality imaging data in ongoing and upcoming surveys, which are forecasted to discover three orders of magnitude more galaxy-scale strong lens systems than have currently been observed, efforts to improve the automation of strong lensing methods capable of exploiting this amount of data have been relatively few and far between. Studies (e.g. Sonnenfeld & Cautun, 2021; Sonnenfeld, 2021a,b, 2022) investigating the prospects of taking advantage of these statistical samples have demonstrated the power of a hierarchical Bayesian analysis to constrain population level parameters of the mass distribution of lens galaxies and also the Hubble constant. However, this is provided the lens selection function can be well-known and more importantly that the necessary individual parameters (such as the Einstein radius) can be modelled for such large samples of lenses. This will undoubtedly require some level of automation to be realised.

CNNs provide a promising approach to modelling large samples of lenses quickly, but few of these methods have been applied to observational data. Among the more traditional strong lensing techniques, Shajib et al. (2021)'s study fitting 23 lenses from the SLACS sample with a uniform approach is encouraging. Furthermore, Pearson et al. (2021)'s success combining CNNs with `PyAutoLens` on simulated data demonstrates how the two methods could in fact be complementary. In this thesis, we use `PyAutoLens` to model the largest sample of observed galaxy-scale strong lenses with a uniform procedure to this date. This process highlighted the strengths and weaknesses of taking an automated approach to strong lens modelling. Ultimately allowing us to recognise what questions we need to be asking to prepare for the influx of data that will soon be here. We conclude by recapping what we have learnt from such a large undertaking.

In Chapter 2 we began by introducing the uniform method. We used `PyAutoLens`, which takes advantage of nonlinear search chaining, to create a pipeline that was suitable for automation. We gave a detailed account of the pipeline that models the mass distribution of the lens galaxy as a PL+ext

profile simultaneously with its light profile, modelled as a double Sérsic profile, while reconstructing the source galaxy on an adaptive voronoi mesh. In testing we recognised that the uncertainties on the mass profile parameters were overconstrained as a result of the discretization bias described by (Nightingale & Dye, 2015).

To investigate this further we simulated a large sample of mock galaxies similar to our observed sample, creating multiple noise realisations of each lens configuration. We described in detail the mechanism behind the underestimation of errors, which results from stochastic peaks of log-likelihood in the sampling procedure, and used our mock data sample to test to what extent they were underestimated. We developed a likelihood cap method that significantly improved the coverage probabilities of every parameter in the non-linear search when tested on mock data, allowing us to recover the true input values close to the accepted rate. We note that larger mock samples would be necessary to quantify any systematics that could be induced by the discretization effect. This is the first area of further study that we believe future large scale samples would benefit from, since underestimated errors on large samples could lead to very precise but inaccurate inferences.

With this final likelihood cap phase of the method developed we applied the uniform pipeline to a sample of 59 SLACS and BELLS GALLERY lenses with an incredible success rate of 85%. However, from here we set out to learn from the 15% of models that do not initially arrive at a good model fit. Ultimately we arrive at successful model fits for 100% of the sample that we classify into varying degrees of quality. More importantly, we establish that the two most prevalent barriers to automation are cleanly subtracting the foreground lens light of the galaxy, and initialising the first approximate lens model. Thus illuminating two further areas of study to prioritise that would improve future automated studies.

With the mass models of the SLACS and GALLERY lenses constrained, in Chapter 3 we investigated the properties of the sample of galaxies and how they evolve with redshift. We focused mainly on the density profile slope, and compared the slopes constrained in this work to those constrained for a sub-sample of the same lenses using an independent lensing and dynamics technique that combines measurements of the Einstein radius with stellar kinematic constraints (Bolton et al., 2008b; Li et al., 2018). We found that our lensing only technique measures a population average density slope that is slightly steeper than isothermal $\langle\gamma\rangle = 2.075^{+0.023}_{-0.024}$ with intrinsic scatter between galaxies $\sigma_\gamma = 0.172^{+0.022}_{-0.032}$, consistent with traditional lensing and dynamic methods. However, we were unable to detect a correlation between the slopes constrained using the independent methods, suggesting that the assumption of a global powerlaw may not be accurate, potentially breaking down the 'bulge-halo conspiracy'. Although a larger sample would be necessary to quantify this with the current level of

uncertainty.

Notably, tension arises when we model how the population mean density slope depends on redshift and other galaxy population parameters. In particular, the correlation coefficient of the slopes measured via lensing only with total surface mass density is constrained to be negative whereas it is positive for the slopes measured using the lensing and dynamics technique. We propose that this could be due to an inflection zone in the true mass distribution of the galaxies that the lensing only method is more sensitive to. We demonstrated how this behaviour could arise if the lensing only method is constrained locally at the Einstein radius using a one-dimensional axisymmetric toy model.

Future samples will provide us with an unprecedented view of the evolution of the mass profiles of early type galaxies. We showed that the lensing only method will be particularly powerful for such studies given that the measurement uncertainties on the density profile slope do not appear to degrade with redshift like they do for methods that rely on dynamical constraints. However, quantifying the apparent deviations of the true underlying mass profiles from a true PL will be a necessary means to this end.

Finally, in Chapter 4 we measured the weak lensing shears of a sub-sample of our SLACS lenses and compared them to the external shears that were constrained in the strong lensing analysis. We found that on average the shears measured from strong lensing are six times greater than those constrained in the weak lensing analysis. Averaging a shear magnitude of 0.09, these are larger than one would typically expect to measure in the Universe. This implied the origin of the shears could be intrinsic to the lens galaxy, a possibility we explored further by comparing the results to a sample of mock galaxies that were simulated with a gNFW+MGE profile (no external shear was simulated) but fitted with a PL+ext. Further to this, we explored the behaviour of the PL mass distributions of both the observed and mock data samples when we removed the external shear parameters from the fit.

This process confirmed that the inferred external shears in the SLACS and GALLERY lenses are, at least in part, being driven by perturbations internal to the lens galaxy. The external shears in the observations share a very similar distribution of shear orientations to those falsely inferred in the mock data sample which result from the lack of freedom in the PL alone to account for the azimuthal asymmetries that are present in the complex gNFW+MGE profiles. Moreover, the much larger external shears inferred in the observations than in the mocks, the presence of b_4 perturbations only in the observations, and the inconsistency of the observed PL orientation angle when the shear is removed from the fit, strongly suggest that the underlying mass distributions of the observed lens galaxies are more complex than the mocks were simulated to be. These results add merit to the conclusions of Chapter 3 that suggested the inconsistencies between the analysis of the lensing only and lensing and

dynamics slope measurements is a result of the underlying mass distributions not following a single power law.

We discussed the necessity for mass models to include the correct azimuthal degrees of freedom in order to avoid the bias described by Kochanek (2020). We observed this effect most clearly in the mock data sample when the external shears were removed from the fit. Determining what mass model will provide the required azimuthal asymmetries is left for future work. It would be interesting to investigate if the external shears in the strong lens models become consistent with those from weak lensing when the mass models are assumed to be more complex. In fact, this should be a requirement of the lens models if we wish to use the external shears from strong lensing to constrain cosmic shear or combine these shears with weak lensing constraints (Kuhn et al., 2020).

Overall, we have demonstrated the power of automated strong lensing methods to constrain the mass distributions of a large sample of observed galaxy-scale lenses and investigate their evolution. Soon, this will be possible on a much larger scale, allowing for extraordinary insight into not only these types of galaxies and their evolution but also the study of cosmology. This is provided we have the means to take advantage of these systems. The work carried out in this thesis has illuminated areas of future study that we believe will accelerate our ability to appropriately model the incoming thousand fold increase of lenses. These include; ways to cleanly subtract the lens galaxy's light profile of complex lenses, large scale mock studies to quantify and investigate mitigation strategies for the discretization bias inherent to pixel-based methods, and understanding the deviations of the underlying mass distributions of ETGs from a single power law.

Appendix A

SIE model conventions

A number of axis conventions have been used in the literature (Kassiolia & Kovner, 1993; Kormann et al., 1994; Keeton & Kochanek, 1998) to describe an SIE mass profile. This is potentially confusing, but here we show that they are equivalent up to a normalization factor, albeit with different definitions of coordinates. For example the parameterisation of the SIE used internally within PyAutoLens code, following from equation 1.4.14, is

$$\kappa(x, y) = \frac{1}{1+q} \frac{\theta}{\sqrt{x^2 + y^2/q^2}}, \tag{A.0.1}$$

that describes an ellipse of minor to major axis ratio q centred on the origin and aligned with the major axis along the x-axis. This choice reflects a simplification of the parameter space that is sampled during the model fitting process, since the scale factor $(1+q)$ makes the $\theta - q$ degeneracy appear more orthogonal (Nightingale et al., 2018). The analytic deflection angles, that determine the parameters during the model fitting procedure, are given by the following simple form

$$\alpha_x = \frac{2\theta}{1+q} \frac{q}{\sqrt{1-q^2}} \text{arctan}\left(\frac{x\sqrt{1-q^2}}{\sqrt{q^2x^2 + y^2}} \right), \tag{A.0.2}$$

$$\alpha_y = \frac{2\theta}{1+q} \frac{q}{\sqrt{1-q^2}} \text{arctanh}\left(\frac{y\sqrt{1-q^2}}{\sqrt{q^2x^2 + y^2}} \right). \tag{A.0.3}$$

Following Kormann et al. (1994), Bolton et al. (2008a) adopt an intermediate-axis normalization, writing the surface mass density profile as

$$\kappa(x', y') = \frac{R_{\text{Ein}}\sqrt{q}}{2\sqrt{x'^2 + q^2 y'^2}}, \tag{A.0.4}$$

where R_{Ein} is the angular Einstein radius equal to that defined from the area within the tangential

critical curve in equation 1.4.13. The corresponding deflection angles are then

$$\alpha_{x'} = \frac{R_{\rm Ein}\sqrt{q}}{\sqrt{1-q^2}} \text{arcsinh}\left(\frac{\sqrt{1-q^2}}{q}\frac{x'}{\sqrt{x'^2+y'^2}}\right), \tag{A.0.5}$$

$$\alpha_{y'} = \frac{R_{\rm Ein}\sqrt{q}}{\sqrt{1-q^2}} \text{arcsin}\left(\sqrt{1-q^2}\frac{y'}{\sqrt{x'^2+y'^2}}\right). \tag{A.0.6}$$

We will now show that both pairs of deflection angles are in fact identical. Assuming the normalization factor

$$R_{\rm Ein} \equiv \frac{2\theta\sqrt{q}}{1+q}, \tag{A.0.7}$$

we see that the x component of the deflection angle given by Equation A.0.2 is

$$\alpha_x = \frac{R_{\rm Ein}\sqrt{q}}{\sqrt{1-q^2}} \text{arctan}\left(\frac{x\sqrt{1-q^2}}{\sqrt{q^2x^2+y^2}}\right). \tag{A.0.8}$$

Changing coordinates $x = y'$ and $y = x'$, this becomes

$$\alpha_x = \frac{R_{\rm Ein}\sqrt{q}}{\sqrt{1-q^2}} \text{arctan}\left(\frac{y'\sqrt{1-q^2}}{\sqrt{q^2y'^2+x'^2}}\right), \tag{A.0.9}$$

a translation that reflects the difference in which axis the SIE is defined along. That adopted by PyAuytoLens is defined with major axis along the x-axis, while Kormann et al. (1994) define the major axis along the y-axis. Using the trigonometric identity $\arctan(\alpha) = \arcsin\left(\frac{\alpha}{\sqrt{1+\alpha^2}}\right)$, we see that

$$\alpha_x = \frac{R_{\rm Ein}\sqrt{q}}{\sqrt{1-q^2}} \text{arcsin}\left(\sqrt{1-q^2}\frac{y'}{\sqrt{x'^2+y'^2}}\right) \equiv \alpha_{y'}, \tag{A.0.10}$$

recovering the result of Kormann et al. (1994) in Equation A.0.6. Similarly, assuming the same normalization factor (Equation A.0.7) and using the trigonometric identity $\text{arctanh}(\alpha) = \text{arcsinh}\left(\frac{\alpha}{\sqrt{1-\alpha^2}}\right)$,, it can be shown that

$$\alpha_y = \frac{R_{\rm Ein}\sqrt{q}}{\sqrt{1-q^2}} \text{arcsinh}\left(\frac{\sqrt{1-q^2}}{q}\frac{x'}{\sqrt{x'^2+y'^2}}\right) \equiv \alpha_{x'}. \tag{A.0.11}$$

Hence, the deflection angle equations for the SIE adopted by PyAutoLens (Equations A.0.2 and A.0.3) are identical to those for the SIE with intermediate axis normalization (Equations A.0.5 and A.0.6) up to the normalization factor in Equation A.0.7.

Appendix B

Without Lens Light Pipeline

The pipelines that make up the uniform analysis for modelling a lensed image that does not contain the lens galaxy's light are presented in Table B.1. This pipeline was used to analyse the mock data in this work. As well as this, a variation on this analysis, that also includes external shear in the mass model, was used to fit the four lenses that required lens subtracted data to arrive at successful model fits. The initial model fit priors, and those used when we choose not to inform priors with prior passing, are given in Table B.2.

Pipeline	Phase	Galaxy Component	Model	Varied	Prior info	Phase Description
Source Parametric	**SP**[1]	Lens mass	SIE	✓	-	Fit the lens mass model and source light profile, comparing the lensed source model to mock image.
		Source light	Sérsic	✓	-	
Source Inversion	**SI**[1]	Lens mass	SIE		**SP**[3]	Fix lens mass parameters to those from the source parametric pipeline and fit pixelization and regularisation parameters on magnification adaptive pixel-grid.
		Source light	MPR	✓	-	
	SI[2]	Lens mass	SIE	✓	**SP**[3]	Refine the lens mass model parameters, keeping source-grid parameters fixed to those from previous phase.
		Source light	MPR		**SI**[1]	
	SI[3]	Lens mass	SIE		**SP**[3]	Fit BPR pixelization and regularisation parameters, using the lensed source image from **SI**[2] to determine the source galaxy pixel centres. Lens mass parameters are fixed to those from previous phase.
		Source light	BPR	✓	-	
	SI[4]	Lens mass	SIE	✓	**SI**[2]	Refine lens mass model parameters on the BPR grid, keeping lens light and source-grid parameters fixed to those from previous phases.
		Source light	BPR		**SI**[3]	
Mass Total	**MT**[1]	Lens mass	PLEMD	✓	**SI**[4]	Fit the lens mass parameters, now with the slope of the density profile free to vary within the uniform prior [1.5-3.0], all other mass priors are informed from **SI**[4].
		Source light	BPR		**SI**[3]	

Table B.1: Pipeline model components for the analysis which fits to a lensed image which does not contain emission from the lens galaxy.

Model	Parameter	Prior
Elliptical Power-Law (PL)	b ($''$)	$\mathcal{U}(0, 8)$
	γ	$\mathcal{U}(1.5, 3)$
	ε_1	$\mathcal{N}(0, 0.3)$
	ε_2	$\mathcal{N}(0, 0.3)$
	x_c ($''$)	$\mathcal{N}(0, 0.05)$
	y_c ($''$)	$\mathcal{N}(0, 0.05)$
Sersic	$R_{\rm eff}$($''$)	$\mathcal{U}(0, 30)$
	n	$\mathcal{U}(0.5, 5)$
	$\log_{10} I_0(e^- s^{-1})$	$\mathcal{U}(-6, 6)$
	ε_1	$\mathcal{N}(0, 0.5)$
	ε_2	$\mathcal{N}(0, 0.5)$
	x_c ($''$)	$\mathcal{N}(0, 0.1)$
	y_c ($''$)	$\mathcal{N}(0, 0.1)$
Shear	$\gamma_{1_{\rm ext}}$	$\mathcal{U}(-0.2, 0.2)$
	$\gamma_{2_{\rm ext}}$	$\mathcal{U}(-0.2, 0.2)$

Table B.2: The initial priors on every parameter of every light and mass profile fitted in this work. Column 1 gives the model component name. Column 2 gives the parameter. Column 3 gives the prior, where $\mathcal{U}(a, b)$ is a uniform prior between a and b, and $\mathcal{N}(\mu, \sigma)$ is a Gaussian prior with mean μ and variance σ^2. Note that due to prior passing the final priors used to fit a model, corresponding to the results given in this work, will be updated from the above values. The priors of every fit can be found at the following link `https://zenodo.org/record/6104823`.

Appendix C

Inferred Model Parameters

We present the best fit model parameters for all SLACS and GALLERY lenses. The PLEMD+ext mass model parameters are given in Tables C.1 (SLACS) and C.2 (GALLERY). The double Sérsic light model parameters for the Gold sample are presented in Tables C.4 (SLACS), and C.3 (GALLERY). We present the light parameters only for the "Gold" sample since the "Silver" and "Bronze" samples either do not fit the lens light or provide models we do not trust. All errors quoted are those derived from the 68% credible region of the PDF output from `dynesty`.

Class	Lens Name	$b\,('')$	γ	ε_1	ε_2	$\gamma_{1_{\rm ext}}$	$\gamma_{2_{\rm ext}}$	$x_{\rm c}\,('')$	$y_{\rm c}\,('')$
Gold	J0008-0004	$1.178^{+0.021}_{-0.015}$	$2.08^{+0.08}_{-0.07}$	$0.16^{+0.028}_{-0.025}$	$0.014^{+0.031}_{-0.033}$	$-0.006^{+0.011}_{-0.015}$	$-0.023^{+0.017}_{-0.017}$	$-0.015^{+0.012}_{-0.012}$	$0.034^{+0.012}_{-0.014}$
	J0029-0055	$0.971^{+0.026}_{-0.015}$	$2.32^{+0.13}_{-0.13}$	$0.089^{+0.05}_{-0.044}$	$0.089^{+0.062}_{-0.04}$	$0.005^{+0.021}_{-0.017}$	$0.012^{+0.019}_{-0.023}$	$-0.019^{+0.014}_{-0.02}$	$-0.017^{+0.014}_{-0.016}$
	J0157-0056	$0.999^{+0.033}_{-0.034}$	$2.23^{+0.08}_{-0.09}$	$-0.198^{+0.067}_{-0.049}$	$-0.199^{+0.054}_{-0.06}$	$-0.077^{+0.022}_{-0.02}$	$-0.165^{+0.023}_{-0.027}$	$-0.137^{+0.026}_{-0.02}$	$0.031^{+0.026}_{-0.026}$
	J0216-0813	$1.188^{+0.013}_{-0.013}$	$1.99^{+0.05}_{-0.06}$	$0.056^{+0.034}_{-0.035}$	$-0.097^{+0.024}_{-0.029}$	$0.001^{+0.02}_{-0.019}$	$0.009^{+0.016}_{-0.016}$	$0.009^{+0.008}_{-0.006}$	$0.011^{+0.008}_{-0.008}$
	J0252+0039	$1.021^{+0.005}_{-0.006}$	$1.92^{+0.08}_{-0.11}$	$-0.041^{+0.01}_{-0.01}$	$-0.045^{+0.01}_{-0.008}$	$-0.02^{+0.005}_{-0.005}$	$-0.013^{+0.005}_{-0.005}$	$0.0^{+0.006}_{-0.005}$	$-0.005^{+0.006}_{-0.006}$
	J0330-0020	$1.113^{+0.022}_{-0.022}$	$2.15^{+0.02}_{-0.02}$	$-0.017^{+0.052}_{-0.046}$	$-0.119^{+0.042}_{-0.043}$	$0.039^{+0.018}_{-0.02}$	$-0.013^{+0.019}_{-0.018}$	$-0.051^{+0.017}_{-0.026}$	$-0.021^{+0.017}_{-0.026}$
	J0728+3835	$1.274^{+0.029}_{-0.024}$	$1.99^{+0.12}_{-0.1}$	$0.145^{+0.03}_{-0.028}$	$-0.122^{+0.027}_{-0.027}$	$0.056^{+0.015}_{-0.02}$	$-0.037^{+0.012}_{-0.013}$	$-0.006^{+0.013}_{-0.012}$	$0.004^{+0.013}_{-0.012}$
	J0737+3216	$0.982^{+0.009}_{-0.008}$	$2.28^{+0.07}_{-0.07}$	$-0.017^{+0.017}_{-0.014}$	$-0.072^{+0.021}_{-0.02}$	$0.038^{+0.007}_{-0.007}$	$0.103^{+0.009}_{-0.01}$	$-0.008^{+0.004}_{-0.004}$	$-0.006^{+0.004}_{-0.004}$
	J0822+2652	$1.235^{+0.034}_{-0.035}$	$2.1^{+0.08}_{-0.07}$	$0.147^{+0.041}_{-0.043}$	$-0.264^{+0.039}_{-0.038}$	$0.057^{+0.025}_{-0.025}$	$-0.082^{+0.017}_{-0.024}$	$-0.014^{+0.022}_{-0.016}$	$-0.103^{+0.022}_{-0.028}$
	J0841+3824	$1.005^{+0.158}_{-0.139}$	$2.27^{+0.2}_{-0.16}$	$-0.149^{+0.089}_{-0.096}$	$-0.104^{+0.175}_{-0.12}$	$-0.118^{+0.043}_{-0.04}$	$-0.083^{+0.049}_{-0.052}$	$-0.25^{+0.046}_{-0.043}$	$-0.204^{+0.046}_{-0.034}$

Table C.1: Mass distribution model fit parameters for the first ten SLACS lenses.

Class	Lens Name	b ($''$)	γ	ε_1	ε_2	$\gamma_{1_{\rm ext}}$	$\gamma_{2_{\rm ext}}$	$x_{\rm c}$ ($''$)	$y_{\rm c}$ ($''$)
Gold	J0029+2544	$1.395^{+0.074}_{-0.039}$	$2.05^{+0.12}_{-0.15}$	$-0.203^{+0.055}_{-0.078}$	$0.014^{+0.045}_{-0.055}$	$-0.025^{+0.03}_{-0.031}$	$-0.049^{+0.025}_{-0.027}$	$0.09^{+0.023}_{-0.026}$	$0.036^{+0.023}_{-0.026}$
	J0113+0250	$1.293^{+0.037}_{-0.028}$	$1.77^{+0.15}_{-0.11}$	$-0.006^{+0.017}_{-0.019}$	$0.068^{+0.013}_{-0.017}$	$0.041^{+0.013}_{-0.013}$	$0.14^{+0.012}_{-0.012}$	$0.031^{+0.009}_{-0.011}$	$0.008^{+0.009}_{-0.008}$
	J0201+3228	$1.727^{+0.022}_{-0.018}$	$2.09^{+0.09}_{-0.1}$	$-0.114^{+0.026}_{-0.02}$	$-0.02^{+0.019}_{-0.012}$	$0.06^{+0.015}_{-0.012}$	$-0.039^{+0.016}_{-0.008}$	$0.002^{+0.016}_{-0.014}$	$0.026^{+0.016}_{-0.013}$
	J0237-0641	$0.615^{+0.117}_{-0.078}$	$1.91^{+0.18}_{-0.1}$	$-0.117^{+0.033}_{-0.018}$	$0.026^{+0.075}_{-0.101}$	$0.006^{+0.051}_{-0.06}$	$-0.015^{+0.068}_{-0.04}$	$0.146^{+0.033}_{-0.033}$	$0.021^{+0.033}_{-0.027}$
	J0742+3341	$1.684^{+0.134}_{-0.097}$	$2.21^{+0.06}_{-0.08}$	$0.506^{+0.053}_{-0.049}$	$0.001^{+0.061}_{-0.061}$	$0.107^{+0.018}_{-0.024}$	$-0.217^{+0.026}_{-0.025}$	$0.136^{+0.018}_{-0.048}$	$-0.062^{+0.018}_{-0.015}$
	J0755+3445	$2.0^{+0.071}_{-0.055}$	$1.77^{+0.08}_{-0.05}$	$0.156^{+0.016}_{-0.014}$	$0.131^{+0.016}_{-0.012}$	$0.201^{+0.008}_{-0.009}$	$0.268^{+0.007}_{-0.011}$	$0.069^{+0.004}_{-0.011}$	$-0.159^{+0.004}_{-0.005}$
	J0856+2010	$1.157^{+0.071}_{-0.087}$	$2.23^{+0.08}_{-0.09}$	$0.474^{+0.079}_{-0.079}$	$-0.151^{+0.069}_{-0.098}$	$-0.021^{+0.032}_{-0.032}$	$-0.014^{+0.027}_{-0.023}$	$0.171^{+0.021}_{-0.039}$	$-0.063^{+0.021}_{-0.018}$
	J0918+5105	$1.642^{+0.035}_{-0.037}$	$2.38^{+0.16}_{-0.18}$	$-0.024^{+0.057}_{-0.064}$	$-0.081^{+0.023}_{-0.041}$	$-0.246^{+0.023}_{-0.033}$	$-0.122^{+0.007}_{-0.007}$	$-0.019^{+0.027}_{-0.014}$	$0.004^{+0.027}_{-0.016}$
	J1110+2808	$0.902^{+0.029}_{-0.026}$	$2.03^{+0.09}_{-0.07}$	$0.041^{+0.053}_{-0.081}$	$-0.045^{+0.056}_{-0.058}$	$0.114^{+0.042}_{-0.037}$	$-0.09^{+0.025}_{-0.029}$	$-0.106^{+0.03}_{-0.023}$	$-0.141^{+0.03}_{-0.035}$
	J1110+3649	$1.188^{+0.011}_{-0.012}$	$2.23^{+0.07}_{-0.08}$	$-0.024^{+0.007}_{-0.008}$	$-0.016^{+0.013}_{-0.013}$	$0.019^{+0.003}_{-0.003}$	$0.129^{+0.007}_{-0.006}$	$-0.0^{+0.003}_{-0.003}$	$-0.009^{+0.003}_{-0.002}$
	J1116+0915	$1.247^{+0.188}_{-0.156}$	$2.22^{+0.16}_{-0.17}$	$0.071^{+0.097}_{-0.101}$	$-0.393^{+0.069}_{-0.072}$	$0.016^{+0.034}_{-0.045}$	$-0.653^{+0.041}_{-0.053}$	$-0.034^{+0.047}_{-0.032}$	$0.086^{+0.047}_{-0.044}$
	J1141+2216	$1.381^{+0.067}_{-0.071}$	$2.13^{+0.09}_{-0.11}$	$0.243^{+0.058}_{-0.069}$	$0.009^{+0.072}_{-0.085}$	$0.042^{+0.032}_{-0.033}$	$-0.117^{+0.032}_{-0.031}$	$0.088^{+0.04}_{-0.033}$	$-0.035^{+0.04}_{-0.028}$
	J1201+4743	$1.221^{+0.023}_{-0.018}$	$2.74^{+0.05}_{-0.21}$	$-0.095^{+0.019}_{-0.032}$	$0.007^{+0.035}_{-0.043}$	$0.069^{+0.0}_{-0.017}$	$-0.016^{+0.007}_{-0.009}$	$-0.046^{+0.001}_{-0.004}$	$0.025^{+0.001}_{-0.011}$
	J1226+5457	$1.385^{+0.008}_{-0.009}$	$2.24^{+0.07}_{-0.1}$	$-0.074^{+0.011}_{-0.015}$	$0.127^{+0.014}_{-0.016}$	$-0.139^{+0.01}_{-0.007}$	$-0.011^{+0.009}_{-0.01}$	$0.023^{+0.004}_{-0.004}$	$0.006^{+0.004}_{-0.003}$
	J2228+1205	$1.338^{+0.072}_{-0.063}$	$2.2^{+0.14}_{-0.1}$	$-0.262^{+0.049}_{-0.08}$	$0.048^{+0.079}_{-0.057}$	$-0.196^{+0.03}_{-0.035}$	$-0.198^{+0.033}_{-0.022}$	$-0.057^{+0.026}_{-0.026}$	$-0.005^{+0.026}_{-0.031}$
	J2342-0120	$1.313^{+0.048}_{-0.044}$	$2.34^{+0.07}_{-0.09}$	$-0.298^{+0.06}_{-0.034}$	$-0.129^{+0.036}_{-0.025}$	$-0.019^{+0.014}_{-0.021}$	$-0.254^{+0.015}_{-0.008}$	$0.051^{+0.013}_{-0.01}$	$0.02^{+0.013}_{-0.014}$

Table C.2: GALLERY mass distribution model fit parameters.

lens	noise	Sérsic	$R_{\rm eff}$ ($''$)	n	I_0 ($\times10^{-3}$)	ϕ	q	ε_1	ε_2	$x_{\rm c}$ ($\times10^{-3}''$)	$y_{\rm c}$ ($\times10^{-3}''$)
J0029+2544	$0.11^{+0.11}_{-0.045}$	I	$16.84^{+3.89}_{-6.68}$	$3.9^{+0.58}_{-0.5}$	$0.04^{+0.01}_{-0.02}$	-2^{+4}_{-4}	$0.33^{+0.09}_{-0.14}$	$-0.04^{+0.07}_{-0.07}$	$0.5^{+0.16}_{-0.18}$	$0.49^{+0.63}_{-0.8}$	$-0.71^{+0.51}_{-1.02}$
		II	$0.59^{+0.04}_{-0.02}$	$3.5^{+0.04}_{-0.04}$	$17.93^{+0.61}_{-1.19}$	-43^{+3}_{-3}	$0.82^{+0.01}_{-0.0}$	$-0.1^{+0.0}_{-0.0}$	$0.01^{+0.01}_{-0.01}$		
J0113+0250	$0.00032^{+0.0012}_{-0.00018}$	I	$2.43^{+0.82}_{-0.6}$	$1.0^{+0.28}_{-0.23}$	$1.5^{+0.36}_{-0.35}$	-71^{+3}_{-3}	$0.35^{+0.07}_{-0.08}$	$-0.29^{+0.06}_{-0.05}$	$-0.38^{+0.09}_{-0.09}$	$5.0^{+1.41}_{-1.5}$	$-2.03^{+1.76}_{-1.55}$
		II	$1.72^{+0.24}_{-0.2}$	$3.9^{+0.21}_{-0.24}$	$2.15^{+0.5}_{-0.38}$	-3^{+0}_{-0}	$0.54^{+0.01}_{-0.02}$	$-0.04^{+0.01}_{-0.01}$	$0.29^{+0.01}_{-0.01}$		
J0201+3228	160^{+370}_{-130}	I	$2.12^{+0.59}_{-0.35}$	$1.4^{+0.19}_{-0.18}$	$7.65^{+1.47}_{-1.69}$	-47^{+2}_{-3}	$0.79^{+0.02}_{-0.02}$	$-0.12^{+0.01}_{-0.01}$	$-0.01^{+0.01}_{-0.01}$	$0.68^{+0.63}_{-0.56}$	$3.2^{+0.63}_{-0.61}$
		II	$1.09^{+0.08}_{-0.08}$	$4.9^{+0.06}_{-0.08}$	$9.03^{+0.75}_{-0.69}$	-85^{+4}_{-4}	$0.91^{+0.01}_{-0.01}$	$-0.01^{+0.01}_{-0.01}$	$-0.04^{+0.01}_{-0.01}$		
J0237-0641	$1.4^{+15}_{-1.4}$	I	$10.62^{+12.78}_{-7.09}$	$3.5^{+1.3}_{-0.8}$	$0.15^{+0.45}_{-0.12}$	3^{+26}_{-17}	$0.64^{+0.31}_{-0.19}$	$0.03^{+0.2}_{-0.07}$	$0.22^{+0.12}_{-0.21}$	$0.48^{+0.7}_{-0.83}$	$-2.23^{+0.71}_{-0.73}$
		II	$0.91^{+0.11}_{-0.14}$	$4.8^{+0.11}_{-0.47}$	$6.92^{+1.71}_{-0.82}$	80^{+20}_{-316}	$0.98^{+0.02}_{-0.05}$	$0.0^{+0.01}_{-0.01}$	$-0.01^{+0.01}_{-0.01}$		
J0742+3341	$1.1^{+28}_{-1.1}$	I	$10.31^{+8.57}_{-8.83}$	$3.1^{+1.28}_{-0.95}$	$0.24^{+2.42}_{-0.14}$	27^{+7}_{-7}	$0.53^{+0.14}_{-0.11}$	$0.25^{+0.09}_{-0.1}$	$0.18^{+0.09}_{-0.13}$	$-0.19^{+0.58}_{-0.63}$	$1.35^{+0.59}_{-0.68}$
		II	$1.04^{+0.25}_{-0.11}$	$4.6^{+0.16}_{-0.23}$	$9.12^{+1.38}_{-2.27}$	62^{+1}_{-2}	$0.71^{+0.01}_{-0.18}$	$0.14^{+0.01}_{-0.01}$	$-0.1^{+0.02}_{-0.01}$		

Table C.3: Light model parameters for the first five GALLERY lenses in order of Right Ascension.

lens	noise	Sérsic	$R_{\rm eff}$ ($''$)	n	I_0 ($\times10^{-3}$)	ϕ	q	ε_1	ε_2	$x_{\rm c}$ ($\times10^{-3}''$)	$y_{\rm c}$ ($\times10^{-3}''$)
J0008-0004	1500^{+210}_{-460}	I	$27.25^{+1.2}_{-22.87}$	$2.2^{+2.65}_{-0.94}$	$0.01^{+0.0}_{-0.0}$	46^{+3}_{-15}	$0.63^{+0.11}_{-0.23}$	$0.23^{+0.2}_{-0.19}$	$-0.02^{+0.04}_{-0.03}$	$-3.25^{+0.0}_{-2.21}$	$4.05^{+0.0}_{-1.36}$
		II	$1.69^{+0.69}_{-0.09}$	$4.3^{+0.28}_{-0.1}$	$27.93^{+0.0}_{-11.49}$	26^{+3}_{-1}	$0.9^{+0.0}_{-0.01}$	$0.04^{+0.01}_{-0.0}$	$0.03^{+0.0}_{-0.0}$		
J0029-0055	470^{+120}_{-100}	I	$0.33^{+0.02}_{-0.02}$	$2.8^{+0.1}_{-0.09}$	$905.32^{+0.08}_{-80.08}$	22^{+0}_{-0}	$0.9^{+0.0}_{-0.0}$	$0.04^{+0.0}_{-0.0}$	$0.04^{+0.0}_{-0.0}$	$-5.57^{+0.0}_{-0.26}$	$1.92^{+0.0}_{-0.25}$
		II	$3.0^{+0.22}_{-0.17}$	$1.6^{+0.11}_{-0.11}$	$49.4^{+0.0}_{-5.06}$	27^{+1}_{-1}	$0.79^{+0.01}_{-0.01}$	$0.09^{+0.01}_{-0.01}$	$0.07^{+0.01}_{-0.01}$		
J0157-0056	$120^{+30.}_{-26}$	I	$1.86^{+0.56}_{-0.34}$	$0.8^{+0.28}_{-0.13}$	$7.3^{+0.0}_{-1.09}$	-58^{+5}_{-6}	$0.72^{+0.05}_{-0.07}$	$-0.15^{+0.04}_{-0.04}$	$-0.07^{+0.04}_{-0.04}$	$-5.09^{+0.0}_{-0.14}$	$1.65^{+0.0}_{-0.31}$
		II	$1.04^{+0.02}_{-0.06}$	$4.9^{+0.04}_{-0.07}$	$66.77^{+0.01}_{-1.89}$	68^{+0}_{-0}	$0.67^{+0.0}_{-0.0}$	$0.13^{+0.0}_{-0.0}$	$-0.14^{+0.0}_{-0.0}$		
J0216-0813	$850^{+52}_{-70.}$	I	$1.54^{+0.33}_{-0.2}$	$3.9^{+0.32}_{-0.24}$	$115.98^{+0.03}_{-28.97}$	85^{+0}_{-0}	$0.81^{+0.0}_{-0.0}$	$0.02^{+0.0}_{-0.0}$	$-0.11^{+0.0}_{-0.0}$	$-7.13^{+0.0}_{-0.39}$	$3.76^{+0.0}_{-0.44}$
		II	$3.75^{+2.41}_{-0.49}$	$0.8^{+0.27}_{-0.13}$	$16.96^{+0.01}_{-10.44}$	50^{+3}_{-5}	$0.66^{+0.07}_{-0.13}$	$0.2^{+0.14}_{-0.05}$	$-0.04^{+0.04}_{-0.04}$		
J0252+0039	210^{+52}_{-43}	I	$0.94^{+0.03}_{-0.03}$	$0.9^{+0.05}_{-0.05}$	$125.89^{+0.0}_{-3.86}$	-65^{+1}_{-1}	$0.77^{+0.01}_{-0.01}$	$-0.1^{+0.01}_{-0.01}$	$-0.09^{+0.01}_{-0.01}$	$-6.69^{+0.0}_{-0.38}$	$-1.61^{+0.0}_{-0.42}$
		II	$0.62^{+0.05}_{-0.04}$	$4.9^{+0.06}_{-0.1}$	$132.34^{+0.01}_{-11.09}$	54^{+20}_{-22}	$0.99^{+0.01}_{-0.01}$	$0.0^{+0.0}_{-0.0}$	$-0.0^{+0.0}_{-0.0}$		

Table C.4: Light model parameters for the first five SLACS lenses in order of Right Ascension.

Appendix D

Model fits

In this study we categorised the model fits into “Gold”, “Silver”, and “Bronze” depending on the quality of the model fit. The “Gold” fits are presented in Figure D.2 for SLACS lenses and Figure D.1 for GALLERY lenses. The “Silver” lenses are then presented in Figure D.3 and the “Bronze” lens in Figure D.4.

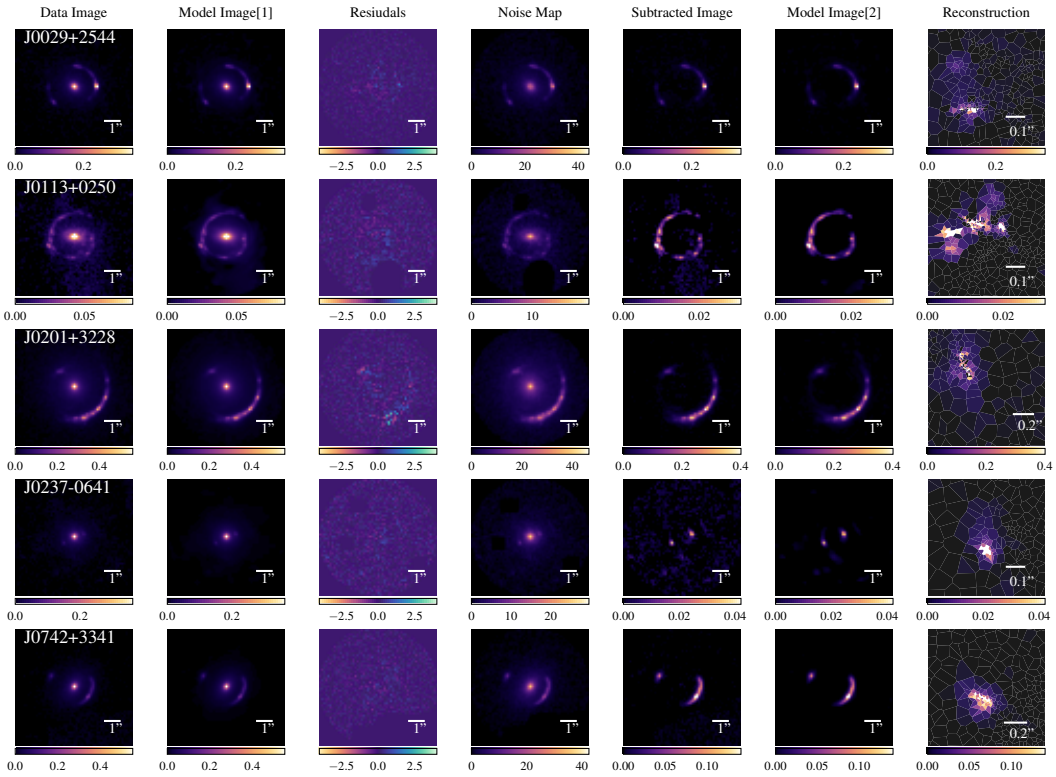

Figure D.1: Model fits for the first five GALLERY lenses in order of Right Ascension. Residuals are the normalised residuals.

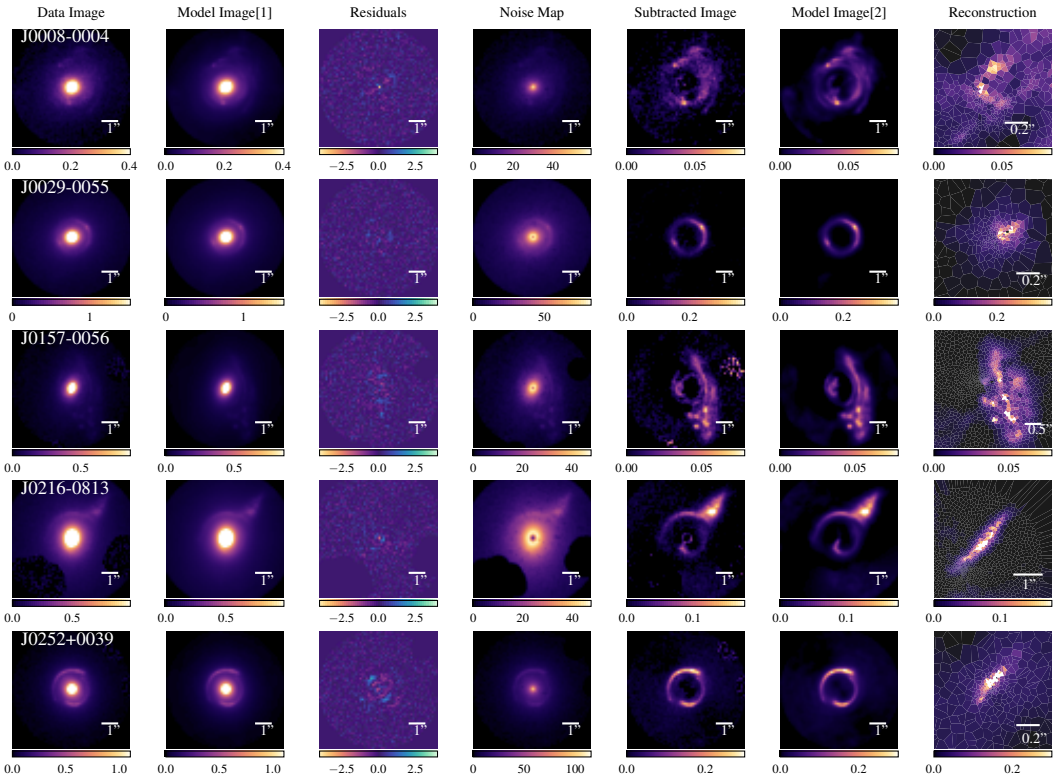

Figure D.2: Model fits for the first five SLACS lenses in the "Gold" sample in order of Right Ascension. Residuals are the normalised residuals.

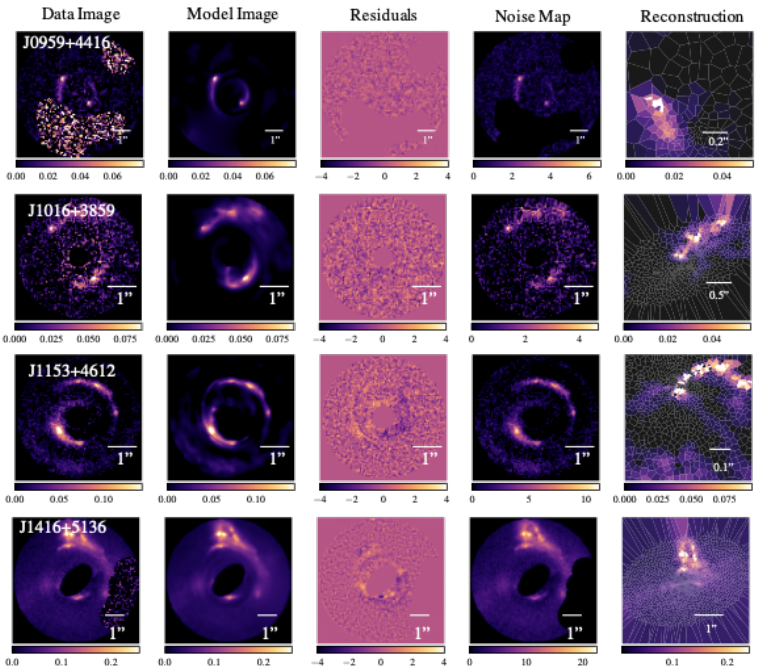

Figure D.3: SLACS "Silver" model fits. Residuals are the normalised residuals.

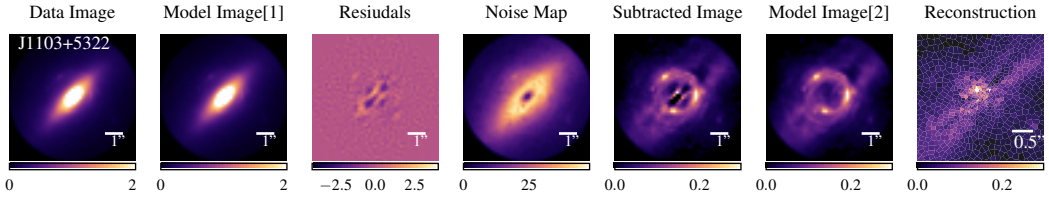

Figure D.4: SLACS "Bronze" model fit. Residuals are the normalised residuals.

Bibliography

Abazajian, K., Adelman-McCarthy, J.K., Ageros, M.A., et al. *The First Data Release of the Sloan Digital Sky Survey*. The Astronomical Journal, **126**(4) (2003), 2081. ISSN 0004-6256.

Abbott, B.P., Abbott, R., Abbott, T.D., et al. *Observation of gravitational waves from a binary black hole merger*. Physical Review Letters, **116**(6) (2016), 1. ISSN 10797114.

Abbott, R., Abbott, T.D., Abraham, S., et al. *Observation of Gravitational Waves from Two Neutron Star–Black Hole Coalescences*. The Astrophysical Journal Letters, **915**(1) (2021), L5. ISSN 2041-8205.

Adams, W.S. *The relativity displacement of the spectral lines in the companion of Sirius*. Proceedings of the National Academy of Sciences,, **II** (1925), 382.

Ade, P.A., Aghanim, N., Arnaud, M., et al. *Planck 2015 results: XIII. Cosmological parameters*. Astronomy and Astrophysics, **594** (2016). ISSN 14320746.

Amorisco, N.C., Nightingale, J., He, Q., et al. *Halo concentration strengthens dark matter constraints in galaxy–galaxy strong lensing analyses*. Monthly Notices of the Royal Astronomical Society, **510**(2) (2022), 2464. ISSN 0035-8711.

Astier, P. *Observational evidence of the accelerated expansion of the universe*. Comptes Rendus Physique, **13**(6) (2012), 521. Understanding the Dark Universe.

Auger, M.W., Treu, T., Bolton, A.S., et al. *The sloan lens ACS survey. IX. colors, lensing, and stellar masses of early-type galaxies*. Astrophysical Journal, **705**(2) (2009), 1099. ISSN 15384357.

Auger, M.W., Treu, T., Bolton, A.S., et al. *The sloan lens ACS survey. X. Stellar, dynamical, and total mass correlations of massive early-type galaxies*. Astrophysical Journal, **724**(1) (2010a), 511. ISSN 15384357.

Auger, M.W., Treu, T., Gavazzi, R., et al. *Dark matter contraction and the stellar content of massive early-type galaxies: Disfavoring "light" initial mass functions*. Astrophysical Journal Letters, **721**(2 PART 2) (2010b), 163. ISSN 20418213.

Barnabè, M., Czoske, O., Koopmans, L.V., et al. *Two-dimensional kinematics of SLACS lenses - II. Combined lensing and dynamics analysis of early-type galaxies at z = 0.08-0.33*. Monthly Notices of the Royal Astronomical Society, **399**(1) (2009), 21. ISSN 00358711.

Bergé, J., Massey, R., Baghi, Q., et al. *Exponential shapelets: basis functions for data analysis of isolated features*. MNRAS, **486**(1) (2019), 544. 1903.05837.

Bertin, E., Arnouts, S. *SExtractor: Software for source extraction.* Astronomy and Astrophysics Supplement Series, **117** (1996), 393.

Birrer, S., Amara, A., Refregier, A. *GRAVITATIONAL LENS MODELING with BASIS SETS*. Astrophysical Journal, **813**(2) (2015). ISSN 15384357.

Birrer, S., Shajib, A.J., Galan, A., et al. *TDCOSMO IV: Hierarchical time-delay cosmography – joint inference of the Hubble constant and galaxy density profiles*. Astronomy & Astrophysics, **1** (2020). URL http://arxiv.org/abs/2007.02941.

Birrer, S., Treu, T., Rusu, C.E., et al. *H0LiCOW - IX. Cosmographic analysis of the doubly imaged quasar SDSS 1206+4332 and a new measurement of the Hubble constant*. Monthly Notices of the Royal Astronomical Society, **484**(4) (2019), 4726. ISSN 13652966.

Birrer, S., Welschen, C., Amara, A., et al. *Line-of-sight effects in strong lensing: Putting theory into practice*. Journal of Cosmology and Astroparticle Physics, **2017**(4) (2017). ISSN 14757516.

Blanton, M.R., Hogg, D.W., Bahcall, N.A., et al. *The Broadband Optical Properties of Galaxies with Redshifts 0.02 < z < 0.22* . The Astrophysical Journal, **594**(1) (2003), 186. ISSN 0004-637X.

Blazek, J., Mandelbaum, R., Šeljak, U., et al. *Separating intrinsic alignment and galaxy-galaxy lensing*. Journal of Cosmology and Astroparticle Physics, **2012**(5) (2012). ISSN 14757516.

Blumenthal, G., Faber, S, M. *CONTRACTION OF DARK MATTER GALACTIC HALOS DUE TO BARYONIC INFALL*. The Astrophysical Journal, **53**(9) (1986), 27. ISSN 1098-6596. URL http://www.elsevier.com/locate/scp.

Boesgaard, A.M., Steigman, G. *Big Bang Nucleosynthesis: Theories and Observations*. Annual Review of Astronomy and Astrophysics, **23**(1) (1985), 319.

Bolton, A.S., Brownstein, J.R., Kochanek, C.S., et al. *The BOSS emission-line lens survey. II. Investigating mass-density profile evolution in the SLACS+BELLS strong gravitational lens sample*. Astrophysical Journal, **757**(1) (2012). ISSN 15384357.

Bolton, A.S., Burles, S., Koopmans, L.V.E., et al. *The Sloan Lens ACS Survey. I. A Large Spectroscopically Selected Sample of Massive Early-Type Lens Galaxies*. The Astrophysical Journal, **638**(2) (2006), 703. ISSN 0004-637X.

Bolton, A.S., Burles, S., Koopmans, L.V.E., et al. *The Sloan Lens ACS Survey. V. The Full ACS Strong-Lens Sample*. The Astrophysical Journal (2008a). ISSN 0004-637X. URL `http://arxiv.org/abs/0805.1931`.

Bolton, A.S., Treu, T., Koopmans, L.V.E., et al. *The Sloan Lens ACS Survey. VII. Elliptical Galaxy Scaling Laws from Direct Observational Mass Measurements*. The Astrophysical Journal, **684**(1) (2008b), 248. ISSN 0004-637X. URL `http://stacks.iop.org/0004-637X/684/i=1/a=248`.

Brownstein, J.R., Bolton, A.S., Schlegel, D.J., et al. *The boss emission-line lens survey (Bells). I. A large spectroscopically selected sample of lens galaxies at redshift 0.5*. Astrophysical Journal, **744**(1) (2012). ISSN 15384357.

Burke, C.J., Aleo, P.D., Chen, Y.C., et al. *Deblending and classifying astronomical sources with Mask R-CNN deep learning*. Monthly Notices of the Royal Astronomical Society, **490**(3) (2019), 3952. ISSN 13652966.

Cabanac, R.A., Alard, C., Dantel-Fort, M., et al. *The CFHTLS strong lensing legacy survey I. Survey overview and T0002 release sample*. Astronomy and Astrophysics, **461**(3) (2007), 813. ISSN 00046361.

Cao, X., Li, R., Nightingale, J.W., et al. *Systematic Errors Induced by the Elliptical Power-law model in Galaxy-Galaxy Strong Lens Modeling*. Research in Astronomy and Astrophysics, **22**(2) (2022). ISSN 16744527.

Cao, X., Li, R., Shu, Y., et al. *LESSER: A catalogue of spectroscopically selected sample of Lyman-α emitters lensed by galaxies*. Monthly Notices of the Royal Astronomical Society, **499**(3) (2020), 3610. ISSN 13652966.

Cappellari, M. *Efficient multi-Gaussian expansion of galaxies*. Monthly Notices of the Royal Astronomical Society, **333**(2) (2002), 400. ISSN 00358711.

Cappellari, M., Scott, N., Alatalo, K., et al. *The ATLAS3D project - XV. Benchmark for early-type galaxies scaling relations from 260 dynamical models: Mass-to-light ratio, dark matter, fundamental plane and mass plane*. Monthly Notices of the Royal Astronomical Society, **432**(3) (2013), 1709. ISSN 13652966.

Castelvecchi, D. *Black hole at the centre of our Galaxy imaged for the first time.* Nature, **605(7910)**(II) (2022), 403.

Cole, S., Aragón-Salamanca, A., Frenk, C.S., et al. *A recipe for galaxy formation*. Monthly Notices of the Royal Astronomical Society, **271**(4) (1994), 781. ISSN 13652966.

Collett, T.E. *The population of galaxy-galaxy strong lenses in forthcoming optical imaging surveys*. Astrophysical Journal, **811**(1) (2015), 20. ISSN 15384357. URL http://dx.doi.org/10.1088/0004-637X/811/1/20.

Collett, T.E., Auger, M.W. *Cosmological constraints from the double source plane lens SDSSJ0946+1006*. Monthly Notices of the Royal Astronomical Society, **443**(2) (2014), 969. ISSN 13652966.

Collett, T.E., Bacon, D.J. *Compound lensing: Einstein zig-zags and high-multiplicity lensed images*. Monthly Notices of the Royal Astronomical Society, **456**(2) (2016), 2210. ISSN 13652966.

Collett, T.E., Smith, R.J. *A triple rollover: A third multiply imaged source at z & 6 behind the Jackpot gravitational lens*. Monthly Notices of the Royal Astronomical Society, **497**(2) (2020), 1654. ISSN 13652966.

Daddi, E., Renzini, A., Pirzkal, N., et al. *Passively Evolving Early-Type Galaxies at 1.4 z 2.5 in the Hubble Ultra Deep Field* . The Astrophysical Journal, **626**(2) (2005), 680. ISSN 0004-637X.

Dawson, K.S., Schlegel, D.J., Ahn, C.P., et al. *The baryon oscillation spectroscopic survey of SDSS-III*. Astronomical Journal, **145**(1) (2013). ISSN 00046256.

Despali, G., Lovell, M., Vegetti, S., et al. *The lensing properties of subhaloes in massive elliptical galaxies in sterile neutrino cosmologies*. Monthly Notices of the Royal Astronomical Society, **17**(July) (2019), 1. URL http://arxiv.org/abs/1907.06649.

Djorgovski, S., Davis, M. *FUNDAMENTAL PROPERTIES OF ELLIPTICAL GALAXIES1*. The Astrophysical Journal,, **313**(1976) (1987), 59.

Dubois, Y., Gavazzi, R., Peirani, S., et al. *AGN-driven quenching of star formation: Morphological and dynamical implications for early-type galaxies*. Monthly Notices of the Royal Astronomical Society, **433**(4) (2013), 3297. ISSN 00358711.

Duffy, A.R., Schaye, J., Kay, S.T., et al. *Impact of baryon physics on dark matter structures: A detailed simulation study of halo density profiles*. Monthly Notices of the Royal Astronomical Society, **405**(4) (2010), 2161. ISSN 00358711.

Dutton, A.A., Treu, T. *The bulge-halo conspiracy in massive elliptical galaxies: Implications for the stellar initial mass function and halo response to baryonic processes*. Monthly Notices of the Royal Astronomical Society, **438**(4) (2014), 3594. ISSN 00358711.

Dye, S., Evans, N.W., Belokurov, V., et al. *Models of the Cosmic Horseshoe gravitational lens J1004+4112*. Monthly Notices of the Royal Astronomical Society, **388**(1) (2008), 384. ISSN 13652966.

Dye, S., Warren, S.J. *Decomposition of the Visible and Dark Matter in the Einstein Ring 00472808 by Semilinear Inversion*. The Astrophysical Journal, **623**(1) (2005), 31. ISSN 0004-637X.

Dyson, F. W., E.A.S., Davidson, C. *A determination of the deflection of light by the Sun's gravitational field, from observations made at the total eclipse of May 29, 1919*. Philosophical Transactions of the Royal Society, **220** (1920), 291.

E. E. Falco, M. V. Gorenstein, I.I.Shapiro. *ON MODEL-DEPENDENT BOUNDS ON H0 FROM GRAVITATIONAL IMAGES: APPLICATION TO Q0957 + 561A,B*. American Astronomical Society, **21**(4) (1985), 289.

Eales, S.A., Baes, M., Bourne, N., et al. *The causes of the red sequence, the blue cloud, the green valley, and the green mountain*. Monthly Notices of the Royal Astronomical Society, **481**(1) (2018), 1183. ISSN 13652966.

Einstein, A. *U berdas Relativitätsprinzip und die aus demselben gezogenen Folgerungen (On the relativity principle and the conclusions drawn from it)*. Jahrbuch der Radioaktivita t und Elektronik, (4) (1907), 411.

Einstein, A. *Die Feldgleichung der Gravitation (The field equations of gravitation)*. Sitzungs berichte, Königlich Preussische Akademieder Wissenschaften (Berlin), (II) (1915), 844.

Einstein, A. *RELATVITY: The Special and the General Theory*. Matheun Co. LTD, London (1920).

Einstein, A. *The Meaning of Relativity*. Princeton University Press (1956).

Enzi, W., Vegetti, S., Despali, G., et al. *Systematic errors in strong gravitational lensing reconstructions, a numerical simulation perspective*. **13**(May) (2019), 1. URL http://arxiv.org/abs/1911.02581.

Fixsen, D.J., Cheng, E.S., Gales, J.M., et al. *The Cosmic Microwave Background Spectrum from the Full COBE FIRAS Data Set* . The Astrophysical Journal, **473**(2) (1996), 576. ISSN 0004-637X.

Fleury, P., Larena, J., Uzan, J.P. *Line-of-sight effects in strong gravitational lensing* (2021). URL http://arxiv.org/abs/2104.08883.

Foreman-Mackey, D., Hogg, D.W., Lang, D., et al. *emcee : The MCMC Hammer* . Publications of the Astronomical Society of the Pacific, **125**(925) (2013), 306. ISSN 00046280.

Galan, A., Peel, A., Joseph, R., et al. *SLIT RONOMY: Towards a fully wavelet-based strong lensing inversion technique*. Astronomy and Astrophysics, **647** (2021). ISSN 14320746.

Gavazzi, R., Marshall, P.J., Treu, T., et al. *Ringfinder: Automated detection of galaxy-scale gravitational lenses in ground-based multi-filter imaging data*. Astrophysical Journal, **785**(2) (2014). ISSN 15384357.

Gavazzi, R., Treu, T., Marshall, P.J., et al. *The SL2S galaxy-scale gravitational lens sample. I. the alignment of mass and light in massive early-type galaxies at z = 0.2-0.9*. Astrophysical Journal, **761**(2) (2012). ISSN 15384357.

Gavazzi, R., Treu, T., Rhodes, J.D., et al. *The Sloan Lens ACS Survey. IV. The Mass Density Profile of Early-Type Galaxies out to 100 Effective Radii*. The Astrophysical Journal, **667**(1) (2007), 176. ISSN 0004-637X.

Gilman, D., Birrer, S., Treu, T. *TDCOSMO III: Dark matter substructure meets dark energy – the effects of (sub)halos on strong-lensing measurements of H_0* (2020). URL http://arxiv.org/abs/2007.01308.

Giraud, E. *A Possible Candidate of Arclike Structure in a Southern Cluster of Galaxies*. ApJ, **334** (1988), L69.

Gomer, M.R., Williams, L.L.R. *Galaxy-lens determination of H_0: constraining density slope in the context of the mass sheet degeneracy*. **13**(July) (2019), 1. URL http://arxiv.org/abs/1907.08638.

Gould, A. *Dynamical evidence for dark matter*. Nuclear Physics B - Proceedings Supplements, **38**(1) (1995), 371.

Graham, A.W., Driver, S.P. *A Concise Reference to (Projected) Sersic R1Quantities, Including Concentration, Profile Slopes, Petrosian Indices, and Kron Magnitudes*. Publications of the Astronomical Society of Australia, **22**(2) (2005), 118. ISSN 14486083.

Guth, E. *New foundation of general relativity*. Physical Review Letters, **21**(2) (1968), 106. ISSN 00319007.

Hartle, J.B. *Gravity: An Introduction to Einstein's General Relativity*. Benjamin Cummings, illustrate edition (2003). ISBN 0805386629. URL http://www.amazon.ca/exec/obidos/redirect?tag=citeulike09-20&path=ASIN/0805386629http://www.amazon.de/exec/obidos/redirect?tag=citeulike01-21&path=ASIN/0805386629http://www.amazon.fr/exec/obidos/redirect?tag=citeulike06-21&path=ASIN/0805386629http://www.amazon.jp/exec/obidos/ASIN/0805386629http://www.amazon.co.uk/exec/obidos/ASIN/0805386629/citeulike00-21http://www.amazon.com/exec/obidos/redirect?tag=citeulike07-20&path=ASIN/0805386629http://www.worldcat.org/isbn/0805386629htt.

Harvey, D., Tam, S.I., Jauzac, M., et al. *The shape of relaxed galaxy clusters and the public release of a HST shape measurement code, pyRRG*. **8**(November) (2019), 1. URL http://arxiv.org/abs/1911.06333.

Hausen, R., Robertson, B.E. *Morpheus : A Deep Learning Framework for the Pixel-level Analysis of Astronomical Image Data* . The Astrophysical Journal Supplement Series, **248**(1) (2020), 20. ISSN 0067-0049. URL http://dx.doi.org/10.3847/1538-4365/ab8868.

He, Q., Li, R., Frenk, C.S., et al. *Galaxy-galaxy strong lens perturbations: line-of-sight haloes versus lens subhaloes*. Monthly Notices of the Royal Astronomical Society, **512**(4) (2021), 5862. URL http://arxiv.org/abs/2110.04512.

He, Q., Nightingale, J., Massey, R., et al. *Testing strong lensing subhalo detection with a cosmological simulation*. **18**(February) (2022), 1. URL http://arxiv.org/abs/2202.10191.

Hewitt, J.N., Turner, E.L., Schneider, D.P., et al. *Unusual radio source MG1131+0456: A possible Einstein ring*. Nature, **333**(6173) (1988), 537. ISSN 00280836.

Hezaveh, Y.D., Dalal, N., Marrone, D.P., et al. *Detection of Lensing Substructure Using Alma Observations of the Dusty Galaxy Sdp.81*. The Astrophysical Journal, **823**(1) (2016), 37. ISSN 0004-637X. URL http://dx.doi.org/10.3847/0004-637X/823/1/37.

Hezaveh, Y.D., Levasseur, L.P., Marshall, P.J. *Fast automated analysis of strong gravitational lenses with convolutional neural networks*. Nature, **548**(7669) (2017), 555. ISSN 14764687.

Hipp, R.D. *SQLite* (2020). URL https://www.sqlite.org/index.html.

Hogg, N.B., Fleury, P., Larena, J., et al. *Measuring line-of-sight shear with Einstein rings: a proof of concept*. **19** (2022), 1. URL http://arxiv.org/abs/2210.07210.

Hubble, E. *Extragalactic nebulae*. ApJ, **64** (1926), 321.

Hubble, E. *A relation between distance and radial velocity among extra-galactic nebulae*. Proceedings of the National Academy of Sciences, **15**(3) (1929), 168. ISSN 0027-8424.

Humphrey, P.J., Buote, D.A. *The slope of the mass profile and the tilt of the Fundamental Plane in early-type galaxies*. Monthly Notices of the Royal Astronomical Society, **403**(4) (2010), 2143. ISSN 00358711.

Humphrey, P.J., Buote, D.A., Gastaldello, F., et al. *A Chandra View of Dark Matter in Early-Type Galaxies* . The Astrophysical Journal, **646**(2) (2006), 899. ISSN 0004-637X.

Hyde, J.B., Bernardi, M. *The luminosity and stellar mass Fundamental Plane of early-type galaxies*. Monthly Notices of the Royal Astronomical Society, **396**(2) (2009), 1171. ISSN 13652966.

Irodotou, D., Fragkoudi, F., Pakmor, R., et al. *The effects of AGN feedback on the structural and dynamical properties of Milky Way-mass galaxies in cosmological simulations*. Monthly Notices of the Royal Astronomical Society, **513**(3) (2022), 3768. ISSN 13652966.

Jiang, G., Kochanek, C.S. *The Baryon Fractions and Mass-to-Light Ratios of Early-Type Galaxies*. The Astrophysical Journal, **671**(2) (2007), 1568. ISSN 0004-637X.

Johansson, P.H., Naab, T., Ostriker, J.P. *Forming early-type galaxies in ΛcDM simulations. I. Assembly histories*. Astrophysical Journal, **754**(2) (2012). ISSN 15384357.

Joseph, R., Courbin, F., Starck, J.L., et al. *Sparse Lens Inversion Technique (SLIT): Lens and source separability from linear inversion of the source reconstruction problem*. Astronomy and Astrophysics, **623** (2019). ISSN 14320746.

Kassiolia, A., Kovner, I. *Elliptic Mass Distributions Versus Elliptical Potentials in Gravitational Lenses*. The Astrophysical Journal, **417**(November 10) (1993), 450.

Keeton, C.R., Kochanek, C.S. *Gravitational Lensing by Spiral Galaxies*. The Astrophysical Journal, **495**(1) (1998), 157. ISSN 0004-637X.

Keeton, C.R., Kochanek, C.S., Seljak, U. *Shear and Ellipticity in Gravitational Lenses*. The Astrophysical Journal, **482**(2) (1997), 604. ISSN 0004-637X.

Kilbinger, M. *Cosmology with cosmic shear observations: A review*. Reports on Progress in Physics, **78**(8) (2015). ISSN 00344885.

Kochanek, C.S. *The Saas Fee Lectures on Strong Gravitational Lensing* (2004), 1. URL `http://arxiv.org/abs/astro-ph/0407232`.

Kochanek, C.S. *Over-constrained Gravitational Lens Models and the Hubble Constant*. **000**(November) (2019). URL `http://arxiv.org/abs/1911.05083`.

Kochanek, C.S. *Over-constrained Models of Time Delay Lenses Redux: How the Angular Tail Wags the Radial Dog*. **000**(March) (2020). URL `http://arxiv.org/abs/2003.08395`.

Koopmans, L.V., Bolton, A., Treu, T., et al. *The structure and dynamics of massive early-type galaxies: On homology, isothermality, and isotropy inside one effective radius*. Astrophysical Journal, **703**(1 PART 2) (2009). ISSN 15384357.

Koopmans, L.V.E., Treu, T., Bolton, A.S., et al. *The Sloan Lens ACS Survey. III. The Structure and Formation of Early-Type Galaxies and Their Evolution since z 1*. The Astrophysical Journal, **649**(2) (2006), 599. ISSN 0004-637X. URL `http://stacks.iop.org/0004-637X/649/i=2/a=599`.

Kormann, R., Schneider, P., Bartelmann, M. *Isothermal elliptical gravitational lens models*. Astronomy & Astrophysics, **284**(September) (1994), 285.

Krist, J. *Tiny Tim: An HST PSF Simulator*. ASP Conference Series, **52**(Astronomical Data Analysis Software and Systems II, ed. R. J. Hanisch, R. J. V. Brissenden, & J. Barnes) (1993), 536.

Kuhn, F.A., Bruderer, C., Birrer, S., et al. *Combining strong and weak lensingestimates in the Cosmos field* (2020), 0. URL `http://arxiv.org/abs/2010.08680`.

Küng, R., Saha, P., More, A., et al. *Gravitational lens modelling in a citizen science context*. Monthly Notices of the Royal Astronomical Society, **447**(3) (2015), 2170. ISSN 13652966.

Le Verrier, U.J.J. *Sur la theórie de Mercure et sur le mouvement du peŕiheĺie decette planeète (On the theory of Mercury and the movement of the perihelion of this planet)*. Comptes Rendus, **49** (1859), 379.

Leauthaud, A., Massey, R., Kneib, J., et al. *Weak Gravitational Lensing with COSMOS: Galaxy Selection and Shape Measurements*. The Astrophysical Journal Supplement Series, **172**(1) (2007), 219. ISSN 0067-0049.

Levasseur, L.P., Hezaveh, Y.D., Wechsler, R.H. *Uncertainties in parameters estimated with neural networks: Application to strong gravitational lensing*. Astrophysical Journal Letters, **850** (2017). ISSN 23318422.

Li, R., Frenk, C.S., Cole, S., et al. *Constraints on the identity of the dark matter from strong gravitational lenses*. Monthly Notices of the Royal Astronomical Society, **460**(1) (2016), 363. ISSN 13652966.

Li, R., Frenk, C.S., Cole, S., et al. *Projection effects in the strong lensing study of subhaloes*. Monthly Notices of the Royal Astronomical Society, **468**(2) (2017), 1426. ISSN 13652966.

Li, R., Li, H., Shao, S., et al. *SDSS-IV Manga: The inner density slopes of nearby galaxies*. Monthly Notices of the Royal Astronomical Society, **490**(2) (2019), 2124. ISSN 13652966.

Li, R., Shu, Y., Wang, J. *Strong-lensing measurement of the total-mass-density profile out to three effective radii for z ˜ 0.5 early-type galaxies*. Monthly Notices of the Royal Astronomical Society, **480**(1) (2018), 431. ISSN 13652966.

Maresca, J., Dye, S., Li, N. *Auto-identification of unphysical source reconstructions in strong gravitational lens modelling*. Monthly Notices of the Royal Astronomical Society, **13**(February 2021) (2020), 1. ISSN 23318422.

Marshall, P.J., Verma, A., More, A., et al. *SPACEWARPS - I. Crowdsourcing the discovery of gravitational lenses*. Monthly Notices of the Royal Astronomical Society, **455**(2) (2016), 1171. ISSN 13652966.

Massey, R., Kitching, T., Richard, J. *The dark matter of gravitational lensing*. Reports on Progress in Physics, **73**(8) (2010). ISSN 00344885.

Massey, R., Refregier, A. *Polar shapelets*. MNRAS, **363**(1) (2005), 197. `astro-ph/0408445`.

Meneghetti, M., Bartelmann, M., Dahle, H., et al. *Arc statistics*. Space Science Reviews, **177**(1-4) (2013), 31. ISSN 00386308.

Miranda, M., MacCiò, A.V. *Constraining warm dark matter using QSO gravitational lensing*. Monthly Notices of the Royal Astronomical Society, **382**(3) (2007), 1225. ISSN 13652966.

More, A., Verma, A., Marshall, P.J., et al. *SPACEWARPS- II. New gravitational lens candidates from the CFHTLS discovered through citizen science*. Monthly Notices of the Royal Astronomical Society, **455**(2) (2016), 1191. ISSN 13652966.

Morningstar, W.R., Hezaveh, Y.D., Levasseur, L.P., et al. *Analyzing interferometric observations of strong gravitational lenses with recurrent and convolutional neural networks*. arXiv, (Mcmc) (2018), 1. ISSN 23318422.

Mukherjee, S., Koopmans, L.V., Benton Metcalf, R., et al. *SEAGLE - I. A pipeline for simulating and modelling strong lenses from cosmological hydrodynamic simulations*. Monthly Notices of the Royal Astronomical Society, **479**(3) (2018), 4108. ISSN 13652966.

Naab, T., Burkert, A., Hernquist, L. *On the Formation of Boxy and Disky Elliptical Galaxies*. The Astrophysical Journal, **523**(2) (1999), L133. ISSN 0004637X.

Naab, T., Ostriker, J.P. *Are disk galaxies the progenitors of giant ellipticals?* Astrophysical Journal, **690**(2) (2009), 1452. ISSN 15384357.

Navarro, J.F., Frenk, C.S., White, S.D.M. *A Universal Density Profile from Hierarchical Clustering*. The Astrophysical Journal, **490**(2) (1997), 493. ISSN 0004-637X.

Nightingale, J., Dye, S., Massey, R. *AutoLens: Automated Modeling of a Strong Lens's Light, Mass and Source*. Monthly Notices of the Royal Astronomical Society, **47** (2018), 1. ISSN 13652966. URL `http://arxiv.org/abs/1708.07377`.

Nightingale, J., Hayes, R., Kelly, A., et al. *PyAutoLens: Open-Source Strong Gravitational Lensing*. Journal of Open Source Software, **6**(58) (2021a), 2825. ISSN 2475-9066.

Nightingale, J.W., Dye, S. *Adaptive semi-linear inversion of strong gravitational lens imaging*. Monthly Notices of the Royal Astronomical Society, **452**(3) (2015), 2940. ISSN 13652966.

Nightingale, J.W., Hayes, R.G., Griffiths, M. *'PyAutoFit': A Classy Probabilistic Programming Language for Model Composition and Fitting*. J. Open Source Softw., **6**(58) (2021b), 2550. URL `https://doi.org/10.21105/joss.02550`.

Nightingale, J.W., He, Q., Cao, X., et al. *Scanning For Dark Matter Subhalos in Hubble Space Telescope Imaging of 54 Strong Lenses*. **26**(2018) (2022), 1. URL `http://arxiv.org/abs/2209.10566`.

Nightingale, J.W., Massey, R.J., Harvey, D.R., et al. *Galaxy structure with strong gravitational lensing: decomposing the internal mass distribution of massive elliptical galaxies*. Monthly Notices of the Royal Astronomical Society (2019). URL http://arxiv.org/abs/1901.07801.

Oh, S., Greene, J.E., Lackner, C.N. *Testing the Presence of Multiple Photometric Components in Nearby Early-type Galaxies Using SDSS*. The Astrophysical Journal, **836**(1) (2017), 115. ISSN 0004-637X.

Oldham, L.J., Auger, M.W. *Dark matter contraction and stellar-mass-to-light ratio gradients in massive early-type galaxies*. Monthly Notices of the Royal Astronomical Society, **476**(1) (2018), 133. ISSN 13652966.

Orban De Xivry, G., Marshall, P. *An atlas of predicted exotic gravitational lenses*. Monthly Notices of the Royal Astronomical Society, **399**(1) (2009), 2. ISSN 00358711.

Oser, L., Ostriker, J.P., Naab, T., et al. *The two phases of galaxy formation*. Astrophysical Journal, **725**(2) (2010), 2312. ISSN 15384357.

Paczynski, B. *Giant luminous arcs discovered in two clusters of galaxies*. Nature, **325**(6105) (1987), 572. ISSN 1476-4687. URL https://doi.org/10.1038/325572a0.

Pearson, J., Maresca, J., Li, N., et al. *Strong lens modelling: comparing and combining Bayesian neural networks and parametric profile fitting*. Monthly Notices of the Royal Astronomical Society, **505**(3) (2021), 4362–4382. URL http://arxiv.org/abs/2103.03257.

Peebles, P.J.E. *Principles of Physical Cosmology* (1993).

Penzias, A., Wilson, R. *A Measurement of Excess Antenna Temperature at 4080 Mc/s.* ApJ, **142** (1965), 419.

Peter Schneider, Christopher S. Kochanek, J.W. *Gravitational Lensing: Strong, Weak and Micro*. Springer Berlin, Heidelberg (2006).

Planck Collaboration, Akrami, Y., Arroja, F., et al. *Planck 2018 results. X. Constraints on inflation* (2018). URL http://arxiv.org/abs/1807.06211.

Poci, A., Cappellari, M., McDermid, R.M. *Systematic trends in total mass profiles from dynamical models of early-type galaxies*. Monthly Notices of the Royal Astronomical Society, **467**(2) (2017), 1397. ISSN 13652966.

Remus, R.S., Dolag, K., Naab, T., et al. *The co-evolution of total density profiles and central dark matterfractions in simulated early-type galaxies*. Monthly Notices of the Royal Astronomical Society, **464**(3) (2017), 3742. ISSN 13652966.

Rhodes, J., Refregier, A., Groth, E.J. *Weak Lensing Measurements: A Revisited Method and Application to Hubble Space Telescope Images* . The Astrophysical Journal, **536**(1) (2000), 79. ISSN 0004-637X. 9905090v2.

Richardson, T.R.G., Stücker, J., Angulo, R.E., et al. *Non-Halo Structures and their Effects on Gravitational Lensing*. **12**(January) (2021), 1. URL http://arxiv.org/abs/2101.07806.

Riemann, B. *U ber die Hypothesen welche der Geometrie zu Grunde liegen (On the Hypotheses that Lie at the Foundations of Geometry)* . (Go ttingen: University of Go ttingen). Habilitationschrift. (1854).

Ritondale, E., Vegetti, S., Despali, G., et al. *Low-mass halo perturbations in strong gravitational lenses at redshift z ˜ 0.5 are consistent with CDM*. Monthly Notices of the Royal Astronomical Society, **485**(2) (2019), 2179. ISSN 13652966.

Robertson, H.P. *Kinematics and world structure*. Astrophysical Journal, **82** (1935), 284.

Rojas, K., Savary, E., Clément, B., et al. *Strong lens systems search in the Dark Energy Survey using Convolutional Neural Networks*. arXiv (2021), 1. URL http://arxiv.org/abs/2109.00014.

Ruff, A.J., Gavazzi, R., Marshall, P.J., et al. *The SL2S galaxy-scale lens sample. II. Cosmic evolution of dark and luminous mass in early-type galaxies*. Astrophysical Journal, **727**(2) (2011). ISSN 15384357.

Salim, S. *Green valley galaxies*. Serbian Astronomical Journal, **1**(189) (2014), 1. ISSN 1450698X.

Schaye, J., Crain, R.A., Bower, R.G., et al. *The EAGLE project: Simulating the evolution and assembly of galaxies and their environments*. Monthly Notices of the Royal Astronomical Society, **446**(1) (2015), 521. ISSN 13652966.

Schneider, P., Sluse, D. *Mass-sheet degeneracy, power-law models and external convergence: Impact on the determination of the Hubble constant from gravitational lensing*. Astronomy and Astrophysics, **559** (2013a), 1. ISSN 00046361.

Schneider, P., Sluse, D. *Source-position transformation – an approximate invariance in strong gravitational lensing*. Astronomy & Astrophysics (2013b), 1. URL http://arxiv.org/abs/1306.4675%0Ahttp://dx.doi.org/10.1051/0004-6361/201322106.

Serra, P., Oosterloo, T., Cappellari, M., et al. *Linear relation between H i circular velocity and stellar velocity dispersion in early-type galaxies, and slope of the density profiles*. Monthly Notices of the Royal Astronomical Society, **460**(2) (2016), 1382. ISSN 13652966.

Sersic, J. *Atlas de Galaxias Australes* (1968).

Shajib, A.J., Treu, T., Agnello, A. *Improving time-delay cosmography with spatially resolved kinematics*. Monthly Notices of the Royal Astronomical Society, **473**(1) (2018), 210. ISSN 13652966.

Shajib, A.J., Treu, T., Birrer, S., et al. *Dark matter haloes of massive elliptical galaxies at z 0.2 are well described by the Navarro-Frenk-White profile*. Monthly Notices of the Royal Astronomical Society, **503**(2) (2021), 2380. ISSN 13652966.

Shankar, F., Sonnenfeld, A., Grylls, P., et al. *Revisiting the bulge-halo conspiracy - II. Towards explaining its puzzling dependence on redshift*. Monthly Notices of the Royal Astronomical Society, **475**(3) (2018), 2878. ISSN 13652966.

Shankar, F., Sonnenfeld, A., Mamon, G.A., et al. *Revisiting the Bulge–Halo Conspiracy. I. Dependence on Galaxy Properties and Halo Mass*. The Astrophysical Journal, **840**(1) (2017), 34. ISSN 15384357. URL http://dx.doi.org/10.3847/1538-4357/aa66ce.

Shu, Y., Bolton, A.S., Brownstein, J.R., et al. *The Sloan Lens ACS survey. XII. Extending strong lensing to lower masses*. Astrophysical Journal, **803**(2) (2015), 1. ISSN 15384357.

Shu, Y., Bolton, A.S., Kochanek, C.S., et al. *THE BOSS EMISSION-LINE LENS SURVEY. III. STRONG LENSING OF Ly α EMITTERS BY INDIVIDUAL GALAXIES* . The Astrophysical Journal, **824**(2) (2016a), 86. ISSN 0004-637X.

Shu, Y., Bolton, A.S., Mao, S., et al. *the Boss Emission-Line Lens Survey. Iv. Smooth Lens Models for the Bells Gallery Sample*. The Astrophysical Journal, **833**(2) (2016b), 264. ISSN 1538-4357.

Shu, Y., Bolton, A.S., Moustakas, L.A., et al. *KILOPARSEC MASS/LIGHT OFFSETS IN THE GALAXY PAIR-Ly α EMITTER LENS SYSTEM SDSS J1011+0143* . The Astrophysical Journal, **820**(1) (2016c), 43. ISSN 0004-637X. URL http://dx.doi.org/10.3847/0004-637X/820/1/43.

Shu, Y., Brownstein, J.R., Bolton, A.S., et al. *The Sloan Lens ACS Survey. XIII. Discovery of 40 New Galaxy-Scale Strong Lenses*. Astrophysical Journal (2017). URL http://arxiv.org/abs/1711.00072.

Silk, J. *Dissipative processes in galaxy formation*. Proceedings of the National Academy of Sciences of the United States of America, **90**(11) (1993), 4835. ISSN 00278424.

Sonnenfeld, A. *Statistical strong lensing. II. Cosmology and galaxy structure with time-delay lenses*. Astronomy & Astrophysics (2021a), 1. URL http://arxiv.org/abs/2109.00009.

Sonnenfeld, A. *Statistical strong lensing. III. Inferences with complete samples of lenses*. Astronomy & Astrophysics (2021b), 1. URL http://arxiv.org/abs/2109.00009.

Sonnenfeld, A. *Statistical strong lensing. IV. Inferences with no individual source redshifts*. Astronomy & Astrophysics (2022), 1. ISSN 0004-6361.

Sonnenfeld, A., Cautun, M. *Statistical strong lensing. I. Constraints on the inner structure of galaxies from samples of a thousand lenses*. Astronomy & Astrophysics (2021). URL http://arxiv.org/abs/2102.08973.

Sonnenfeld, A., Gavazzi, R., Suyu, S.H., et al. *The SL2S Galaxy-scale lens sample. III. lens models, surface photometry, and stellar masses for the final sample*. Astrophysical Journal, **777**(2) (2013a). ISSN 15384357.

Sonnenfeld, A., Treu, T., Gavazzi, R., et al. *Evidence for dark matter contraction and a salpeter initial mass function in a massive early-type galaxy*. Astrophysical Journal, **752**(2) (2012). ISSN 15384357.

Sonnenfeld, A., Treu, T., Gavazzi, R., et al. *THE Sl2S Galaxy-scale lens sample. IV. the dependence of the total mass density profile of early-type galaxies on redshift, stellar mass, and size*. Astrophysical Journal, **777**(2) (2013b). ISSN 15384357.

Speagle, J.S. *Dynesty: A Dynamic nested sampling package for estimating bayesian posteriors and evidences*. Monthly Notices of the Royal Astronomical Society, **493**(3) (2020), 3132. ISSN 23318422.

Spergel, D.N., Verde, L., Peiris, H.V., et al. *First-Year Wilkinson Microwave Anisotropy Probe (WMAP) Observations: Determination of Cosmological Parameters* . The Astrophysical Journal Supplement Series, **148**(1) (2003), 175. ISSN 0067-0049.

Springel, V., Wang, J., Vogelsberger, M., et al. *The Aquarius Project: The subhaloes of galactic haloes*. Monthly Notices of the Royal Astronomical Society, **391**(4) (2008), 1685. ISSN 13652966.

Springel, V., White, S.D.M., Jenkins, A., et al. *Simulating the joint evolution of quasars, galaxies and their large-scale distribution*. Nature, **435**(7042) (2005), 629. URL `http://arxiv.org/abs/astro-ph/0504097%0Ahttp://dx.doi.org/10.1038/nature03597`.

Strateva, I., Ivezić, , Knapp, G.R., et al. *Color Separation of Galaxy Types in the Sloan Digital Sky Survey Imaging Data*. The Astronomical Journal, **122**(4) (2001), 1861. ISSN 00046256.

Suyu, S.H. *Cosmography from two-image lens systems: Overcoming the lens profile slope degeneracy*. Monthly Notices of the Royal Astronomical Society, **426**(2) (2012), 868. ISSN 00358711.

Suyu, S.H., Bonvin, V., Courbin, F., et al. *H0LiCOW - I. H0 Lenses in COSMOGRAIL's Wellspring: Program overview*. Monthly Notices of the Royal Astronomical Society, **468**(3) (2017), 2590. ISSN 13652966.

Suyu, S.H., Marshall, P.J., Hobson, M.P., et al. *A Bayesian analysis of regularized source inversions in gravitational lensing*. Monthly Notices of the Royal Astronomical Society, **371**(2) (2006), 983. ISSN 00358711.

Tagore, A.S., Jackson, N. *On the use of shapelets in modelling resolved, gravitationally lensed images*. Monthly Notices of the Royal Astronomical Society, **457**(3) (2016), 3066. ISSN 13652966.

Tagore, A.S., Keeton, C.R. *Statistical and systematic uncertainties in pixel-based source reconstruction algorithms for gravitational lensing*. Monthly Notices of the Royal Astronomical Society, **445**(1) (2014), 694. ISSN 13652966.

Talbot, M.S., Brownstein, J.R., Bolton, A.S., et al. *SDSS-IV MaNGA: The spectroscopic discovery of strongly lensed galaxies*. Monthly Notices of the Royal Astronomical Society, **477**(1) (2018), 195. ISSN 13652966.

Talbot, M.S., Brownstein, J.R., Dawson, K.S., et al. *The completed SDSS-IV extended Baryon Oscillation Spectroscopic Survey: A catalogue of strong galaxy-galaxy lens candidates*. Monthly Notices of the Royal Astronomical Society, **502**(3) (2021), 4617. ISSN 13652966.

Tam, S.I., Jauzac, M., Massey, R., et al. *The distribution of dark matter and gas spanning 6 Mpc around the post-merger galaxy cluster MS 045103*. Monthly Notices of the Royal Astronomical Society, **496**(3) (2020), 4032. ISSN 13652966.

Tessore, N., Bellagamba, F., Metcalf, R.B. *LENSED: A code for the forward reconstruction of lenses and sources from strong lensing observations*. Monthly Notices of the Royal Astronomical Society, **463**(3) (2016), 3115. ISSN 13652966.

Tiley, A.L., Swinbank, A.M., Harrison, C.M., et al. *The shapes of the rotation curves of star-forming galaxies over the last 10 Gyr*. Monthly Notices of the Royal Astronomical Society, **485**(1) (2019), 834. ISSN 13652966.

Tojeiro, R., Masters, K.L., Richards, J., et al. *The different star formation histories of blue and red spiral and elliptical galaxies*. Monthly Notices of the Royal Astronomical Society, **432**(1) (2013), 359. ISSN 13652966.

Torrey, P., Hopkins, P.F., Faucher-Giguère, C.A., et al. *The impact of AGN wind feedback in simulations of isolated galaxies with a multiphase ISM*. Monthly Notices of the Royal Astronomical Society, **497**(4) (2020), 5292. ISSN 13652966.

Tortora, C., La Barbera, F., Napolitano, N.R., et al. *Systematic variations of central mass density slopes in early-type galaxies*. Monthly Notices of the Royal Astronomical Society, **445**(1) (2014), 115. ISSN 13652966.

Treu, T. *Strong Lensing by Galaxies*. Annu. Rev. Astron. Astrophys., (48) (2010), 87. ISSN 0066-4146. URL http://arxiv.org/abs/1003.5567%0Ahttp://dx.doi.org/10.1146/annurev-astro-081309-130924.

Treu, T., Koopmans, L.V. *The Internal Structure and Formation of Early-Type Galaxies: The Gravitational Lens System MG 2016+112 at z=1.004*. The Astrophysical Journal, **575** (2002), 87.

Treu, T., Koopmans, L.V., Bolton, A.S., et al. *The Sloan Lens ACS Survey. II. Stellar Populations and Internal Structure of Early-Type Lens Galaxies*. The Astrophysical Journal, **640**(2) (2006), 662. ISSN 0004-637X. URL http://stacks.iop.org/0004-637X/640/i=2/a=662.

Treu, T., Koopmans, L.V.E. *Massive Dark Matter Halos and Evolution of Early-Type Galaxies to z 1*. The Astrophysical Journal, **611**(2) (2004), 739. ISSN 0004-637X. URL http://stacks.iop.org/0004-637X/611/i=2/a=739.

Trujillo, I., Conselice, C.J., Bundy, K., et al. *Strong size evolution of the most massive galaxies since z 2*. Monthly Notices of the Royal Astronomical Society, **382**(1) (2007), 109. ISSN 13652966.

Unruh, S., Schneider, P., Sluse, D. *Ambiguities in gravitational lens models: The density field from the source position transformation*. Astronomy and Astrophysics, **601** (2017), 1. ISSN 14320746.

Van De Vyvere, L., Gomer, M.R., Sluse, D., et al. *TDCOSMO: VII. Boxyness/discyness in lensing galaxies: Detectability and impact on H 0*. Astronomy and Astrophysics, **659** (2022a), 1. ISSN 14320746.

Van De Vyvere, L., Sluse, D., Gomer, M.R., et al. *Consequences of the lack of azimuthal freedom in the modeling of lensing galaxies* (2022b). URL `https://github.com/sibirrer/lenstronomy`.

Van De Vyvere, L., Sluse, D., Mukherjee, S., et al. *The impact of mass map truncation on strong lensing simulations*. Astronomy and Astrophysics, **644** (2020), 1. ISSN 14320746.

Van Dokkum, P.G., Whitaker, K.E., Brammer, G., et al. *The growth of massive galaxies since $z = 2$*. Astrophysical Journal, **709**(2) (2010), 1018. ISSN 15384357.

Vegetti, S., Koopmans, L.V. *Statistics of mass substructure from strong gravitational lensing: Quantifying the mass fraction and mass function*. Monthly Notices of the Royal Astronomical Society, **400**(3) (2009), 1583. ISSN 00358711.

Vegetti, S., Koopmans, L.V., Bolton, A., et al. *Detection of a dark substructure through gravitational imaging*. Monthly Notices of the Royal Astronomical Society, **408**(4) (2010), 1969. ISSN 00358711.

Velliscig, M., van Daalen, M.P., Schaye, J., et al. *The impact of galaxy formation on the total mass, mass profile and abundance of haloes*. Monthly Notices of the Royal Astronomical Society, **442**(3) (2014), 2641. ISSN 13652966.

Vika, M., Bamford, S.P., Häußler, B., et al. *MegaMorph - multiwavelength measurement of galaxy structure: Physically meaningful bulge-disc decomposition of galaxies near and far*. Monthly Notices of the Royal Astronomical Society, **444**(4) (2014), 3603. ISSN 13652966.

Vogelsberger, M., Genel, S., Springel, V., et al. *Introducing the illustris project: Simulating the coevolution of dark and visible matter in the universe*. Monthly Notices of the Royal Astronomical Society, **444**(2) (2014), 1518. ISSN 13652966.

Wagner-Carena, S., Park, J.W., Birrer, S., et al. *Hierarchical Inference with Bayesian Neural Networks: An Application to Strong Gravitational Lensing*. The Astrophysical Journal, **909**(2) (2021), 187. ISSN 0004-637X.

Walker, A.G. *On Milne's theory of world structure,*. Proceedings of the London Mathematical Society, Series, **42**(2) (1936), 90.

Walsh, D., Carswell, R.F., Weymann, R.J. *0957+561 A, B: Twin quasistellar objects or gravitational lens?* Nature, **279**(5712) (1979), 381. ISSN 00280836.

Wang, Y., Vogelsberger, M., Xu, D., et al. *Early-type galaxy density profiles from IllustrisTNG - II. Evolutionary trend of the total density profile*. Monthly Notices of the Royal Astronomical Society, **490**(4) (2019), 5722. ISSN 13652966.

Wang, Y., Vogelsberger, M., Xu, D., et al. *Early-type galaxy density profiles from IllustrisTNG – I. Galaxy correlations and the impact of baryons*. Monthly Notices of the Royal Astronomical Society, **491**(4) (2020), 5188. ISSN 0035-8711.

Warren, S.J., Dye, S. *Semilinear Gravitational Lens Inversion*. The Astrophysical Journal, **590**(2) (2003), 673. ISSN 0004-637X.

White, S., Rees, M. *Core ondensation in heavy halos: a two-stage theory for galaxy formation and clustering*. Monthly Notices of the Royal Astronomical Society, **183**(3) (1978), 341.

Witt, H.J., Mao, S. *Probing the structure of lensing galaxies with quadruple lenses: The effect of 'external' shear*. Monthly Notices of the Royal Astronomical Society, **291**(1) (1997), 211. ISSN 00358711.

Wong, K.C., Suyu, S.H., Chen, G.C.F., et al. *H0LiCOW XIII. A 2.4% measurement of H_{0} from lensed quasars: 5.3σ tension between early and late-Universe probes*. Monthly Notices of the Royal Astronomical Society, **498**(1) (2019), 1420–1439. URL `http://arxiv.org/abs/1907.04869`.

Wu, K., L.O..R.M. *The large-scale smoothness of the Universe*. Nature, **397** (1999), 225.

Xu, D., Sluse, D., Schneider, P., et al. *Lens galaxies in the illustris simulation: Power-law models and the bias of the Hubble constant from time delays*. Monthly Notices of the Royal Astronomical Society, **456**(1) (2016), 739. ISSN 13652966.

Xu, D., Springel, V., Sluse, D., et al. *The inner structure of early-type galaxies in the Illustris simulation*. Monthly Notices of the Royal Astronomical Society, **469**(2) (2017), 1824. ISSN 13652966.

York, D.G., Adelman, J., Anderson, Jr., J.E., et al. *The Sloan Digital Sky Survey: Technical Summary*. The Astronomical Journal, **120**(3) (2000), 1579. ISSN 00046256.

Zwicky, F. *On the Masses of Nebulae and of Clusters of Nebulae*. ApJ, **86** (1937), 217.